Development of Ambient-Kinetic Energy Harvester for

Clean Energy Generation

Krit Koyvanich

A Thesis Submitted in Fulfillment of the Requirements for the

Degree of Doctor of Philosophy in Physics

Prince of Songkla University

2018

Development of Ambient-Kinetic Energy Harvester for Clean Energy Generation

Krit Koyvanich

A Thesis Submitted in Fulfillment of the Requirements for the Degree of Doctor of Philosophy in Physics Prince of Songkla University 2018

Thesis Title	Development of Ambient-Kinetic Energy Harvester for Clean Energy Generation
Author	Mr. Krit Koyvanich
Major Program	Physics

Major Advisor

....
(Assoc. Prof. Dr. Nantakan Muensit)

Co-advisor

....
(Assoc. Prof. Dr. Pruittikorn Smithmaotrie)

Examining Committee:

....Chairperson
(Assoc. Prof. Dr. Jompob Waewsak)

....Committee
(Assoc. Prof. Dr. Nantakan Muensit)

....Committee
(Assoc. Prof. Dr. Pruittikorn Smithmaotrie)

....Committee
(Asst. Prof. Dr. Chalongrat Daengngam)

    The Graduate School, Prince of Songkla University, has approved this thesis as fulfillment of the requirements for the Doctor of Philosophy Degree in Physics.

....
(Prof. Dr. Damrongsak Faroongsarg)
Dean of Graduate School

This is to certify that the work here submitted is the result of the candidate's own investigations. Due acknowledgment has been made of any assistance received

....Signature

Assoc. Prof. Dr. Nantakan Muensit

Major Advisor

....Signature

Assoc. Prof. Dr. Pruittikorn Smithmaotrie

Co-advisor

....Signature

(Mr. Krit Koyvanich)

Candidate

I hereby certify that this work has not been accepted in substance for any degree, and is not being currently submitted in candidature for any degree.

....Signature

(Mr. Krit Koyvanich)

Candidate

ชื่อวิทยานิพนธ์	พัฒนาการชุดเก็บเกี่ยวพลังงานจลน์จากสิ่งแวดล้อมเพื่อพลังงานสะอาด
ผู้เขียน	นายกฤช โกยวาณิชย์
สาขา	ฟิสิกส์
ปีการศึกษา	2560

บทคัดย่อ

ช่วงหลายปีที่ผ่านมามีความพยายามอย่างมากในการใช้พลังงานทดแทนที่มีอยู่ในธรรมชาติ ในงานวิจัยนี้แสดงให้เห็นถึงการทดลองและการคำนวณแหล่งพลังงานทางเลือกที่เป็นพลังงานสะอาด ได้จากอุปกรณ์เก็บเกี่ยวพลังงานขนาดเล็กอาศัยหลักไพอิโซอิเล็กทริก อุปกรณ์นี้มีความสามารถดักจับและแปลงพลังงานจากของไหลรอบตัว อุปกรณ์ชนิดแรกคือฟิล์มโพลิเมอร์ไพอิโซอิเล็กทริก โพลิไวนิลลิดีนฟลูออไรด์ (PVDF) ถูกใช้เป็นต้นแบบในการใช้ประโยชน์จากพลังงานจลน์การไหลของของไหลเพื่อทำให้เกิดการสั่น เรียกว่าการสั่นของน้ำวน ในงานวิจัยนี้ได้รับการพัฒนาทางทฤษฎีสอดคล้องกันกับผลการทดลอง แรงดันไฟฟ้าที่เกิดขึ้นจากอุปกรณ์ต้นแบบนี้มีค่า 1.3 มิลลิโวลต์ที่ความถี่ 0.23 Hz และ 4.2 มิลลิโวลต์ที่ 1.02 เฮิร์ต อุปกรณ์ชนิดที่สองคือกังหันลมแนวนอนขนาดเล็กที่สามารถปรับตัวเองได้ (SABSS-HAWT) มีความสามารถดักจับกระแสลมโดยการปรับมุมปะทะ (β) ของใบพัดให้สัมพันธ์กับความเร็วของกระแสลม ประสิทธิภาพการแปลงพลังงาน (η) จากกังหันสามารถจำแนกได้เป็น ประสิทธิภาพเชิงกล (η_{mech}) ประสิทธิภาพทางไฟฟ้า (η_{elec}) โดยมีค่าสูงสุดที่ β เท่ากับ 45° ข้อดีและจุดเด่นของใบพัดที่สามารถปรับระดับเองในงานนี้คือสามารถดักจับและแปลงกระแสลมที่ความเร็ว (U) ต่ำสุดที่ 0.5 m/s และงานวิจัยในส่วนสุดท้ายคือการนำพลังงานที่ได้จากอุปกรณ์เก็บเกี่ยวพลังงานจากการไหลของของไหลป้อนพลังงานเข้าสู่แบตเตอร์รี่เพื่อนำไปใช้ในงานเครือข่ายเซ็นเซอร์ไร้สาย (WSN) ผลแสดงให้เห็นว่าสามารถนำไปใช้งานในทางปฏิบัติได้จริงแม้ว่าพลังงานที่ได้จากการเก็บเกี่ยวนั้นจะมีขนาดน้อยมากเนื่องจากเกิดการสูญเสียระหว่างขั้นตอนการแปลงพลังงาน การนำพลังงานที่ได้ไปใช้ในงานด้านมอนิเตอร์ข้อมูลผ่านเวปไซต์และแอพลิเคชันบนมือถือเป็นตัวอย่างของการนำพลังงานมาใช้ประโยชน์ได้จริง

Thesis title	Development of Ambient-Kinetic Energy Harvester for Clean Energy Generation
Author	Mister Krit Koyvanich
Major Program	Physics
Academic Year	2017

Abstract

For the past several years, considerable effort is focused on the use of renewable energy coming from natural resources. This research has demonstrated experimentally and computationally an alternative source of clean energy derived from small scale energy harvester which taking advantage of the piezoelectric effect. The developed energy harvester is capable of capturing and converting ambient fluid flow. Firstly, piezoelectric polymer films of poly(vinylidene fluoride) or PVDF was used in a prototype and utilized kinetic energy of fluid flow to induce the vibrations. The so-called vortices induced vibration (VIV) was theoretically developed agreed well with experimental results. The voltage outputs from the prototype were obtained for 1.3 mV at 0.23 Hz and 4.2 mV at 1.02 Hz. Secondly, Self-Adjustable Small Scale Horizontal Axis Wind Turbine (SABSS-HAWT) has been proposed in this work. It is able to capture a wind flow by adjustable attacking angle (β) of the blades related to changed wind speed. The efficiency conversion (η) classified by mechanical (η_{mech}) and electrical conversion (η_{elec}) had been maximized at β of 45°. The most advantage and a benefit of self-adjustable blades in this work is its capability to capture and convert the wind flow at a speed with U as low as 0.5 m/s. Finally, Implementations of fluid flow energy harvesting as the generator supplied to batteries for WSN application are possible although the harvested power was low due to the loss during the energy conversion processes. Webpage monitoring and mobile phone application monitoring were successfully demonstrated

ACKNOWLEDGMENTS

First and foremost, I would like to express my sincere gratitude to my advisor Assoc. Prof. Dr. Nantakan Muensit for the continuous support with her patience and immense knowledge of my Ph.D. study and research. Her guidance assisted me all the time of research and writing of this thesis. I could not have imagined having a better advisor and mentor for my Ph.D. study.

Beside my advisor, I would like to thank my supervisor Assoc. Prof. Dr. Pruittikorn Smithmaitrie for his suggestions and also insightful comments. My sincere thanks also goes to all officers in Faculty of Engineering for assisting me in solving problems, my beloved Faculty of Science and technician staffs in the Physics Department for supporting the workshop instruments. I also thank the Prince of Songkla Scholarship by Graduated School (PSU), Center of Excellence in Nanotechnology for Energy (CENE), and Research and Development Office (RDO) for financial support.

Last but not least, I would like to thank my mother Ms. Amon Koyvanich for giving me an education as well as the moral, encouragement and minor financial supports throughout my challenging time.

Krit Koyvanich

CONTENTS

CONTENTS (CONTINUED)

CONTENTS (CONTINUED)

CONTENTS (CONTINUED)

CONTENTS (CONTINUED)

CONTENTS (CONTINUED)

LIST OF TABLES

LIST OF TABLES (CONTINUED)

LIST OF TABLES (CONTINUED)

LIST OF FIGURE

LIST OF FIGURE (CONTINUED)

LIST OF FIGURE (CONTINUED)

LIST OF FIGURE (CONTINUED)

LIST OF FIGURE (CONTINUED)

LIST OF FIGURE (CONTINUED)

LIST OF FIGURE (CONTINUED)

LIST OF FIGURE (CONTINUED)

LIST OF FIGURE (CONTINUED)

LIST OF FIGURE (CONTINUED)

LIST OF FIGURE (CONTINUED)

LIST OF FIGURE (CONTINUED)

CHAPTER 1

INTRODUCTION

1.1 Scientific background and motivation for the research

For some years a remarkable evolution of the self-powered devices can be noted. These devices are conceived to work in a standalone manner, for instance, in rural places and water ways during long time periods. However, the continuity of the power feeding is still a crucial issue. With the development of the electronic components with ultralow consumption, the use of micro-energies opens up new ways for powering energy. By using the piezoelectric-based methods, the needed electrical energy can be harvested on ambient sources such as vibration, temperature variation or water waves. This leads to a clean and renewable energy due to there is no combustion involved in the energy conversion process. This project, thus, aims to develop an energy harvester that permits an effective way of the continuously operation of that device with the reduction of replacing or reloading a great number of batteries. This is because the energy harvester will convert the head pressure on surface water and the flow of water fluctuation into useful electricity. A possible design of the energy harvester. Thus, harvesting energy from vibration and flow using piezoelectric materials provides an ideal energy solution for self-powered wireless (low power) and portable devices.

Piezoelectric materials convert mechanical strain energy into electrical energy. They have high electromechanical coupling and energy density compared to other conversion methods (Priya, 2007). The piezoelectric devices provide high voltage and low currents (Amirtharajah, 1999). However, the voltage and current levels really depend on the design and the particular electrical load circuit. In reality, it is easy to design a system that produces voltages and currents in the useful range. Therefore, like electrostatic conversion, one of the advantages of piezoelectric conversion is the direct generation of the appropriate voltage and current. A second advantage is that no separate voltage source is needed to initiate the conversion process. Additionally, there is generally no need for mechanical stops. Therefore, these devices can be designed to exhibit very little mechanical damping. One can say that piezoelectric converters combine the advantages of electromagnetic and electrostatic conversions. It is also shown that piezoelectric materials are compatible with the MEMS processes thus allow miniaturized piezoelectric energy harvesters for micro devices (Renaud *et al*., 2008; Shen *et al*., 2009).

In recent years, self-powered and micro turbines have been received a considerable amount of attention, and several research groups have demonstrated the effectiveness of small airflow harvesters. Sardini *et al*. (2011) has represented the experimental system of the self-powered wireless sensor permitting air temperature and velocity measurements. To designed and fabricated, demonstrating the air flow harvester with turbine and servomotor can generated electrical energy with the optimum load (*R*) of 5-9 V, 5-45 mW, and efficiency conversion of 7-11% depended on flow velocities by using electromagnetic principle. The system can be used for real-time monitoring of temperature and velocity. The sensor module placed into the duct required no batteries.

Kishore *et al*. (2014) reported an ultra-low start-up speed windmill that consists of a 72 mm diameter horizontal axis wind turbine rotor with 12 alternating polarity magnets around its periphery and a $60\times20\times0.7$ mm^3 piezoelectric bimorph element having a magnet at its tip. This wind turbine operates at very low Reynolds number of around 2×10^4, but still it has reasonably high-power coefficient of about 11% at the optimal tip speed ratio of 0.7. It was found to produce peak electric power of 450 µW at the rated wind speed of 4.2 mph. An extremely low start-up wind speed of 2.4 mph was achieved by operating the bimorph in actuator mode.

Priya *et al*. (2004) studied a technology, "Piezoelectric Windmill", for generating the electrical power from wind energy. The electric power-generation from wind energy is based on piezoelectric effect and utilizes the bimorph actuators. Piezoelectric Windmill consists of piezoelectric actuators arranged along the circumference of the mill in the cantilever form. Using the camshaft gear mechanism an oscillating torque is generated through the flowing wind and applied on the actuators. A working prototype was fabricated utilizing 12 bimorphs ($60\times20\times0.5$ mm^3) having a preload of 23.5 gm. Under a nominal torque level corresponding to normal wind flow and oscillating frequency of 6 Hz, a power of 10.2mW was successfully measured across a load of 4.6 kΩ after rectification. Combined with the wireless transmission, this technology provides a practical solution to the remote powering of sensors and communication devices.

This research focuses on a design, development and prototyping on micro-scale energy harvesting systems. By means of the piezoelectric principle it is possible to operate this harvester at low power of flow velocity. Piezoelectric polymer films are used as a functional part of the harvester. Although they have lower efficiency conversion than piezoelectric ceramics. But the lower elastic modulus is very suitable for scavenging on low power density of fluid flow, while impossible to induce a deformation of piezoelectric ceramic. Moreover, an enhancement of energy conversion has been employed for increasing energy output for the consumption of electronic wireless devices.

1.2 Aims of the research

1.2.1) Simulation-based design of an energy harvesting module using the direct piezoelectric effect.

1.2.2) Prototyping the energy harvester for converting flow energy.

1.2.3) Implementation of developed energy harvester for a low-speed wind to be converted into an electrical power to feed small-scale electronics.

1.3 Thesis outline

The thesis consists of six chapters. The first chapter introduces the motivation of the research and general properties, types of piezoelectric materials. The principle of energy harvesting (EH) and their conceptual applications are mentioned.

Chapter 2 reviews literature of polyvinylidene fluoride or PVDF and its energy harvesting by using vortex induced vibration (VIV) principle. This includes the proposal of using commercial PVDF films as an energy harvester on the water ways. Finally, computational -based models and the efficiency for all the techniques has been presented.

Chapter 3 shows the designed self-adjustable blades small-scale adjustable-horizontal axis wind turbine (SABSS-HAWT) energy harvester, using commercial lead zirconate titanate, $Pb(Zr,Ti)O_3$ or PZT ceramics as converters. The methodology and resultant efficiency and computer fluid analysis (CFA) are discussed.

Chapter 4 represents the SABSS-HAWT components. Its calibration, the controlling system and average generated electric power have been

Chapter 5, the implementations of an electrical output for SABSS-HAWT energy harvester for wireless and mobile technology (internet of things) are demonstrated.

Finally, Chapter 6 summarizes the main conclusion stated in various chapters of this thesis and the prospective research for future work are given.

1.4 State-of-the-art of energy harvester

Energy harvesting or energy scavenging is the process of capturing small amount of energy from ambient environment through various sources of energy. Available energy for harvesting is mainly provided by ambient light (artificial and natural lighting), ambient radio frequency, thermal sources and mechanical sources.

A reduction in size and energy consumptions on sensing applications, including to lower demand in electronic IoT (internet of Things) circuit were exploded novel

research lines on charging batteries related with energy sources. The harvester had been employed by recharging batteries function in various saturations, such as; residential building (Matiko, *et al.*, 2013); industries (Digi-Key's European Editors, 2012); automotive (Elfrink, *et al.*, 2011); the military as for unmanned aerial vehicles (Erturk *et al.*, 2008); and wearable devices (Swallow *et al.*, 2008). These remarkable work increase the possibility to use a harvester as a battery charger, which led to a maintenance free for wireless sensor network applications (Tan *et al.*, 2010). Recent report is the applications in biomedical systems, where the energy could be harvested during cyclic loading. The piezoelectric generator in the so-called bio-micro-electro-mechanical systems (BioMEMS) is for dentistry and drug delivery systems (Allamaeh *et al.*, 2007). Recent research also related to thermal energy harvesting by using human warmth converted body heat into electricity for wireless body network (WBAN). This has been used for monitoring the body state of patients (Hoang *et al.*, 2009).

The major energy harvesting technologies can be summarized by the classifications shown in figure 1.1. Energy harvesting from fluid flow can be arranged as follows: the harvester embedded in kinematic surrounding; there might be directly collects (or convers) flow input into rotation (or vibration) then pass its to transducer; at the end of the system chain, a management circuit was applied for manipulates the electrical signals. This work specifically focuses on piezoelectric harvesting techniques by fluid flow actuation.
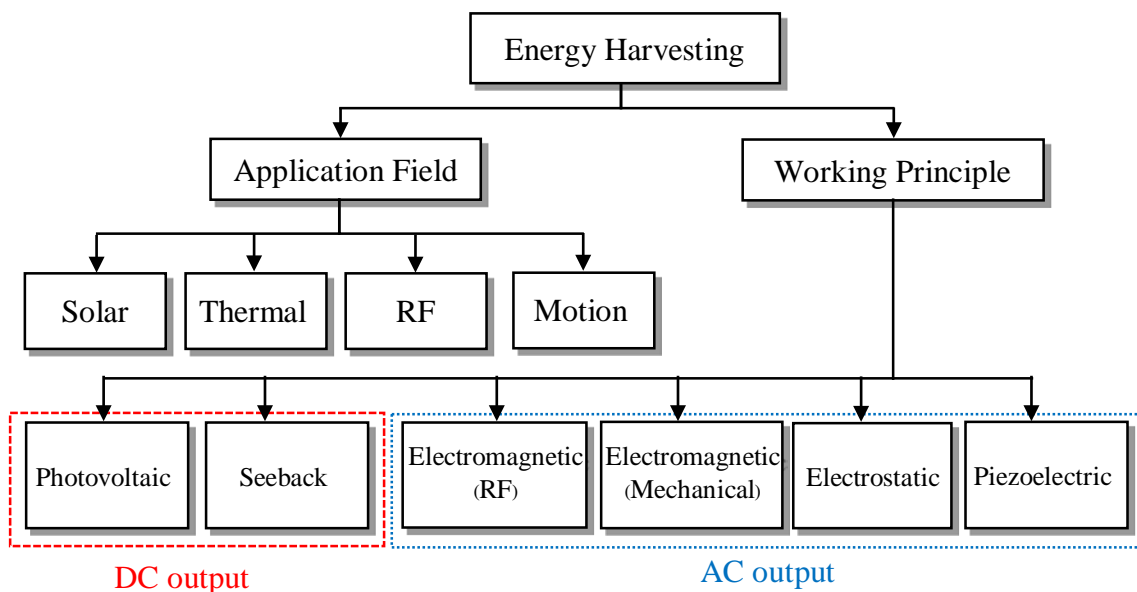
Figure 1.1 The classifications of energy harvesting technology.

The possibility and the effectiveness of extracting energy from fluid flows energy has been under study for years. As a matter of fact, continuous power can potentially be available: from fluctuation and vortex induce vibration (VIV) of fluid flow (Wang and Ko, 2010), including efficiency of harvester and the manipulated circuits (Worthington, 2010). In this work the state of the art of fluid flows based on energy harvesting has been reviewed.

Among available fluid flow energy, piezoelectric transduction offers higher power densities when compared to electrostatic transduction. The first works without an external electrical filed. A so call "poling" field is used only when to generate a polarization (Jordan and Ounaies, 2001). Also, piezoelectric technologies are benefit when compared to electromagnetic ones where the limitations involve with magnet dimension and electrical current circuit miniaturization with micro-fabrication processes (Baborowski, 2004).

1.5 Transduction principles

A piezoelectric substance produces an electric charge on surfaces when a mechanical stress is applied, i.e. the substance is squeezed or stretched. Conversely, a mechanical deformation, i.e. the substance shrinks or expands, is produced when an electric field is applied. It is based on the fundamental structure of crystals lattice that have no center of symmetry. Certain crystalline structures have a charge balance with negative and positive polarization, which neutralize along the imaginary polar axis. When this charge balance is perturbed with external stress onto the crystal mesh, the energy is transferred by electric charge carriers creating a current in the crystal. Conversely, with the piezoelectric effect an external charge input will create an unbalance in the neutral charge state causing mechanical stress.

The relation between piezoelectricity and crystal symmetry are intimately established. The piezoelectric effect is observed in crystals without center of symmetry, and the relationship can be illustrated with mono-crystalline and polycrystalline structures.

In a mono-crystal as shown in figure 1.2, all polar axes of the charge carriers exhibit one-way directional characteristics. These crystals demonstrate symmetry, where the polar axes (dipole) throughout the crystal would lie unidirectional even if it was separate into pieces. The resultant polar axes of pieces would lie in the same direction as the original.
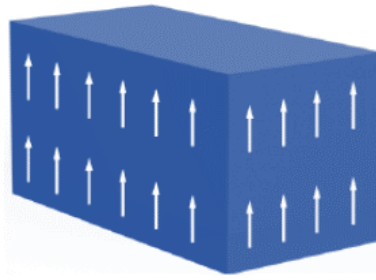
Figure 1.2 Mono-crystal structure with single polar axis (Caliò *et al*., 2014).

In contrast, poly-crystal as shown in figure 1.3, there are different regions within the material that have a different polar axis. It is asymmetrical because there is no point at which the crystal could be cut that would leave the two remaining pieces with the same resultant polar axis.
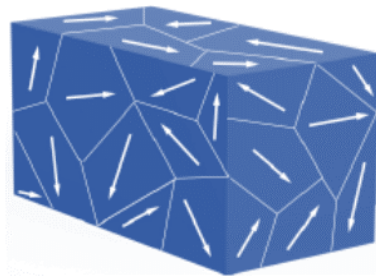
Figure 1.3 Mono-crystal structure with random polar axis (Caliò *et al*., 2014).

In order to produce the piezoelectric effect, the polycrystalline is heated under the application of a strong electric field to the Curie point. The heat allows the molecules to move more freely and the electric field forces the dipoles all of the dipoles in the crystal to line up and face in nearly the same direction of the external field. The remnant polarization are present although the external electric field removed as shown in figure 1.4.
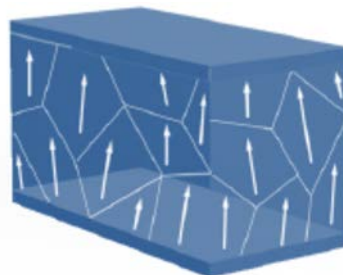
Figure 1.4 The remnant polarization (Caliò *et al*., 2014).

As a result, the material possesses piezoelectric effect: a voltage of the same polarity as of the poling voltage appears between electrodes when the material is compressed; and opposite polarity appears when stretched.

In the contraction, material deformation had been occurred by the different voltage applied on surface, while an AC signal is occupied the material will vibrate at the same frequency as the signal.

1.6 Constitutive equations

A piezoelectric material develops an internal electric filed E when strained S, so call "direct effect". On the contrary, a piezoelectric material experiences strain when an electric field is applied to it, so call "convers effect". Their reactions, electric field and mechanical behavior, can be in either direction. Meaning that depending on the material, an electrical field in one direction can lead to a mechanical reaction in any direction. As a result, equations governing piezoelectricity are usually expressed with tensor. However, to avoid any complicated calculations, either parallel or perpendicular to the strain that is applied to it.

The state of strain is described by a second rank tensor S_{ij}, and the state of stress is also described by a second rank tensor T_{kl}. The relationships relating the stress tensor to the strain tensor, compliance s_{ijkl}, and stiffness c_{ijkl}, are then fourth rank tensors. The relationship between the first rank tensor of electric field E_j and the electric displacement D_i is the second rank tensor of permittivity e_{ij}. Assuming no variation in temperature and low frequencies, constitutive equations of both phenomena thus become:

$$Di \quad = \quad \varepsilon_{ik}^T E_k + d_{ikl}T_{kl} \; ; \qquad \text{(direct effect)} \qquad (1.1)$$

$$S_{ij} \quad = \quad d_{kij}E_k + s_{ijkl}^E T_{kl} \; ; \qquad \text{(convert effect)} \qquad (1.2)$$

where the third rank tensor d_{ikl} and d_{kij} are piezoelectric constant. Superscripts T and E denote that the dielectric constant (clamp permittivity: ε_{ik}) and the elastic constant (Young's Modulus: s_{ijkl}) are measured under conditions of constant stress T and constant electric field E respectively (Heitzler, 1987). For each couple of constitutive equations there is a different piezoelectric coefficient, defined as:

$$d_{ip} \quad \triangleq \quad \left(\frac{\delta D_i}{\delta S_p}\right)^E \quad = \quad \left(\frac{\delta T_p}{\delta E_i}\right)^S \qquad (1.3)$$

$$e_{ip} \quad \triangleq \quad \left(\frac{\delta D_i}{\delta T_p}\right)^E \quad = \quad \left(\frac{\delta S_p}{\delta E_i}\right)^T \qquad (1.4)$$

$$g_{ip} \quad \triangleq \quad \left(\frac{\delta E_i}{\delta S_p}\right)^D \quad = \quad \left(\frac{\delta T_p}{\delta D_i}\right)^S \qquad (1.5)$$

$$h_{ip} \quad \triangleq \quad \left(\frac{\delta E_i}{\delta S_p}\right)^D \quad = \quad \left(\frac{\delta S_p}{\delta D_i}\right)^T \qquad (1.6)$$

where $i, j, k = 1, 2, 3$ and $p, q = 1, 2, 3, 4, 5, 6$. Related of the piezoelectric constants d, e, g, h to each other as following to equation (1.7)-(1.10).

$$d_{ip} = \varepsilon_{ik}^S g_{kp} \tag{1.7}$$

$$e_{ip} = d_{iq} s_{pq}^E \tag{1.8}$$

$$g_{ip} = d_{kp} \big/ \varepsilon_{ik}^S \tag{1.9}$$

$$h_{ip} = g_{iq} s_{cq}^D \tag{1.10}$$

An important parameter is the electromechanical coupling factor k_{ip} which describes the conversion between mechanical and electrical energy. It can be written in terms of coefficients of the material as given by equation (1.11).

$$k_{iq}^2 = \frac{W_i^{(electrical)}}{W_q^{(mechanical)}} = \frac{e_{iq}^2}{\varepsilon_{ik}^S c_{pq}^E} = \frac{e_{iq}^2}{\varepsilon_{ik}^T c_{pq}^E + e_{iq}^2} \tag{1.11}$$

The efficiency of energy conversion η is described, at resonance, as given by equation (1.12):

$$\eta = \frac{\dfrac{k^2}{2(1-k^2)}}{\dfrac{1}{Q} + \dfrac{k^2}{2(1-k^2)}} \tag{1.12}$$

where, Q is the quality factor of the generator (Beeby *et al*., 2006). To understand relation of the electrical quantities as voltage (V) and current (I) are related to the mechanical ones like force (F) and displacement (z), the particular case of a piezoelectric disk can be considered. In this case, from equation (1.1)-(1.2) the following relationships can be obtained by:

$$F_p = M\ddot{z} + \zeta\dot{z} + K_{PE} z - \alpha V \tag{1.13}$$

$$I = \alpha\dot{z} + C_0 \frac{dV}{dt} = -\frac{V}{R} \tag{1.14}$$

where K_{PE} is the stiffness of the piezoelectric disk when it is short-circuited; C_0 is its clamped capacitance and α is the force factor. These equations are derived considering the following approximations:

$$E = -\frac{V}{L}; \quad S = \frac{z}{L}; \quad I = A\frac{dD}{dt}; \quad F_p = AT \tag{1.15}$$

and the featured quantities K_{PE}, C_0, α and can be written as:

$$K_{PE} = \frac{c_{33}^E A}{L}\ ;\quad C_0 = \frac{\varepsilon_{33}^T A}{L}\ ;\quad \alpha = \frac{e_{33} A}{L} \qquad (1.16)$$

where, A and L are the section and thickness of the piezoelectric disk. In a more generic case of a mechanical stress in direction p and an induced electric field in direction i, the open-circuit voltage of a piezoelectric device can be written as follows:

$$K_{PE} = T_p\ g_{ip}\ l \qquad (1.17)$$

assuming that, the voltage coefficient g_{ip} is constant with the stress T, and where l is the gap between the electrodes.

1.7 Piezoelectric energy harvesting devices

Most piezoelectric energy harvesters and transduction principles discussed above are based on vibrational motion, which generates maximum power when the resonant frequencies of the harvesters are matched with the vibrational frequency of the ambient sources. A slight deviation will result in a significant decrease in power generation efficiency. The resonant frequency of a harvester is fixed after its fabrication, while the energy sources could be different from one another. Therefore, a mismatch between the resonant frequency of a harvester and the vibrational frequency of an energy source is easily encountered. Indeed, properly selected materials for the transducer are more significantly important for the peculiarity of the ambient source. Extremely challenged is that a harvester can adjust vibrational frequencies according to the kinematics of surrounding change. To obtain maximum efficiency conversion, understanding of the fundamental of each piezo-energy harvesting by previous works are necessary, a brief introduction and literature review are given in this subsection.

1.7.1) Cantilever beam device

Cantilever beam can be defined as a beam which is supported on only one end. That means one end is fixed and the other end is exposed beyond the support. The beam transfers the load to the support where it can manage the moment of force and shear stress. Moment of force is the tendency of a force to twist or rotate an object. Shear stress is defined as a stress which is applied parallel to the face of a material. In term of the energy harvesting, there rotational motion at the free end had been generated the vibration by excitation force from surrounding source. PZT, which is a poled ferroelectric ceramic of the perovskite structure is the most commonly used materials in the cantilever device.

To understanding and estimate the harvester efficiency, the analytical model of the 'cantilever-based energy harvester' parameterized are discussed in the sub-section

below, which corresponded with section 1.5. The relations between the mechanical and electrical terms are described afterwards.

1.7.1.1) Resonance device

Piezoelectric transducers are frequently used in vibrational movement closed to resonance frequency of an inertial generator. A single degree-of-freedom oscillator gives a good description of a vibrating structure. In case of the mechanical structure it is vibrating with little displacements for which the motion remained linear. The harvesting structure can be simply modeled by the system (rigid mass+piezo element+spring+damper) shown in figure 1.5(a) (Lefeuvre *et al.*, 2006).

(a)   (b)
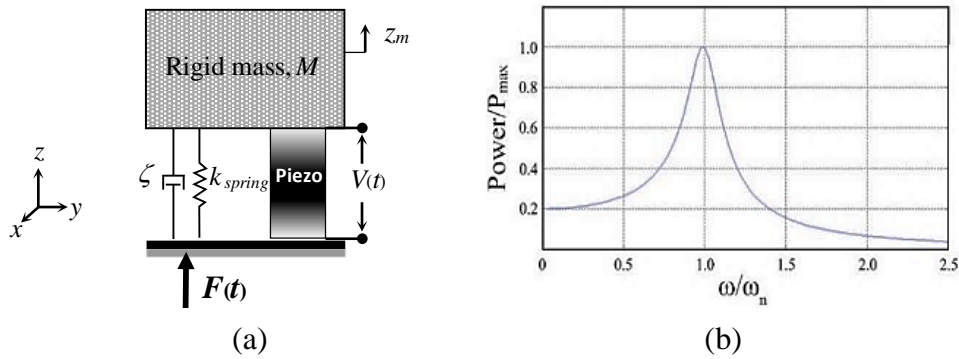
Figure 1.5 (a) Mass-spring-damper-piezo model and (b) peak of the power generated at resonance frequency (Hehn, and Manoli, 2015).

Inertial generators can be described as a second order mass-spring-damper system, along with a piezoelectric element connected parallel to the damper (Lefeuvre *et al.*, 2006). The system is governed by the following equation of motion:

$$M\,\ddot{z}_M(t) + \zeta\,\dot{z}_M(t) + k\,z_M(t) \quad = \quad F(t) \qquad (1.18)$$

where M, ζ, k and $F(t)$ are rigid mass, damping coefficient, spring stiffness and external force applied onto the device respectively. The considered electromechanical structure is a rigid mass bonded on the top of piezoelectric disk, including the bottom side of the disk is bonded on a reference rigid base. Although this model is not based on the experimental structure presented in section 1.5, it actually gives a faithful description of the behavior of the vibration-powered electrical generator. Moreover, only a few measurements are needed to determine all the model parameters. Each a vibration system is characterized by a natural or resonant angular frequency (ω_n) given by equation (1.18).

$$\omega_n = \sqrt{\frac{k}{M}} \tag{1.18}$$

In practical cases, ω_n has to be designed to match the expected ambient excitation angular frequency (ω). The maximum energy as peak power from variation of ω is extracted from the transducer, as shown in figure 4(b).

In case of cantilever oscillation by width (w), length (l), mass (m), elastic modulus (E) of beam parameter; Ghassoul (2007) derived first mode resonance vibration in his thesis as given by equation (1.19).

$$\omega_n(1^{st}) = \frac{1}{2\pi}\sqrt{\frac{(3wEt^3)}{12L^3(0.236m)}} \tag{1.19}$$

Stress generated (T) by a beam vibration of length L_p, and thickness of t_p, attached on elastic beam length L had been presented by Nechibvute $et\ al.$ (2011) as shown in equation (1.20).

$$T_{1^{st}}(x,y) = \frac{3a}{2L^3}E_p t_p \left(L - L_p\right) \tag{1.20}$$

where $a = y(L)$ is the displacement at the cantilever beam end.

The deflection (y) at the tip of a cantilever beam with an area of moment inertia cross section (I) by static load (F) had been presented by Hunt $et\ al.$ (2013) as given in equation (1.21).

$$y = \frac{F \cdot L^3}{3E\ I} \tag{1.21}$$

The power that the transducer can extract while working at resonance can be derived solving equation (1.16) for the rigid mass displacement (z_M). The harvested power is obtained by formulating the portion of the power flowing through the damper related to the transducing mechanism as given by equation (1.22);

$$P_e = \frac{M\ \zeta_e\ a^2}{4\omega_n\ (\zeta_p + \zeta_e)^2} \tag{1.22}$$

where, $a = \omega_n^2 z$ is the acceleration in the case of sinusoidal vibratory excitation. The displacement of the device is $z = Z \cdot \sin(\omega t)$; the transducer and the mechanical damping ratio are given by ζ_e and ζ_p, respectively; where $\zeta = b/2M\ \omega_n$. A high mechanical damping would flatten out the power curve P_e. The maximum extracted power is achieved when the electrical damping equals the mechanical damping as shown in figure 1.6.
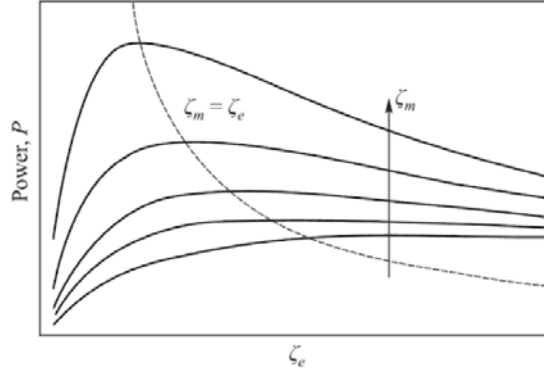
Figure 1.6 Power of the piezoelectric generator as a function of the electrical damping ratio (Hehn *et al.*, 2015).

In similarity of power generated by free end oscillation of cantilever beam, which oscillation beam was consisted with piezo beam attached on steel plate. Mineto *et al.* (2010) summarized the amplitude of the current (I_m) generated as equation (1.23):

$$I_m = \frac{\omega\, w\, t_b\, e_{31}\big[\, \varphi(0) - \varphi(L_b)\,\big]}{2\left(1 + b\, L_p\, \varepsilon_{33}\, \dfrac{\omega R}{t_a}\right)} \tag{1.23}$$

where I_m as function of beam width (w), steel length (L_b), peizo length (L_p), steel thickness (t_b), peizo thickness (t_p), dielectric constant (ε_{33}), piezo constant (e_{31}), resistance (R) and $\varphi(x)$ is slope of beam deflections at *x*-position.

1.7.1.2) Non-Resonant Devices

A novel approach based on non-resonate (nonlinear) oscillators had been presented with inverted pendulum concept by Cottone and colleagues (2015). They were demonstrated that a bi-stable oscillator provided better performances compared to a linear oscillator in terms of the energy extracted from a generic wide spectrum vibration. The designed device interacted with two permanent magnets at one on the tip mass of cantilever, and the other at in front on an adjustable stage. Another attractive bi-stable model, Andò and colleagues (2010) developed a MEMS harvester based on the bi-stable oscillator by added magnetic interaction on the tip mass of cantilever as show in figure 1.7. It can be referred to a mass-spring-damper system, similar to equation (1.17), but with an additional nonlinear term described by a nonlinear (bi-stable: double wall) potential energy function as equation (1.24):

$$M\,\ddot{z}_M(t) + \zeta\,\dot{z}_M(t) + \psi = f(t) \tag{1.24}$$

where M is the mass of beam; ζ is the damping coefficient; $f(t)$ is the excitation force; z is the displacement of the cantilever and ψ is a nonlinear term, which also includes the elastic constant k as given by equation (1.25).

$$\psi \triangleq \frac{\partial U(z)}{\partial z} \tag{1.25}$$

The selected bi-stable potential energy function is a standard quadratic equation as given by equation (1.26) (Bulsara and Gammaitoni, 1996; Gammaitoni and Bulsara, 2002):

$$U(z) \triangleq -\alpha z^2 + \beta z^4 \tag{1.26}$$

where α and β are two parameters that allow determining the potential shape (bi-stable or mono-stable); z is the distance parameter of potential energy function. Without magnetic interaction due to the distance between the two magnets, the system assumed to be linear oscillator system and parabolic function describes the energy as shown in Figure 6(a). The bi-stable behavior is described by the potential energy function of equation (1.20), fixed points at $z = \pm (\alpha/2\beta)^{1/2}$ and the barrier of the potential is $U_0 = (\alpha^2/4\beta)^{1/2}$. Two equilibrium states z_1 and z_2 will appear, while z_0 represents the instable condition as shown in figure 6(b).
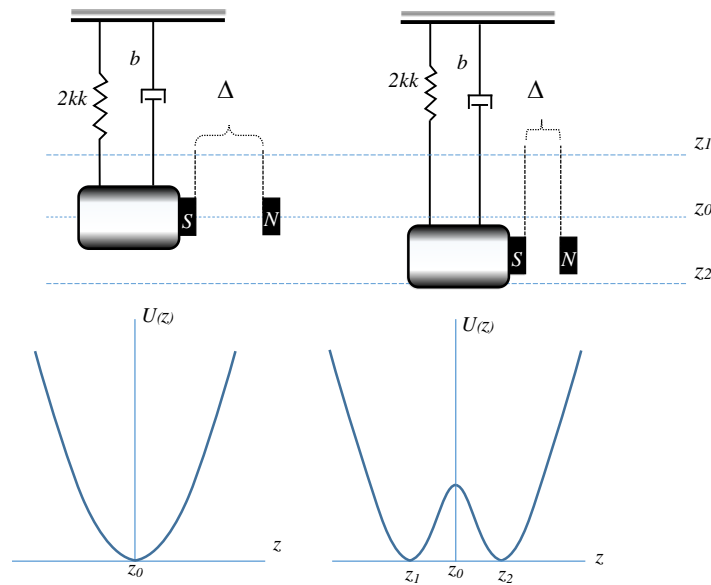
Figure 1.7 The comparison model with respect to potential energy function of (a) linear and (b) nonlinear oscillator (Cottone *et al.* 2009).

The difference in characteristic graphs indicates the effect of the repulsive force given by the magnets. The magnets distance of Δ=1.7 mm has been experimentally detected as the optimal condition of widen vibrational rang for the nonlinear system. In fact, an analysis magnet distance shows the single stable state in the presence of a bi-stability with high potential barrier $\Delta \sim 1.5$ mm, whereas high values of Δ evinces the single stable state dictated by the parabolic shape of the energy function. Figure 1.8(a) shows the displacement spectrum of both systems, which show the improvement of the nonlinear system in terms of displacement and spectrum that appear wider with respect to the linear case as consequence of the nonlinear dynamic. Figure 1.8(b) shows the output voltage as a function of the distance between the two magnets. The nonlinear system has been compared with the linear system, in which the results are in agreement with the theory and the nonlinear system tends asymptotically to the linear system in the presence of a high value of Δ.
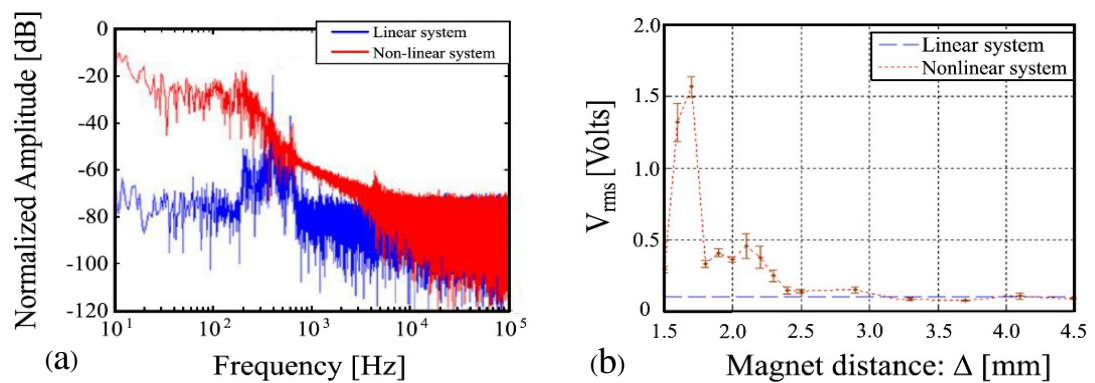
Figure 1.8. The experimental results of linear and nonlinear model (a) amplitude spectrum with respect to frequency and (b) voltage output with the variation of Δ (Cottone *et al.* 2009).

1.7.2) Membrane/elastic devices

Many studies on the previous section have been made to exploit the mechanical vibration (resonance/non-resonance) of a rigid piezoelectric cantilever beam to harvest energy from ambient source. Although, these solid crystal materials show good piezoelectric property, but it cannot be used in biomedical applications due to its rigid, and high acoustic impedance characteristics of piezoelectric crystals. However, flexible piezoelectric polymer exhibited good candidate material for harvesting application. Especially, polyvinylidene fluoride (PVDF) is a poled electroactive polymer and has and approximately 10 times larger piezoelectric response than other polymers and higher piezoelectric voltage constant (Kawai, 1969). Both characteristic piezoelectric properties for PZT ceramic and PVDF polymer are show in table 1. For the harvesting

implementation, the main difference in these 2 cases is the way they apply force to sensing elements. For the flexible materials, thin membrane transfers the external force directly to the sensing elements, while the rigid material transducer need seismic mass to apply the forces for the accelerate detection. Moreover, embedding in fluid flow and wearable implementation is an available for energy harvesting by membrane flexible devices.

Table 1.1 Properties of PZT and PVDF (Roundy, 2003)

Properties	d_{31} (10^{-2} m/V)	k_{31} (CV/Nm)	d_{33} (10^{-2} m/V)	k_{33} (CV/Nm)	Elastic modulus (N/m^2)	Tensile strength (N/m^2)
PZT	320	0.44	650	0.75	5.0	2.0
PVDF	20	0.11	30	0.16	0.3	5.2

Taylor *et al*. (2001) proposed a new device that uses piezoelectric polymers to convert the mechanical flow energy, from oceans and rivers into electrical power. That generator device was inspired by the bodies and the motion of eels, which consists of a bluff body and flexible piezoelectric films. Under fluid flow condition, eel generators were applied by traveling vortices pressure behind a bluff body to strain the piezoelectric elements which lead polymer trip oscillates in a motion similar to the undulating motion of the eel. On the experimental results, harvesting device with 8 piezo-polymer strips obtained a peak voltage about for 0.5 m/s of flow velocity and the mechanical to electrical power conversion efficiency per element was about 37%.

Simultaneously, Allen and Smith (2001) performed the similar experiments of the piezo eel generator from the flow energy. Their objective is to maximize the strain energy and mechanical power by coupling the unsteady flow field with the vibration of the membrane. The resonance condition to achieve the optimal coupling was about reduce damping effect on the vortex field. The additional mathematic model of membrane behavior under fluid flow condition by using Euler-Bernoulli as given by equation (1.27):

$$\frac{d^2 y}{dt^2} + \frac{\zeta}{\rho_{ell}} \frac{d y}{dt} + \frac{EI}{\rho_{ell}} \frac{d^4 y}{dx^4} - T \frac{d^2 y}{dx^2} \ = \ f(x,t) \qquad (1.27)$$

where ρ_{ell}, ζ and T is mass density, damping coefficient and stress generated of piezoelectric membrane, respectively; coefficient of EI / ρ_{ell} represents the effective stiffness of the eel in response to bending; and force function $f(x, t)$ is the effect of the fluid on the membrane.
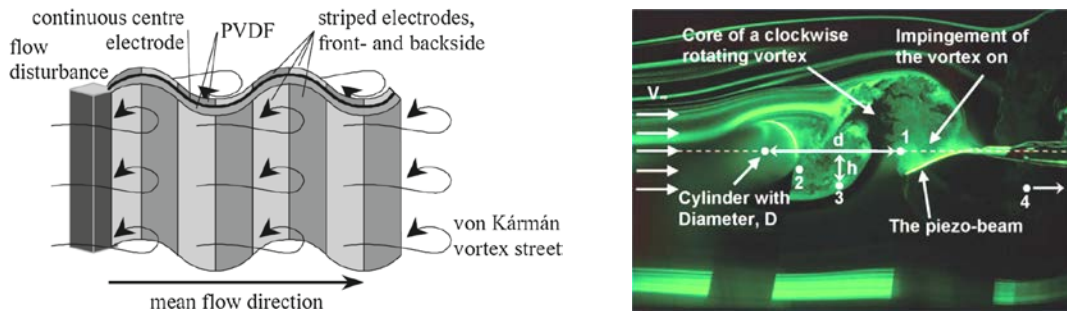
Figure 1.9. (a) Double layer piezoelectric PVDF flag and (b) cantilever PVFD beam behind a cylinder in the flow.

Three years later, Pobering and Schwesinger (2004) also presented a design for the electrical generator that is similar to the previous mentions of eel concept above. It consists of a piezo membrane like flag made of two embedded PVDF layers. The flag is attached to a rigid bar that generates the separation of incoming flow, which results to the instability flow separation travel along the top and bottom sides of the flag as shown in figure 1.9(a). This induce the fluttering of the flag and produced charges on their surfaces because of the flow pressure stress which were applied on the piezo flag. Power density approximated for this design was about 11-32 W/m^2.

The other study on polymerized piezoelectric membrane as a functional of cantilever beams was presented by Akaydin and his collaborate (2010). The energy harvesting ability of a PVDF beam in unsteady turbulent air flows was performed in over 10,000 for Reynolds number range. For the experimental detail, optimal the location of the harvester in the turbulent wake of buff body had been performed, in which shed vortices pass along the surfaces of the polymerized PVDF beam as shown in figure 1.9(b). The coupled interaction numerical simulation that related the aerodynamics subject, which structural of beam was modeled with a single degree of freedom as similar in the subsection 1.7.1.1 by figure 1.5. The governing equation of the electromechanical respond were described in equation (1.13) - (1.14) of section 1.5. Resonance of PVDF beam vibration at 47.6 Hz was existed at a flow velocity of 7.23 m/s and corresponding to the with Strouhal frequency. Maximum power generated by peak to peak voltage was found to be 4 mW by the resistance of 0.1 MΩ. In the additional Based on the numerical simulations, the mechanical power; the power harvested; and the conversion efficiency was about 60uW, 7uW, and 11%, respectively.

1.7.3) Rotational devices

Although the piezoelectric effect is inherently related to axial elongations, several device configurations were proposed as rotary harvesters, mainly by transforming a rotatory excitation into a longitudinal strain (Yeatman, 2012).

Khameneifar and colleagues (2013; 2011) proposed the models and experimental by combining the piezoelectric cantilever concept to a rotating shaft. The harvesting energy from rotary motion is as shown in figure 1.10(a), and a motional model with the Cartesian coordinate system in figure 1.10(b). The Euler-Bernoulli equation of a beam with small deformation, the partial differential equation describing vibrations of the cantilever beam is given by equation (1.28):

$$EI \frac{\partial^4 w(\xi,t)}{\partial \xi^4} + \rho A L^4 \frac{\partial^2 w(\xi,t)}{\partial t^2} = 0 \tag{1.28}$$

where the deflection of the beam relative to its base is denoted by $w(\xi, t)$; $\xi = x/L$ is the normalized position x along the beam of length L; E is Young's modulus; I the area moment of inertia; ρ the mass density; and A the cross-sectional area of the beam.
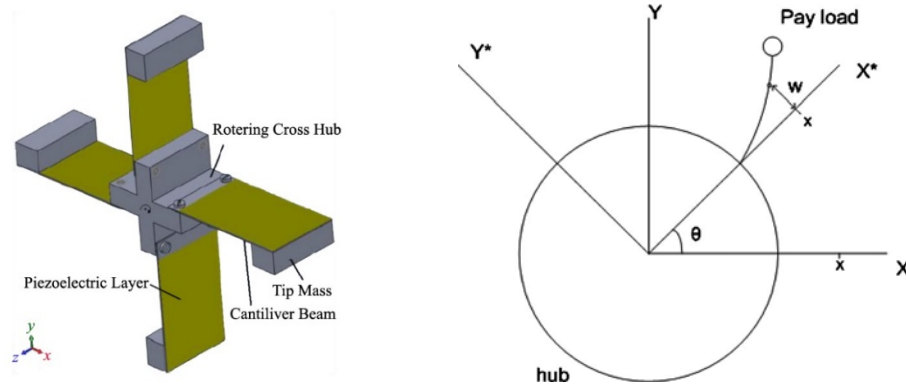
Figure 1.10. (a) Schematic view of the energy harvester mounted on a rotating hub (Khameneifar, 2011) (b) system for harvesting energy from rotary motion application (Khameneifar, 2013)

Due to the uniform distribution of the piezoelectric layers, E, I, ρ, and A are constants. This approach allows employing piezoelectric devices for monitoring rotating machines like turbines. The device used a single PZT element with a beam length of 5 cm and a single tip mass of 105 g. The power was about 6.4 mW at 40 kΩ and an output voltage of about 16 V (Khameneifar, 2013).

1.8 Circuitry

Energy harvesting systems deal with power management with scientific and technological challenges. Thes management circuits are responsible for passing conditions of harvested energy from a generator to a consumptive device and in most cases supply to battery as a storage element. A typical schematic diagram of a power manager is shown in figure 1.11. A power management unit is available both for DC and AC sources, and a bridge rectifier unit is necessary as an alternate source. They

typically employ a DC-DC converter is mainly used for turning impedance by modifying a voltage to battery charging level. In case of direct current sources, the maximum power point tracker (MPPT) is method for turning impedance for the maximum power output.
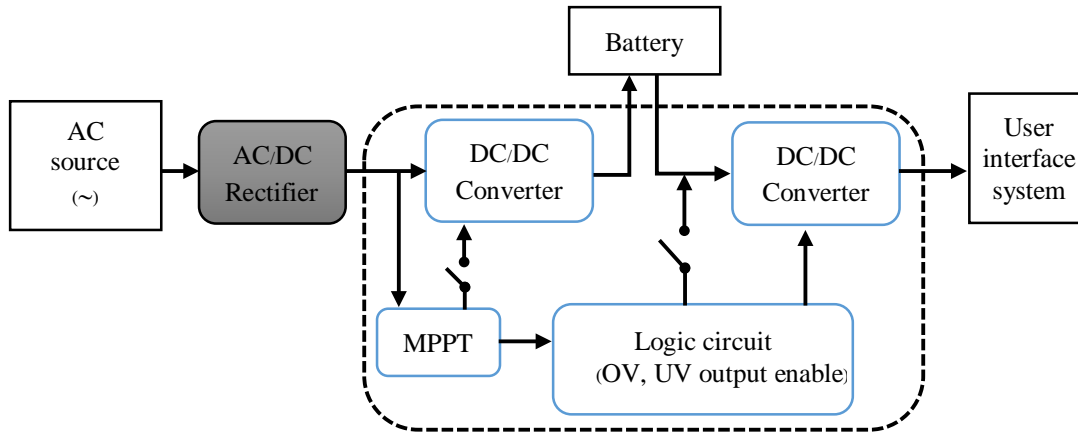
Figure 1.11 Typical schematic diagram of a power management unit.

1.8.1) Regular diode bridge rectifier

More over valuable of MPPT unit for DC sources, Yi and colleagues presented concept of energy-adaptive MPPT power management unit for harvesting energy from very low-level vibration (Yi *et al*., 2008). The logic circuitry is assigned to maintain the charge and discharge phases of the battery. The energy-adaptive MMPT allows the PMU to activate different operation modes according to the available power level. The harvested energy is processed by an ac-dc voltage increase followed by Fully-integrated time-interleaved charge pumps with variable conversion ratios for higher efficiency. The AC-DC converter can be followed by a DC-DC converter, for power optimization and voltage regulation. The simplest rectifier can be a diode bridge rectifier (Ottman, 2002).
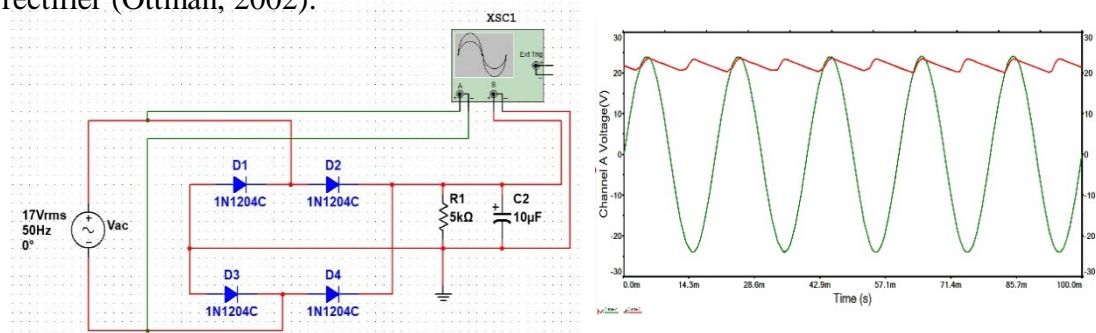
Figure 1.12 Circuit simulation by NI Multisim 14.0 (a) Diode bridge rectifier (b) the detected voltage results (green: input; red: output).

1.8.2) The parallel-synchronized switch harvesting on inductor (SSHI) circuit

Other implementation of a circuital interface is the parallel-synchronized switch harvesting on inductor (SSHI), which is composed of a non-linear processing circuit connected in parallel with the piezoelectric element electrodes and the input of the rectifier bridge. This process from the circuit can increase the voltage amplitude on the capacitor of the piezoelectric element and effort to enhance the coupling coefficient of the electromechanical system using piezo-materials. The nonlinear processing circuit of parallel-SSHI is very simple, comprising the addition of an inductor and a switch, as shown in figure 1.13.
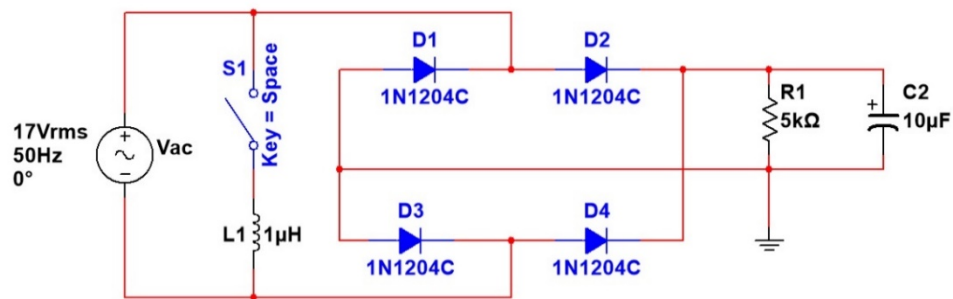
Figure 1.13 Synchronized switch harvesting on inductor circuit

1.8.3) The series-synchronized switch harvesting on inductor circuit

In a similar concept, a series-SSHI rectifier allows to dramatically increase the voltage output or to obtain the same output of a standard interface device while reducing the volume of the piezoelectric element. They consist of an inductor-switch branch added in series to the piezoelectric element, there series-SSHI rectifier followed by a diode bridge rectifier as show in figure 1.14.
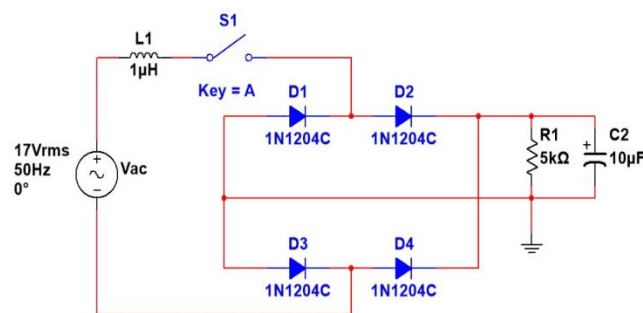
Figure 1.14 Series-SSHI circuit configuration

Lefeuvre and his associates (2006) reported a synchronous charge extraction interface, which consists in removing periodically the electric charge accumulated on the internal capacitor of the piezoelectric element and transferring the corresponding amount of electrical energy to the load/storage element as shown in figure 1.15. The extraction state has been generated by the boundary displacement *u* of the vibrational structure model with piezoelectric element. The circuit mechanism when switch **S1** is closed, the electrical energy from the piezoelectric unit is transferred to the inductor **L1**. Those stored energies from inductor **L1** had been transferred to the downstream smoothing capacitor by re-opening switch **S1**. Experimental had been validate with the vibrating structure including a piezoelectric element model for synchronous charge extraction interface configuration. In the generally, the maximum harvested power can be driven in various techniques and it also need different values of the electro-mechanical coupling factor. Practically, the synchronous charge extraction technique can be obtaining the maximum for lower electromechanical coupling factors by redactor added in required amount of piezoelectric materials. Moreover, synchronous charge extraction is not need the impedance matching method.
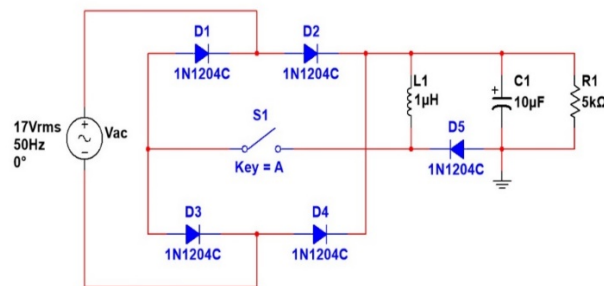
Figure 1.15 Synchronous charge extraction interface circuit

1.8.4) The double synchronized switch harvesting circuit

Lallart and his associate (Lallart *et al*. 2008) colleagues presents a new technique for optimized energy harvesting using piezoelectric micro-generators, it called double synchronized switch harvesting (DSSH). There are consist with piezoelectric element, the switch **S1**, the inductor **L1**, the diode bridge rectifier **R1-R4**, and the intermediate capacitor **C1** as shown in figure 1.16. Which all is corresponding to the previous explanation of the series – SSHI. The additional is composed by the switch **S2** the inductor **L2**, and the diode **D5** is a buck-boost static converter. More explanation by fully charged of C1 and C2 by the diode bridge rectifier, the switch S2 is need closed only when is fully charged by the diode bridge rectifier, while S1 is ON when energy on L2 is maximum.
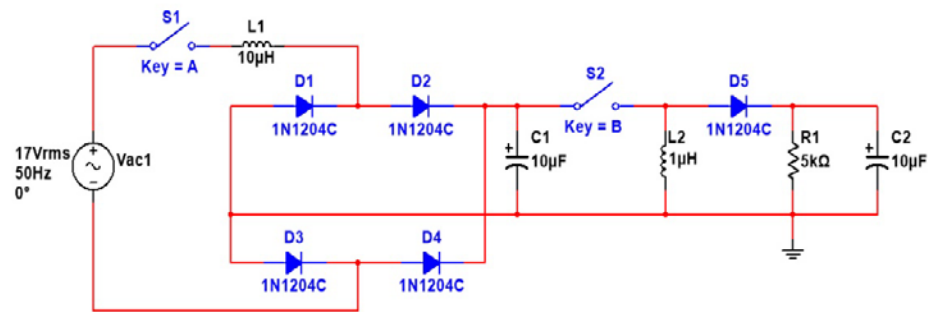
Figure 1.16 Energy extraction of the DSSH circuit

Commercial solutions are also made available as a result by the research progresses achieved in the last few years. Linear Technology (2018) is a manufacturer for a series of conditioning devices for energy harvesting. Those circuits are targeted for piezoelectric-based harvesters provide high efficiency conversion to regulated voltages or to charge batteries and super capacitor storage elements. Implementation of low-loss full-wave bridge rectifier followed by a buck or a buck-boost converter was applied, including with boost converters that operate from battery chargers with maximum power point capability expand the possibilities for wide range applications.

1.9 Conclusions

First energy harvesting using piezoelectric materials in biological envelopment had been presented in 1984 by Häsler and colleagues (1984). It continues as an emerging technology in many important areas of interest. Most energy harvesting applications are intensive focusing on low power devices because of their limited transmission efficiency (Tan and Panda, 2010). Nowadays, researchers all over the world still keep going to develop piezoelectric energy harvesting technology. New type of materials and novel model configuration approaches are under investigations.

Resonant cantilever beams by a stress parallel to the vibrational direction need optimization, many harvesters involve the additional attachment as seismic mass or vibrational frame and effort to a single resonance point. Bi-stable system is an advantage for widening a range of resonance by applying excitation force as magnetics field interaction at the free end of beam. Some surrounding source are constant at low frequency oscillations and piezoelectric plymer membrane might be a great solution because of their high shear-stress constant, voltage piezoelectric constant, flexibility, including reliability for non-resonance effect. Especially on the low velocity of kinematic fluid flow phenomena, it will interact with the shade vortices and create bending stresses in the transducer material, resulting in charges separation on electrode surfaces.

Management energy unit as batteries, rectifier, regulator and the other; are necessary on the energy harvesting implementation. Appropriate selections of regular bridge rectifier circuit had encouraged applications to work efficiently.

For the unsteady of the power sources, self- adaptive controlling on efficiency conversion is the intelligent device for the energy harvesting device, which is also aimed in this work. More detail of mechanism and controlling system will be described in Chapter 4.

CHAPTER 2

PIEZOELECTRIC POLYMER ENERGY HARVESTING ON VORTEX INDUCED VIBRATION

2.1 Piezoelectric polymers

The first developments and applications of piezoelectric polymers had been published since 1976 by Nakamura and his collaborates, but their attraction was increased in early 2000 due to the possibility of biomedical applications (Foster *et al.*, 2000; Murayama, 2000). Ordinary rigid piezoelectric ceramics were applied in many applications; for example, aerospace, electronics, and even automotive industry. Physical, electrical and piezoelectric properties of PVDF are presented in table 2. Piezoelectric strain constant (d_{31}) .for the polymers is lower than that of the ceramic. However, higher piezoelectric voltage constant (g_{31}) of piezo-polymers than piezo-ceramics indicates the better implementation of sensing. Sensors and actuators piezoelectric-based polymers are flexible and light, including simple to fabricate into large scale and complex shapes. Piezoelectric polymers also possesses high strength, impact resistance (Bauer and Bauer, 2008). Other features are low dielectric constant, elastic stiffness, and bulk density which can be turned into an excellent sensing function with high voltage sensitivity characteristics. An acoustic impedance of piezoelectric polymers is as water (1.4 μkg/m^2·s) and human body (1.6 μkg/m^2·s), leading to medical and underwater applications. Polymers also have a high dielectric breakdown and operating field strength, which means a driving field can be higher than ceramics. Poling on the selected region surface can be performed. These features promote piezoelectric polymers for technical applications and productive device configurations.

Table 2.1 Material properties of piezoelectric materials (Xu *et al.* 2009)

Material property	PVDF	Nylon 11	PVC	PZT	BaTiO$_3$
Density (g/cm^3)	1.78	1.15	1.45	7.5	5.7
Stress constant: d_{31} (pC/N)	23	0.26	0.7	1200	1700
Voltage constant: g_{31} (V·m/N)	216	2.5	6.6	10	5
Acoustic impedance ($\times 10^6$ kg/m^2·s)	2.7	2.9	3.27	30	30

The crystallinity of the PVDF polymers is usually a major factor on the piezoelectric behavior. Internal dipole moments in bulk PVDF are randomly oriented without any external processes such as mechanical stretching (Wolff *et al*. 2015) or electrical poling (Vinogradov and Holloway, 1999). These conditions are neutralized for net dipole moment. This type of structure is called α-phase PVDF having no piezoelectric response due to an alignment of all dipole moments cancel each other, as shown in figure 2.1(a). The α-phase PVDF is commonly used as insulating material because of its low thermal conductivity, low density, and high chemical and heat resistance (Bauer and Bauer, 2008).
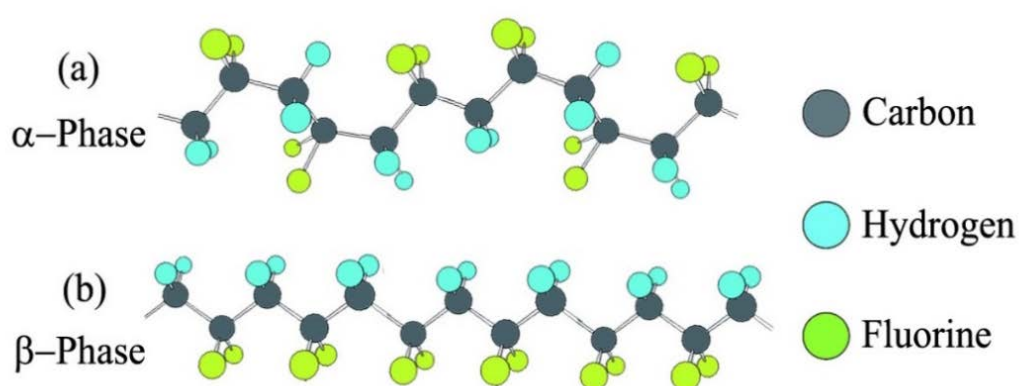
Figure 2.1 Molecular structure (a) α-phase and (b) β-phase of PVDF polymers.

On the other hand, the PVDF structure with fluorine on the one side and hydrogen on the other side is called β-phase as shown in figure 2.1(b). Various studies show ways to increase the β-phase portion by mechanical or electrical poling (Ruan *et al*. 2018).
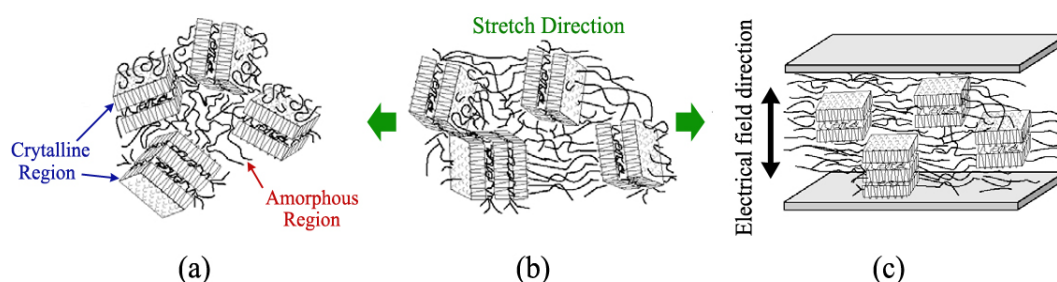
Figure 2.2 Schematic illustration showing random stacks of amorphous and crystal lamellae in PVDF polymers (a) represents the morphology after the film is melt cast; (b) is after orientation of the film by mechanically stretching to several times its original length; (c) is after depositing metal electrodes and poling through the film thickness (Harrison and Ounaies, 2001).

The morphology of such polymers consists of crystallites dispersed within amorphous regions as shown in figure 2.2(a). The amorphous region has a glass transition temperature that dictates the mechanical properties of the polymers, while the crystallites have a melting temperature that dictates the upper limit of the use temperature.

By the application of post processes such as electrical poling under a high electric field, crystalline regions inside the bulk PVDF film will align in electric field direction. An electric field on the order of 50 MV/m is typically sufficient to affect the crystalline orientation. This will form a net dipole moment in a stacked direction inside the β- phase PVDF crystalline regions. The β-phase PVDF film retains its morphology unless there are severe changes in temperature to the film.

When mechanical stretching is applied to this stacked polymer chain region, crystalline structures will be align in the stretch direction as shown in figure 2.2(b), it will change the local dipole distributions and induce an electric field in the stack. The induced electric field accumulates the charges at both the top and bottom of the film, demonstrating the principle of piezoelectric effect as shown in figure 2.2(c). The higher β-phase portion of PVDF film shows a higher piezoelectric constant as sensor materials. Typically, around 90~95% of β-phase portion shows a strong piezoelectric response for PVDF polymers (Martin *at el*. 2014).

2.2 Literature reviews of vortex induced vibrations

On the energy harvesting application, different prototypes have been developed to captures this form of energy such as current and marine turbines. Extraction such energy is done by transforming the vibrations in the fluid flows into an electrical energy through a generator placed in the current stream. This works is based on the coupling between the flow-induced vibrations and the piezoelectric polymers patches.

2.2.1) Flow-induced vibrations

Two different types of flow-induced vibrations are used for energy harvesting, which is "Vortex Induced Vibrations" (VIV) and "Self-Excited Vibrations" (SEV). Designs based on VIV are the most common and be discussed by a qualitative as well as technical description, relevant background, and a mathematic model. The two main goals can be seen as explaining the principals of VIV, and then using those principals to create a model for energy harvester which will in turn be used in designing and choosing conditions for the experimental apparatus.
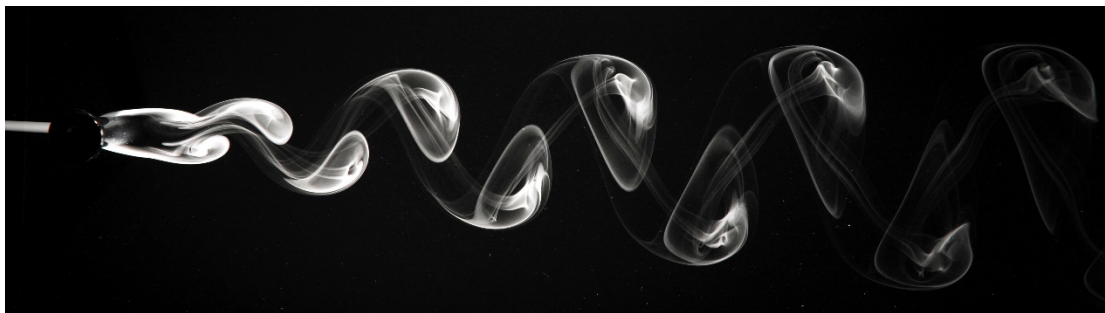
Figure 2.3 Vortex Street behind a circular cylinder in air (Wagner, 2014).

Vortex shedding is a widely occurring phenomenon applicable to nearly any bluff (non-streamlined) body submerged in a fluid flow. Since any real fluid flow is viscous, there will be a significant boundary layer on the bodies's surface. The vortices on each side of the body are opposite in sign and will form a regular periodic pattern in the wake in which leading to an oscillation flow pass a body as known as a vortex street as shown in figure 2.3.

At some points along the bodies' surface, a separation of the boundary layers will be occurred, depending on the exact surface geometry. This separated layers, which bound the wake and free stream, tend to cause fluid rotation. Its outer side is in contact with the free stream, moving faster than its inner side which is in contact with the wake. The rotation then results in the formation of individual vortices, which are then shed from the rear of the body and traveled down the wake. Typically, a pattern of periodic, alternating vortex shedding in the flow behind the body and is referred to as a vortex street.

When the pattern of shed vortices is not symmetrical about the body, which is the case in any vortex street, an irregular pressure distribution is formed on the upper and lower sides of the body, which results in a net lift force perpendicular to the flow direction. Since the vortices are shed in a periodic manner, the resulting lift forces on the body also vary periodically with time, and there for can induce oscillatory motion of the body. This occurrence alone would qualify as vortex induced vibration; however, there is a more interesting and important phenomenon, similar to linear resonance, which can occur when the frequency of vortex shedding f_S is close to the natural frequency of the body in motion, f_N. In this phenomenon, referred to as "lock in", the vortex shedding frequency actually shifts to match the bodies' natural frequency, and as a result, much larger amplitudes of vibration can occur.

Accordingly, the range of shedding frequencies within vortex induced vibration will be discussed in more details relevant to the design of an energy harvesting device.

2.2.2) Vortex shedding

Vortex street formation is directly dependent on Reynolds number, which is defined as the ratio of inertial forces to viscous forces. The Reynolds number is a dimensionless parameter that depends on the fluid velocity (U), the characteristic length of the body (D), and the kinematic viscosity of the fluid (v) as given by equation (2.1). Referring to most studies in literature were in fact performed using a submerged cylinder, so the correlation length of cylinder diameter used in Re is appropriate and widely applicable as many submerged structures are typically cylindrical in shape.

$$\text{Re} \;\; = \;\; \frac{U \cdot D}{\upsilon} \tag{2.1}$$

Depending on the characteristics of the flow behaviors, mainly the Reynolds number, different types of vortex streets may form as presented in figure 2.4. Below Re = 5, the flow follows the contour of the cylinder and no vortices are formed. From $5 \leq \text{Re} \leq 40$, the flow separates behind the cylinder, and a pair of symmetric vortices form. For the lowest two regimes, periodic vortex shedding is nonexistent, and no resulting lift forces act on the body. As the Reynolds number increases, one of the vortices breaks away, triggering the formation of a vortex street.

Form 40<Re<150, a vortex street begins to form in a wake, which does in fact result in varying lift forces, since the vortices shed non symmetrically from the top and bottom of the cylinder. Over the next range of Reynolds numbers from $150 < \text{Re} < 300$, the first transition zone occurs, in which the vortex street changes from laminar flow to turbulent. Although the boundary layer and free stream are still laminar, but there are still no organized shedding or lift occurs in this region.

From $300 < \text{Re} < 3 \times 10^5$, there is a stronger periodic shedding, which produces a vortex street that is fully strong turbulent and stable. The second transition region occurs when the flow around the cylinder changes from laminar to turbulent, and again vortex shedding is disrupted and irregular. This is the range of Reynolds's numbers in which most VIV experiments have been conducted, as it produces the most stable vortex streets and lift forces. In additional, in the range of $10^3 < \text{Re} < 10^4$ is well clear of both the transition zones.
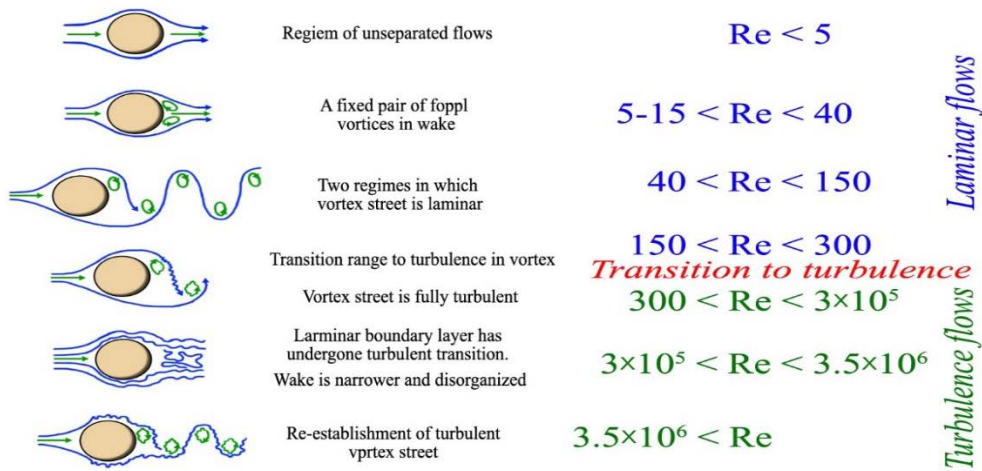
Figure 2.4 Regimes of fluid flow across smooth circular cylinders (Lienhard, 1966).

As the Reynolds's number increases past 3×10^5, the boundary layer becomes turbulent, and the wake becomes disorganized and unpredictable. At some point around a Reynolds number of 3.5×10^6, regular vortex shedding resumes with a turbulent boundary layer. Vortex shedding has been observed at Reynolds numbers as high as 10^{11}, such as in wind-driven cloud formations (Blevins, 1990).

The Strouhal number (*St*) is another dimensionless parameter that is significant in VIV because it characterizes oscillating flow mechanisms, which describe to the frequency of vortex shedding (f_s) to the flow conditions as given by equation (2.2).

$$St \;=\; \frac{f_s \cdot D}{U} \tag{2.2}$$
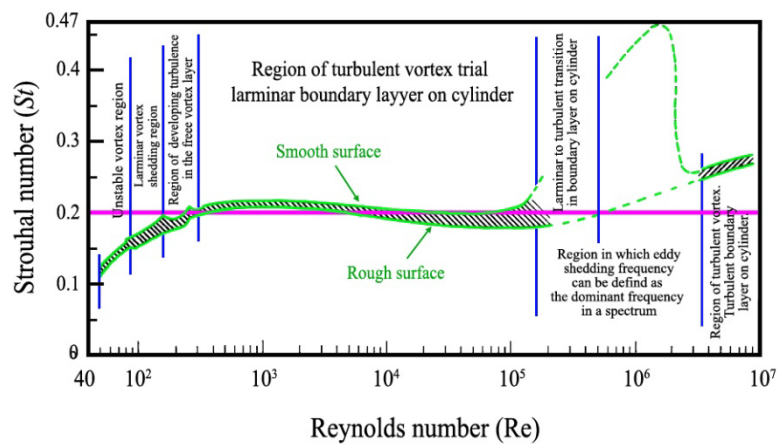
Figure 2.5 The Strouhal-Reynolds number relationship for circular cylinders as defined by existing empirical data (Lienhard, 1966).

For a wide range of Reynolds number, the Strouhal number for a cylinder is a function of the Reynolds number, the surface roughness, and the free stream turbulence and the variation can essentially be taken as a constant as shown in figure 2.5. Between in the regime of Reynolds numbers from $300 < Re < 3 \times 10^5$, the Strouhal number is close to constant at a value of 0.2, which corresponds very well to the fully developed turbulent vortex street as described above (Benaroya and Gabbai, 2005). Taking the Strouhal number to be constant is useful for simplifying equations, because it makes the vortex shedding frequency a function of only the flow speed and the cylinder diameter, it's more convenient to calculate parameter of f_s.

2.2.3) Synchronization (Lock in)

A key feature of vortex induced vibration is the existence of a region of synchronization or "lock-in." In this region, there is a significant increase in the amplitude of the oscillations of the cylinder, meaning that the energy of the system will be at a maximum. Synchronization is similar to linear resonance, as it occurs when the vortex shedding frequency approaches the natural frequency of the oscillator. However, unlike resonance, synchronization is nonlinear and will occur over a band of frequencies. Additionally, synchronization does not have a sharp peak in amplitude when the shedding frequency and the natural frequency are exactly equal. In the lock-in region, the vibration of the cylinder controls the shedding frequency. Synchronization is also described as being self-limiting, because when the amplitude grows too large the symmetric pattern of vortices breaks up (Blevins, 1990).

The most important result from lock in studies has been the phenomenon occurring over wide ranges of shedding frequencies. This means that even at shedding frequencies significantly different than the bodies' natural frequency. The non-dimensional parameter used in many experiments measuring vibration amplitude is the reduced velocity U^*, given by equation (2.3).

$$U^* \quad = \quad \frac{U}{f_s \cdot D} \qquad\qquad (2.3)$$

The vortex induced vibration is also affected by the mass ratio (m^*), which defined as the ratio of the oscillator mass to the mass of the fluid it displaces as given by equation 2.4. In case of cylinder bar, m_{dis} is equal to $\rho \pi L D^2/4$, where D is the diameter of the cylinder; L is the length of the cylinder; and ρ is the density of the fluid.

$$m^* \quad = \quad \frac{m_{osc}}{m_{diss}} \qquad\qquad (2.4)$$

For the current understanding of lock-in is based on empirical or semi-empirical studies; an analytical model of lock-in has not been fully developed. One of the most important findings about the lock-in region is its dependence on the reduced velocity. Assuming a value of 0.2 for the Strouhal number, the reduced velocity (U^*) is equal to 5 when the vortex shedding frequency and the natural frequency are exactly equal. It has been experimentally determined that synchronization will generally occur for $4 < U^* < 8$ (Blevins, 1990).
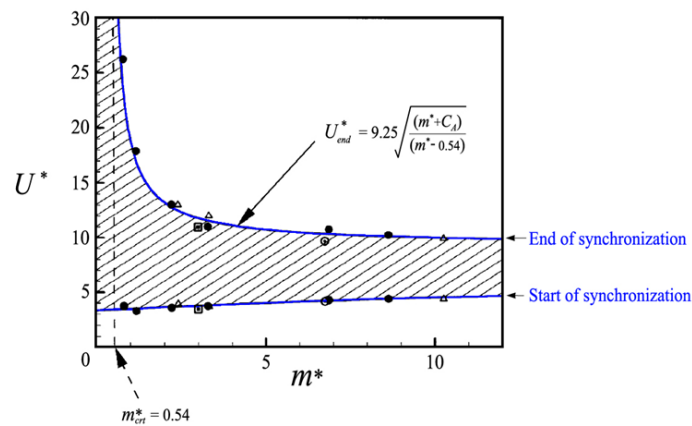
Figure 2.6 Synchronization range of a cylinder as a function of m^* and U^* (Williamson & Govordhan, 2004)

Figure 2.6 shows the synchronization range as it relates to both m^* and U^* for a cylinder while lock-in will occur within the shaded region. For instead, the reduced velocity is the best indicator of whether or not synchronization will occur, it has also been found that the mass ratio affects the size of the lock-in region. For high values of m*, the lock-in region is relatively constant between reduced velocities of 4 and 8. As the mass ratio is decreased, the lock-in region becomes larger, until it reaches a critical point where the lock-in band becomes infinitely large. Williamson and Govordhan found that this critical mass ratio was equal to 0.54. This value was determined specifically for systems with a low mass and low damping for an elastically supported cylinder. However, the existence of a critical mass has been demonstrated for different geometries and damping factors.

2.2.4) Mathematical of the VIV model

Due to the variable and non-linear nature of vortex induced vibrations, there is not one set of governing equations to describe it. However, since vortex shedding is approximately sinusoidal, VIV of a cylinder can be reasonably modeled as a linear harmonic oscillator (Blevins, 1990). The lift force exerted on the cylinder by the vortex shedding can therefore be modeled as equation (2.5):

$$F_L = \frac{1}{2}\rho DLC_L U^2 \sin(\omega_s t) \tag{2.5}$$

where F_L is the lift force perpendicular to the free stream; ρ is the fluid density; U is the free stream velocity; D is the cylinder diameter; L is the length of the cylinder; t is time; and ω_s is the angular vortex shedding frequency. In the lock in region, angular vortex shedding frequency is equal to $2\pi f_s$. This force is applied to a cylinder mounted elastically using springs of combined stiffness (k) and damping coefficient (ζ). The motion of the cylinder can then be described by equation (2.6) and the angular natural frequency of the cylinder given by equation (2.7).

$$m\ddot{y} + 2m\zeta\omega_n \dot{y} + ky = \frac{1}{2}\rho DLC_L U^2 \sin(\omega_s t) \tag{2.6}$$

$$\omega_s = 2\pi f_n = \sqrt{\frac{k(1-\zeta^2)}{m_{osc}+m_{dis}}} \tag{2.7}$$

For a linear oscillator model, the damping factor is taken as an average and assumed to be constant. General solution of the second order differential equation can be solved to produce an equation for the vertical linear displacement of the cylinder $y(t)$ with respect to time as given by equation (2.8), and the amplitude at resonance can be found by setting $\omega_s=\omega_n$; where φ is the phase angle.

$$y(t) = \frac{\frac{1}{2}\rho DLC_L U^2 \sin(\omega_s t+\varphi)}{k\sqrt{\left(1-\left(\frac{\omega_s}{\omega_n}\right)^2\right)^2+\left(2\zeta\left(\frac{\omega_s}{\omega_n}\right)^2\right)^2}} \tag{2.8}$$

In the reality, maximum amplitude will occur over a range of frequencies, not at exact resonance. However, using the linear harmonic oscillator model provides a relatively accurate approximation of the motion of a cylinder undergoing VIV.

The linear harmonic oscillator model of VIV also allows for the theoretical maximum power to be calculated. The velocity as a function of time for the cylinder can be obtained by differentiating equation (2.8) for displacement, resulting in the following equation (2.9).

$$v(t) = \frac{\omega_s\frac{1}{2}\rho DLC_L U^2 \cos(\omega_s t+\varphi)}{k\sqrt{\left(1-\left(\frac{\omega_s}{\omega_n}\right)^2\right)^2+\left(2\zeta\left(\frac{\omega_s}{\omega_n}\right)^2\right)^2}} \tag{2.9}$$

Power (P) as function of time is found by multiplying the lift force and the cylinder velocity $v(t)$ were given by equation (2.10).

$$P(t) \;=\; \frac{\omega_s \frac{1}{4}(\rho D L C_L)^2 U^4 \cos(\omega_s t + \varphi)}{k\sqrt{\left(1 - \left(\frac{\omega_s}{\omega_n}\right)^2\right)^2 + \left(2\zeta\left(\frac{\omega_s}{\omega_n}\right)^2\right)^2}} \tag{2.10}$$

The maximum power will occur when $\omega_n = \omega_s$. Given that for a cylinder $\varphi = \pi/2$, the equation for the maximum power is given as equation (2.11).

$$P_{\max} \;=\; \frac{\omega_s(\rho D L C_L)^2 U^4 \sin^2(\omega_s t)}{8k\zeta} \tag{2.11}$$

2.3 Experimental fluid flow piezoelectric vortex induced vibration

This future of the apparatus is the combination of water flow source, flowing measurement, joint connections plastic tube, harvesting, laser displacement sensor and the electrical output measurement unit and all were joined together as show in figure 2.7.
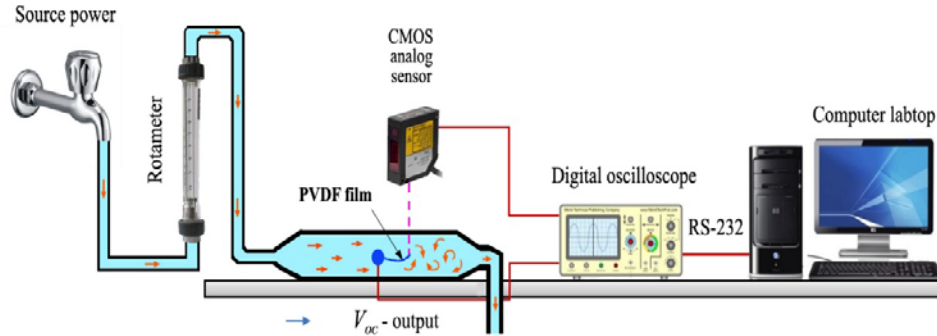
Figure 2.7 Schematic diagram of the fluid flow energy harvesting setup

2.3.1) Flowing measurement unit

Flow meters are used in fluid systems (liquid and gas) to indicate the rate of flow of the fluid, typically rotameter is a device that measures the volumetric flow rate of fluid in a closed tube as present in figure 2.8(a). It belongs to a class of meters called variable area meters, which measure flow rate by allowing the cross-sectional area the fluid travels through to vary, causing a measurable effect. There are consists of a tapered tube, typically made of glass with a "float" inside that is pushed up by the drag

force of the flow and pulled down by gravity. The drag force for a given fluid and float cross section is a function of flow speed squared only, as given by equation (2.12) (Batchelor, 1967):

$$F_D \quad = \quad \frac{1}{2}\rho A C_D U^2 \tag{2.12}$$

where ρ, A, U and C_D is fluid density, flowing cross section, flows velocity and drag coefficient, respectively,

A higher volumetric flow rate through a given area increases flow speed and drag force, so the float will be pushed upwards. However, the area around the float shape through which the medium flows increases, the flow speed and drag force decrease until there is mechanical equilibrium with the float's weight as show in figure 2.8(b). The "float body" must not float in the fluid: it has to have a higher density than the fluid, otherwise it will float to the top even if there is no flow.

(a)   (b)
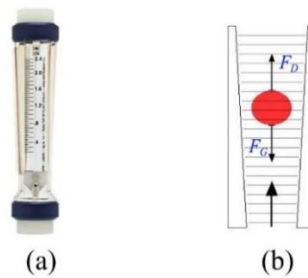
Figure 2.8 (a) Rotameter and (b) mechanical force equilibrium of floating body in side rotameter.

2.3.2) The designed harvester unit

The harvester consists of a flow channel, bluff body, piezoelectric PVDF film, and inlet/outlet covers. The size of the flow channel by length × width × depth is 26 mm × 36 mm × 146 mm, and was made from acrylic sheet series of Xhac-001 provided by Xinghua Manufacturer (RP.China), with its thickness of 8 mm. A 6 mm-high and 20 mm-wide rectangular bluff body with rounded edges was placed in the flow channel at the center height and 50 mm from the inlet boundary. A water proof laminated flexible piezoelectric PVDF film is from the LTD1-028K/L series manufactured by Measurement Specialties Inc., (U.S.A.) (Measurement Specialties, 1999). The properties of the material are presented in table 2. The piezoelectric film was cleaved behind to the buff body. Inlet and outlet boundaries were each covered by rectangular cone with 50 mm in length and 10 mm of cavity diameter, there combination of harvester assembly as shown in figure 2.9. All the ABS plastic accessories as bluff body

and both inlet/outlet covered had been designed and manufactured by using a Makerbot replicator 2x experimental 3D printer (U.S.A.).

Table 2.2 Summary of the PVDF film properties.

Density (kg/m^3)	Young modulus (10^9 N/m^2)	Capacitance (nN/cm^2) @1 kHz	Relative permittivity: ε_r	Piezo strain constant (10^9 C/N)		Piezo coupling factor	
				d_{33}	d_{31}	k_{31}	k_t
1,780	2-4	1.38	12-13	-33	23	12	14
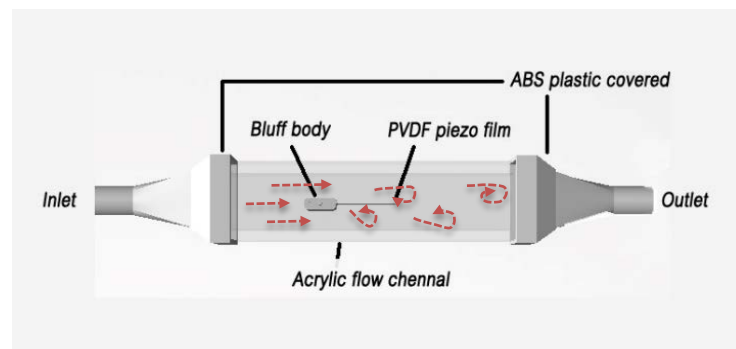
Figure 2.9 Assembly of the harvester unit

2.3.3) Data collections

On the voltage output generated by VIV experimental, digital oscilloscope model TPS-2014 by Tektronix manufacturing, P.R. China had been used at 2,500 samples rate measurements. Signal output were detected from voltage peak-to-peak mode for 10.0 seconds. To the signal transferring was applying by wire probe for harvester-to-oscilloscope and RD-200 cable for oscilloscope-to-computer, which raw measurement data were not induced by any electronic components.

2.3.4) Methodology

(a) Connected elastic plastic tube 1/2" from water power source (tap water) to bottom side of rotameter.

(b) On the top of rotameter, joined flow meter to inlet side of flows channel (harvester) with elastic tube.

(c) On the other side, connected plastic tube to the harvester outlet and the other side of tube is flows water into sink bath.

(d) For the harvester unit, connected piezo wire directly to oscilloscope's probe, the VIV apparatus is present in figure 2.10.

(e) Turning flows power to flowing rate Q=0.1 gallon/min.

(f) Wait until flowing system is reach to steady state (liquid filled).

(g) Record voltage signals ($V_{oc.}$) data by laptop computer interface.

(h) Repeat from (e)-(g), but increase flow rate for 0.1 gallon/min per round.
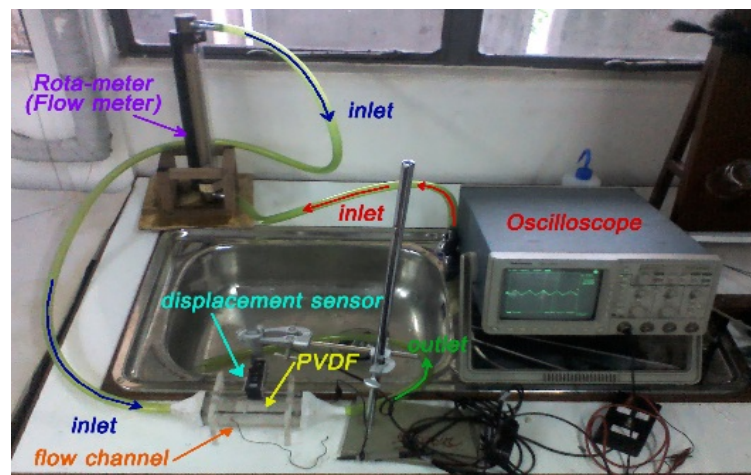
Figure 2.10 Vortex induced vibration energy harvesting apparatus.

2.4 Computational elastic oscillations by vortex induced vibration

In this study, the COMSOL Multi-physics software was used for analyzing the VIV modeling numerically along with problem solving the coupling of Computational Fluid Dynamic (CFD) and Finite Element Analysis (FEA) techniques for section 2.4.1. Package software MATLAB Simulink had been employed to analyze mathematical of piezoelectric energy harvesting model on the vibrating oscillation.

2.4.1) Flow induced vibration

The flow of fluid behind a blunt body such as an automobile is difficult to compute due to the unsteady flows. The wake behind such a body consists of unordered eddies of all sizes that create large drag on the body. In contrast, the turbulence in the

thin boundary layers next to the streamlined bodies of aircraft create only weak disturbances of flow. An exception to this occurs when you place a slender body at right angles to a slow flow because the eddy organize. A von Kármán Vortex Street appears with a predictable frequency and involves the shedding of eddies from alternating sides.

2.4.1.1) Theoretical related to flow induced vibration

The wake interference around the cylinder has been widely investigated in the past because of its inherent importance and practical significance in engineering applications. Flow-induced vibration of cylinders is closely related to fluctuating flow pattern given rise by vortex shedding from the cylinders. The governing equations are the incompressible unsteady Navier–Stokes equations and the continuity equation, which can be written in dimensionless vector form as given by equation (2.13)-(2.14).

$$\frac{\partial \mathbf{U}}{\partial t} + \mathbf{U} \cdot \nabla \mathbf{U} = -\nabla p + \frac{1}{\mathrm{Re}} \nabla^2 \mathbf{U} \tag{2.13}$$

$$\nabla \cdot \mathbf{U} = 0 \tag{2.14}$$

where $\mathrm{Re} = U_\infty D/\nu$ is the Reynolds number, U_∞ is the oncoming mainstream velocity, ν is the fluid kinematic viscosity, $\mathbf{U}$ is the non-dimensional velocity vector in the Cartesian coordinate system (x, y) with its two velocity components u and v, and p is the non-dimensional static pressure. The numerical simulation is carried out using finite-element method based multi-physics code COMSOL.

The bluff body structures are subjected to current and wave loading, which induce lift and drag forces. These forces are described by the Morrison's equations as given by equation (2.15)-(2.16), respectively.

$$F_D = \frac{1}{2} C_D \rho D U^2 \tag{2.15}$$

$$F_L = \frac{1}{2} C_L \rho D U^2 \tag{2.16}$$

2.4.1.2) Methodology of VIV simulation

The parametric of dimensional of flow cannel and fluid flows characteristic are summarized in table 3. Radius variation of the circular bluff body with 4, 5, and 6 cm. were aligned in the length of 20 cm from the inlet and wall boundary. Meshing process were obtained 27,080 domain elements and 990 boundary elements for FEM analysis on the condition of U = 1 m/s and D_h = 5 cm as shown in figure 2.11(a). Boundary wall had been applied on upper and lower cannel edges, including the bluff body circular surface by the condition of $\mathbf{U}$=0. Incompressible flow condition is assuming with non-pressure flows (p=0) on any domain region from inlet through to outlet as shown in figure 2.11(b).

Table 2.3 Fluid flow characteristic and flow channel dimension.

Flow channel dimension		Bluff body	Fluid flow characteristic		
width (cm)	height (cm)	Radius (cm)	mean velocity (m/s)	density (kg/m³)	viscosity (Pa·s)
220	40	4, 5, 6	0.8, 1, 1.2	1	1×10^{-3}
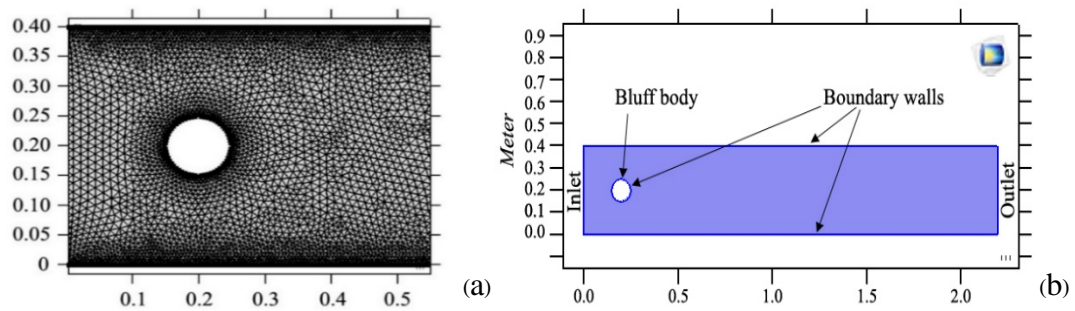
Figure 2.11 (a) Meshing element of FEM around the bluff body and (b) boundary condition in fluid flows domain.

2.4.2) Fluid structure interaction

Fluid-structure interaction (FSI) is a multi-physics coupling between the laws that describe fluid dynamics and structural mechanics. This phenomenon is characterized by interactions – which can be stable or oscillatory – between a deformable or moving structure and a surrounding or internal fluid flow.

2.4.2.1) Fluid flow properties

The Navier-Stokes equations govern the motion of fluids and can be seen as Newton's second law of motion for fluids. In the case of a compressible Newtonian fluid, the different terms correspond to the inertial forces, pressure forces, viscous forces, and the external forces applied to the fluid as given by equation (2.17). (Reynolds, 1985)

$$\rho\left(\frac{\partial \mathbf{U}_{fluid}}{\partial t}+\mathbf{U}_{fluid}\cdot\nabla\mathbf{U}_{fluid}\right)=\nabla\cdot\left[\underbrace{\rho\mathbf{I}}_{pressure\ forces}+\mu\left(\underbrace{\nabla\mathbf{U}_{fluid}+\left(\nabla\mathbf{U}_{fluid}\right)^T-\frac{2}{3}\mu\left(\nabla\cdot\mathbf{U}_{fluid}\right)\mathbf{I}}_{viscouse\ force}\right)\right]+\underbrace{\mathbf{F}}_{external\ force} \tag{2.17}$$

where ρ, $\mathbf{U}_{fluid}$, μ and $\mathbf{I}$ is fluid density, flow velocity, viscosity and identity matrix. The external force ($\vec{F}$) is such as the gravity, inertia, or electrostatic force. Superscript T indicates stress deviator tensor Superscript T indicates stress deviator tensor. These equations are always solved together with the continuity as given by equation (2.18).

$$\frac{\partial \rho}{\partial t} + \nabla \cdot (\rho \mathbf{U}_{fluid}) = 0 \tag{2.18}$$

The Navier-Stokes equations represent the conservation of momentum, while the continuity equation represents the conservation of mass. For the special case of an incompressible flow, the pressure constrains the flow so that the volume of fluid elements is constant. This is often a good approximation for liquids at low Re<100 (lower flow velocity), which are much less compressible than gases. In this case, the density is assumed to be constant and the continuity equation reduces to $\nabla \cdot u = 0$, and equation (2.17) reduced to equation (2.19), while neglected the external and gravitational force.

$$\rho \frac{\partial \mathbf{U}_{fluid}}{\partial t} + \left(\mathbf{U}_{fluid} \cdot \nabla \right) \mathbf{U}_{fluid} - \nu \nabla^2 \mathbf{U}_{fluid} = 0 \tag{2.19}$$

2.4.2.2) Fluid-solid interface boundary

The interface uses an arbitrary Lagrangian-Eulerian (ALE) method to combine the fluid flow formulated using an Eulerian description and a spatial frame with solid mechanics formulated using a Lagrangian description and a material (reference) frame.

The total force exerted on the solid boundary by the fluid is the negative of the reaction force on the fluid related with pressure and viscose force. Because the Navier-Stokes equations are solved in the spatial (deformed) frame while the solid mechanics interfaces are defined in the material (un-deformed) frame, a transformation of the force between both frames is given by equation (2.20).

$$\mathbf{F} = \mathbf{f} \cdot \frac{dv}{dV} \tag{2.20}$$

where *dv* and *dV* are mesh element scale factor for spatial frame and the material (reference) frame, respectively.

The coupling in the other direction consists of the structural velocities (the rate of change for the displacement of the solid), which act as a moving wall for the fluid domain. The predefined Fluid-Solid Interface Boundary condition includes these couplings for bi-directionally coupled FSI simulations. The solid mechanics formulation supports geometric nonlinearity (large deformations). The spatial frame also deforms with a mesh deformation that is equal to the displacements $\mathbf{U}_{solid}$ of the solid within the solid domains. The mesh is free to move inside the fluid domains, and it adjusts to the motion of the solid walls as defined in equation (2.21). On the boundary domains, stress tensors of solid material and stress flow were interacted on the boundary wall as given by equation (2.22), while stress flow of fluid domain is defining as equation (2.23).

$$\mathbf{U}_{fluid} = \mathbf{U}_{wall} \quad ; \quad \mathbf{U}_{wall} = \frac{\partial \mathbf{U}_{solid}}{\partial t} \tag{2.21}$$

$$\sigma \cdot \mathbf{n} = \Gamma \cdot \mathbf{n} \tag{2.22}$$

$$\Gamma = -\mathbf{pI} + \mu \left[\mathbf{U}_{fluid} + (\nabla \mathbf{U}_{fluid})^T - \frac{2}{3}\mu(\nabla \mathbf{U}_{fluid})\mathbf{I} \right] \tag{2.23}$$

2.4.2.3) Linear elastic material

Piezoelectric membrane assigned as the linear elastic material model which has the equations and features for stress analysis and general linear and nonlinear solid mechanics. The general solutions are solving for the displacements and the linear elastic equation for the displacements is given by equation (2.24)

$$\rho \frac{\partial^2 \mathbf{U}_{solid}}{\partial t^2} - \nabla \cdot \sigma = \mathbf{F}v \tag{2.24}$$

where $\mathbf{U}_{solid}$, σ, v and $\mathbf{F}$ is solid surface displacement, stress tensor, viscosity and fluid force acting on solid wall.

For linear elastic materials, the total strain tensor (ε) is written in terms of the displacement gradient as given by equation (2.25)

$$\varepsilon = \frac{1}{2}\left(\nabla U + \nabla U^T\right) \tag{2.25}$$

The Duhamel-Hooke' law relates the stress tensor (s) to the strain tensor (ε) and temperature (θ) as given by equation (2.26)

$$s = s_0 + C : (\varepsilon - \varepsilon_0 - \alpha\theta) \tag{2.26}$$

where C is the 4th order elasticity tensor; the symbolic ":" is stands for the double-dot tensor product (or double contraction); s_0 and ε_0 are initial stresses and strains; $\theta = T - T_{ref}$ and α is the thermal expansion tensor. Then the elastic energy is given by equation (2.27).

$$W_s = \frac{1}{2}(\varepsilon - \varepsilon_0 - \alpha\theta) : C : (\varepsilon - \varepsilon_0 - \alpha\theta) \tag{2.27}$$

For large deformations, the particles is initially located at the coordinate X, which given by $\mathbf{x} = \mathbf{x}(\mathbf{X}, t)$. While their displacement $\mathbf{U}$ were generated by the deformations, the un-deformed and deformed positions are measured in the same coordinate system can be changed to $\mathbf{x} = \mathbf{X}+\mathbf{U}$. The deformation gradient (F) infinitesimal by line element $d\mathbf{X}$ is mapped to the corresponding deformed line element $d\mathbf{x}$ is given by equation (2.28).

$$d\,\mathbf{x} \;=\; \frac{\partial \mathbf{x}}{\partial \mathbf{X}} d\,\mathbf{x} \;=\; F\, d\,\mathbf{X} \tag{2.28}$$

The deformation gradient (F) contains the complete information about the local straining and rotation of the material. It is a positive definite matrix, as long as material cannot be annihilated. The ratio between current and original volume (or mass density) is defined by the deformation state (J) as given by equation (2.29). In terms of displacement gradient, it can be written as $F = \nabla \mathbf{U} + \mathbf{I}$, where $J = 1$ is often called incompressible.

$$\frac{dV}{\partial V_0} \;=\; \frac{\rho}{\rho_0} \;=\; \det(F) \;=\; J \tag{2.29}$$

The symmetric stress tensor (σ) describes stress in a material, which consist of the 3 normal stresses and 6 shear stresses. In case of symmetry, shear stresses are used 3, as given by equation (2.30).

$$\sigma = \begin{bmatrix} \sigma_x & \tau_{xy} & \tau_{xz} \\ \tau_{yx} & \sigma_y & \tau_{yz} \\ \tau_{zx} & \tau_{zy} & \sigma_z \end{bmatrix}; \quad \tau_{xy} = \tau_{yx}; \quad \tau_{xz} = \tau_{zx}; \quad \tau_{yz} = \tau_{zy} \tag{2.30}$$

More additional for large deformation and hyper elastic material model, stress tensor Cauchy stress (σ) are consist with Cauchy stress (s_x), first Piola-Kirchhoff stress (P_x) and second Piola-Kirchhoff stress (S_x). The definition of Cauchy stress (s_x) is a force per deformed area in fixed directions not following the body. First Piola-Kirchhoff stress (P) is an un-symmetric two-point tensor for the anisotropic materials, and the second Piola-Kirchhoff stress (S) is a symmetric tensor, for small strains same as Cauchy stress tensor but in directions following the body. There stress tensors are related with the other parameter as given in equation (2.31)-(2.32).

$$\sigma \;=\; J^{-1}\mathbf{PF} \;=\; J^{-1}\mathbf{FSF}^T \quad ; \; where \quad \mathbf{S} = \mathbf{F}^T\mathbf{P} \tag{2.31}$$

$$\mathbf{F} \;=\; (\mathbf{I} + \nabla\mathbf{U}_{solid}) \tag{2.32}$$

2.4.2.4) Two ways boundary coupling

When a fluid flow encounters a structure, stresses and strains are exerted on the solid object-forces that can lead to deformations. To calculated fluid-structure interaction (FSI) of both fluid and solid behavior were accomplished by using two ways boundary coupling framework in COMSOL multi-physics 5.3 as presented in figure 2.12. Navier-Stokes and continuity equation were used for solving fluid flow solution by using equation (2.18)-(2.19). The solution of solid deformation had been approached by the equation of motions of linear elastic material as given by equation (2.24). Moving mash is mainly given solid deformation movement following on fluid pressure

and solid information. On the FSI boundary condition, pressure stress (Γ) from fluid flows is a force transferring to the solid boundary wall in the opposite direction as describe in equation (2.22)-(2.23). Fluid velocity has assisted on the solid velocity at boundary wall and the velocity of the boundary wall is equal to time derivative of the solid displacement as given in equation (2.21). The solution of the both fluid flow and solid had been solve until solutions converges.
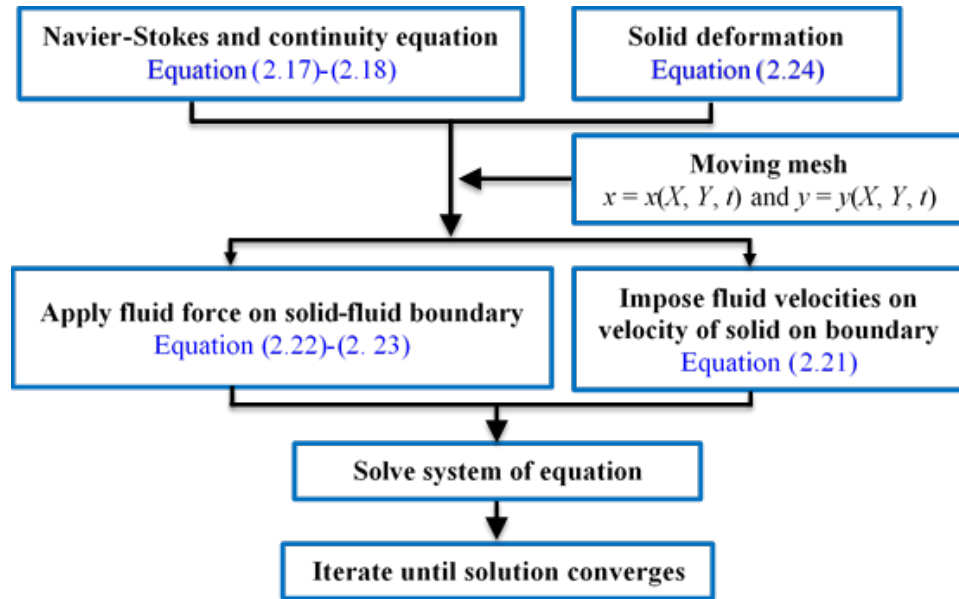
Figure 2.12 Two ways boundary coupling diagram

2.4.2.5) Methodology of the FSI

The fluid domain is a 2.5 m long and 0.41 m high channel. The structure is composed of a fixed circular domain with 0.05 m radius and centered at (0.2, 0.2) of coordinate system. The second domain of the structure is a 0.35 m by 0.02 m rectangular beam made of elastic material. The fluid enters the channel from the left with a variation of free velocity and the inlet velocity profile is assumed to be fully developed. With the inlet boundary so close to the solid structure, one can expect the inlet velocity condition to affect the flow pattern. Complete mesh consists of 14,148 domain elements and 601 boundary elements, which figure $2.13(a)$ is present finite element around bluff body. Incompressible flow condition of FSI is assuming with non-pressure flows ($p = 0$) on any domain region from inlet through to outlet as shown in figure $2.13(b)$. The mean inlet velocity (V_f) is define as in equation (2.31). In this section the FSI problems are consist with FSI-1, FSI-2, FSI-3 and FSI-4, which fluid flow profile and elastic material properties are presented in table 2.4.

$$V_f = \frac{3U \cdot y(H - y)}{2\left(H/2\right)^2} \tag{2.31}$$

Table 2.4 The FSI problem definition of flows profile and elastic material properties.

Parameter		FSI-1	FSI-2	FSI-3	FSI-4
Flows profile	Fluid density (kg/m^3)	0.5	1	2	4
	Dynamic viscosity (Pa·s)	1.0			
	Free velocity (m/s)	1×10^3			
Material properties	Eleatic density (kg/m^3)	1×10^3			
	Poisson ratio	0.4			
	Young's modulus (Pa)	5.6×10^6			
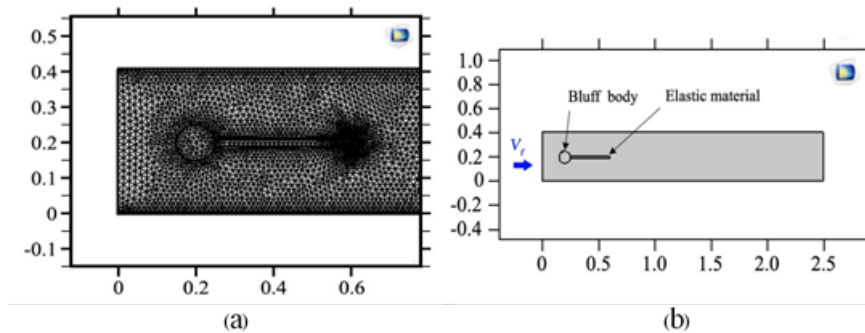
Figure 2.13 (a) Meshing FSI element and (b) model geometry including solid and fluid domains.

2.4.3) Equivalent circuit model

The modeling of the general vibration-based kinetic energy harvester is discussed, mainly corresponding to previous of section 1.7.1. Besides the dependency of the excitation frequency, it is described how the transducer affects the characteristics of the system, and what the upper limit for the extractable output power is. In addition, the electrical equivalent circuit is presented, allowing the computer-aided simulation. For this section, there are consisting of the combination by the mechanical and electrical models.

2.4.3.1) Theoretical related to mechanical model

The energy harvester model can be equivalent as a damping mass-spring mechanical system by the degree of freedom (DOF) diagram as shown in previously of figure 1.5(a). The seismic mass connected to movable body by a spring with a stiffness of k and the damper with coefficient of ζ. For the harvesting conversion, ζ is comprised of both the parasitic losses of ζ_p and electrical energy extracted by the transduction mechanism of ζ_b; $\zeta = \zeta_p + \zeta_b$. This system consisted with seismic mass of m fixed on

the moving body and the system is excited by an external force of F(t) acting on with sinusoidal vibration, $Z(t) = Z_M \sin(\omega t)$. At the resonance frequency, there is a net displacement of $Z_M(t)$ between mass and frame, then the equation of motion of the seismic mass system can be described by equation (1.17) (Telba and Ali, 2012).

2.4.3.2) Theoretical related to electrical model

The mechanical system can be described with an equivalent diagram with electrical components of the electrical model as shown in figure 2.14 (Staworko and Uhl, 2008). The inductance of L represents the seismic mass and inertia of the harvester, C_k is inversely proportional to a stiffness of k, C_b represents the static capacitance of the harvester, and R is the insulation leakage resistance of the harvester element, or its represents the damping coefficient of ζ. For the electric equivalent of a piezoelectric generator model can be described by applying Kirchhoff's current and voltage law referring to equation (2.32)-(2.34) which similar to equation (1.13)-(1.14), respectively (Koyvanich *et al.*, 2015).

$$\sigma_{in} = L_m \ddot{q} + R_b \dot{q} + \frac{1}{C_k} q + nV \tag{2.32}$$

$$i = C_b \dot{V} + \frac{V}{R} \; ; \qquad V = \frac{1}{C_b} \int i \cdot dt \tag{2.33}$$

$$V = \sigma_{in} - V_{C_k} - V_{L_m} - V_R = \sigma_{in} - \frac{1}{C_k} \int i \cdot dt - L_m \frac{di}{dt} - R \frac{dV}{dt} \tag{2.34}$$
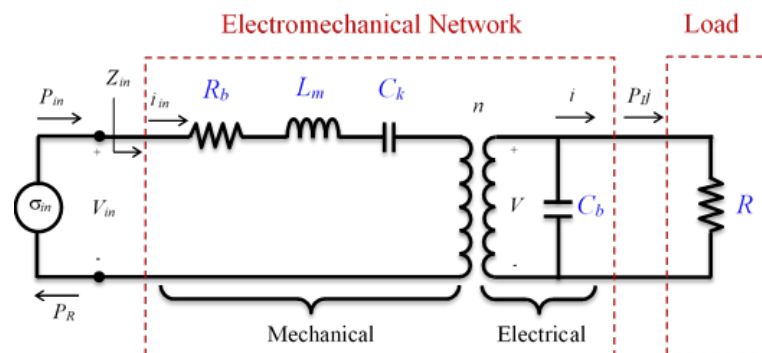
Figure 2.14 Equivalent circuit representation of the piezoelectric generator along with power definitions. (Ahmad *et al.*, 2011)

For more expression to be transformed into a usable system of mechanical model, equivalent expressions have been derived as given equation (2.35)-(2.39) (Ahmad *et al.*, 2011);

$$n = \frac{-a\,d_{31}c_p}{2t_c} \tag{2.35}$$

$$R_b = k_1 k_2 b_m \tag{2.36}$$

$$L_m = k_1 k_2 m \tag{2.37}$$

$$C_b = \frac{a^2 \varepsilon\, wl}{2t_c} \tag{2.38}$$

$$C_k = c_p^{-1} \tag{2.39}$$

where n, d_{31}, c_p, k_1, k_2, a, w, l and t_c is turn ratio, piezoelectric strain coefficient, elastic modulus, constant relating stress to force, constant relating the strain to the deflection, piezo- constant on electrode direction, width, length and thickness of piezoelectric material.

Considering on electro- mechanic model, to obtained maximum powering were achieved by the resonance condition on the specifically frequency variation. The current output for RLC series circuit with voltage (V_{pp}) and impedance (Z) is defined as equation (2.40).

$$I = \frac{1}{Z} = \frac{V_{pp}}{\sqrt{R_b^2 + \left(\omega L_m - \dfrac{1}{\omega C_b}\right)}} \tag{2.40}$$

The power transferred to the load as a result of the mechanical stress evaluated at zero electric field is given as equation (2.41):

$$P = \frac{1}{2\omega^2} \cdot \frac{RC_b^2 \cdot \left(\dfrac{2c_p d_{31}t_c}{k_2 a\varepsilon}\right)^2 A_{in}^2}{(4\zeta^2 + k_{31}^2)(RC_b\omega)^2 + 4\zeta k_{31}^2(RC_b\omega) + 4\zeta^2} \tag{2.41}$$

where the damping term (b_m/m) can be rewritten in terms of the unit-less damping ratio (ζ) as $2\zeta\omega n$ (Roundy and Wright, 2004).

The optimal load resistance can then be found by differentiating equation (2.41) with respect to R, setting the result equal to zero, and solving for R. The resulting optimal load resistance is shown in equation (2.42).

$$R_{opt} = \frac{1}{\omega C_b} \cdot \frac{2\zeta}{\sqrt{4\zeta^2 + k_{31}^2}} \tag{2.42}$$

2.4.3.3) Methodology of MATLAB Simulink

As with purely electrical circuits, the system equations are then determined using Kirchhoff's voltage law (KVL) and Kirchhoff's current law (KCL). Taking the sum of 'voltages' around the mechanical side of the circuit yields the expression in equation (2.32). Summing the currents output (*i*) in figure 2.12 yields the expression in equation (2.33). The parameter of the input stress (σ_{in}) is equal to $k_1 F_{in}$, where F_{in} were obtained by solution of the FSI problem in section 2.5.2. Material properties (table 2.5) were substituted into equivalent circuit parameters of equation (2.35)-(2.39), then the generated power by PVDF (*P*) with *R* variations had been calculated by using equation (2.40). The optimum lord resistance (*R*) at resonance frequency (ω_n) calculates by using equation (2.42).

Table 2.5 Parameters and material properties for equivalent circuit model.

Parameter	Value	Unit
Beam length (l)	0.04140	m
Beam width (w)	0.01630	m
Beam thickness (t)	0.000134	m
Beam permittivity (ε)	1800	F/m
electrode length (l_e)	0.0256	M
electrode width (w_e)	0.0122	M
electrode thickness (t_e)	0.0002	M
Electrode permittivity (ε_e)	190	F/m
Piezo strain constant (d_{31})	-1.9×10^{-10}	C/N
Coupling factor ($k_{31)}$	0.32	-
Young's modulus (E)	6.2×10^{10}	N/m^2
Directional constant (a)	1 or 2	-
Constant relating stress to force (k_1)	-0.33	-
Constant relating the strain to deflection (k_2)	-0.033	-
Damping ratio (ζ)	0.175	-
Resonance frequency 1 (f_1)	0.217	Hz
Resonance frequency 2 (f_2)	1.03	Hz

2.5 Results

The outcome in this chapter where there is a combination of simulation and experimental data is as follow;

2.5.1) Fluid flow vortex induced vibration piezoelectric energy harvesting is experimental results of the VIV apparatus in laboratory.

2.5.2) Computational fluid flow vortex induced vibration is for studying flow energy transform to mechanical oscillation energy and the other factors which effort to their mechanical energy.

2.5.3) Fluid structure interaction is the computational results studying on effect of vibrational behavior on piezoelectric transducer film in the variation of flows conditions.

2.5.4) MATLAB Simulink is the comparison of the results of precious sections (2.5.2)-(2.5.3) with mathematical model by using MATLAB Simulink software.

2.5.1) Fluid flow piezoelectric vortex induced vibration

The vortex induced vibration energy harvesting apparatus is shown in figure 2.8. The results of signal output without resistance load in the variation of flow rate are present in figure 2.15. It shows that almost all output signal are increased with the flow rate up to $Q = 0.4$ gallons/min in a voltage range of 5-63 mV. For more results of voltage output with the flow rates (Q) variation were presented in Appendix A (V). However, an electrical harvested signals had been detected at 50 Hz. They were possibly from stress conversion by the VIV effects or from electromagnetic noise induction during the electrical measurement. Appling the low-pass filtering technique to cutting-off frequency over 10 Hz, it shown that the FFT signals peaks by PVDF vibration at flows rate sampling of $Q = 0.6$ gallons/min. Their measured signals were used as the experimental data compared with the mathematical model results in the next section.
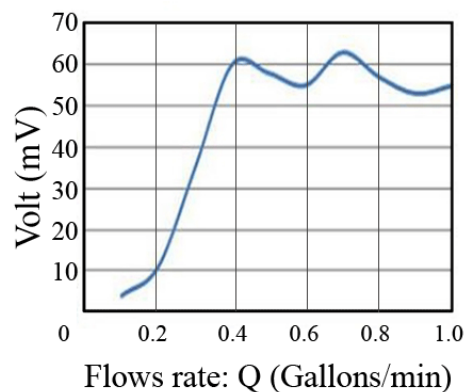
Figure 2.15 Voltage signal output without resistance load in the variation of flow rate.

2.5.2) Computational fluid flow vortex induced vibration

The commercial software COMSOL-multi Physics were used to simulated 9 studied cases of VIV saturations. Applied variation of dimensional length (D_h) of 4, 5, and 6 cm on the bluff body which generated VIV behavior, including with the flows speed variation of 0.8, 1.0, and 1.2 m/s had been performed. Unit-less parameter of drag and lift coefficient were obtained by integrated pressure force acting on the bluff body boundary surface as given in equation (2.15)-(2.16). Figure 2.16 is presented time variation of drag coefficient acting on bluff body which larger Dt were generated larger Cd and higher flow velocities were generated higher C_d than the other respectively. The vibrational induced drag force by U of 1.2, 1.0 and 0.8 m/s were generated at $t = 3.5$, 5.0, and 9.0 m/s respectively. In the same saturation, figure 2.17(a)-2.17(c) are presented time variation of lift coefficient acting on bluff body which larger Dt were generated larger amplitude of C_L. The higher flow velocities were generated higher amplitude of C_L than the lower respectively. The vibrational induced lift force by U of 0.8, 1.0 and 1.2 m/s were generated at t = 6.0, 3.0, and 2.0 m/s respectively.
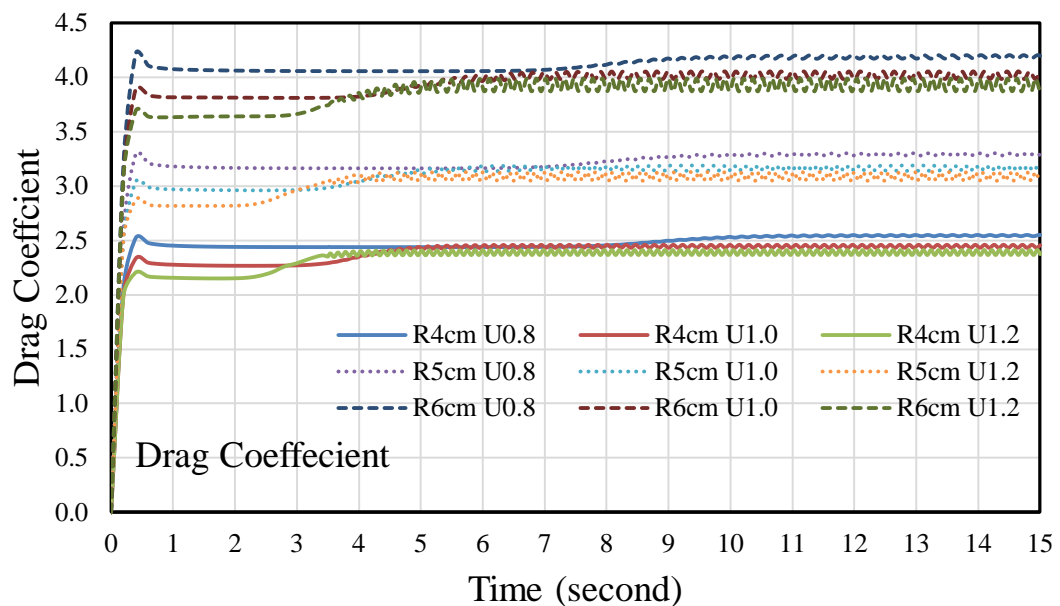
Figure 2.16 Drag coefficient (C_d) of VIV simulation with variation Dt of 0.8, 1.0, 1.2 cm by U at 0.8, 1.0, 1.2 cm/s.
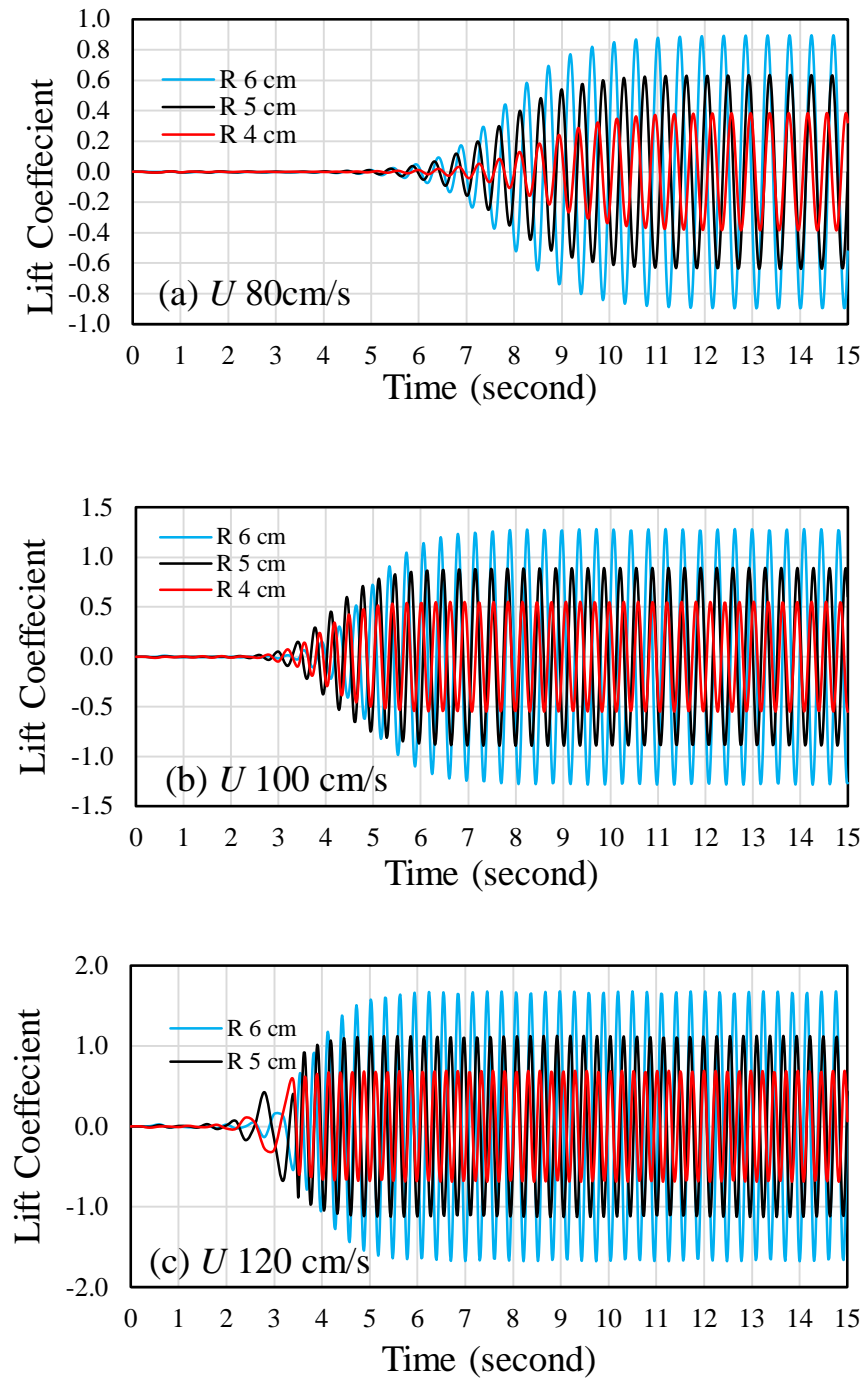
Figure 2.17 Lift coefficient (C$_L$) of VIV simulation for variation of Dt of 0.8, 1.0, 1.2 cm by U at (a) 0.8, (b)1.0, and (c) 1.2 m/s.

Figure 2.17 represents the Lift coefficient (C_L) of the VIV simulation results though the variation of Dt = 0.8, 1.0, 1.2 cm with variation of U at (a) 0.8, (b)1.0, and (c) 1.2 cm/s. The highest C_L appeared for highest of Dt = 1.2 cm, same as the results of C_d calculation, similarly to lowest C_L were generated at Dt = 0.8 cm/s. For the variation of U, the results show that the generated C_L of U = 0.8, 1.0, 1.2 m/s had been induced since t = 6.0, 3.0 and 2.0 respectively, while the t of induced Cd was increase for U decrease.

The FFT frequency oscillation of the drag and lift coefficients of the variation of flow profiles are presented in figure 2.18-2.19. The largest amplitude peaks were appeared in U of 1.20 m/s for each of Dt and the lowest were generated by U of 0.8 m/s. The VIV oscillations of lift force are in a range of 1.70-3.25 Hz while the drag force is in a range of 4.5-8.3 Hz.
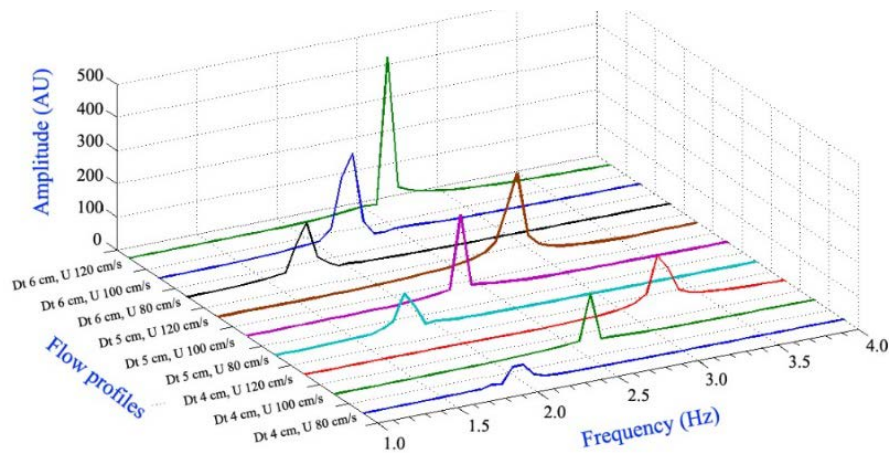
Figure 2.18 The FFT of lift coefficients with variation of flows profiles.
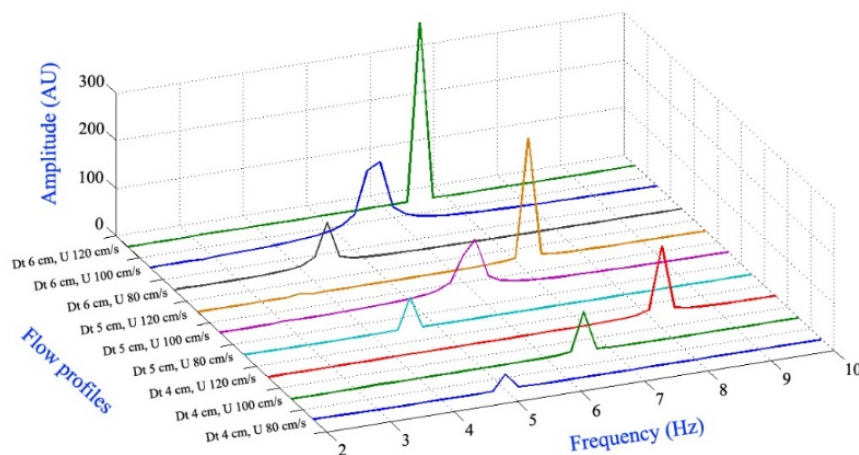
Figure 2.19 The FFT of drag coefficients with variation of flows profiles.
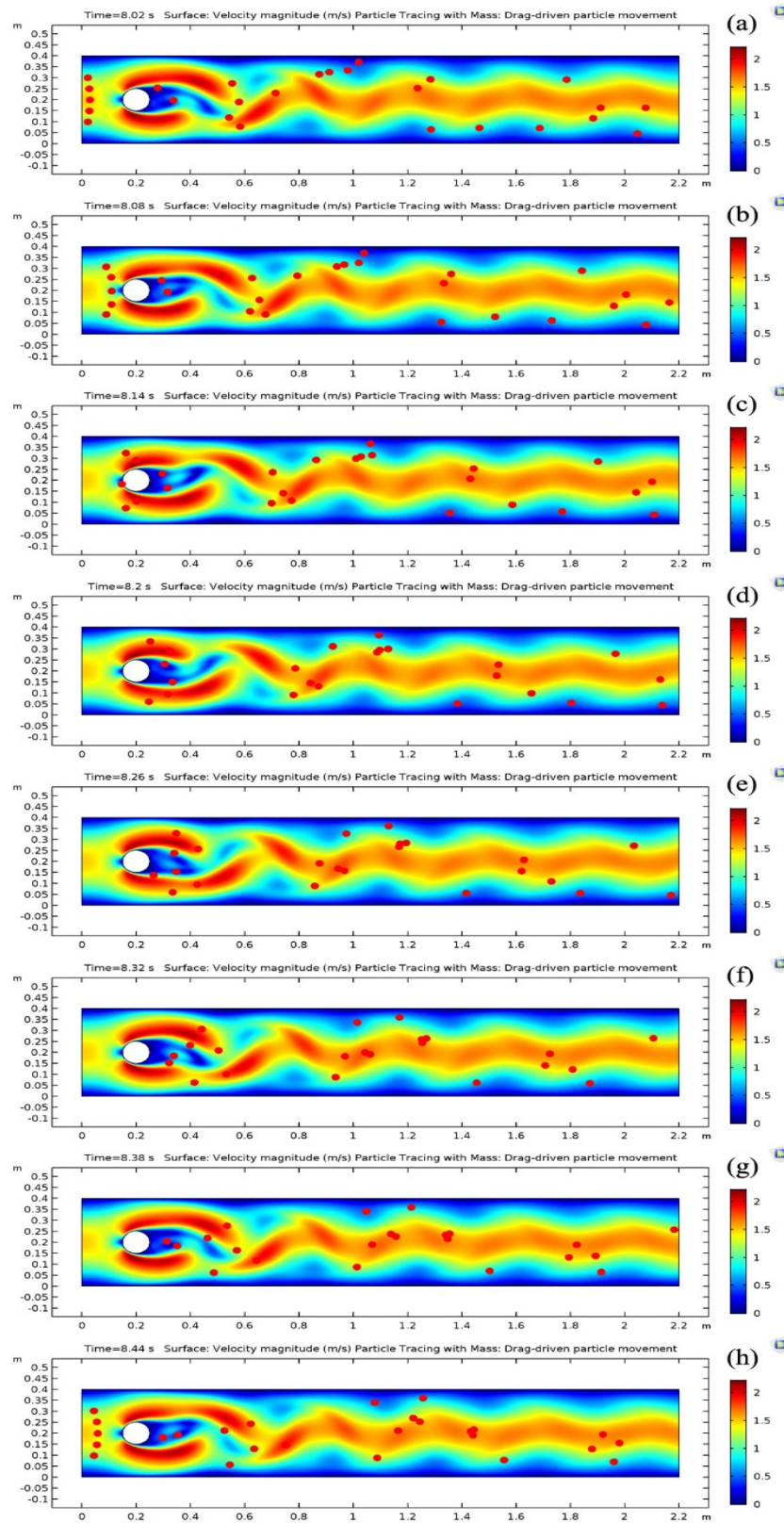
Figure 2.20 Time variation of surface velocity magnitude (m/s) and particles tracing with mass (red dots).
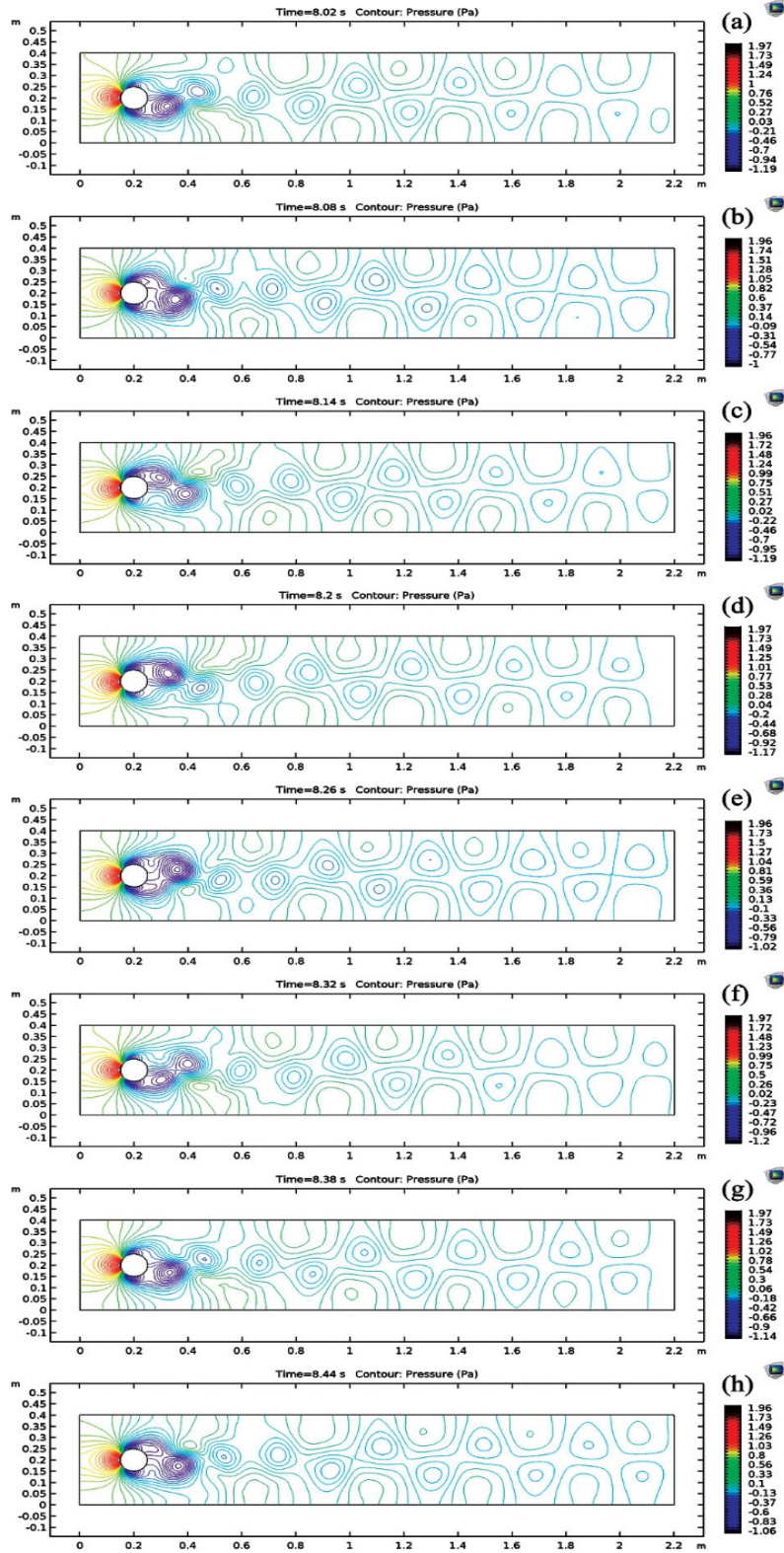
Figure 2.21 Time variation of the contour pressure equipotential line represented generated vortices behind bluff body of Dt = 1.0 cm and U = 1.0 m/s.

Figure 2.20 (a)-(h) represents the time variation between 8.02-8.44 second of surface velocity magnitude (m/s) and particles tracing with mass (red dots) for U = 1.0 m/s and D_t = 1.0 cm, which represented drag particles movement by the interaction of vortices. The solution of flow velocity and pressure of any mesh for fluid domain were solved by using equation (2.18)-(2.19). Higher velocity indicated by legend of velocity were generated at top and bottom position of the bluff body. The zero velocity was appeared behind away 0.1 m from the bluff body surface for U=1.0 m/s condition. From time to time as in the same region, magnitude of velocity fluid was changed increase and decrease for over and over and it was generated the fluctuation on flow steam region behind the bluff body object. Figure 2.21 (a)-(h) represents the time variation between 8.02-8.44 second of the contour pressure equipotential line for the VIV of Dt = 1.0 cm with U = 1.0 m/s. The circular line was indicated fully wake fluctuation of velocity and pressure which developed behind bluff body as von Kármán Vortex Street involves the shedding of eddies from alternating sides vortices generated behind bluff body. The fully stabilized state of VIV effect was appeared after initial at t > 8.0 sec and the variation of time steps is 0.06 sec. The results of VIV parameters are summarized in table 2.6.

Table 2.6 The resultant parameters calculated from the VIV simulation.

D_t (cm)	0.8			1.0			1.2		
U (m/s)	0.8	1.0	1.2	0.8	1.0	1.2	0.8	1.0	1.2
Max-lift coefficient	0.392	0.563	0.705	0.647	0.911	1.148	0.913	1.309	1.172
Min-lift coefficient	-0.392	-0.562	-0.702	-0.650	-0.911	-1.415	-0.913	-1.310	-1.710
Lift frequency (Hz)	2.00	2.60	3.20	1.80	2.33	2.87	1.73	2.20	2.60
Lift peak amplitude (A.U.)	53.4	150.6	151.7	112.3	241.2	259.4	156.8	265.5	458.7
Max-drag coefficient	2.57	2.48	2.42	3.33	3.22	3.16	4.26	4.09	4.03
Min-drag coefficient	0.0	0.0	0.0	0.0	0.0	0.0	0.0	0.0	0.0
Drag frequency (Hz)	5.0	6.6	8.2	4.6	6.0	7.2	4.4	5.6	6.7
Drag peak amplitude (A.U.)	0.685	1.712	2.883	1.339	2.255	5.104	1.846	2.949	6.725
Max-velocity (m/s)	1.595	2.075	2.549	1.670	2.218	2.702	1.784	2.339	2.839
Min-velocity (m/s)	0.0	0.0	0.0	0.0	0.0	0.0	0.0	0.0	0.0
Max-pressure (Pa)	1.13	1.73	2.42	1.22	1.89	2.65	1.34	2.05	2.89
Min-pressure (Pa)	-0.52	-0.91	-1.60	-0.61	-1.19	-1.82	-0.66	-1.31	-2.14

2.5.3) Fluid structure interaction

Four studied cases were estimated the FSI situations with FSI-1, FSI-2, FSI-3, and FSI-4 by variation of flow velocity of U = 0.5, 1.0, 2.0 and 4.0 m/s as given in table 2.4. The lift and drag coefficient were obtained by using equation (2.15)-(2.16) and the frequency oscillation had been achieved by FFT technique.
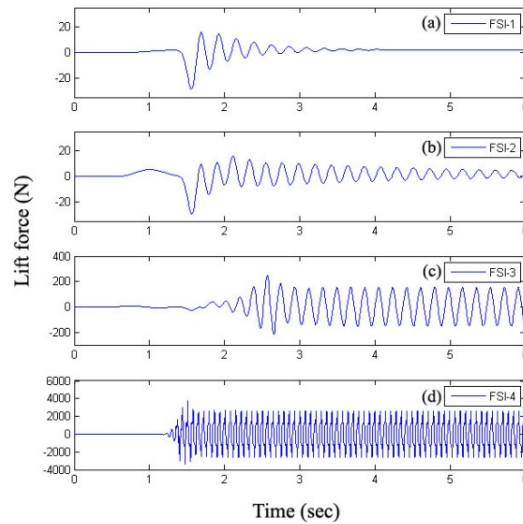
Figure 2.22 Time variation of lift coefficient (C_L) with variation of flows profiles of (a) FSI-1, (b) FSI-2, (c) FSI-3, and (d) FSI-4.
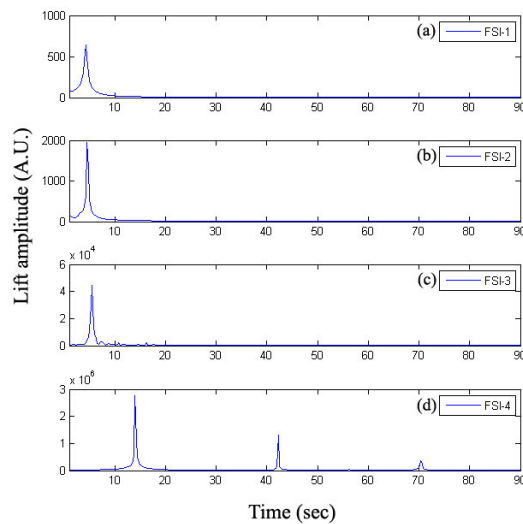
Figure 2.23 The FFT spectrum of lift coefficient (C_L) with variation of flows profiles of (a) FSI-1, (b) FSI-2, (c) FSI-3, and (d) FSI-4.
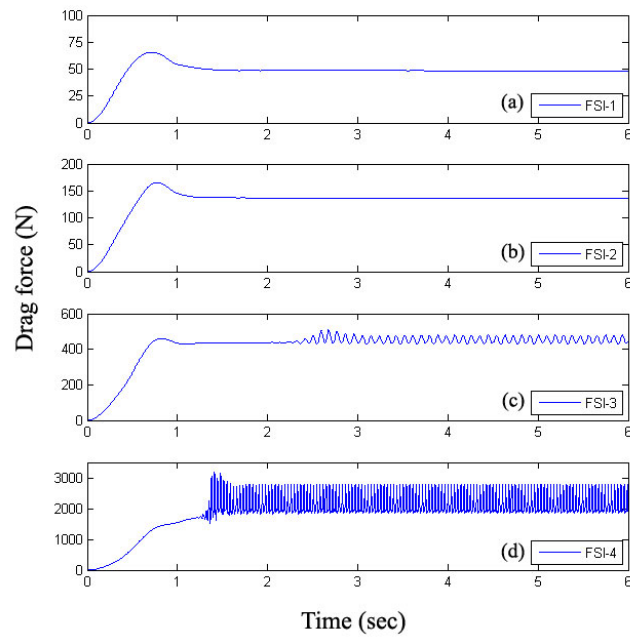
Figure 2.24 Time variation of drag coefficient (C_D) with variation of flow profiles of (a) FSI-1, (b) FSI-2, (c) FSI-3, and (d) FSI-4.
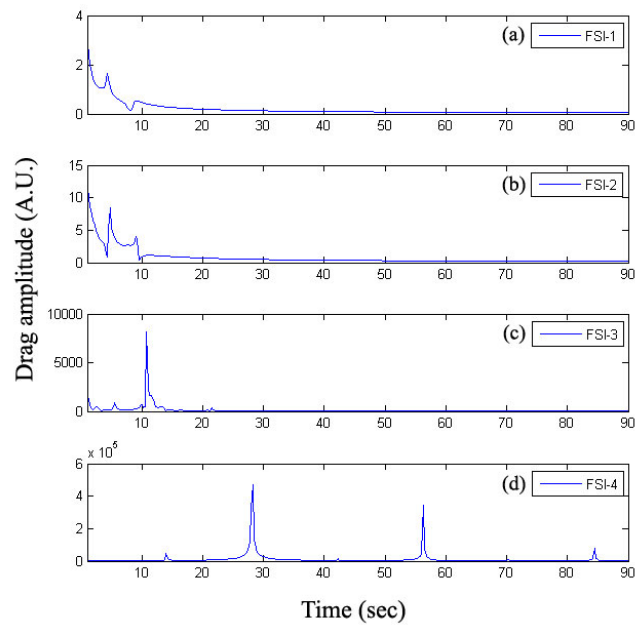
Figure 2.25 The FFT spectrum of drag coefficient (C_D) with variation of flow profiles of (a) FSI-1, (b) FSI-2, (c) FSI-3, and (d) FSI-4.
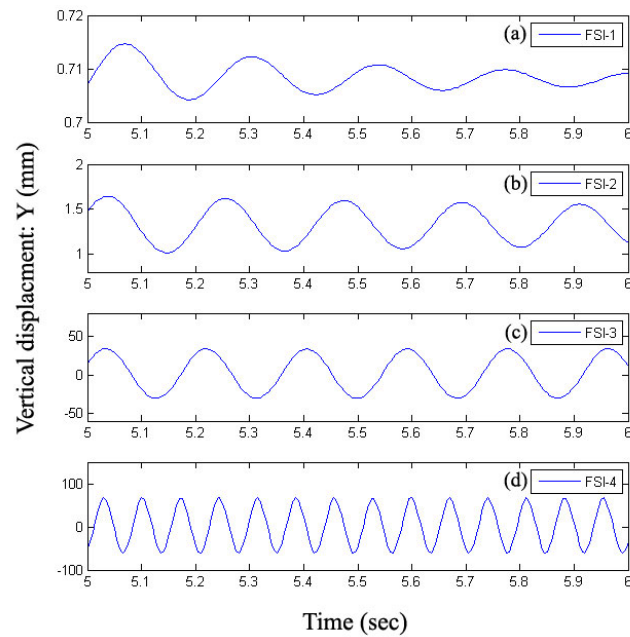
Figure 2.26 Time variation of vertical displacement (Y) at the free end of elastic beam interval t = 5.0-6.0 sec for (a) FSI-1, (b) FSI-2, (c) FSI-3, and (d) FSI-4.
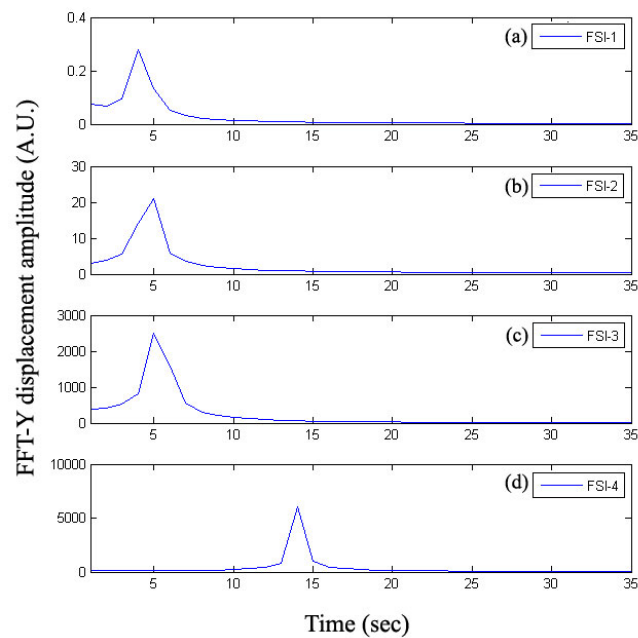
Figure 2.27 FFT frequency spectrum of vertical oscillation of the elastic beam at the free end for (a) FSI-1, (b) FSI-2, (c) FSI-3, and (d) FSI-4.
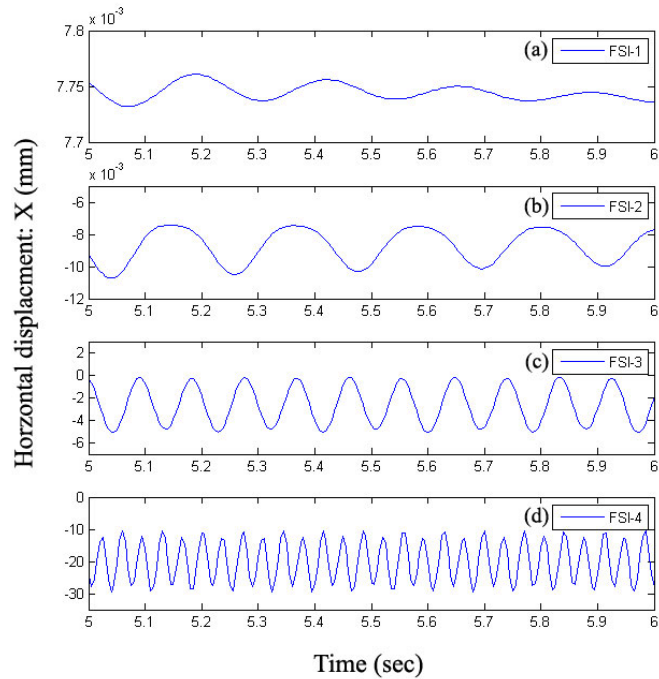
Figure 2.28 Time variation of horizontal displacement (X) at the free end for elastic beam interval t = 5.0-6.0 sec for (a) FSI-1, (b) FSI-2, (c) FSI-3, and (d) FSI-4.
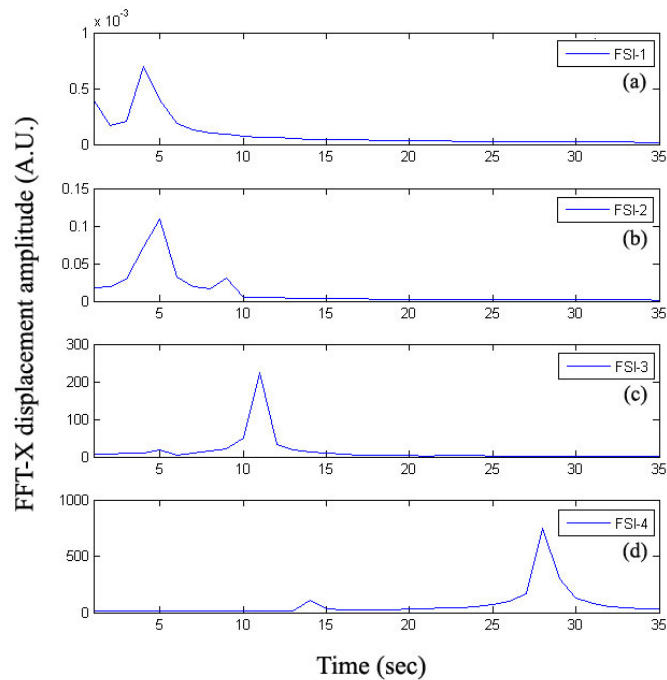
Figure 2.29 FFT frequency spectrum of horizontal oscillation of the elastic beam at the free end for (a) FSI-1, (b) FSI-2, (c) FSI-3, and (d) FSI-4.

Figures 2.22 and 2.24 represent the time variation interval t = 0-6 sec of lift coefficient C_L and drag coefficient C_D, respectively, with variation of flows profiles for FSI-1, FSI-2, FSI-3, and FSI-4. For FSI-1, life force was activated since t =1.5 s then they were reducing and vanished till t=4.0 s. Similarly, FSI-2 started at the same time with the similar amplitude range but the damping efficiency was less than the FSI-1. For the last situation of FSI-3 and FSI-4, the F_L of FSI-3 start generated at t=1.2 s and FL of FSI-4 were began at t=5 s including the F_L of FSI-3 was induced at t=2.5 s and the F_L of FSI-3 was started radically oscillation at t = 1.5 s. The steady state oscillations were established at t = 3 and 1.8 s for the FSI-3 and FSI-4 condition, respectively. For the drag force induction, the F_D increasing was reached to the maximum and approached to the steady state for t =0-1 s. After the increment, vanish mechanical oscillating were appeared for FSI-1 and FSI-2. The F_D was started induced at t = 2.4, 1.3 s for the FSI-3 and FSI-4 respectively. The development of time variation for F_D were similarly as the F_L conditions.

The FFT spectrum of the lift and drag oscillation were presented in figures 2.23 and 2.25 respectively. The lift oscillations were generated with FSI-1 and FSI-2 for 4.25 and 4.5 respectively, while the drag oscillating were not induced as the small peak amplitude appeared. For the FSI-3, the oscillation of F_L was appeared at 5.5 Hz and F_D for 10.75 Hz which the oscillating of F_L was double price of F_D. The FSI-4 situation, FL were appeared at 14, 44 and 72 Hz including FD at 28.25, 57.5 and 65 Hz.

The horizontal and vertical displacement at free end of elastic beam were presented in figures 2.26 and 2.28 respectively. The X and Y oscillation of FSI-1 interval 5 to 6 s were very small as 0.71 and 0.14×10^{-4} mm respectively and it were reduced with time as dimpling effect. In the similarly, the vibrational of X and Y are 1.64262 and 1.651×10^{-3} mm for FSI-2. Without damping effect, the displacement oscillation of elastic beam in Y direction were 33.68 and 67.98 mm for FSU-3 and FSI-4, likewise X direction was 2.46 and 9.49 respectively. Figures 2.27 and 2.29 were presented frequency spectrums of the elastic beam oscillation in horizontal and vertical direction. Both X and Y displacement oscillation were generated with the same frequency of 4 Hz for FSI-1 and 5 Hz for FSI-2 which represented small scale amplitude vibration. The vertical oscillation was generated by 5 Hz for FSI-3 and 14 for FSI-4, while horizontal vibrations were induced at 11 Hz for FSI-3 and 28 for FSI-4 respectively.
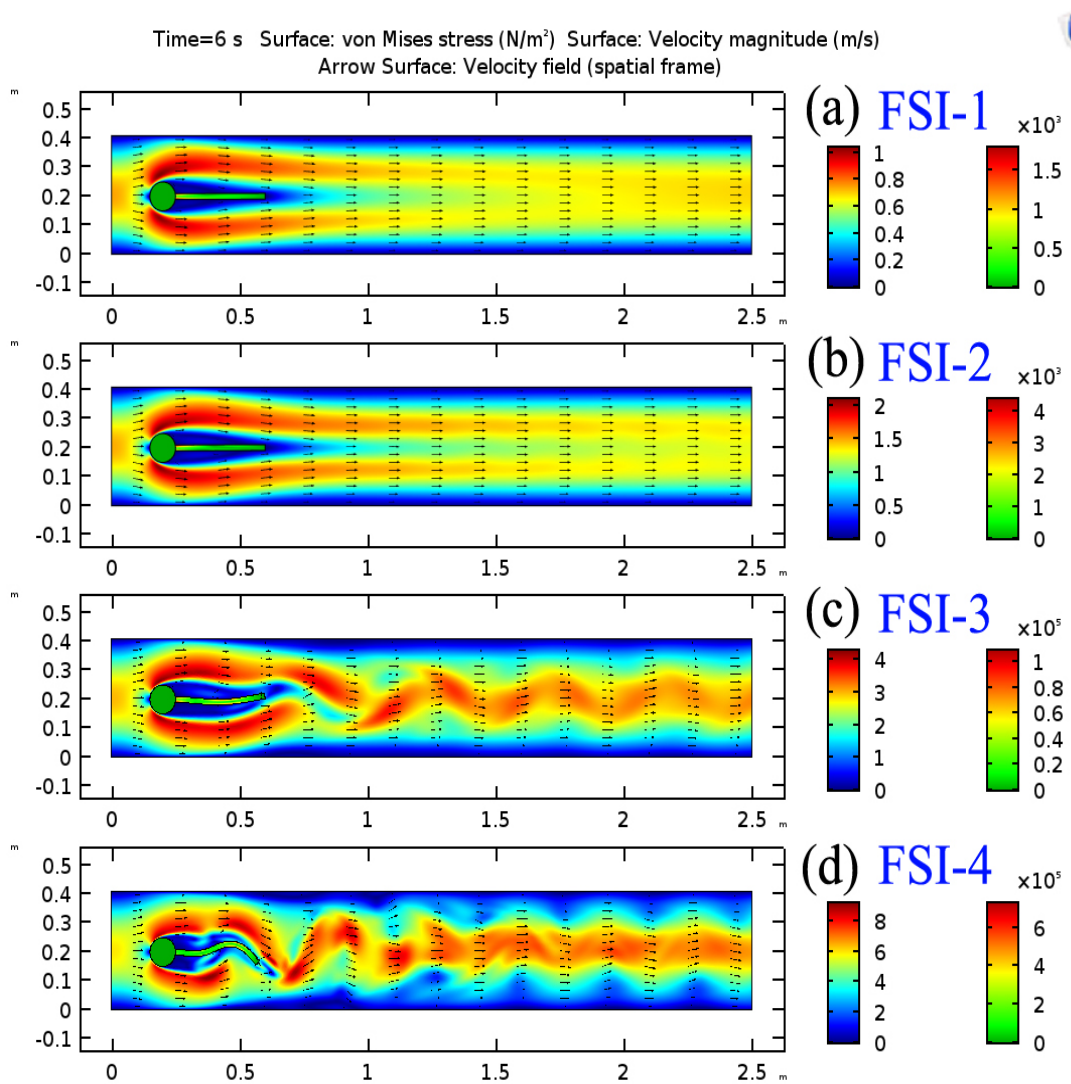
Figure 2.30 Magnitude fluid velocity with arrow indicated velocity direction in fluid domain for (a) FSI-1, (b) FSI-2, (c) FSI-3, and (d) FSI-4.
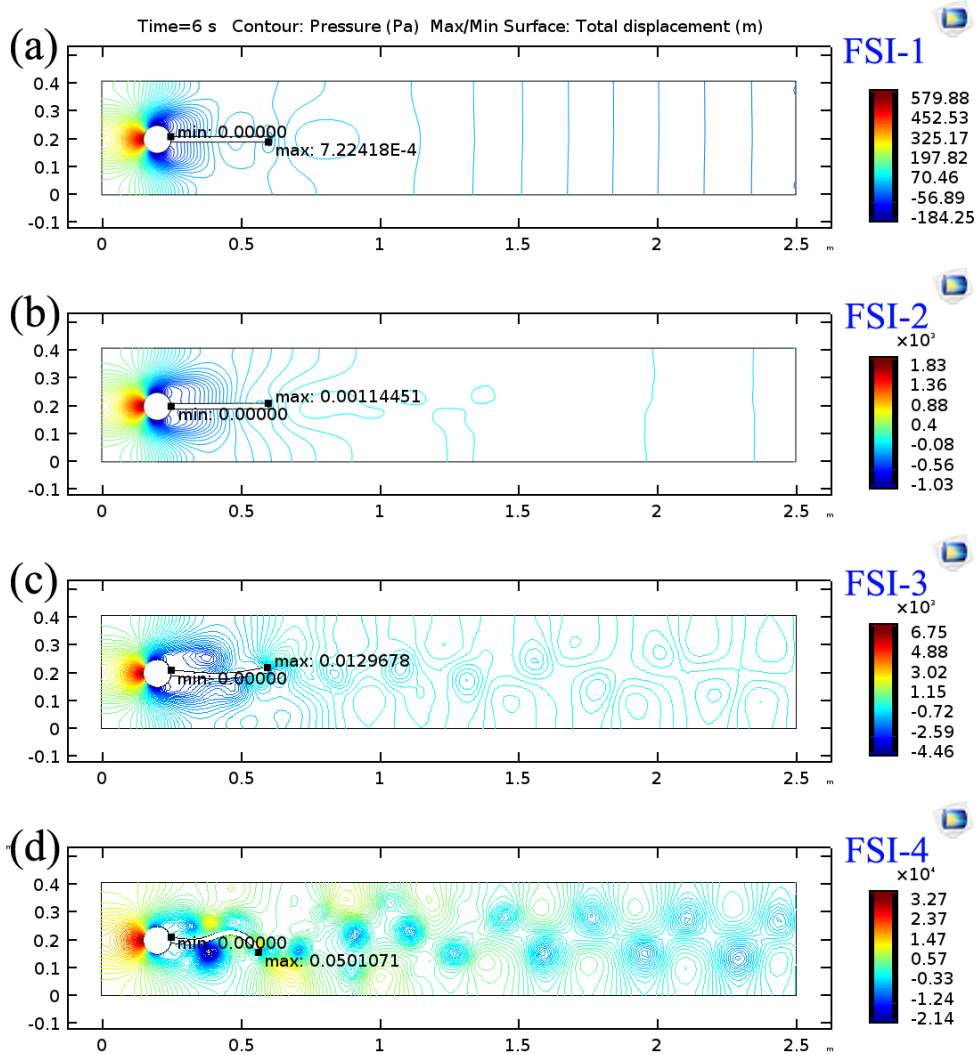
Figure 2.31 Magnitude of the contour pressure equipotential lines represented generated vortices leading to the VIV behavior for (a) FSI-1, (b) FSI-2, (c) FSI-3, and (d) FSI-4.

Figure 2.30 is represented magnitude fluid velocity with arrow indicated velocity direction in fluid domain and the figure 2.29 is presented the magnitude of the contour pressure equipotential lines represented generated vortices leading to VIV behavior for FSI-1, FSI-2, FSI-3 and FSI-4. Without vortex shading pattern behind bluff body is correspond with Re = 25 for FSI-1, which described fixed vortices pair in wake behind the bluff body (figure 2.4). In additional, there are agree with the results of equipotential for pressure line as shown in figure 2.29(a). Likewise, lift and drag force generated at *t* > 5.0 s by figure 2.20 (a), 2.22(a) were indicated in the similar way of non-exciting state as the laminar flows.

Although vortex shading pattern in the wake was absent in the FSI-2 similar with FSI- 1, but non- vanish damping of the lift force were generated vortices in wake (indicated by equipotential of pressure loop) behind the bluff body as presented in figure 2.29(b). By the reason of Re = 39 which the fixed stabilizing vortices in wake were established. It leads to 5 Hz of the beam oscillation in both vertical and horizontal direction.

The FSI-3 with U = 2.0 m/s was obtained Re = 78, which induced two regions in wake for laminar vortex street as shown in figure 2.4 condition. The certain platform of alternate fluctuation by velocity in fluid domains as presented in figure 2.30(c). Similarly with many circular equipotential loops occurred in the wake region which indicated to Karma Vortices Street as shown in figure 2.31(c). They are consistent with the absence of damping by lift and drag force in steady state for $t > 5$ as shown in figure 2.22(b) and 2.24(b) respectively. The vibrational is laminar flows and it induced 5 Hz, 33 mm's displacement in vertical oscillation and 11 Hz, 2.46 mm's displacement in horizontal oscillation

The FSI-4 with U=4 m/s was generated Re =155, which indicated the transition in vortexes from laminar to turbulence state (figure 2.4). Non-regular fluctuation pattern of fluid velocity as show in figure 2.30(d) were agreed with the large scale of lift and drag force generated as show in figure 2.22(d) and 2.24(d) respectively.
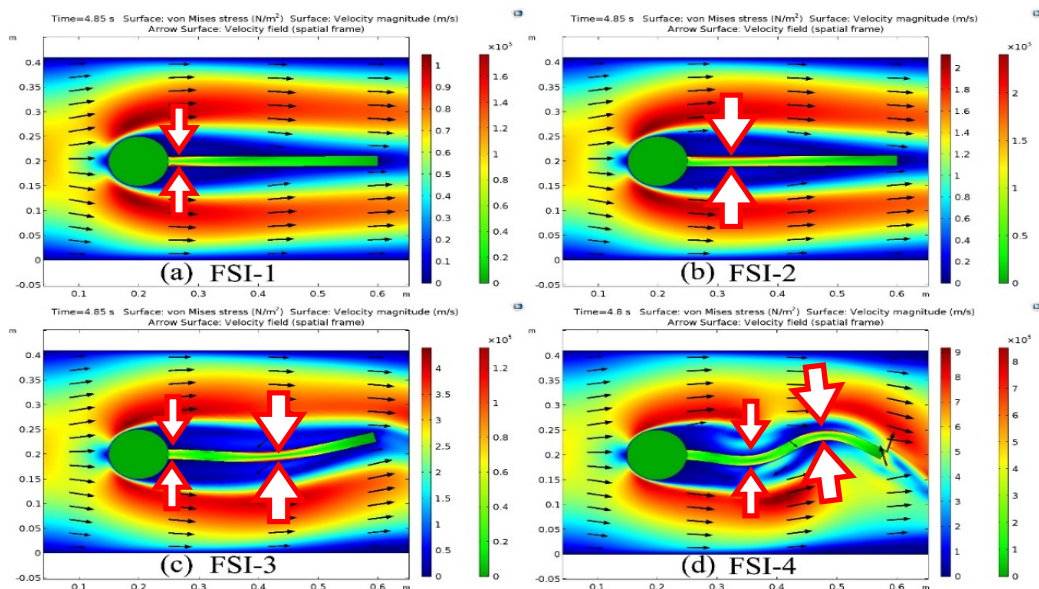
Figure 2.32 Magnitude of fluid velocity and stress generated on the vibrational elastic beam in case of (a) FSI-1, (b) FSI-2, (c) FSI-3, and (d) FSI-4.

Connection of the fluid force related to elastic beam oscillation can be describe by figure 2.32, which represented the magnitude of fluid velocity and stress generated on the vibrational elastic beam in the case of FSI-1, FSI-2, FSI-3, and FSI-4.

Although without velocity fluctuation in wake of FSI-1, but X, Y oscillation were occurred with 0.714 mm in vertical direction. That are generated stress between the connection of the fixed and elastic materials because the remains displacement oscillation.

By the increasing of the displacement oscillation for the FSI-2 condition, induced stress extend to increased surface of the elastic beam by materials deformation with 5 Hz by the vertical displacement of 1.64 mm. In FSI-3 is fully generated the stabilizing vortexes of laminar flows as presented in definition of figure 2.4 and results of figure 2.28(c). The generated stresses were developed at the connected point of fixed elements and the elastic unit, and the stress was mainly generated on the middle of beam length. But the stress which developed in the joint were not effort to fluid flow and elastic beam oscillation.

In the transition to turbulence in the vortex of the FSI-4 condition, the induced oscillations were generated at the positions of 1/3 and 2/3 length of the elastic beam. The major stress was developed at 2/3 beam length by the lift force with 14 Hz oscillation and the minor stress was developed at 1/3 beam length by the lift force with 43 Hz oscillation. Both coupling frequencies mode oscillation of both lift and drag force were induced coupling frequencies oscillation in horizontal direction and single mode frequency oscillation in vertical direction. The smaller horizontal displacement is not comparable with the larger vertical displacement oscillation. This is because the stretching of elastic beam represents the spontaneous oscillation. The results of VIV parameters are summarized in table 2.7

Table 2.7 Calculated parameters from the FSI simulation.

D_t (cm)	FSI-1	FSI-2	FSI-3	FSI-4
U (m/s)	0.5	1.0	2.0	4.0
Reynolds umber (Re)	25	63	125	251
Max-lift force (N)	15.71	15.80	251.01	3742.1
Min-lift force (N)	-28.76	-29.63	-214.60	-3352.6
Lift frequency (Hz)	4.25	4.5	5.5	14
FFT-lift peak amplitude (A.U.)	644.6	1955.0	44570	2752000
Max-drag force (N)	65.6	165.4	508.4	3173.5
Min-drag force (N)	0.0	0.0	0.0	0.0
FFT-drag frequency (Hz)	-	-	10.75	28.25
FFT-drag peak amplitude (A.U.)	-	-	8127	470000
Y-displacement of beam (mm)	0.7146	1.6426	33.681	67.984
Y frequency oscillation (Hz)	4	5	5	14
X-displacement of beam (mm)	0.000014	0.00165	2.45953	9.49104
X frequency oscillation (Hz)	4	5	11	28
Max-velocity (m/s)	1.0	2.1	4.6	9.0
Min-velocity (m/s)	0	0	0	0
Max-pressure (kPa)	0.58784	1.89	6.82	31.0
Min-pressure (kPa)	-0.16833	-0.97	-4.57	-18.4
Maximum stress (kN/m^2)	1.8	5.0	46.0	460.0

2.5.4) The validation of experimental with equivalent circuit model

The results in this section are the validation of the experimental results in subsection 2.5.1 and mathematical model of the equivalent circuit for piezoelectric generator in figure 2.14 were solved by MATLAB Simulink software. Table 2.7 summarises all the parameters. The frequency variation of the signal results for the electromechanical part (figure 2.14) is presented in figure 2.31. The experimental results from the selected Q of 0.6 gallons/min in subsection 2.5.1 is represented as solid line and the model results as presented in dash line.
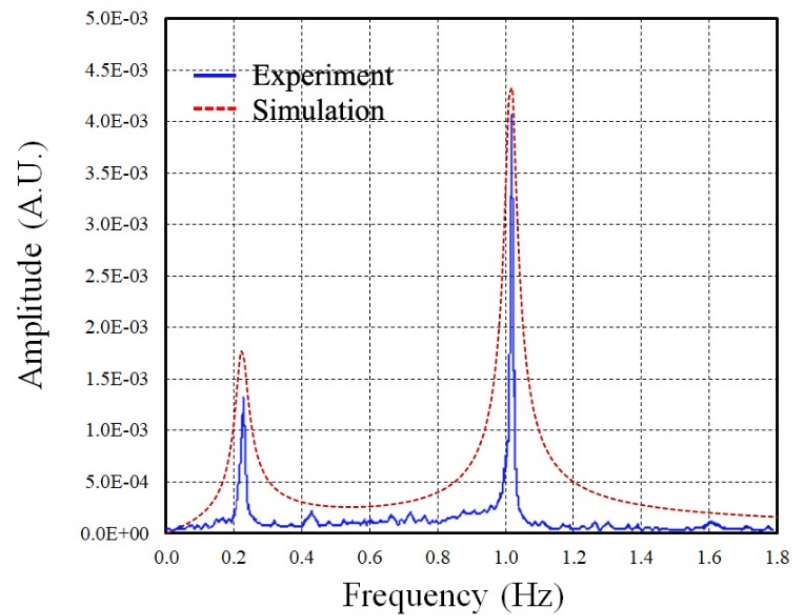
Figure 2.33 Frequency respond of signal output by the VIV harvesting at Q = 0.6 gallons/min (a) experimental and (b) equivalence circuit results.

The results show that two FFT-peaks were generated at 0.26 and 1.02 Hz for both experimental and model calculation results. As the flow rate condition with Q = 0.6 min/min were consequently to Re = 23 which indicated fixed pair of induced vortices in wake. For the instead, higher perk amplitude was obtained from vertical oscillation (1.02 Hz) due to piezoelectric stress constant ($\cong$-216 mV/m) effort to generated voltage output (V_{op}) from lift force were larger than V_{op} of drag force. However, the apparent of 0.23 Hz vibration shows the existence of total drag vibration.

On the equivalence circuit model, two peaks frequency responded were occurred by 2 directional vibrations (in case of 2 different frequencies oscillation) and/or 2 materials type of vibration beam (in case dominant of 1.0 Hz oscillation). The vertical and horizontal oscillations by lift and drag forces are obtained from VIV simulation results. More addition, PVDF and silver (as electrode) exhibited as elastic vibration beam, materials properties of both type were described in table 2.5.

For the powering with variation of resistance responded were obtained by using equation (2.42) and the results presented in figure 2.14. Two different types of material acting as elastic beam were given maximum powering output at 300 MΩ on 1.02 Hz oscillation by 1.8 μW.
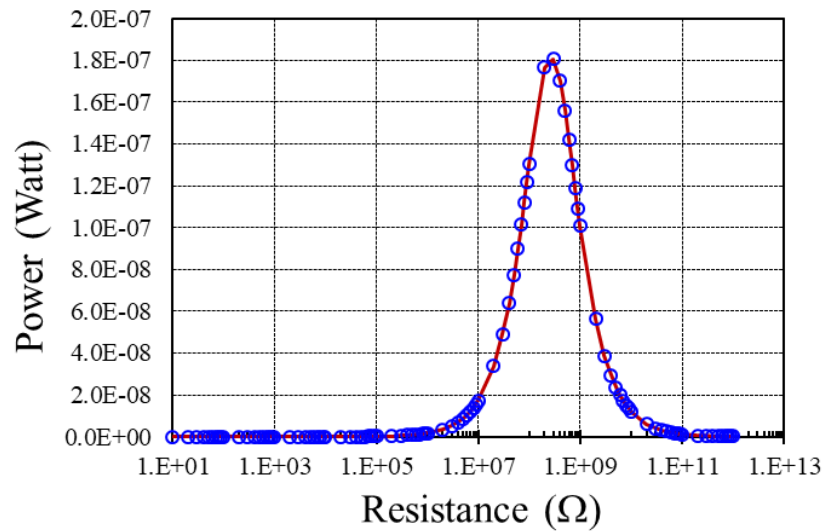
Figure 2.34 Powering output with the resistance variation for equivalence circuit model.

Energy conversion efficiency were estimated by flows power input divide by electrical power output as given by equation (2.39).

$$\text{Efficiency } (\eta) \quad = \quad \frac{\text{power input}}{\text{power output}} \quad = \quad \frac{44 \ \mu\text{W}}{0.18 \ \mu\text{W}} \quad = \quad 4.4\% \qquad (2.39)$$

2.6 Conclusions

Piezoelectric polymers had been applied in many fields, especially biomedical applications. Their specifically properties as acoustic impedance are similar to an inner of human body. The distinctive features of piezoelectric polymers are light weight; including high value of the modulus, voltage sensitivity and dielectric breakdown. The other properties which more prominent than ceramics is piezoelectric voltage constant (g_{31}). This parameter of PVDF is 20 times higher than that of PZT, when the charges induced by a pressure stress perpendicular to the electrode direction (stretching). This is excellent for sensor or generator applications. The piezoelectricity of polymer materials had been promoted by the alignment of internal dipole by a high voltage at the Curie temperature. On the other hands, an applied stretching process was used to increase β phase which has larger the amount of dipole moment per unit volume.

Energy harvesting implementation of polymer piezoelectric films as vortices induced vibrations (VIV) effect are utilized by taking advantage on kinetic energy of fluid flow to vortices oscillation. The Re no. was indicated by fluid flows velocity; including shape and size of bluff body represents the flow characteristic behavior. The St Number was given as vortices shading frequencies. The VIV phenomena usually consists of lift force (vertical) and drag force (horizontal).

Computational Fluid Dynamic (CFD) of the VIV and Fluid Structure Interaction (FSI) using Navier-Stokes and continuity equation provides that;

- The VIV behavior: higher flow velocity (U) was generated F_L and F_D faster than lower U; In case of U constant, the peak amplitude of F_L and F_D increased with bluff body's diameter (D_t) ; In case of D_t constant, the peak amplitude of F_L and F_D increased with U . In terms of frequency oscillation (f), lift force frequencies oscillation (f_L) is twice in magnitude of drag force frequencies oscillation (f_D). With U increasing the amplitudes and frequencies of F_L and F_D increased. With U constant, Dt increased while F_L and F_D slightly decreased.

- The FIS behavior: which represented flow behavior, as laminar or transition or turbulence state (referring by Re number). For the FSI-1 (Re=25) indicated the laminar flow, and FSI-2 (Re=39) represented the fixed pairs of the stabilizing vortices in wake. The oscillation had been illustrated by a displacement at the free end with damping oscillation. FSI-3 (Re=125) and FSI-4 (Re=250) show the transition and turbulence state, respectively. The FSI-3 presented the damping effect of turbulence state and the FSI-4 presented the fully turbulence state.

- Elastically deformation term: only a pressure stress was generated on an elastic beam in case of laminar flows (FSI-1, FSI-2) and the vibrational displacement increased with U. In the case of turbulence state, a deformation by pressure stress was occurred at more than one position on the beam depending on the vibration mode. Pressured stresses were generated proportional to the displacement, frequency oscillation, induced F_L and F_D, and flow velocity of U which in turn induced the vortices.

Equivalent circuit model can be used to calculate a power output (electrical) from the FIV effect which is computationally estimated for F_L and F_D. For the instead state, substituted electrical parameters as R_b, L_m, C_k (mechanical part) and C_b (electrical part) representing as dummy parameters for the equivalent circuit model of piezoelectric transducer. It can be evaluated electrical power output including optimized resistance (R_{opt}) by using characteristic parameters of PVDF material. By the comparison of the experimental with the simulation results the total efficiency is obtained to be 4.4% from both methods.

CHAPTER 3

SMALL SCALE HORIZONTAL AXIS WIND TURBINE
WITH ADJUSTABLE BLADES

The wind is characterized by its speed and direction, which are affected by several factors. Wind turbines interact with the wind, capturing part of its kinetic energy and converting it into usable energy. This energy conversion is the result of several phenomena as wind speed, attacking angle that are explored in this chapter.

3.1 Wind power

The wind in a given site near the surface of the Earth results from the combination of the geostrophic and local winds. Therefore, it depends on the geographic location, the climate, the height above ground level, the roughness of the terrain and the obstacles in the surroundings. These are the winds the wind turbines interact with. An interesting characterization of these surface winds is their kinetic energy distribution in the frequency domain. The concentration of energy around two clearly separated frequencies allows splitting the wind speed signal U into two components as defined in equation (3.1);

$$U = U_{\mathrm{m}} + u \tag{3.1}$$

where the quasi-steady wind speed (usually called mean wind speed) U_m is obtained as the average of the instantaneous speed over an interval t_p as given by equation (3.2).

$$U_m = \frac{1}{t_p} \cdot \int_{t_0 - t_p/2}^{t_0 + t_p/2} U(t) \cdot dt \tag{3.2}$$

The probability distribution of the mean wind speed is predicted from measurements collected during several years. All these data are usually arranged in a histogram. The wind distribution experimentally obtained can be approximated by a Weibull distribution, such as that shown in figure 3.1. (Bianchi, *et al.*, 2007)

The kinetic energy stored in a flow per unit volume is $E_k = 0.5\rho U^2$, where ρ is the density of the fluid. For a stream flowing through a transversal area A, the flow rate is AU. Therefore, the power in the wind passing through an area A with speed U is defined by equation (3.3).

$$P_V = \frac{1}{2} \cdot \rho A U^3 \tag{3.3}$$
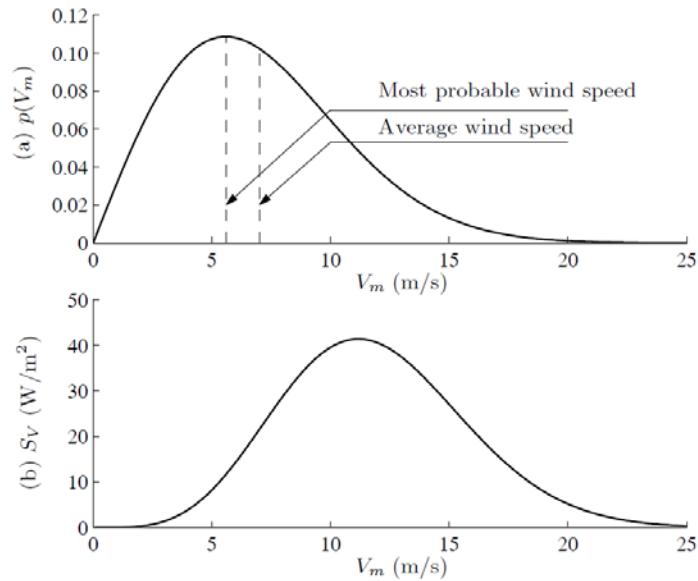
Figure 3.1 (a) Weibull probability distribution of mean wind speed and (b) power density vs wind speed.

The energy available in the wind is obtained by integrating (3.3) during a time interval T_p as given by equation (3.4).

$$\text{Average Energy} \quad = \quad \frac{1}{2}\rho A \int_{0}^{T_p} U^3 \cdot dt \qquad (3.4)$$

The most probable wind speed or the average wind speed from the Weibull distribution is taken to estimate the average energy. Figure 3.1(b) shows the power density, that is the distribution of energy at different wind speeds. This graph is obtained by combining the probability distribution of the wind speed with the power at each wind speed. As the example in figure 3.1(b), the average energy corresponds to a wind speed of 11.2 m/s. The wind distribution experimentally obtained can be approximated by a Weibull distribution as given by equation (3.5).

$$p(V_m) \quad = \quad \frac{k}{C}\left(\frac{U_m}{C}\right)^{k-1} \cdot e^{-\left(U_m / C\right)^k} \qquad (3.5)$$

where k and C are the shape and scale coefficients, respectively. These coefficients are adjusted to match the wind data (Global Wind Atlas, 2017).

In selection of non-stabilized flows, the knowledge of wind turbulence intensity is crucial for the stability of wind power production. The wind turbulence intensity (I)

is defined as the ratio of the standard deviation σ_u to the mean wind velocity (U_m) as given by equation (3.6).

$$I \quad = \quad \frac{\sigma_u}{U_m} \tag{3.6}$$

3.2 Wind turbine

After a brief description of the wind power estimation, some relevant notions of aerodynamics and derive expressions for the torque and forces developed on the wind turbines were discussed in this section.

Wind turbines are the mechanical devices specifically designed to convert part of the kinetic energy of the wind into useful mechanical energy. Several designs have been devised throughout the times. Most of them comprise a rotor that turns round propelled by lift or drag forces, which result from its interaction with the wind. Depending on the position of the rotor axis, wind turbines are classified into vertical-axis and horizontal-axis ones. Only horizontal-axis wind turbines are treated in this thesis, which occupied more efficacy than the other.

3.2.1) Torque

The mechanical power (P_{mech}) for a wind turbine running without an external load is determined by the product of angular velocity and torque. The measurement of the torque was developed in this work by using the definition of torque as given in equation (3.7).

$$\Gamma \quad = \quad \frac{d\,\vec{J}}{dt} \quad = \quad \frac{d\,(I\omega)}{dt} \quad = \quad I \cdot \frac{d\,(\omega)}{dt} \quad = \quad I\alpha \tag{3.7}$$

3.2.2) Turbine power

Running turbine generated rotational power (P) by capturing kinetic flow energy. This power is based on the angular motion of rigid body, it define as products of torque (Γ) and angular speed (ω) given by equation (3.8) (Serway and Jewett, 2004)

$$P_{mech} \quad = \quad \Gamma \cdot \omega \tag{3.8}$$

Although the rotational power is directly depend on the rate of change of angular velocity (ω) with respect to time (i.e. $\alpha = d\omega/dt$), but technically the rotational speed is increased to a constant value (maximum) of ω_{max}. Therefore, the harvested power was generated by turbine friction while driving. More information of energy conversion and energy loss was described in Chapter 4.

3.2.3) Power coefficient

The conversion of wind energy into electrical energy involves primarily two stages: in the first stage, kinetic energy in wind is converted into mechanical energy to drive the shaft of a wind generator. The critical converting devices in this stage are wind blades. For maximizing the capture of wind energy, wind blades need to be carefully designed.

The power coefficient C_p deals with converting efficiency in the first stage, defined as the ratio of the actually captured mechanical power by blades ($P_{mech.}$) to the available power (P_w) in wind as given by equation (3.9) (Carriveau, 2011).

$$C_p \quad = \quad \frac{P_{mech.}}{P_w} \quad = \quad \frac{\Gamma \cdot \omega}{\frac{1}{2}\rho A V_m^3} \tag{3.9}$$

Because there are various aerodynamic losses in wind turbine systems, for instance, blade-tip, blade-root, profile, and wake rotation losses, etc., the real power coefficient C_p is much lower than its theoretical limit, usually ranging from 30 to 45%. Figure 3.2 depicts the Betz, ideal constant, and actual wind turbine power coefficient as a function of the TSR.
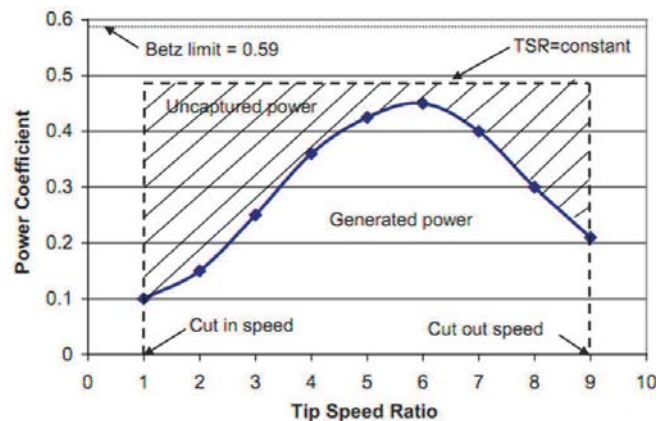
Figure 3.2 Power coefficient as a function of TSR for a two-bladed rotor (Carriveau, 2011).

As shown in figure 3.2, maximum power extraction occurs at the optimal TSR, where the difference between the actual TSR (blue curve) and the line defined by a constant TSR is the lowest. This difference represents the power in the wind that is not captured by the wind turbine. Frictional losses, finite wing size, and turbine design losses account for part of the uncaptured wind power, and are supplemented by the fact that a wind turbine does not operate at the optimal TSR across its operating range of wind speeds.

3.2.4) Lanchester–Betz limit

The theoretical maximum efficiency of an ideal wind turbine machine was derived by Lanchester in 1915 and Betz in 1920. It was revealed that no wind turbine machines could convert more than 16/27 (59.26%) of the kinetic energy of wind into mechanical energy. This is known as Lanchester–Betz limit.

As shown in figure 3.3, U_1 and U_4 are the mean velocities far upstream and downstream from the wind turbine; U_2 and U_3 are the mean velocities just in front and back of the wind rotating blades, respectively. By assuming that there is no change in the air velocity right across the wind blades (i.e. $U_2 = U_3$) and the pressures far upstream and downstream from the wind turbine are equal to the static pressure of the undisturbed airflow (i.e. $p_1 = p_4 = p$), it can be derived as equation (3.10) and (3.11).
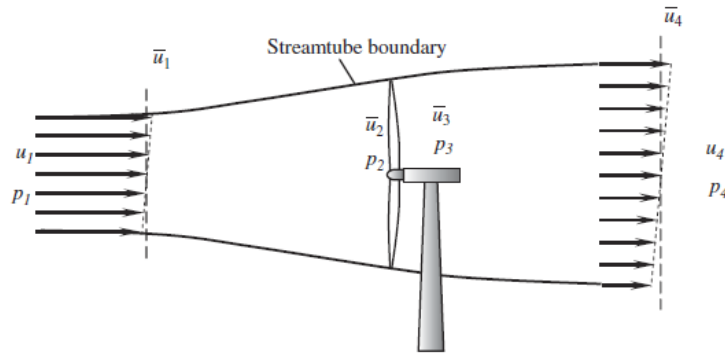
Figure 3.3 Airflow through a wind turbine (Biadgo and Aynekulu, 2017).

$$p_2 - p_3 \;=\; \frac{1}{2}\cdot\rho\!\left(U_1^2 - U_4^2\right) \qquad\qquad (3.10)$$

$$U_2 \;=\; U_3 \;=\; \frac{1}{2}\cdot\left(U_1 + U_4\right) \qquad\qquad (3.11)$$

Thus, the power output of mechanical energy captured by wind turbine blades is given by equation (3.12);

$$P_{mech.} \;=\; \frac{1}{2}\rho A U_2\!\left(U_1^2 - U_4^2\right) \;=\; \frac{1}{2}\rho A U_1^3\, 4a\left(1-a\right)^2 \qquad (3.12)$$

where a is axial induction factor, defined as equation (3.13).

$$a \;=\; \frac{U_1 + U_2}{U_1} \qquad\qquad (3.13)$$

Substitute equation (3.12) into (3.9) (where $U_1 = U$), we obtain turbine efficiency as defined in equation (3.14).

$$C_p = 4a(1-a)^2 \tag{3.14}$$

This indicates that the power coefficient is only a function of the axial induction factor a. It is easy to derive that the maximum power coefficient reaches its maximum value of 16/27 when $a = 1/3$ as described in figure 3.4.
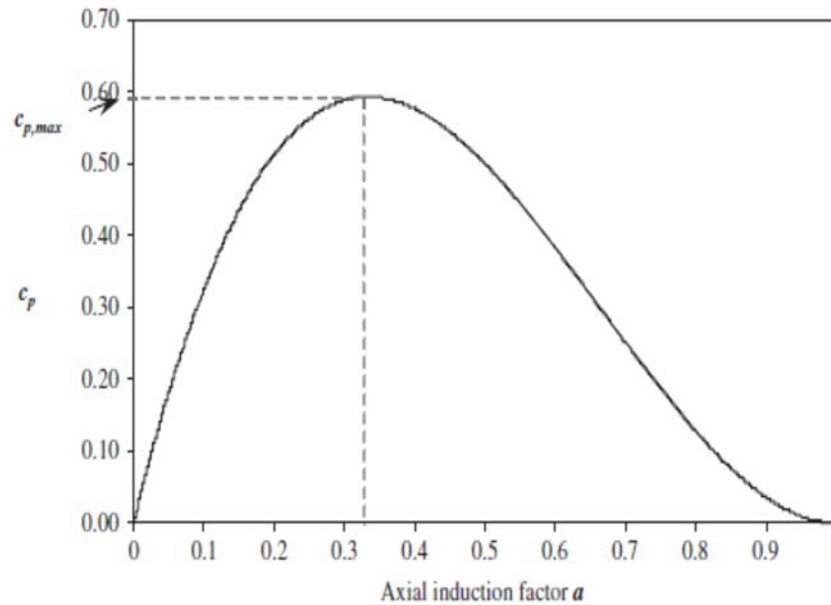
Figure 3.4 Power coefficient as a function of axial induction factor a (Tong, 2010).

The power curve of a wind turbine displays the power output (either the real electrical power output or the percentage of the rated power) of the turbine as a function of the mean wind speed. Power curves are usually determined from the field measurements. As shown in figure 3.5, the wind turbine starts to produce usable power at a low wind speed, defined as the cut-in speed. The power output increases continuously with the increase of the wind speed until reaching a saturated point, to which the power output reaches its maximum value, defined as the rated power output.

Correspondingly, the speed at this point is defined as the rated speed. At the rated speed, more increase in the wind speed will not increase the power output due to the activation of the power control. When the wind speed becomes too large to potentially damage the wind turbine, the wind turbine needs to shut down immediately to avoid damaging the wind turbine. This wind speed is defined as the cut-out speed. Thus, the cut-in and cut-out speeds have defined the operating limits of the wind turbine.
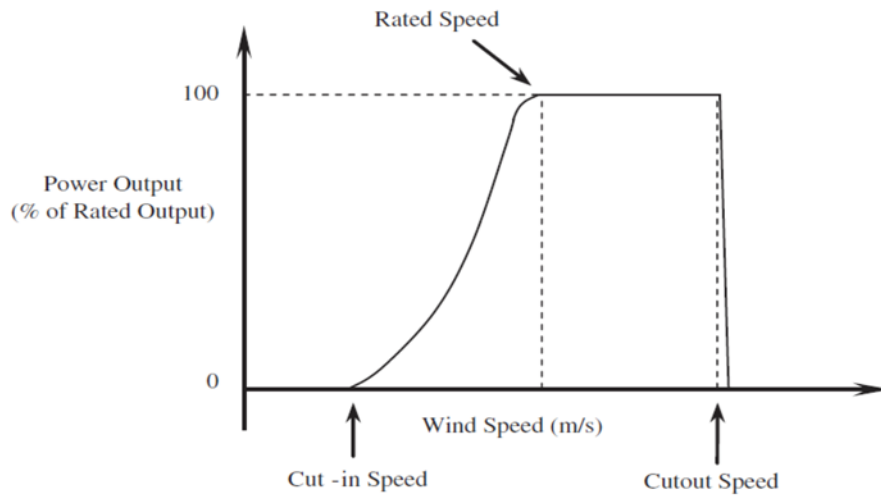
Figure 3.5 Typical wind turbine power curve (Tong, 2010).

3.2.5) Tip speed ratio

The tip speed ratio is an extremely important factor in wind turbine design, which is defined as the ratio of the tangential speed at the blade tip to the actual wind speed as given by equation (3.15):

$$\lambda = \frac{(l+r)\omega}{\overline{U}} \tag{3.15}$$

where l is the length of the blade, r is the radius of the hub, and ω is the angular speed of blades. In case of blade angular speed ω is too small, most of the wind may pass undisturbed though the blade swept area making little useful work on the blades. On the contrary, if ω is too large, the fast rotating blades may block the wind flow reducing the power extraction. Therefore, there exists an optimal angular speed at which the maximum power extraction is achieved. For a wind turbine with n blades, the optimal angular speed can be approximately determined as equation (3.16). (Regheb, 2014):

$$\omega_{opt} = \frac{2\pi}{n} \cdot \frac{\overline{U}}{s} \tag{3.16}$$

where s is the length of the strongly disturbed air stream upwind and downwind of the rotor. Substituting equation (3.16) into (3.15), the optimal tip speed ratio becomes equation (3.17).

$$\lambda_{opt} = \frac{2\pi}{n} \left(\frac{l+r}{s} \right) \tag{3.17}$$

Empirically, the ratio $(l + r)/L$ is equal to about 2. Thus, for three-blade wind turbines (i.e. $n = 3$), $l_{opt} \approx 4\pi/3$. If the airfoil blade is designed with care, the optimal tip speed ratio may be about 25–30% higher than the calculated optimal values above. Therefore, a wind turbine with three blades would have an optimal tip speed ratio (Regheb, 2014).

$$\lambda_{opt} = \frac{4\pi}{3}(1.25 \approx 1.30) \cong 5.24 - 5.45 \tag{3.18}$$

3.2.6) Aerodynamic load

Aerodynamic load is generated by lift and drag of the blades airfoil section were shown in figure 3.6 and 3.7, which is dependent on wind velocity (U), blade velocity (w), surface finish, angle of attack (α) and yaw. The angle of attack is dependent on blade twist and pitch. The aerodynamic lift and drag produced are resolved into useful thrust (T) in the direction of rotation absorbed by the generator and reaction forces (R).
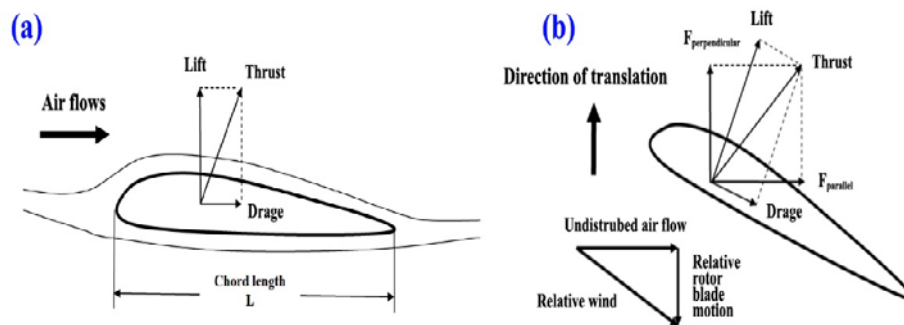
Figure 3.6 (a) Force on a stationary rotor blade in an air flow (b) parallel and perpendicular components of the lift and drag force acting on a translating in an air stream (Ragheb, 2013).

Pressures are given in aerodynamic literature, from incompressible to hypersonic flow, in terms of the dimensionless pressure coefficient Cp in aerodynamic defined as equation (3.13). (John, 2001)

$$C_p = \frac{p - p_0}{q_0} = \frac{p - p_0}{\frac{1}{2}\rho_0 U_0^2} \tag{3.13}$$

where p is local pressure, q_o is dynamic pressure and p_o is free stream static pressure. The dynamic pressure is given by Bernoulli's equation as equation (3.14).

$$q_0 \quad = \quad \frac{1}{2}\rho_0 U_0^2 \tag{3.14}$$

In incompressible flow, the pressure coefficient can be expressed in term of the velocity. Taking into account the flow over an aerodynamic body immersed in free stream with pressure p_0 and velocity U_0. Bernoulli's equation for an arbitrary point in the flow of pressure is p, and velocity is U as given by equation (3.15).

$$q_0 + \frac{1}{2}\rho_0 U_0^2 \quad = \quad p + \frac{1}{2}\rho U^2 \quad = \quad \text{constant} \tag{3.15}$$

Incompressible flow, flow density is constant then obtained equation (3.16).

$$p - p_0 \quad = \quad \frac{1}{2}\rho_0 (U_0^2 - U^2) \tag{3.16}$$

From the relation of equation (3.15), the pressure coefficient can be expressed as equation (3.17).

$$C_p \quad = \quad \frac{\frac{1}{2}\rho_0 (U_0^2 - U^2)}{\frac{1}{2}\rho_0 U_0^2} \quad = \quad 1 - \left(\frac{U^2}{U_0^2}\right) \tag{3.17}$$
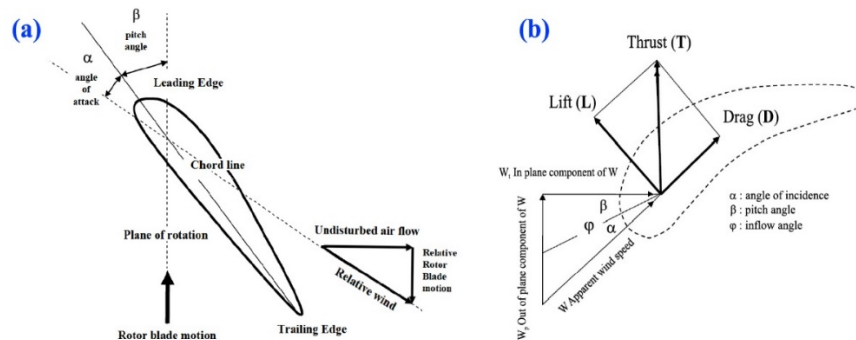
Figure 3.7 (a) Pitch angle (β) and angle of attack (α); and (b) geometry of force acting on airfoil (Ragheb, 2013).

The lift force (F_L) arises in a direction that is perpendicular to the air stream caused by the Bernoulli Effect that lowers the pressure on top of airfoil compared with the pressure at its bottom. The curvature on the top leads to a higher stream velocity than at the bottom and hence a lower pressure. The F_L defined to be perpendicular to direction of the incoming airflow, it described by the lift coefficient (C_L) as equation (3.18);

$$C_L = \frac{(F_L / A_L)}{\frac{1}{2}\rho U^2} \tag{3.18}$$

where F_L and A_L is lift force and the cross-sectional area of the airfoil, respectively. Similarity, the drag force (F_D) is described by the drag coefficient (C_D) as given by equation (3.19).

$$C_D = \frac{(F_D / A_D)}{\frac{1}{2}\rho U^2} \tag{3.19}$$

where F_D and A_D are the drag force and the cross-sectional area of the airfoil, respectively.

Both lift and drag parameters very with the angle that the rotor blade makes with the direction of the air stream designated as the angle of attack φ. The resultant of the F_L and F_D constitutes the thrust force (T) that effectively rotates the rotor blade. Lift and drag ratio (F_L/F_D) is function of the angle of attack (φ), while the maximum value of F_L/F_D profile corresponds to the optimal of φ for the maximum efficiency of the turbine rotor blade.

3.3 Methodology

3.3.1) Wind speed measurement

To measure turbine efficiency, the wind flow is important and activated as energy input. They were generated by an electric fan of 150 watts with 20-inch diameter. The wind velocity were varied with a distance away from source increased as defined in equation (3.20) (Whelan and Hodgson, 1978). The wind speed parameters had been measured at the distance (L) of 0.18, 0.48, 1.08, 1.38, 1.68, 1.98, 2.28, 2.58, 2.89, 3.18, 3.48, 3.78, 4.08, 4.38, 4.68, 4.98, 5.28, 5.58, 5.88, 6.18, 6.48, 6.78, and 7.08 m for each steps. Digital anemometer was recorded wind speed for 90 second per each distance conditions. Gaussian distribution were estimated the probability density of the represented of wind speed (U_n) for each distance conditions as given by equation (3.21); (Walck, 2007)

$$\bar{U} = \bar{\nabla}\Phi = \frac{\partial\Phi}{\partial x}\hat{i} + \frac{\partial\Phi}{\partial y}\hat{j} + \frac{\partial\Phi}{\partial z}\hat{k} \tag{3.20}$$

$$U_n(x) = \frac{1}{\sqrt{2\pi}\sigma}\exp\left(\frac{-(x-\mu)^2}{2\sigma^2}\right) \tag{3.21}$$

where Φ, μ, and σ is velocity potential, mean value of wind speed, and standard deviation, respectively. The schematic of wind speed measurement apparatus was shown in figure 3.8.
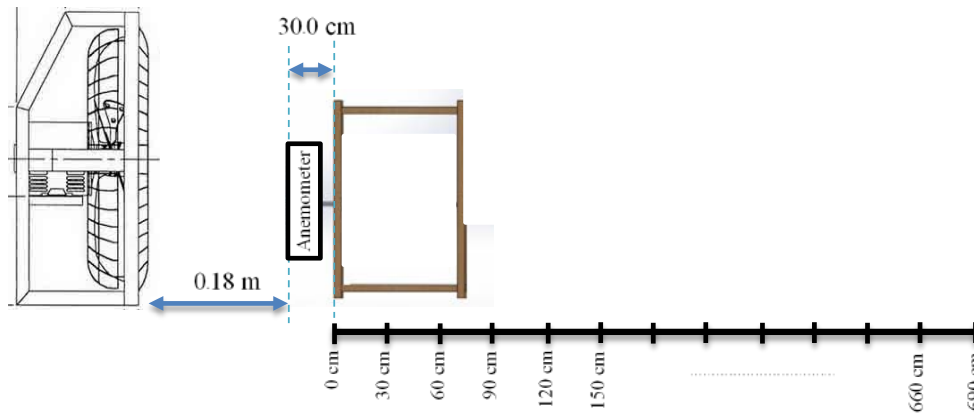
Figure 3.8 The schematic of wind speed measurement apparatus.

3.3.2) Turbine performance parameters measurement

Self-blades adjustable of small scale horizontal axis wind turbine (SBASS-HAWT) had been designed by 3D commercial SolidWorks software and fabricated by 3D printer Makerbot 2X with plastics ABS filaments for all parts of turbine assembly. An experiment was conducted in a quiet room of 6m×13m×3m. An industrial fan (Toshiba) with a 24 inches in diameter was used as a wind energy source, photograph of the turbine performance measurement setup is show in figure 3.9. Aerodynamic characteristics of the SBASS-HAWT and the wind speed power were studied at a distance (L) of 0.18, 0.48, 1.08, 1.38 m … for each conditions as previous description above. Figure 3.10 shows the blades with angle parameters (α) used for the calculation of power efficiency.

Figure 3.9 Turbine performance measurement setup.
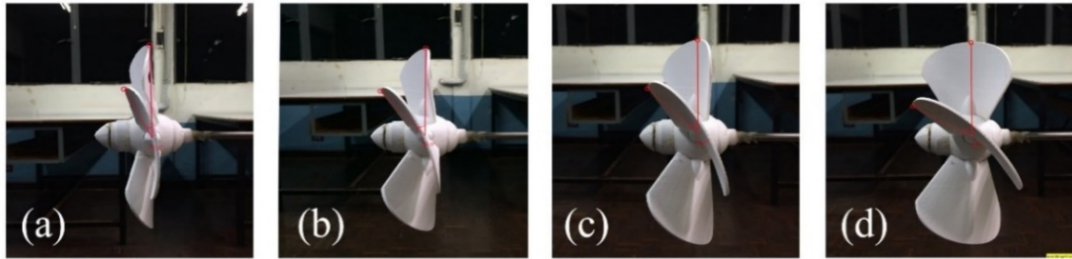
Figure 3.10 Twist blade angle (α) of the turbine of: (a) 24°, (b) 40°, (c) 45° and (d) 60°.

The blade twist angle from the rotor (α), also known as attacking angle (β) is an important conditions to determine the designed turbine efficiencies at a low velocity by the variation of β conditions. While the average wind velocity (U) is represented to the variation of flow energy input for the turbine efficiency estimation. In this case, the measurements of the angular velocity (ω) and angular acceleration (α) were performed by using the tracking technique by the rotational of turbine motion. For angular speed (ω) and angular acceleration (α) measurements of the SBASS-HAWT, each condition of attacking angle (β) was set at 24°, 40°, 45°, and 60°, as shown in figure 3.10.

To track rotational of turbine motion, black spots of 5 mm diameter were attached on the blade, and Tracker software version 4.98 was used to analyze and track the object (black spot) movement following the rotational of blades motion for over 15 s with the frame rate of 0.033 sec, as shown in figure 3.11 (Brown, D., 2008). The relationship of the measured data of θ, β, and α can be expressed by equation (3.22), where c_1 and c_2 are the constants.

$$\theta_n = \omega_n t + c_1; \qquad \omega_n = \alpha_n t + c_2 \qquad (3.22)$$

The other efficencies parameter as initial torque by the wind turbine were defind in equation (3.8), while the moment of inertial of the assembly (blades, rotor, and shaft) around any axises can be estimated from the CAD assembly by using comercial SolidWorks software 2.14 ×64 bit edition. The tip speed ratio (λ) is an important factor defined as the ratio of angular speed of rotor by wind speed; as given by equation (3.23), where R is a turbine blade radius.

$$\text{Tip speed ratio (TSR)}: \lambda = \frac{\omega R}{U_O} \qquad (3.23)$$
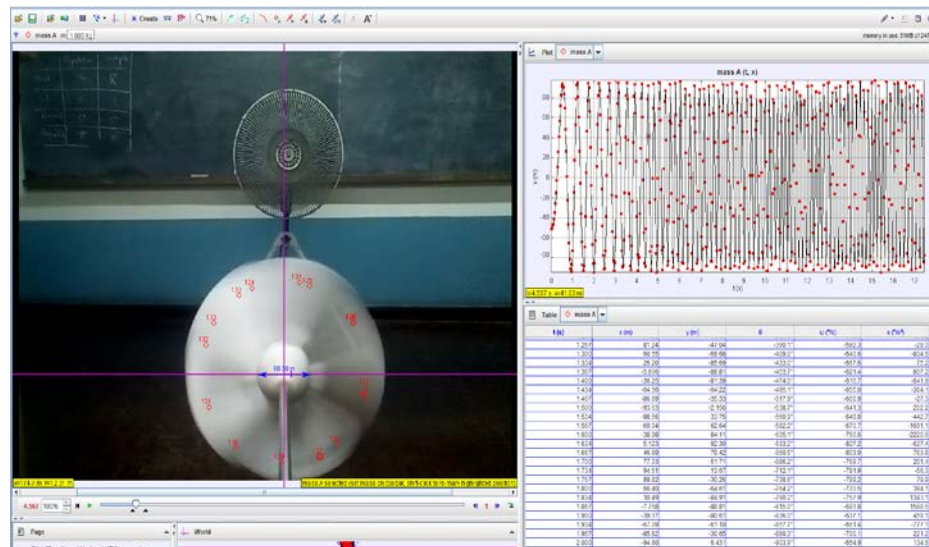
Figure 3.11 Angular displacement estimation by Tracker software.

3.3.3) Calculation/CFD simulation

The efficiency of the designed wind turbines is estimated by using Computer Fluid Analysis (CFA) and Menter's Shear-Stress Transport model (SST) with type of the incompressible flow and Mach number less than 0.3 (Menter, 1994). The governing equations for turbulence flow on time-average fluid interactions were expressed by Reynolds-averaged Navier-Stokes (RANS) equation (Reynolds, 1985). They are based on the combination of momentum conservation with continuity of fluid flow as shown in equations (2.17) and (2.18).

To simulate a far flow field condition, a semicircle connected with a rectangular region was chosen as the computation domain as shown in figure 3.12. The upstream, top and bottom edges of the computational domain are located away from the center of blade mass at 100 times of the blade widths. The downstream edge is located away at 200 times of the blade widths. This is to minimize the effect of the applied boundary conditions. Inlet boundary condition is defined by flow velocity as $U_o = 3.5$ m/s and the flow angle (β) varied from 0° to 60° as an attack angle following to the experiment which needs to be as the calculated parameters. The open boundary condition set as zero normal stress at the outlet, and the nonslip solid boundary condition adopted the 2D cross section on the blade surface. For comparison with the experimental data, the Reynolds number of the flow field was set to be 0.8×10^6 and the velocity at the inlet was set to be 3.5 m/s. To obtain accurate details of the flow around the turbine blade, the total number of grids in the whole computation by 57,026 triangle domains and 546 boundaries were established as fluid flow elements. Over 1500 iteration numbers were estimated, the error for all solutions on CFD in the stationary model is less than 10^{-4}.
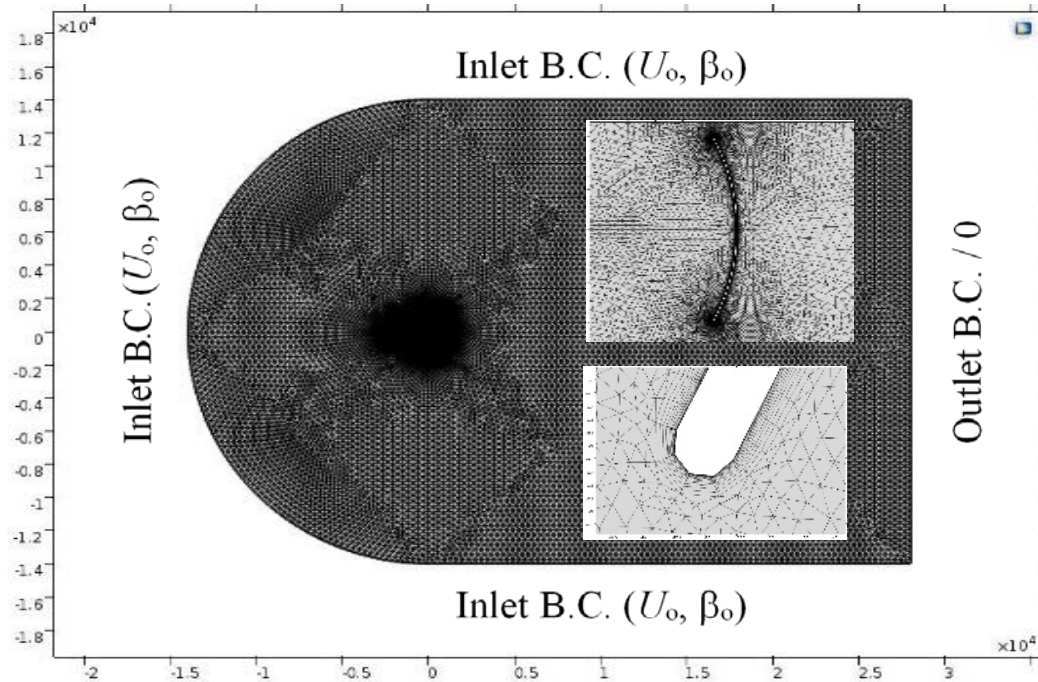
Figure 3.12 Computational fluid domain 2D definitions.

3.4 Results

In this section is the combination of the experimental data and simulations solutions, which can be classified as;

3.4.1) the wind speed measurement is an estimation of the energy input level, while the energy level depended on the distance of the wind source;

3.4.2) the rotation of the angular displacement, velocity, acceleration, and rotation frequencies were estimated by established tracking technique;

3.4.3) the CFA simulation represented the visualized fluid flows data of pressure and velocity through the turbine.

3.4.1) Wind speed measurement

For wind velocity measurement, 90 samples of U per second were recorded by an anemometer for each conditions of L-distance and β-attacking angle. Distribution of their measured data was represented by density function (square bars); and the normal distribution was applied by probability density function in equation (3.5) (solid line); as shown in appendix A (I). The experimental results of mean value of wind velocity (U_n) [equation (3.4)] and turbulence intensity (I_n) [equation (3.6)] with a variation of L-distance away from a power source are shown in figure 3.13.

Summing of the numerical results of mean value (μ_n), standard deviation (σ_n) and turbulence intensity (I_n) of wind speed (U_n) at the variation of distance (L) were presented in table 3.1. The results shown that the mean value of winds velocity (U_n) decrease with L-distance increase corresponded to the free boundary for winds diffusion (Walters, 1967). For the I_n increase with L-distance increase, because of when I_n increased with more L-distance added represented the increment of turbulence state. Turbulence state parameter of I_n were indicate reliable values of winds speed. It was necessary for an efficiencies calculation, so that $I_n > 0.2$ was ignored. In this case, turbine parameters can be observed at wind speed over 1 m/s.

Table 3.1 Summary of mean value (μ), standard deviation (σ) and turbulence intensity (I) of wind speed at the variation of distance (L) away from the source.

Distance L (m)	μ (m/s)	σ (m/s)	I	Distance L (m)	μ (m/s)	σ (m/s)	I
0.18	3.24	±0.278	0.0859	3.78	1.420	±0.184	0.1291
0.48	2.95	±0.316	0.1071	4.08	1.145	±0.340	0.2974
0.78	2.85	±0.168	0.0592	4.38	1.260	±0.193	0.1530
1.08	2.68	±0.157	0.0586	4.68	1.131	±0.231	0.2040
1.38	2.33	±0.282	0.1209	4.98	0.918	±0.234	0.2547
1.68	2.26	±0.224	0.0989	5.28	0.677	±0.202	0.2991
1.98	2.03	±0.141	0.0696	5.58	0.747	±0.200	0.2677
2.28	1.90	±0.175	0.0919	5.88	0.402	±0.312	0.7756
2.58	1.79	±0.170	0.0950	6.18	0.446	±0.245	0.5502
2.88	1.63	±0.305	0.1872	6.48	0.481	±0.137	0.2842
3.18	1.50	±0.186	0.1242	6.78	0.437	±0.171	0.3911
3.48	1.42	±0.161	0.1129	7.08	0.084	±0.111	1.3202
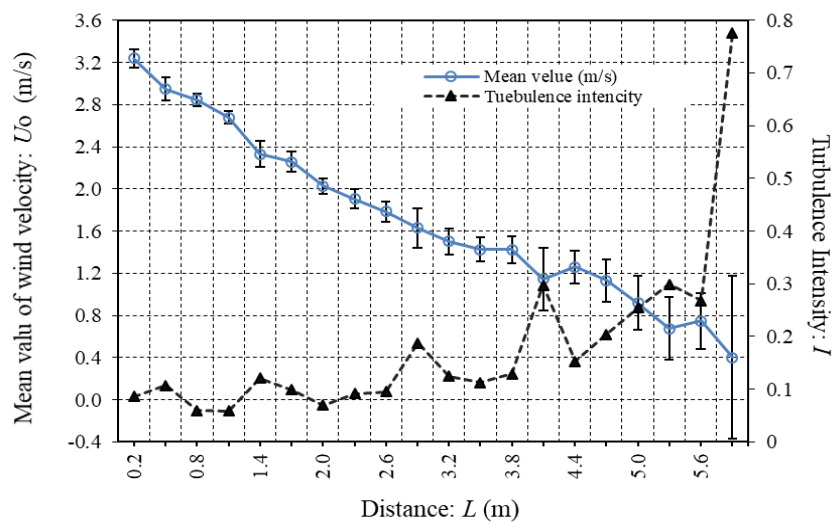
Figure 3.13 Mean value (μ) and turbulence intensity (I) of wind speed at the variation of distance (L) away from the source.

3.4.2) Angular velocity estimation

To calculated turbine efficiency, parameters of the operating turbine such as rotational speed (ω) and acceleration (α) were necessary. In this work, video tracking motion of the operating turbine had been applied to estimated angular speed (ω_n) of turbine operation with wind speed (U_n) variation. By using measured parameter of angular displacement (θ_n), the parameter of ω_n for each conditions had been estimated by applying linear fitting following to equation (3.22). The results of this linear fitting estimation were presented in appendix A (II), including to the numerical results of the θ_n, constant of c_1, and square of correlation coefficient of R^2 for each β conditions of 24°, 40°, 45°, and 60° were summarized in table 3.2. The experimental results of ω_n with the variation of U_n for the β of 24°, 40°, 45°, and 60° is shown in figure 3.14, it shows that ω_n increased with U_n increased for all angles of β. Tendency slop of ω_n with U_n variations were aligned descending with β of 45°, 40°, 60°, and 24° respectively.
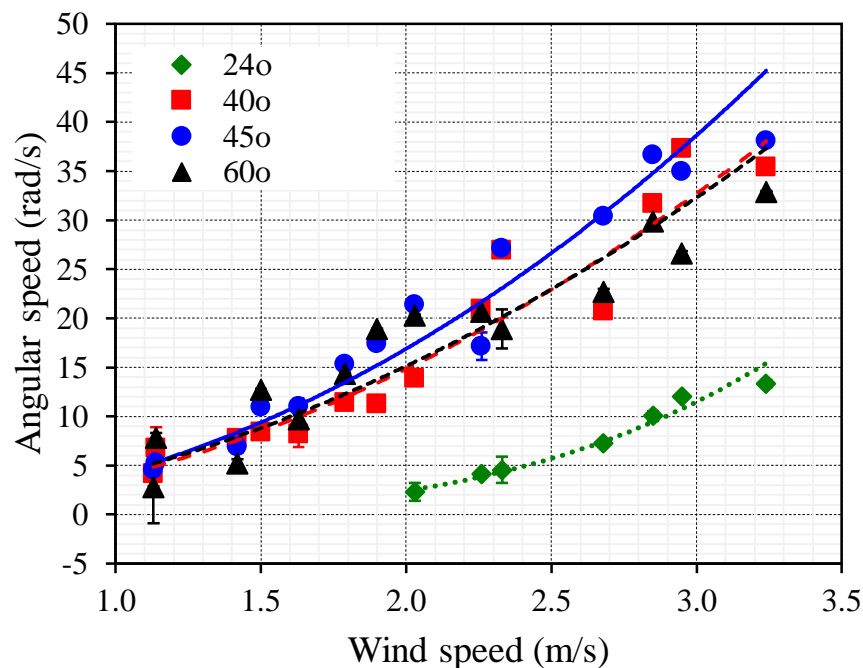
Figure 3.14 Tendency slop of ω_n with U_n variations for the β conditions of 24°, 40°, 45°, and 60°.

Table 3.2 Summary of angular speed (ω), fitting constant (c_2) and correlation coefficient (R^2) of the variation wind speed (U_n) at attacking angle (β) 25°, 40°, 45°, and 60°.

U_n (m/s)	Attacking angle (β)											
	25°			40°			45°			60°		
	ω	c_2	R^2	ω	c_2	R^2	ω	c_2	R^2	ω	c_2	R^2
3.24	13.324	50.833	0.9962	35.454	42.265	0.9997	38.121	56.183	0.9991	32.916	69.872	0.9993
2.95	12.025	27.925	0.9981	37.331	74.876	0.9992	34.994	69.184	0.9985	26.644	71.510	0.9978
2.85	10.068	25.405	0.995	31.684	99.448	0.9971	36.691	36.286	0.9992	29.865	60.150	0.9998
2.68	7.2627	18.94	0.9997	20.734	41.968	0.9958	30.422	68.345	0.9992	22.706	24.501	0.9969
2.33	4.5634	17.99	0.9866	26.958	55.401	0.9998	27.157	57.344	0.9991	18.902	11.460	0.9801
2.26	4.1551	6.7075	0.9994	20.918	44.903	0.9977	17.174	27.892	0.9860	20.710	25.686	0.9989
2.03	2.2928	4.5941	0.9908	13.898	27.549	0.9992	21.394	68.302	0.9979	20.269	26.472	0.9988
1.90	-	-	-	11.317	13.504	0.9986	17.403	48.952	0.9951	18.896	44.570	0.9992
1.79	-	-	-	11.387	18.726	0.9963	15.356	43.918	0.9972	14.368	17.783	0.9990
1.63	-	-	-	8.1893	14.750	0.9871	11.020	13.740	0.9921	9.7151	12.026	0.9954
1.50	-	-	-	8.4424	20.468	0.9982	10.945	30.748	0.9975	12.699	17.883	0.9990
1.42	-	-	-	7.7935	16.941	0.9996	6.9260	6.4208	0.9936	5.2488	0.6679	0.9961
1.14	-	-	-	6.7545	8.869	0.9783	5.2594	9.4497	0.9967	7.8453	41.225	0.9952
1.13	-	-	-	4.1809	14.532	0.9875	4.5864	65.327	0.9924	2.7726	22.607	0.9632
0.91	-	-	-	-	-	-	3.0044	11.122	0.9902	2.5534	20.942	0.9393

3.4.3) Angular acceleration estimation

The other related efficiency parameter of the operating turbine as angular acceleration (α_n) is the initial slop of angular speed (ω_n) with time as given in equation (3.22). By the reason of turbulence state, the time variation of angular speed (ω_n) had been approximated by polynomial fitting function as given in equation (3.24) (Kishore *et al.*, 2013). This approbation were performed by using curve fit function of MATLAB,

$$\omega(t) \;=\; a_1 e^{-6} t^6 - a_2 e^{-4} t^5 + a_3 e^{-2} t^4 - a_4 e^{-1} t^3 - a_5 e^{-1} t^2 + a_6 t \qquad (3.24)$$

where a_1-a_6 are fitting coefficients. The angular acceleration (α_n) can be obtained by using equation (3.22) fitting in linear range of initial state. The fitting curve results were presented in appendix A (III). Numerical results of α_n, constant of c_2 and square of the correlation coefficient of R^2 for each β conditions of 24º, 40º, 45º, and 60º were summarized in table 3.3. The experimental results of α_n with the U_n variation for the β of 24º, 40º, 45º, and 60º is shown in figure 3.15, it shows that ω_n increased with U_n increased for all angles of β. Tendency slop of α_n with U_n variations were aligned descending with β of 45º, 60º, 40º, and 24º respectively.
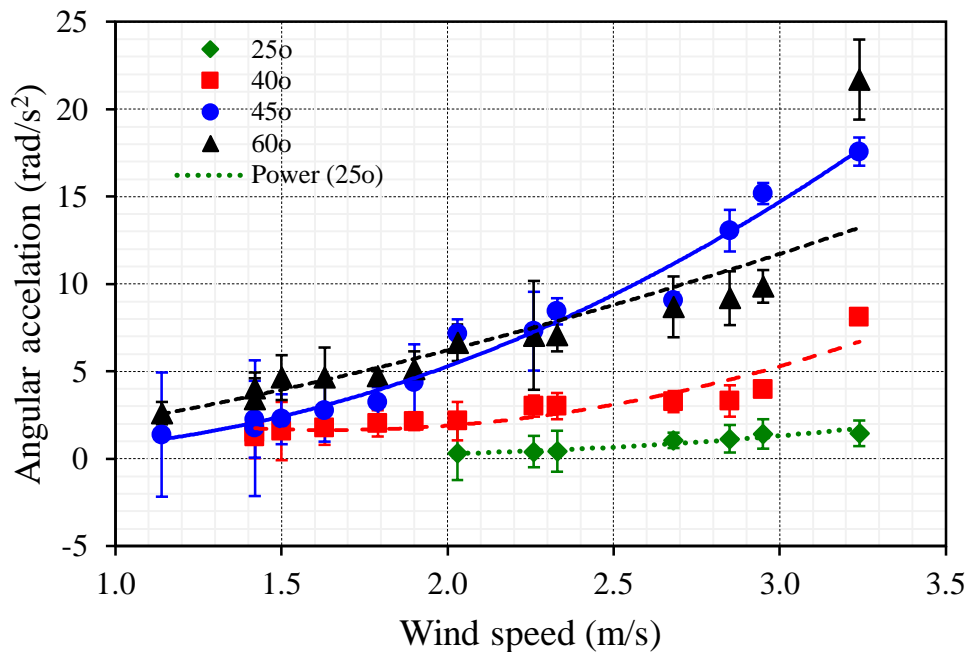
Figure 3.15 Tendency slop of α_n with U_n variations for the β conditions of 24º, 40º, 45º, and 60º.

Table 3.3 Summary of angular acceleration (α), fitting constant (c_1) and correlation coefficient (R^2) of the variation wind speed (U_n) at attacking angle (β) 25º, 40º, 45º, and 60º.

U_n (m/s)	Attacking angle (β)											
	25º			40º			45º			60º		
	α	c_1	R^2	α	c_1	R^2	α	c_1	R^2	α	c_1	R^2
3.24	1.452	1.4938	0.9274	8.123	0.967	0.9579	17.572	0.4722	0.9199	21.685	0.4722	0.771
2.95	1.410	3.1840	0.9157	3.9856	0.9464	0.9654	15.186	1.2464	0.9387	9.8714	0.9244	0.9068
2.85	1.140	1.3424	0.9205	3.3235	1.0316	0.9105	13.056	2.0441	0.8808	9.1964	2.0441	0.8467
2.68	1.050	0.2375	0.9563	3.267	-1.567	0.9398	9.0788	0.9004	0.9552	8.6806	0.9004	0.8259
2.33	0.430	0.4907	0.8816	3.0243	1.0444	0.9259	8.4484	0.0173	0.9255	7.0741	0.0173	0.906
2.26	0.416	0.1963	0.9111	3.0217	0.3898	0.9382	7.3098	1.5262	0.774	7.0596	2.0266	0.6896
2.03	0.330	0.1754	0.8475	2.17	1.1334	0.8900	7.1494	0.952	0.9172	6.6431	0.9520	0.895
1.90	-	-	-	2.1467	1.705	0.9484	4.3895	0.5572	0.7832	5.1399	-0.5572	0.9001
1.79	-	-	-	2.0298	0.6445	0.9236	3.2400	0..3881	0.9124	4.736	0.3881	0.9722
1.63	-	-	-	1.7877	0.5491	0.9012	2.7572	0.5491	0.8210	4.6624	0.5491	0.8289
1.50	-	-	-	1.595	0.7508	0.8323	2.2696	0.5004	0.8577	4.6483	0.5004	0.8735
1.42	-	-	-	1.5235	0.2833	0.9562	2.2649	0.6000	0.7803	4.0491	0.6000	0.9437
1.14	-	-	-	0.7984	-1.903	0.666	1.3839	0.0847	0.6455	2.613	0.0847	0.9355
1.13	-	-	-	3.9856	0.1938	0.7879	15.186	0.1077	0.9524	9.8714	0.1751	0.9292

3.4.4) Rotational frequency

The related efficiencies parameter of the operating turbine as rotational frequency of $f_R(f)$ can be obtained by applying Fast Fourier Transform to the $\theta_n(t)$ parameter as given by equation (3.25).

$$F(f) \quad = \quad \sum_{n=0}^{N-1} \theta(t) \exp\left(-2\pi j \frac{f \cdot t}{N}\right) \tag{3.25}$$

Due to turbulence state generated non-single rotational frequencies, multi-frequency spectrums had been fitting by Origin LAB software v.8.0 Gaussian fitting function. Numerical results of $f_R(f)$, standard deviations of σ_n, and fitting parameter of R-square for each condition were summarized in table 3.4. The fitting results for spectrum of rotational frequencies peaks were presented in appendix A (IV).

Single dominant peak results which represented the $F(f)$ with the U_n variation for the β of 24°, 40°, 45°, and 60° as shown in figure 3.16. The results shown that while U_n increased make the $F(f)$ increased. For the instead, only $U_n \approx 3.0$ m/s exhibited similar single spectrum which represented laminar state. In the same value of U_n, the maximum of $F(f)$ were appeared in the β of 45° and the minimum generated by β of 24°. The β conditions of 40° and 60° were presented similarly results of $F(f)$.
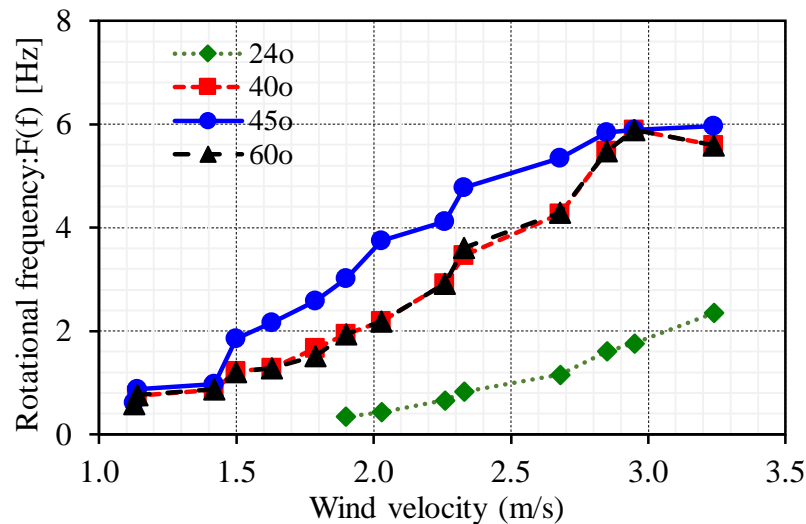
Figure 3.16 Rotational speed of turbine with U_n variations for the β conditions of 24°, 40°, 45°, and 60°.

Table 3.4 Summary of the Gaussian single peak fitting parameter of the turbine rotational frequencies with β is 24º, 40º, 45º, and 60º.

U_n (m/s)	Attacking angle (β)											
	24º			40º			45º			60º		
	$F(f)$ (Hz)	σ_f (Hz)	R^2	$F(f)$ (Hz)	σ_f (Hz)	R^2	$F(f)$ (Hz)	σ_f (Hz)	R^2	$F(f)$ (Hz)	σ_f (Hz)	R^2
3.24	2.354	0.0040	0.52740	5.592	0.0049	0.56577	5.965	0.0027	0.48578	5.594	0.0047	0.56577
2.95	1.765	0.0580	0.50230	5.889	0.0106	0.61791	5.886	0.0092	0.61791	5.886	0.0093	0.61791
2.85	1.608	0.0012	0.88700	5.478	0.0048	0.55301	5.837	0.0352	0.57246	5.478	0.0027	0.55301
2.68	1.159	0.0032	0.90700	4.273	0.0061	0.61999	5.344	0.0024	0.50649	4.292	0.0578	0.61999
2.33	0.832	0.0054	0.47840	3.458	0.0291	0.83697	4.781	0.0194	0.62208	3.618	0.0072	0.83609
2.26	0.660	0.0036	0.89490	2.918	0.0051	0.39871	4.124	0.0028	0.25457	2.914	0.0719	0.40089
2.03	0.435	0.0247	0.74650	2.184	0.0241	0.56601	3.742	0.0078	0.55687	2.184	0.0250	0.55313
1.90	0.347	0.0044	0.43500	1.938	0.0030	0.86406	3.022	0.0219	0.3397	1.940	0.0022	0.86533
1.79	-	-	-	1.667	0.0326	0.51534	2.580	0.0057	0.49393	1.519	0.0133	0.48812
1.63	-	-	-	1.282	0.0469	0.55766	2.167	0.0308	0.38185	1.282	0.0573	0.51769
1.50	-	-	-	1.220	0.0166	0.58023	1.856	0.0261	0.75107	1.215	0.0235	0.58124
1.42	-	-	-	0.868	0.0353	0.76401	0.978	0.0188	0.58098	0.871	0.0419	0.77088
1.14	-	-	-	0.752	0.0056	0.62176	0.874	0.0219	0.53525	0.768	0.0298	0.59268
1.13	-	-	-	0.874	0.02675	0.51479	0.620	0.0043	0.54399	0.595	0.0214	0.45837

3.4.5) Tip speed ratio (λ)

Tip speed ratio is a turbine constant parameter defined as linear velocity of blades divided by wind speed velocity as given by equation (3.15). The calculated experimental results of tip speed ratio (λ) with the variation of U_n for the β of 24°, 40°, 45°, and 60° was shown in figure 3.17. Numerical results of λ_n and standard deviations of σ_n were summarized in table 3.5. The results shown that λ_n for all conditions of β were increased with U_n increased, while β of 45° was induced maximum performance of λ with U variation. However, β of 45° was generated λ higher than the others when U is lower 1.7 m/s.
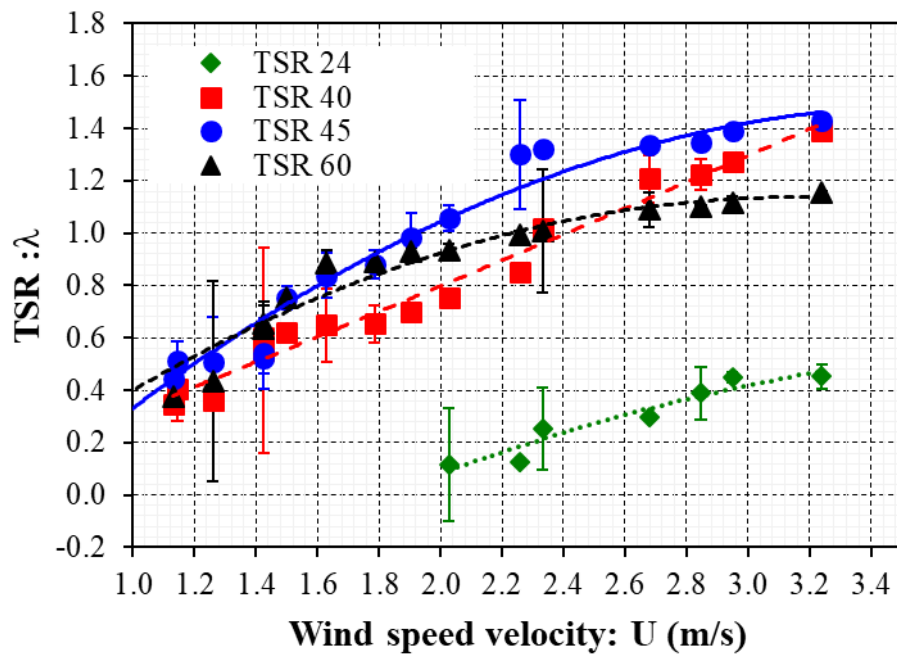
Figure 3.17 The results of λ_n with the variation U_n for the β conditions of 24°, 40°, 45°, and 60°.

Table 3.5 Summary of the calculated tip speed ratio (λ) and the standard deviations with the wind speed variation (U_n) for β of 24°, 40°, 45°, and 60°.

U_n (m/s)	Attacking angle (β)							
	24°		40°		45°		60°	
	λ	σ	λ	σ	λ	σ	λ	σ
3.24	0.905	0.0456	1.392	0.0036	1.432	0.0108	1.154	0.0084
2.95	0.897	0.0200	1.272	0.0084	1.392	0.0158	1.118	0.0232
2.85	0.778	0.0992	1.224	0.0575	1.349	0.0159	1.100	0.0040
2.68	0.597	0.0064	1.207	0.0892	1.338	0.0170	1.091	0.0658
2.33	0.431	0.1584	1.019	0.0024	1.321	0.0106	1.009	0.2352
2.26	0.405	0.0089	0.852	0.0342	1.301	0.2083	0.994	0.0164
2.03	0.249	0.2175	0.754	0.0189	1.058	0.0496	0.933	0.0284
1.90	-	-	0.701	0.0267	0.982	0.0933	0.931	0.0152
1.79	-	-	0.654	0.0725	0.882	0.0549	0.892	0.0196
1.63	-	-	0.648	0.1410	0.839	0.0863	0.885	0.0503
1.50	-	-	0.619	0.0323	0.754	0.0448	0.754	0.0179
1.42	-	-	0.602	0.0083	0.540	0.1325	0.656	0.0807
1.14	-	-	0.553	0.3931	0.524	0.0598	0.637	0.0870
1.13	-	-	0.407	0.1225	0.511	0.0745	0.435	0.3608

3.4.6) Torque

For the rotation motion, torque (Γ) is required to produce an angular acceleration (α) of an object which it is the function of time. The amount of torque required to produce an angular acceleration depends on the distribution of the mass of the rotational parts. The moment of inertia (*I*) is a value that describes the distribution as defined in equation (3.26). SolidWorks software had been applied for solving *I* parameter around rotation axis and more information were described in appendix A (VI).

$$I = \oint_V r^2 \cdot \rho \, dV \tag{3.26}$$

As the definition of Γ from equation (3.8) and the previous of experimental results of a α constant (section 3.4.3), solutions of initial torque (Γ) can be calculated as a constant by variations of U_n as shown that in figure 3.18. Generated of Γ for all β were increased with U_n increase and the tendency slop of Γ_β were aligned descending with β of 45°, 60°, 40°, and 24° respectively. The tendency descending results of this Γ_β were similarly as the α_β results.
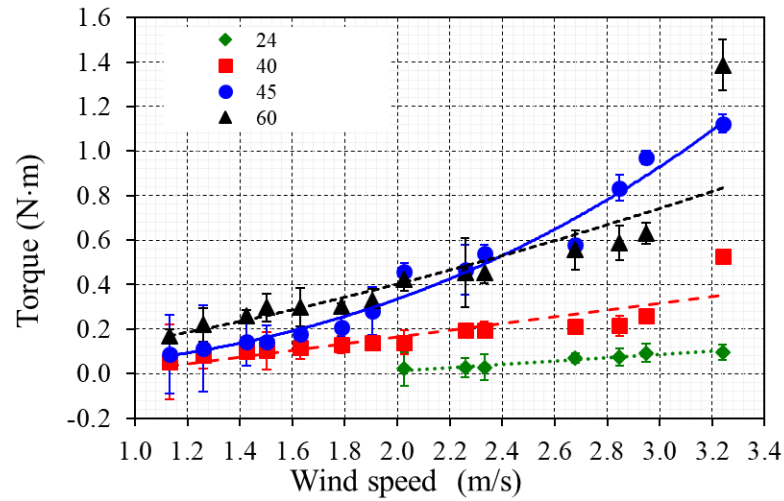
Figure 3.18 Initial torque with U variation for the β conditions of 24º, 40º, 45º, and 60º.

3.4.7) Extracted power

Captured kinetic flows power were generated wind turbine power by the rotation motion. The extracted power (P_{mech}) of SBASS-HWAT were defined as product of angular torque (Γ) with angular turbine velocity (ω) as given in equation (3.9). The experimental results of calculated extracted power for β conditions of 24º, 40º, 45º and 60º with U_n variation were presented in figure 3.19. Numerical of initial torque and extracted power results with their standard deviations were summarized in table 3.6. The results show that, extracted turbine power were increased with U_n increased. The polynomial tendency line (slop) of P_{mech} with the variation of U_n were decreasing by 45º, 60º, 40º and 24º.
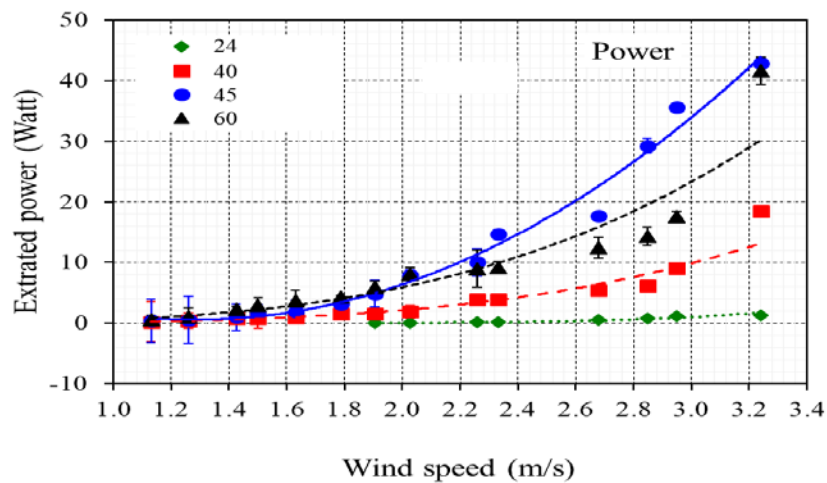
Figure 3.19 Extracted turbine power with U variation for the β conditions of 24º, 40º, 45º and 60º.

Table 3.6 Summary of the extracted torque, generated power and their standard deviation (σ_Γ, σ_P) of SBASS-HWAT with variation of U for $\beta = 24°$, $40°$, $45°$, and $60°$.

U (m/s)	Attacking angle: β (degree)															
	24°				40°				45°				60°			
	Torque $\times 10^{-2}$ (N·m)		Power (watt)		Torque $\times 10^{-2}$ (N·m)		Power (watt)		Torque $\times 10^{-2}$ (N·m)		Power (watt)		Torque $\times 10^{-2}$ (N·m)		Power (watt)	
	Γ	σ	P	σ	Γ	σ	P	σ	Γ	σ	P	σ	Γ	σ	P	σ
3.24	9.58	3.630	1.28	0.106	52.78	2.105	18.49	0.008	112.41	4.005	42.85	0.801	138.72	11.450	41.58	2.290
2.95	9.30	4.215	1.12	0.060	25.90	1.730	9.06	0.346	97.14	3.065	35.64	0.613	63.15	4.660	17.51	0.932
2.85	7.52	3.975	0.76	0.084	21.60	4.475	6.11	0.895	83.52	5.960	29.23	1.192	58.83	7.665	14.27	1.533
2.68	6.93	2.185	0.50	0.005	21.23	3.010	5.41	0.602	58.08	2.240	17.67	0.448	55.53	8.705	12.43	1.741
2.33	2.84	5.920	0.13	0.378	19.65	3.705	3.94	0.741	54.04	3.725	14.68	0.745	45.25	4.700	9.18	0.940
2.26	2.74	4.445	0.11	0.013	19.64	3.090	3.92	0.618	46.76	11.300	10.00	2.260	45.16	15.520	8.95	3.104
2.03	2.18	7.625	0.05	0.130	14.10	5.500	1.85	1.100	45.74	4.140	7.96	0.828	42.50	5.250	8.08	1.050
1.90	-	-	-	-	13.95	2.580	1.57	0.516	28.08	10.840	4.82	2.168	32.88	4.995	5.86	0.999
1.79	-	-	-	-	13.19	3.820	1.47	0.764	20.73	4.380	3.18	0.876	30.30	1.390	4.28	0.278
1.63	-	-	-	-	11.62	4.940	0.94	0.988	17.64	8.950	1.94	1.790	29.82	8.555	3.71	1.711
1.50	-	-	-	-	10.36	8.385	0.82	1.677	14.52	7.115	1.59	1.423	29.74	6.325	2.85	1.265
1.42	-	-	-	-	9.90	2.190	0.79	0.438	14.49	10.985	1.00	2.197	25.90	2.815	2.24	0.563
1.14	-	-	-	-	8.23	6.115	0.38	1.223	11.25	19.375	0.52	3.875	21.94	7.585	1.02	1.517
1.13	-	-	-	-	-	-	-	-	8.85	17.725	0.35	3.545	16.72	3.225	0.58	0.645

3.4.8) Turbine efficiencies

Performance of turbine efficiencies (C_p) can be estimate by using equation (3.7) which equal to extracted power (section 3.4.7) divided by the measured of wind power (P_w). The calculated results of C_p with U_n variation for the β conditions of 24°, 40°, 45° and 60° were presented in figure 3.20. Numerical results of C_p, standard deviation (σ) and mechanical loss (δ_{mech}) for the β conditions of 24°, 40°, 45° and 60° were summarized in table 3.7. The results show that, performance of C_p were increased with U_n increased. The polynomial tendency line (slop) of C_p with the U_n variation were decreasing sort by 45°, 60°, 40° and 24°. Moreover, the results C_p by the β condition of 60° is higher than 45° for range of U <1.8 m/s. On the other hand, the polynomial tendency line (slop) of C_p with U_n variation were decreasing by 45°, 60°, 40° and 24°, similar as the P_{mech} results.
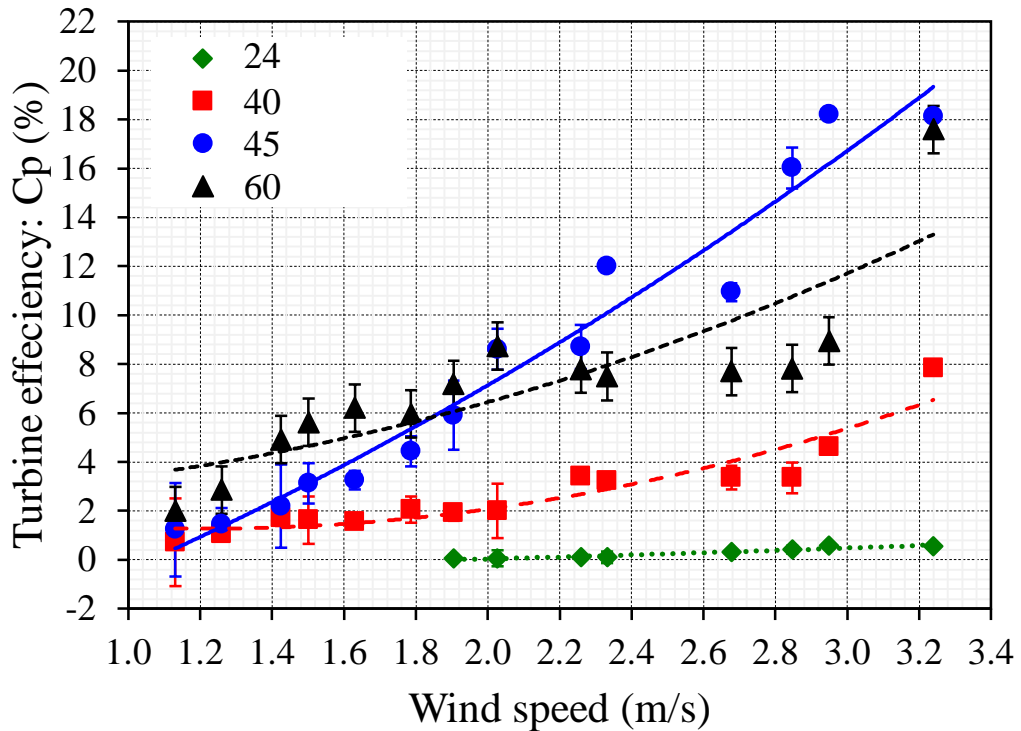
Figure 3.20 Turbine efficiencies with U variation for the β conditions of 24°, 40°, 45° and 60°.

Table 3.7 Performance of turbine efficiencies (C_p) and the mechanical loss (δ_{mech}) with the variation of wind speed (U) for the β conditions of 24º, 40º, 45º and 60º

U_n (m/s)	24º			40º			45º			60º		
	C_p (%)	σ	δ_{mech} (W)	C_p (%)	σ	δ_{mech} (W)	C_p (%)	σ	δ_{mech} (W)	C_p	σ	δ_{mech} (W)
3.24	0.54	0.068	0.753	7.82	0.002	0.581	18.13	0.207	0.337	17.60	0.593	0.350
2.95	0.57	0.030	0.566	4.63	0.069	0.487	18.21	0.123	0.221	8.95	0.187	0.402
2.85	0.42	0.149	0.512	3.35	0.634	0.458	16.02	0.845	0.227	7.82	1.086	0.377
2.68	0.31	0.009	0.427	3.35	0.488	0.378	10.94	0.364	0.256	7.70	1.413	0.308
2.33	0.10	0.238	0.284	3.22	0.186	0.246	11.99	0.187	0.139	7.50	0.236	0.194
2.26	0.01	0.013	0.258	3.42	0.246	0.220	8.71	0.901	0.159	7.79	1.237	0.170
2.03	0.05	0.326	0.187	2.00	1.106	0.169	8.60	0.833	0.108	8.74	1.056	0.107
1.90	0.04	0.068	0.155	1.92	0.337	0.140	5.90	1.416	0.107	7.17	0.652	0.097
1.79	-	-	-	2.05	0.529	0.114	4.43	0.606	0.096	5.96	0.192	0.085
1.63	-	-	-	1.56	0.212	0.088	3.25	0.385	0.078	6.21	0.368	0.060
1.50	-	-	-	1.62	0.969	0.068	3.13	0.823	0.060	5.62	0.731	0.048
1.42	-	-	-	1.72	0.338	0.057	2.20	1.695	0.055	4.90	0.434	0.043
1.14	-	-	-	1.05	0.212	0.041	1.44	0.670	0.040	2.85	0.262	0.035
1.13	-	-	-	0.72	1.793	0.030	1.23	1.903	0.029	2.00	0.346	0.027

3.4.9) Calculation/CFD simulation

In this section, to analyzed turbine characteristics were mainly focusing on the power prediction for the energy input of $U_o = 3.5$ m/s acting on the edge of blade with the variation β conditions. Figure 3.18 shows upstream lines that mostly flew through the front (below) of blade and less at the back (above). The net force of lift direction (total direction of fluids velocity) acting on the blade is indicated by the white arrows. For the β of 24º, the lift force were pointed to the backward direction of the rotor. The β of 40º, an average net direction of fluid flow velocity was moved close to rotational direction of the rotor. For the β of 45º, the direction of white arrows was completely in direction with blades rotation, which is supported the maximum results of extracted value ω, α, $F(f)$, λ, Γ, P, and C_p. Finally for the β of 60º the total direction of flow velocity was shifted to the horizontal axis which against to fluid flow direction.
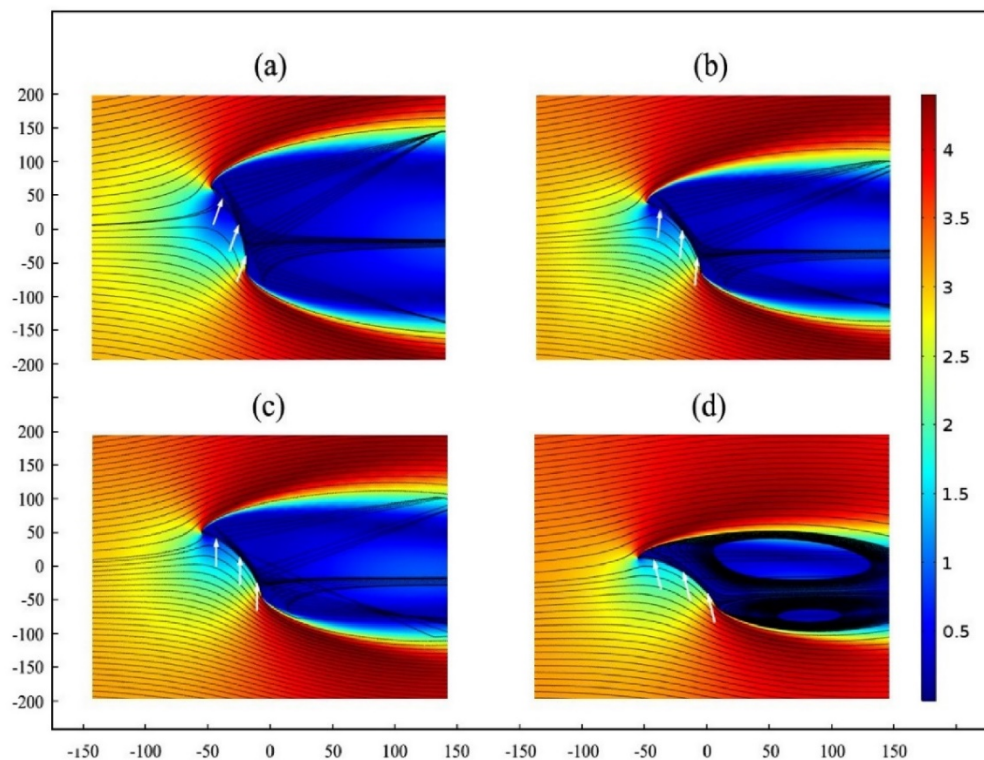
Figure 3.21 Flow velocity profile for the designed blade with the β conditions of (a) 24°, (b) 40°, (c) 45°, and (d) 60°.

3.5 Conclusions

From the experimental set-up of wind power measurements, the results reveal the relation of wind speed (U) with the distance (L) away from wind energy source. They showed that U_n decreased with L, and for turbulence state I_n increases with L. This leads to a decreased pressure density (Walters, 1967). For the CFA visualization of flow energy acting on the surface of blade by a constant of $U_o = 3.5$ m/s, The results show that flow velocity under blade region was faster than that in the upper blade region. That is because the major factor of the lift force generated by the difference of flow pressure as revealed by Bernoulli's principle. Total net force direction by fluid pressure acting on blades was indicated the β direction of 45° which corresponded to the tangential speed direction of the tip blades. This is in good agreement with the experimental results of Γ and TSR from the measured ω_n and α_n for each β condition.

For turbine characteristics, the results show that the tendencies line (slope) of Γ, P_mech, and C_p with U_n variation for each β descending alignment is related to 45°, 60°, 40°, and 24°, respectively. That is because it is similar to the β condition as the slope of α with U_n variation. For the wind speed lower than 1.85 m/s, the initial torque

and the captured efficiencies of β condition of 60° were higher than those of β at 45°. It implies that the angle of 60° is the best position for the initial state of turbine or low wind speed velocity. On the other hand, tendencies line (slope) of λ with the wind speed variation (U_n) for β conditions were descending alignment related to 45°, 40°, 60°, and 24°, respectively. That is similar to the condition of β as the slope of ω with U_n variation. The CFA results are consistent. It shows that total force direction acting on blade is exactly the rotational turbine direction.

The prototype of the SABSS-HAWT in this work is aimed to drive a maximum power through a well-designed blade rotational motion. The adjustable turbine efficiency by changing attacking angles was depended on the changeable ambient energy. A fundamental was developed for designing the controlling SABSS-HAWT system corresponding to the envelopment change. The envelopment data of wind speed had been detected by a sensor (estimator) unit. Sensing data of U were processed by a microcontroller and they were assigned the β position corresponding to the magnitude of U. The major proposal for the designed of SABSS-HAWT is to have the ability of capturing energy of a very low wind speed.

CHAPTER 4

CONTROLLING SELF-ADJUSTABLE BLADES SMALL SCALE HORIZONTAL AXIS WIND TURBINE (SABSS-HAWT) WITH PIEZOELECTRIC GENERATORS

4.1 Literature reviews

For implementation of the wind power energy harvesting, the ability of energy conversions is the most important parameters to achieve maximum of usable power. In this works, the energy harvester consists of three components which are; 1) capture part for converting wind power; 2) detection part for wind speed or sensor unit; 3) energy generator unit. As the theoretical review of fundamental wind turbine (section 3.2) and transduction principles (section 1.5) were described previously, literature review of the wind speed sensor unit was laid down in the following section.

4.1.1) Wind speed sensing parameters

Natural wind in the open air is a three-dimensional vector that has the directions of north, south, east and west in addition to vertical components and magnitude (i.e., wind speed). As the vertical component is ignored for most operational meteorological purposes, a surface wind is practically considered as a two-dimensional vector.

Wind blowing over the Earth's surface is turbulent, and is characterized by random fluctuations of speed and direction. Wind speed is classified into instantaneous and average types. The average wind speed is the average of the instantaneous wind speed over a several-minute period. As described above, however, wind speed fluctuates continuously, and measured values of instantaneous wind speed are affected by anemometer response characteristics. Defined below are some basic terms and units used in wind measurement, with a focus on those related to response characteristics that affect anemometer performance.

4.1.1.1) Wind passage: L (m) is the distance that wind (air mass) covers over a given period of time.

4.1.1.2) Instantaneous wind speed: U_i (m/s) is the wind speed at a quick change, and the numerical expression for instantaneous wind speed (U_i) at a time (t) is expressed as shown in equation (4.1).

$$U_m = \lim_{\Delta t \to 0} \frac{\Delta L}{\Delta t} = \frac{dL}{dt} \tag{4.1}$$

4.1.1.3) Average wind speed: U_m (m/s) is the numerical expression for the average wind speed (U_m) at time (t), in m/s, is defined as previous equation (3.2).

4.1.1.4) Starting threshold speed: U_o (m/s) is the lowest wind speed at which a rotating anemometer mounted in its normal position starts to turn continuously.

4.1.1.4) Response length: L_d (m) is the distance that an air mass moving through a rotating anemometer travels in a given time period (time constant) required for the output of an anemometer's sensor to reach 63% of the equilibrium wind speed after a step change. The numerical expression for the response length Ld is defined as equation (4.2).

$$L_d = U \times \tau \tag{4.2}$$

4.1.1.5) Critical damping: indicates the damping actuated when the direction of a wind vane changed stepwise and reaches its equilibrium with the fastest transient response without overshoot.

4.1.1.6) Overshoot: (θ) indicates he amplitude of a wind vane's deflection when it oscillates after a release from the initial displacement.

4.1.1.7) Overshoot ratio: (Ω) is meaning to the ratio of two successive overshoots as expressed by equation (4.3).

$$\Omega = \theta_{(n+1)} / \theta_n \tag{4.3}$$

where θ_n and $\theta_{(n+1)}$ are the nth and $(n+1)^{th}$ overshoots, respectively.

In practice, since deflections after the first overshoot are usually small, the overshoot ratio is determined by the deflection of the initial release point (n = 0) and the first deflection after release (n = 1) as shown in figure 4.1.
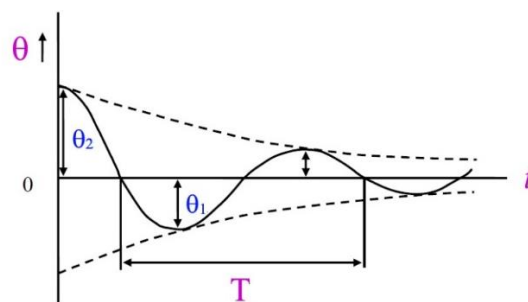
Figure 4.1 Overshoot of damping oscillation.

4.1.2.8) Damping ratio (ξ) indicated the ratio of actual damping to critical damping as expressed by the following equation (4.4).

$$\xi = \frac{\ln(1/\Omega)}{\sqrt{\pi^2 + [l_n(1/\Omega)]^2}} \tag{4.4}$$

$\xi < 1$ Under damping $\xi = 1$ Critical damping $\xi > 1$ Over damping

(a)   (b)   (c)
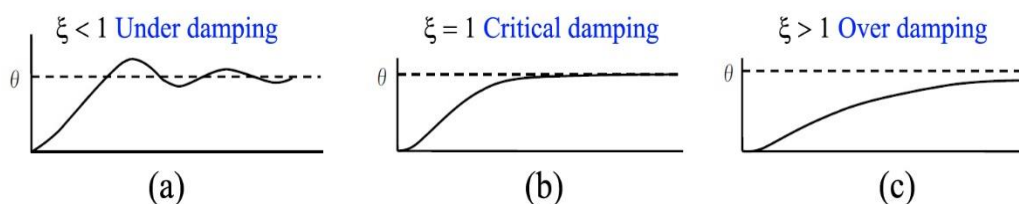
Figure 4.2 Oscillation changes by damping ratio (a) under damping, (b) critical damping, and (c) over damping.

4.1.2) Rotating anemometer

There are two types of rotating anemometer i. e. the cup anemometer, and propeller anemometer. This work focuses on a cup-like anemometer, which has three or four cups mounted symmetrically around a freewheeling vertical axis. The difference in the wind pressure between the concave and the convex side of the cup causes it to turn in the direction from the convex side to the concave side of next cup. The revolution speed is proportional to the wind speed irrespective of wind direction.

Both cup and propeller anemometer are relied on the principle that the revolution speed of the cup or propeller rotor is proportional to the wind speed. Rotating anemometers can be classified as the generator type or the pulse generator type according to the type of signal generator used. The generator type is a kind of wind power generator whose cup or propeller axis is directly coupled to the axis of a generator that generates voltage from their rotation. As the generated voltage is proportional to the revolution speed of the cup or propeller rotor and thus to the wind speed, the wind speed can be measured.

Two different types of measured signals from generator are AC and DC and DC generators are widely used. The average wind speed is obtained using either the pulse-of- wind- passage method or with a CR (combination of capacitors and resistors) integrated circuit, or alternatively with a microprocessor. These measurement principles are explained in the following sections.

4.1.3) Principles of wind speed measurement

Generator-type cup anemometer has a small AC generator coupled to its axis. The wind turns the cups and the generator to generate a voltage proportional to the instantaneous wind speed, and the signal is transmitted to the indicator as shown in figure 4.3. The CR integrated circuit calculates the average wind speed as the circuit charges and discharges the capacitor over a certain period.

A pulse generator-type cup anemometer counts the number of cup-wheel rotations, which is proportional to the wind passage. The number of rotations in a particular period is counted, and the wind passage is obtained by multiplying the factor specified for the anemometer by this number. The wind speed is obtained by dividing the wind passage by the number of time units in this period.
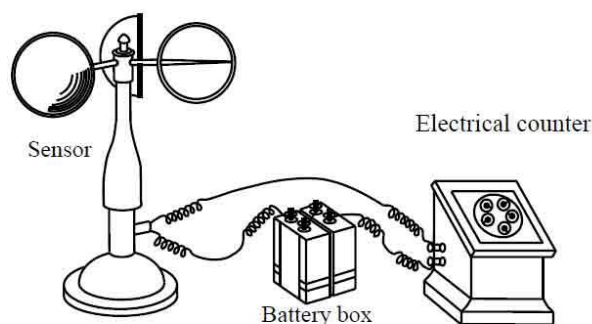
Figure 4.3 Generator-type cup anemometer.

The optical or magnet pulse generator type is mainly used now, having replaced the electrical contact breaker type. An optical pulse generator consists of a perforated disk directly fixed to the rotating axis of the cup wheel and a photo coupler, while magnetic pulses were add non-symmetry shape on the rotating axis. As the cup wheel rotates, the chopper disk turns and either allow or interrupt the passage of a beam of light between the light transmitter and the light receiver of the photo coupler. Magnetic pulse, period, variations of magnetic field had been detected by a magnetic sensor. They are creating pulse signals with a frequency proportional to wind speed. After P/A (pulse-analog) conversion, a DC voltage proportional to the number of pulses in a specific period is generated. This voltage is then converted to give an instantaneous wind speed. Some cup anemometers with a pulse generator digitize signals and indicate the instantaneous wind speed with a microprocessor.

A CR integrated circuit or a microprocessor are used to obtain the average wind speed. For details of these methods, refer to the next section regarding pulse generator-type to the microcontroller.

4.1.4) Controlling system

4.1.4.1) Wind turbine modes of operation
Wind turbines operate at different modes for different wind speeds. These modes are determined by minimum rotational speed, rated power and rated rotational speed, as well as cut-in, cut-out and rated wind speeds. The lowest wind speed at which the turbine starts to generate power is called the cut-in wind speed. Cut-out

wind speed is the speed at which the turbine is designed to shut down in order to prevent damage. The wind turbine starts to produce rated power. Figure 4.4 shows rotational speed and generated power of a wind turbine in steady states as functions of wind speed and table 4.1 shows different operating modes of a wind turbine.
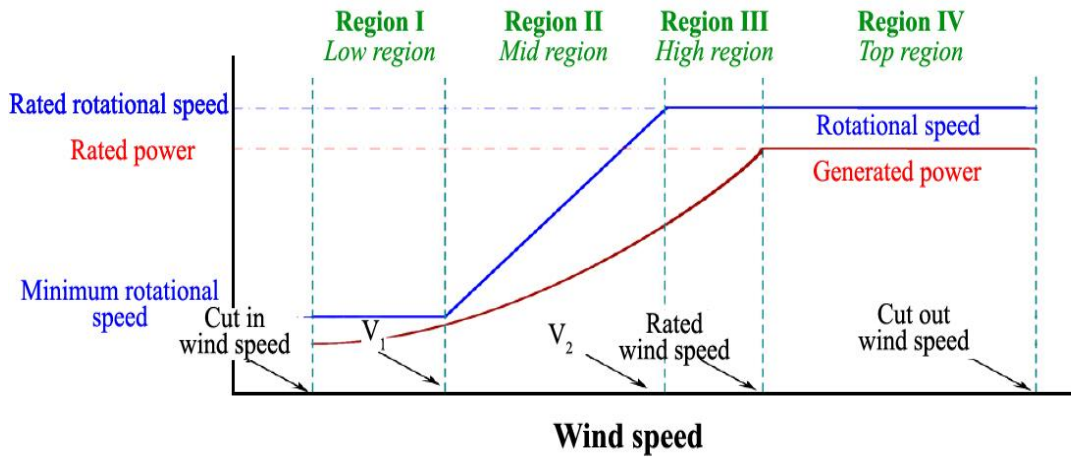
Figure 4.4 Rotational speed and generated power as functions of wind speed in different operating regions.

Table 4.1 Different operating regions of wind speed.

Regions	Wind speed	Rotational speed	Power
Region I: Low region	$U_{\text{cut-in}} \le U_e \le U_1$	$\omega_{\min}$	$P_{\max}(v_e)$
Region II: Mid region	$U_1 \le U_e \le U_2$	$\omega_{\min} \le \omega \le \omega_{\text{rated}}$	$P_{\max}(v_e)$
Region III: High region	$U_2 \le U_e \le U_{\text{rated}}$	ω_{rated}	$P_{\max}(v_e)$
Region Iʙ: Low region	$U_{\text{rated}} \le U_e \le U_{\text{cut-out}}$	ω_{rated}	P_{rated}

The first three regions (regions I, II and III) are called partial load where the machine is not operating at its rated values and the last region (region IV) is called full load where wind speed is above rated value and the turbine is producing its rated power while rotating at rated rotational speed. Control objective are different for the partial load and the full load. In the partial load the objective is to maximize captured power, while in the full load we try to regulate the produced power and the rotational speed at their rated values while minimizing the dynamic loads. The different control objectives need different control strategies. This work mainly focuses on full load operation of the turbine.

4.1.4.2) Wind turbine pitch control

Pitch control allows to change the pitch angle of WT's blades in order to control its aerodynamic efficiency. The pitch angle is a major WT parameter as it determines the wind's angle of attack (Hau and von Renouard, 2005). Thus, turning the blades around their own axes changes the relative wind flow and consequently the aerodynamic loads exerted on the rotor. Moreover, the power coefficient Cp (λ, β) varies according to the pitch angle and consequently the power capture varies as well. Therefore, pitch angle control has a twofold role: power regulation and load reduction as shown in figure 4.5. The diagram shows that the speed of the wind that hits the turbine can vary significantly across the rotor plane. Rotor speed measurements and wind speed estimator are both usually the measurements used in the feedback loops for both the generator torque control and the blade pitch control.

These are prominent in operation on Region 3, where the power production must be limited to the rated one and the high wind speeds imposes severe loads to WT structure and rotor (Johnson *et al.*, 2011). Different concepts have been proposed along the years for power regulation and load reduction of WTs. The early WTs were controlled by passive means using the blades' aerodynamic characteristics. The airfoils were designed to stall when subjected to high wind regimes, which is called passive stall control. None additional actuator was necessary, thus a simple and low-cost power control was realized. However, the controllability was very limited as it was based on a natural stall phenomenon without any active control. In passive stall control, the WT is subjected to more power fluctuations, torque spikes and varying load effort.
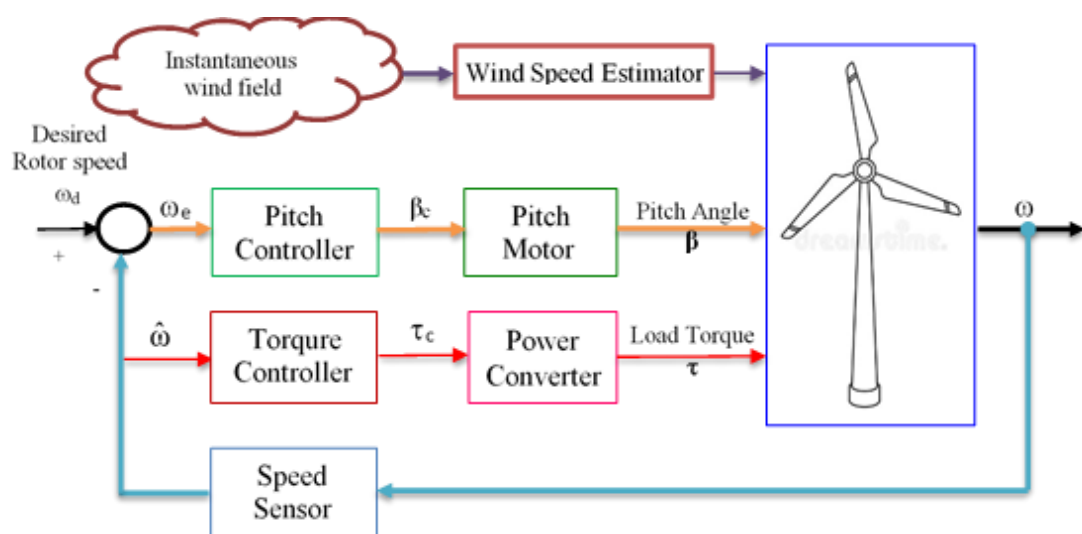
Figure 4.5 Schematic of a wind turbine closed-loop control system.

For overcoming these drawbacks, modern WTs use active pitch control, with electrical or hydraulic pitch actuators (Chiang, 2011). In Region 3, the generator torque is usually imposed to be constant while the pitch control should be working to maintain constant rotor speed. While changing the pitch angle the control system is also changing the wind torque and accelerating or decelerating the turbine. As torque and speed are set to be constant, the power production is limited and mechanical loads are reduced, reaching the control objectives of Region 3. Typically, the pitch control loop uses only the rotor speed as feedback signal and the pitch commanded value is the same for the three blades.

4.1.4.3) Pitch Servo

In variable-pitch wind turbines, the blade angle is controlled by a pitch servo. The main control system produces a blade reference angle and the pitch servo is the actuator, which actually turns the turbine blades to the ordered angle. The pitch servo is subject to constructional limitations, such as angular limits θ_{min} and θ_{max}. That means that the blades can only be turned within certain physical limits. For active stall-controlled wind turbines, the permissible range will be between -90° and 0° (or even a few degrees to the positive side), whereas for active pitch-controlled wind turbines the permissible range will lie between 0° and þ90^o (or even a few degrees to the negative side). The control system may impose other, normally narrower, limits on the reference angle, though. Likewise, there are limitations on the pitch speed, $d\beta/dt$. The pitch speed limit is likely to be higher for pitch controlled wind turbines than for active-stall-controlled wind turbines, which have a higher angular sensitivity. The pitch speed limit may differ significantly for a positive $d\beta/dt_{pos}$, max) and negative ($d\beta/dt_{neg}$, max) turning of the blade. The pitch speed is normally less than 5° per second, although the pitch speed may exceed 10° per second during emergencies.

The dynamic behavior of the pitch actuator operating in its linear region is described by the differential equation (4.5); where β and β_d is desired and actual pitch angle respectively (Maheswari and Tamilvendhan, 2012).

$$\dot{\beta} \;=\; \left(\frac{1}{\tau}\beta - \frac{1}{\tau}\beta_d \right)$$

$$(4.5)$$

Pitch servo for controlling the wind turbine can classify in mode of below rated wind speed control and above rated wind speed control.

A) Below rated wind speed control: which pitch and torque control are used at below rated conditions to generate as much power as possible. To ensure as much as possible energy yield, during partial load the electric torque set point is set such that the tip speed ratio, (λ) is maintained at its optimal value ($\lambda_{opt.}$) with the optima tip speed ratio, ($\lambda_{opt.}$) $\lambda_{opt} = \lambda$ while $C_p = C_{p,max}$. The rotor speed is adjusted proportional to the wind speed by electric torque control, in such a way that the aerodynamic power extracted by the rotor (efficiency) is maximal.

B) Above rated wind speed control: Design of an algorithm to control rotor speed above rated wind speed as follows pitching the rotor blades simultaneously in feathering direction. The "constant power" control of the generator and the rotor inertia (fly wheel) will then establish good power quality. For this reason, aerodynamic torque variations will result in rotor speed variations. The amount of rotor speed variation above its rated value, to maintain rated power, is restricted both by the maximum speed of the generator and perhaps by the tower Eigen frequency to avoid tower resonance.

4.1.5) Microcontroller

A microcontroller (MCU for microcontroller unit) is a small computer on a single integrated circuit. In modern terminology, it is similar to, but less sophisticated than, a System on a Chip (SoC); an SoC may include a microcontroller as one of its components. A microcontroller contains one or more CPUs (processor cores) along with memory and programmable input/output peripherals.

Microcontrollers are used in automatically controlled products and devices, such as automobile engine control systems, implantable medical devices, remote controls, office machines, appliances, power tools, toys and other embedded systems. By reducing the size and cost compared to a design that uses a separate microprocessor, memory, and input/output devices, microcontrollers make it economical to digitally control even more devices and processes. Mixed signal microcontrollers are common, integrating analog components needed to control non-digital electronic systems.

The basic internal designs of microcontrollers are pretty similar. Figure 4.6 shows the block diagram of a typical microcontroller. All components are connected via an internal bus and are all integrated on one chip. The modules are connected to the outside world via I/O pins. The following list contains the modules typically found in a microcontroller.

4.1.5.1 Processor Core: The CPU of the controller. It contains the arithmetic logic unit, the control unit, and the registers (stack pointer, program counter, accumulator register, and register file, etc.).
4.1.5.2 Memory: The memory is sometimes split into program memory and data memory. In larger controllers, a DMA controller handles data transfers between peripheral components and the memory.
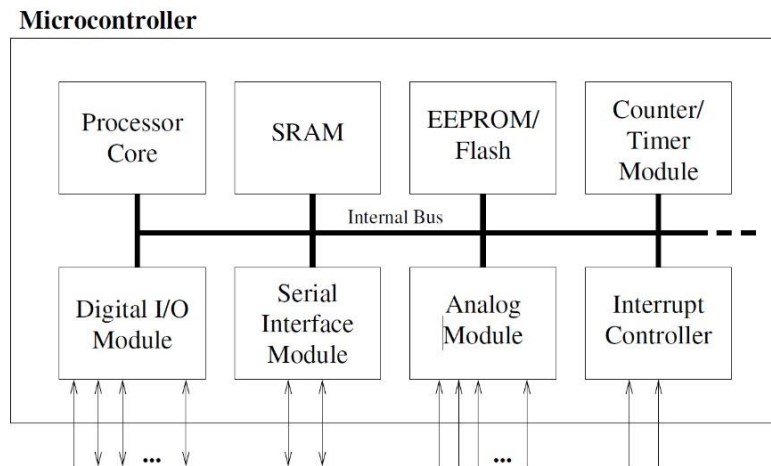
Figure 4.6 Basic layout of a microcontroller.

4.1.5.3 Interrupt Controller: Interrupts are useful for interrupting the normal program flow in case of (important) external or internal events. In conjunction with sleep modes, they help to conserve power.

4.1.5.4 Timer/Counter: Most controllers have at least one and more likely 2-3 Timer/Counters, which can be used to timestamp events, measure intervals, or count events. Many controllers also contain PWM (pulse width modulation) outputs, which can be used to drive motors or for safe breaking (antilock brake system, ABS). Furthermore, the PWM output can, in conjunction with an external filter, be used to realize a cheap digital/analog converter.

4.1.5.5 Digital I/O: Parallel digital I/O ports are one of the main features of microcontrollers. The number of I/O pins varies from 3-4 to over 90, depending on the controller family and the controller type.

4.1.5.6 Analog I/O: Apart from a few small controllers, most microcontrollers have integrated analog/digital converters, which differ in the number of channels (2-16) and their resolution (8-12 bits). The analog module also generally features an analog comparator. In some cases, the microcontroller includes digital/analog converters.

4.1.5.7 Interfaces: Controllers generally have at least one serial interface which can be used to download the program and for communication with the development PC in general. Since serial interfaces can also be used to communicate with external peripheral devices, most controllers offer several and varied interfaces like SPI and SCI. Many microcontrollers also contain integrated bus controllers for the most common (field) busses. Larger microcontrollers may also contain PCI, USB, or Ethernet interfaces.

4.1.5.8 Watchdog Timer: Since safety-critical systems form a major application area of microcontrollers, it is important to guard against errors in the program and/or the hardware. The watchdog timer is used to reset the controller in case of software "crashes".

4.1.5.9 Debugging Unit: Some controllers are equipped with additional hardware to allow remote debugging of the chip from the PC. So there is no need to download special debugging software, which has the distinct advantage that erroneous application code cannot overwrite the debugger.

4.1.6) Efficiency and energy loss

Completely a 100% of the energy conversions from one to another are not possible, some were released in losses of heart, friction, oscillation during to the conversion process. Including to the incomplete efficiency conversion ratio by overall input energy were not transformed the uncaptured energy to actual power output. So that the indicator of total wind turbine efficiency is defined by the proportion of actual electrical power produced by wind power into turbine as shown in equation (4.6).

$$C_p = \frac{\text{Actual electrical power produced}}{\text{Wind power into turbine}} = \frac{P_{out}}{P_{in}} \tag{4.6}$$

The wind turbine energy consisted of three conversion sections which are turbine, mechanical and electrical performances. Firstly, the turbine efficiency (η_t) is not over/higher than 59.3% as given by Bitz's limit because an energy losses (δ_t) had been occurred by fluid flow slipped through the moving blades without any momentum interaction. Secondly, the mechanical performance or mechanical conversion (η_m), the rotation of the rotor by lift force drove the turbine shaft converting to mechanical energy. Energy loss (δ_{mech}) was generated from rotational and vibrational of the friction loss. Finally, the generated electrical performance, the rotational/vibrational energy was converted into electrical energy base on the generator principle. The efficiency conversions (η_e) and efficacy loss (δ_{ele}) were developed by several cases such as the batteries loss (by impedance) and circuitry loss (by resistance of the electronic components). Then the combination of C_p from the efficiencies of all the subsystem components define the total efficiency conversion as given by equation (4.7). Energy flow diagram for SABSS-HAWT energy harvester is presented in figure 4.7.

$$C_p = \eta_t \cdot \eta_m \cdot \eta_e \tag{4.7}$$
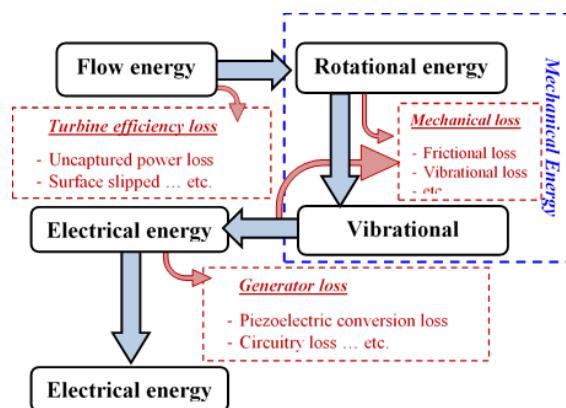
Figure 4.7 Energy flow diagram of SABSS-HAWT energy harvester.

4.2 Methodology

Controlling of self-blades adjustable for small scale horizontal axis wind turbine with piezoelectric generator were consisted with 4 experimental validations as; 1) anemometer calibration, 2) pitch blade angle controlling, 3) piezoelectric generator and COMSOL piezoelectric cantilever vibrations.

4.2.1) Wind speed estimator calibration

Sensing elements unit of SBASS-HWAT is a flow kinetic detector from the surrounding, the obtained measured data from its used for generated the proper direction for attacking angle of blades corresponding to the instantaneous wind speed (U_i) at time (t). Anemometer of SBASS-HWAT were modulated from flows sensor model YF-S201 and it consists with non-symmetric magnet, rotational axis, hall sensor and CR integrated circuit. Pulse digital signals were generated by non-symmetric magnet rotation and hall sensor will send those pulse signal to microcontroller Arduino UNO. Distance between modulated cup anemometer and blower of wind power source is about 0.78 m which indicated minimum turbulence state as show by the results of wind speed measurement in Chapter 3. The schematic of the experimental for anemometer calibration is show in figure 4.8.
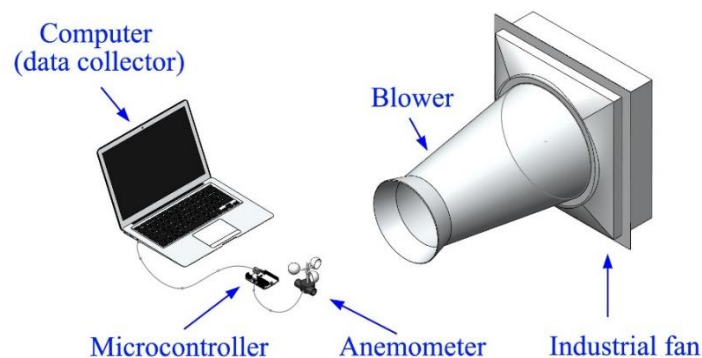
Figure 4.8 Schematic of the experimental for anemometer calibration.

While signals detecting from anemometer experiment were perform, commercial digital anemometer TM-826 had been recorded wind speed value by video camera. To compare the measured plus signal with the detected standard of wind speed by TM-826, 200 seconds had been measured by both methods at the same time. Detected plus signal had been modified by FFT technique for rotational frequencies of anemometer. Both detected pulse signals of 200 seconds and standard wind speed measured by TM-826 of 100 seconds had been estimated mean values and standard deviations. Five speed variations were obtained by potentiometer series with industrial fan.

4.2.2) Generator unit and the modeling

Vibrational piezoelectric generator experiments are consist with signal generator, vibrational oscillator, oscilloscope, laser displacement sensor (KEYENCE-IA 030, Japan) as shown in figure 4.9, and PZT-5A with the dimensional of 45×7.5×0.25 mm. Steel plate of 1 mm thickness and 11 mm width were attached with PZT-5A by 4 lengths variations by 52, 59, 69 and 76 mm. Vibrational were generated to 4 samples with length variation of attached PZT-5A in range of 10-100 Hz with step size of 10 Hz by function generator. The displacement vibration had been detected with voltage signal output by laser sensor. For the V_{oc} experimental results of piezoelectric cantilever beam vibration had been validated by COMSOL multiphasic.

Figure 4.9 Vibrational piezoelectric generator experiments setup.

4.2.3) Controlling system

By transferring and communicate data processing were compiled by using microcontroller of Arduino UNO-R3. Frequencies of pulse signal are changed when wind speed changed; the relation of both parameters as presented in the results of anemometer in section 4.3.1. The logical of work flow was described in figure 4.10. At the first state, the device was defined its initial angle of servo device to the Arduino memory. Pulse signal that changed with wind speed was imported to digital pin input of microcontroller. The pules signal represented wind speed have been classified to 3 level; while the attacking angle were transformed to the angle of 24º, 40º, 45º, and 60º corresponding to wind speed conditions over 3, 2.5, 1.0 and less than 1.0 m/s, respectively. To obtain the angular position of attacking angle by blades, MCU will generated command and send it passed analog pin output to servo motor. Programing code for the controlling pitch blades position by pulse signal of wind speed estimator was presented in appendix B (I).
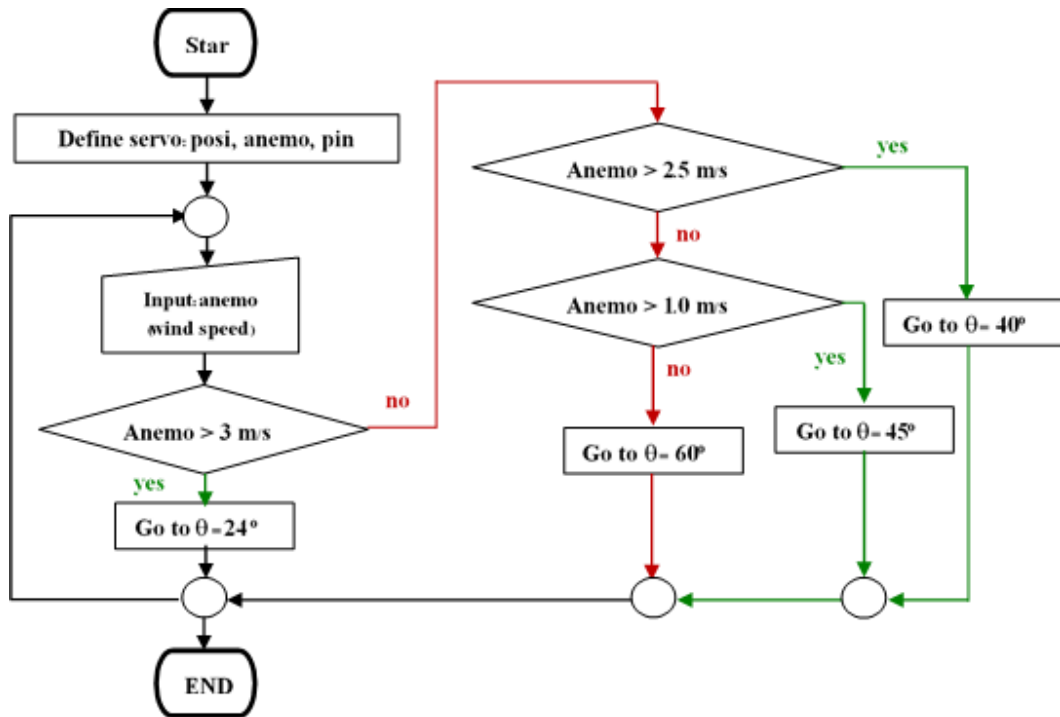
Figure 4.10 Flow chart of controlling the attacking angle by pulse signal of wind speed anemometer.

4.2.4) Efficiency conversion

In this section, an estimation of the efficiency can be classified by mechanical (η_{mech}) and electrical conversion (η_{elec}). The η_{mech} is defined by rotational power output (P_{mech}) divided by wind power input. The η_{elec} is defined by electrical power output (P_{elec}) divided by mechanical power input (P_{mech}) as given below.

$$\eta_{elec} \;=\; \frac{P_{elec}}{P_{mech}} \;=\; \frac{I \cdot V}{\Gamma \cdot \omega} \;=\; \frac{V^2/R}{I \cdot \alpha \cdot \omega} \tag{4.8}$$

To obtain the calculated η_{elec} parameter of SABSS-HAWT harvester for each different operating regions, the specific dimension of piezoelectric generator of 45 mm $\times$ 7.5 mm $\times$ 0.25 mm had been estimated the generated electrical voltage output (V_m) by using equivalent circuit model. The PZT-5A material parameters in table 4.2 were used, the model outputs were then validated with the experimental data.

To obtain the electrical efficiency conversion (η_{elec}), an optimized resistance (R_{opt}) had been estimated by using equation (2.41), which indicated maximum electrical power output (P_{elec_max}) by the variations of R. The R_{opt} parameter is obtained for R at

the P_{elec_max} result was represented, generated electrical power $P_{elec} = V^2/R$ that leads to the estimated η_{elec} as in equation (4.7) for each operating regions of this controlling system. Mean value of U, P_{mech}, P_{elec}, had been calculated for η_{elec} to represent in low, high and top region, while a root mean square were applied for middle region.

Table 4.2 Parameters and material properties of PZT-5A for equivalent circuit model.

Parameter	Value	Unit
Piezo length (l)	0.04500	m
Piezo width (w), Steel width (w_s)	0.00750	m
Piezo thickness (t),	0.00025	m
Piezo permittivity (ε)	2300	F/m
Young's modulus (E)	5.5×10^{-10}	N/m^2
Piezo strain constant (d_{31})	-1.9×10^{-10}	C/N
Coupling factor (k_{31})	0.4	-
Directional constant (a)	1 or 2	-
Steel length (l_s)	0.052	m
Steel thickness (t_s)	0.001	m
Constant relating the strain to deflection (k_2)	-0.033	N/m^2
Damping ratio (ζ)	0.02	-
Resonance frequency (f)	45	Hz

4.3 Results

In this section is the combination of the experimental data of anemometer calibration and vibrational piezoelectric energy harvesting including the simulations of piezoelectric vibration;

4.3.1) Anemometer calibration is using the detected pulse signal anemometer and calibrated it with commercials standard anemometer by linear regression technique of Gaussian data distribution.

4.3.2) Controlling unit is experimental powering estimation by piezoelectric vibrations with the variation of beam length and vibrational frequencies.

4.3.3) Controlling unit were described the schematic controlling system including algorithm structure.

4.3.1) Wind speed estimator calibration

The SBASS-HWAT needs the sensing unit to detect changing of surrounding kinetic energy. Five values of a wind speed were generated by potentiometer series with industrial fan at the constant distance. Digital anemometer was measured data of U_n for 100 seconds. Normal distribution of mean and standard deviation of wind speed for five conditions of I, II, III, IV, and V were shown in figure 4.11 (a)-(e), respectively. Numerical results in figure 4.11 were summarized in table 4.3.

Pulse signals had been detected by flow sensor YF-S201 interval 200 seconds, including Gaussian curve fitting function by 5 conditions of I, II, III, IV, and V were show in figure 4.12 (a)-(e). Numerical parameters of curve fitting results were summarized in table 4.4.

To calibrate a flow sensor YF-S201 with the wind speed measured by digital wind anemometer TM-826, a comparison of measured data by linear regression was carried out, and the first and the second measured data represented x, and y parameters, respectively. The results of linear the regression of both data were shown in figure 4.13 and summarized in table 4.5.
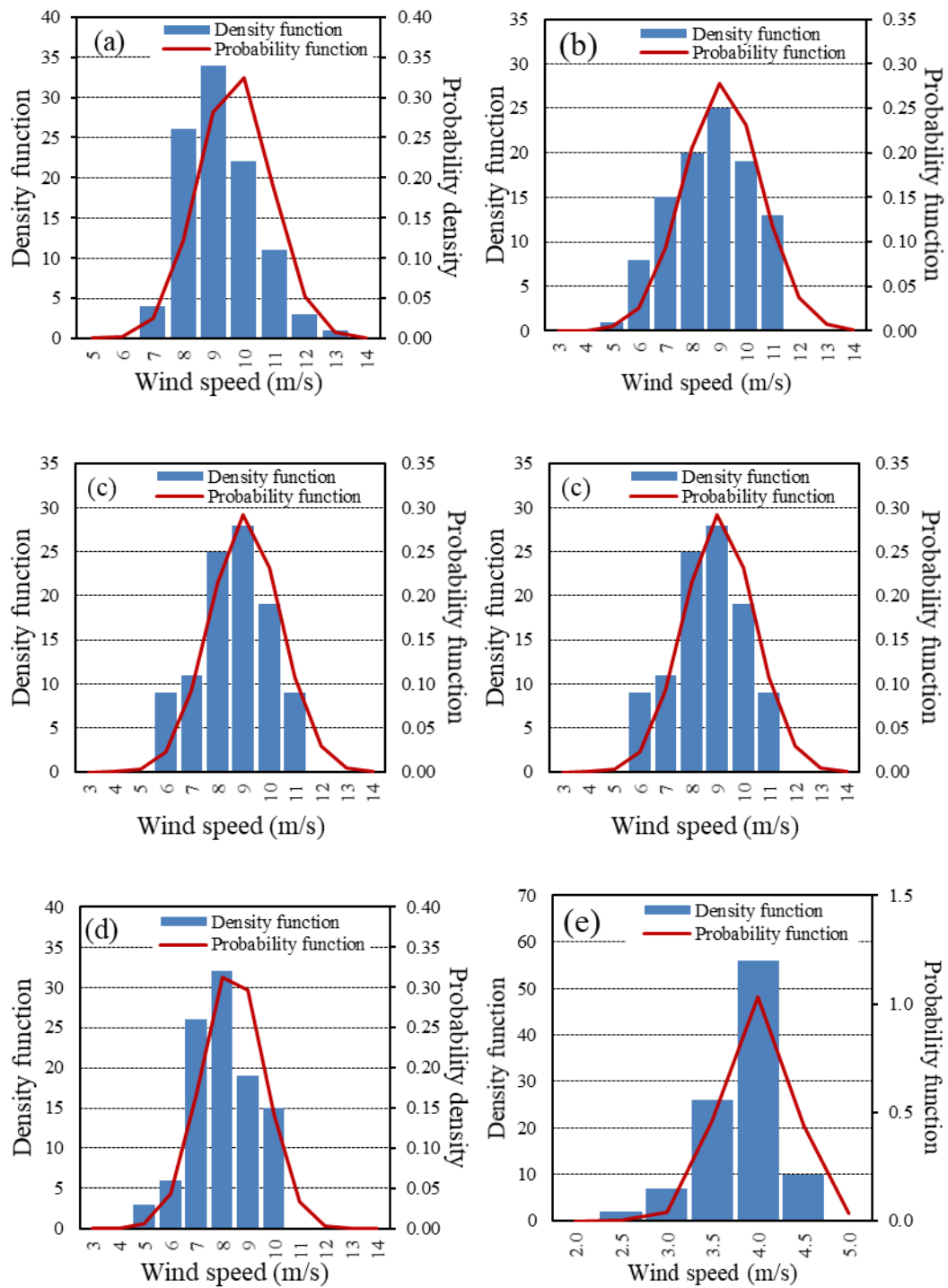
Figure 4. 11 Density and probability function of wind speed measured by digital anemometer TM-826 of (a) I, (b) II, (c) III, (d) IV, and (e) V conditions interval 100 seconds.

Table 4.3 Mean values and standard deviation including the density and probability function of wind speed measured by a digital anemometer TM-826 by I, II, III, IV, and V conditions interval 200 seconds.

U_n (m/s)	Conditions									
	I		II		III		IV		V	
	Mean	SD.	Mean	SD.	Mean	SD.	Mean	SD.	Mean	SD.
	9.702	1.1908	9.124	1.4316	9.073	1.3629	8.425	1.2020	3.992	0.3867
	Density function	*Probability function*	*Density function*	*Probability function*	*Density function*	*Probability function*	*Density function*	*Probability function*	*Density function*	*Probability function*
2.0	-	-	-	-	-	-	-	-	0	0.00
2.5	-	-	-	-	-	-	-	-	2	0.00
3.0	-	-	-	-	-	-	-	-	7	0.04
3.5	-	-	-	-	-	-	-	-	26	0.46
4.0	-	-	-	-	-	-	-	-	56	1.03
4.5	-	-	0	0.00	-	-	0	0	10	0.44
5.0	-	-	1	0.00	0	0	3	0.01	0	0.03
6.0	0	0	8	0.03	9	0.02	6	0.04	0	0.00
7.0	4	0.03	15	0.09	11	0.09	26	0.16	-	-
8.0	26	0.12	20	0.20	25	0.21	32	0.31	-	-
9.0	34	0.28	25	0.28	28	0.29	19	0.30	-	-
10.0	22	0.32	19	0.23	19	0.23	15	0.14	-	-
11.0	11	0.18	13	0.12	9	0.11	0	0.03	-	-
12.0	3	0.05	0	0.04	0	0.03	0	0	-	-
13.0	1	0.01	0	0.01	0	0	-	-	-	-
14.0	0	0	0	0.00	0	0	-	-	-	-
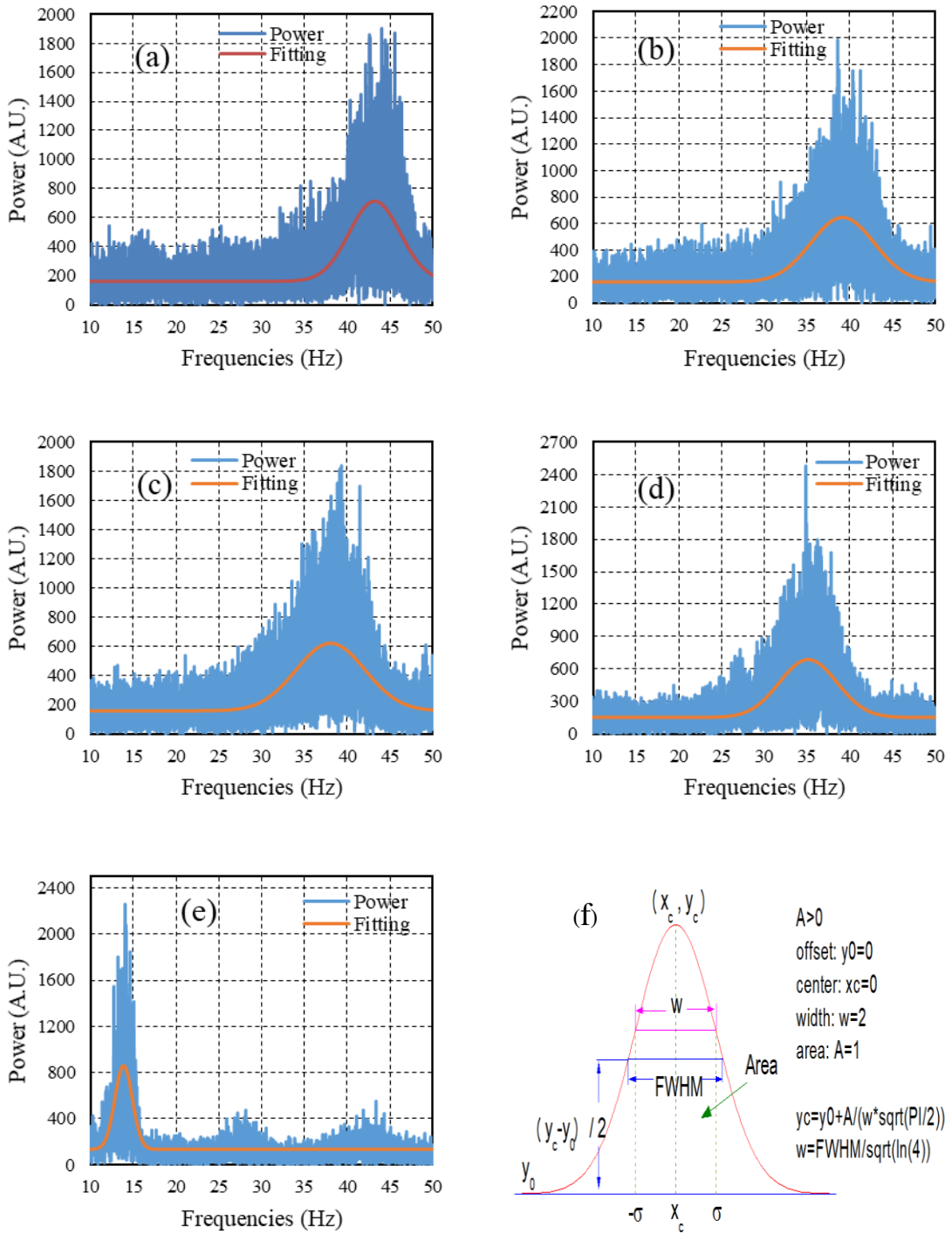
Figure 4.12 Power FFT spectrum of pulse rotational signals by flow sensor YF-S201 measured interval 200 second with the conditions of (a) I, (b) II, (c) III, (d) IV, (e) V, and (f) Gaussian fitting parameters

Table 4.4 Fitting parameters of Gaussian curve as mean value (y_o), base line (X_c), width (W), area (A), standard deviation (sigma), full width at half maximum (FWHM), and height for I, II, III, IV, and V conditions of the pulse signal generated by flow sensor YF-S201 interval 200 seconds.

U_n (m/s)	Conditions									
	I		II		III		IV		V	
	Value	SD.	Value	SD.	Value	SD.	Value	SD.	Value	SD.
y_o	162.667	1.8556	159.366	1.9817	159.118	2.0366	153.221	1.9387	136.338	3.1354
X_c	43.200	0.0370	39.135	0.0461	38.042	0.0506	35.122	0.0400	13.845	0.0310
W	5.974	0.0796	7.403	0.1011	8.063	0.1125	6.718	0.0870	2.041	0.0633
A	4123.396	52.7748	4524.692	62.2034	4673.134	66.7079	4508.149	57.9394	1852.989	51.6463
sigma	2.987	0.0398	3.702	0.05054	4.032	0.0562	3.359	0.0435	1.020	0.0316
FWHM	7.034	0.0937	8.717	0.1190	9.494	0.1324	7.910	0.1025	2.403	0.0745
Hight	550.669	6.0887	487.633	5.4514	462.435	5.2405	535.400	5.6848	724.398	19.1918
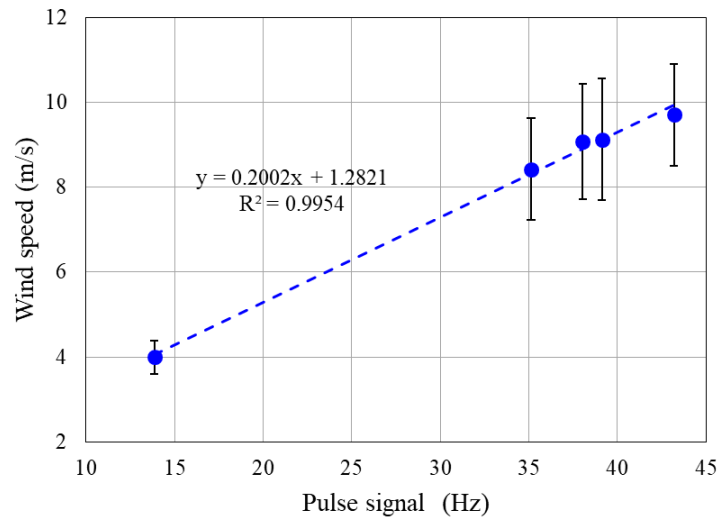
Figure 4.13 Linear regression of measured data; (wind speed by TM-826 and pulse signal by YF-S201) for the estimator calibration.

Table 4.5 Five measured conditions for the linear regression by mean value and standard deviation of the wind speed (U_n) by TM-826 and pulse signals by YF-S201.

Condition	x-parameter		y-parameter	
	Pulse [YF-S201] (Hz)	SD. (Hz)	U_n [TM-826] (m/s)	SD. (m/s)
I	43.200	0.0370	9.702	1.1908
II	39.135	0.0461	9.124	1.4316
III	38.042	0.0506	9.073	1.3630
IV	35.122	0.0400	8.425	1.2020
V	13.845	0.0310	3.992	0.387

4.3.2) Generator unit and the modeling

After captured kinetic energy from flows and there transferred to the mechanical energy of rotation motion, electrical generator is an important component for the converting the power to useable electricity. In this section, the electrical power was generated by converting the mechanical energy to electrical power by piezoelectric materials. A PZT-5A of 45 mm × 7.5 mm × 0.25 mm was glued on a cantilever made from steel plate of length (*l*) (variation of 52, 59, 69 and 76 mm) and 1 mm-thick and 11 mm-wide. The cantilever was vibrated at its free end with the frequencies (*f*) in a range of 10-100 Hz. The results of the generated peak-to-peak voltage with no load

displayed by an oscilloscope with the variation of frequencies oscillation (*f*) for each beam length were presented in figure 4.14. The results of the vibrational displacement with *f* variations for each beam length were presented in figure 4.15.
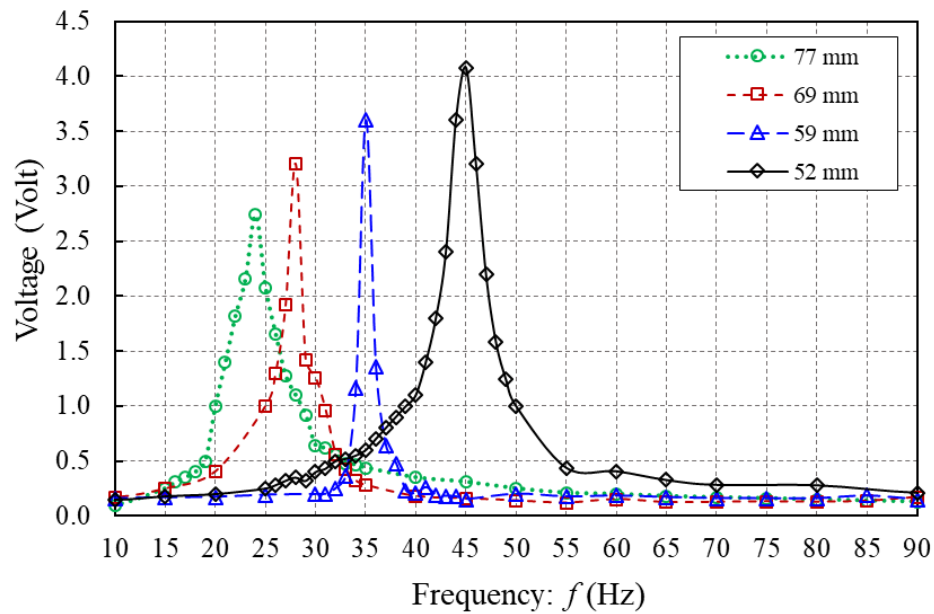
Figure 4.14 Voltage output with the frequency variation for vibrational cantilever beam of the length of 52, 59, 69 and 76 mm.
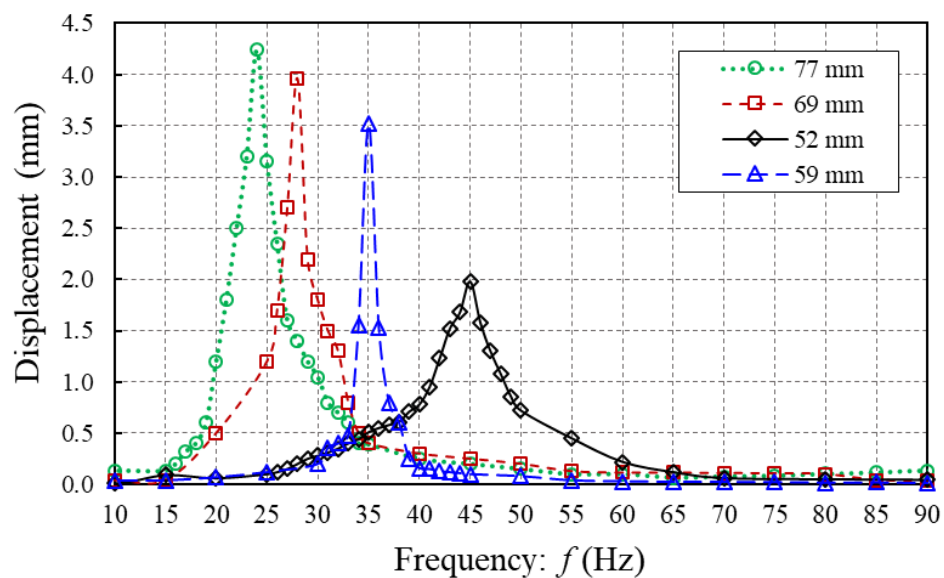
Figure 4.15 Vibrational displacement with the frequency variation for the cantilever oscillation from the beam length of 52, 59, 69 and 76 mm.

The generated voltage (V_n) by the cantilever beam oscillations were increased as a function of beam length, corresponding to the first resonance   increased when beam length, as shown in figurea 4.14, and 4.16. The increment of resonance frequencies (f_n) as a function of beam length (L_n) was followed equation (1.19) given by Ghassoul, N. (2007). An amplitude of current in equation (1.21) (Mineto, *et al*. 2010) explained the reason of how V_n increased as a function of L_n distressed. The other reason for the V_n increased with L_n was related to the generated beam stress as in equation (2.20). There stresses were mainly developed while there was a reverse proportional of triple beam length ($1/L^3$), which indicated V_n increased whereas L_n decreased.

Figure 4.15 presents oscillation displacement (y_n) at the free end with the *f* variations by beam length conditions of 52, 59, 69 and 76 mm. The results show that y_n increased with L_n increased because of y_n is proportional to triple of beam length parameter (L^3) as described in equation (1.21) by Hunt, *et al*. (2013). For the natural frequency increasing with L_n are using similar reason of equation (1.19).
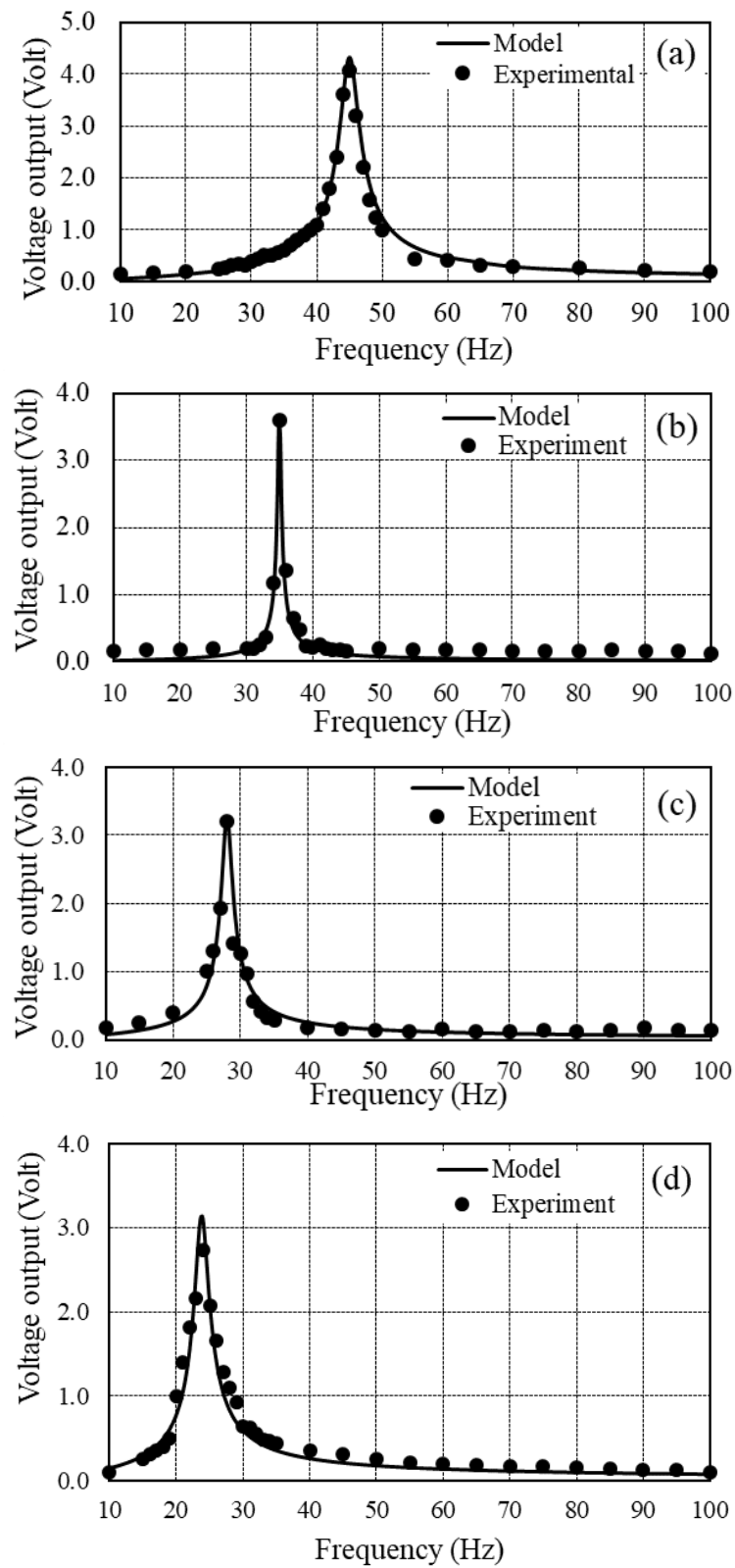
Figure 4.16 Comparison voltage output (V_n) with the results of equivalence circuit model by piezoelectric cantilever beam oscillation for the beam length conditions of (a) 52 mm, (b) 59 mm, (c) 69 mm, and (d) 77 mm.

4.3.3) Controlling system

The results in this section representing the controlling systems of SABSS-HAWT energy harvesting depending on wind speed for the maximum powering achievement. When a wind speed changed, attacking angle (β) of the blades were changed following to the changing of wind velocity information. Wind power captured by SABSS-HAWT in different operating regions were separated by the range of wind speed as represented in figure 4.17. It were estimated by the efficiencies investigation as mention in Chapter 3. Numerical information of the attacking angle (β), wind speed region (U), responded rotational frequency (f_R) informations for the different of wind speed region were represented in table 4.6.
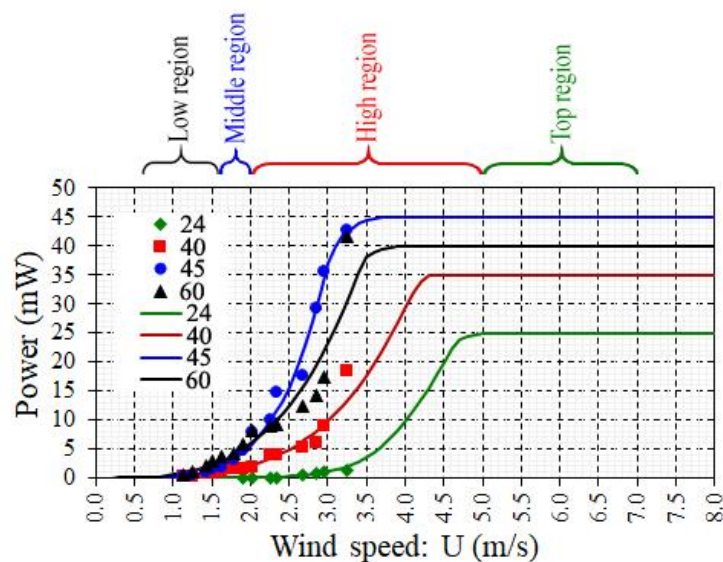
Figure 4.17 Extracted mechanical power estimated by SABSS-HAWT.

Table 4.6 Summary of different operating regions

Regions	θ (degree)	Wind speed (m/s)	Rotational frequency (Hz)	P_{mech} (mW)	η_{mech} (%)
Region I: Low	60	0.6 - 1.6	0.5 - 2.6	0.5 - 1.6	2.0 - 6.2
Region II: Mid	45	1.6 - 2.0	1.6 - 4.2	3.0 - 7.0	3 - 8
Region III: High	40	2.0 -5.0	3.0 - 5.0	5 - 45	8.5 - 48.5
Region IV: Top	24	≥ 5.0	2.4 – 3.0	45	1.0 - 15.0

As mentioned earlier in subsection 4.2.4.1, it had been approached by figure 4.17 for the controlling systems of SABSS-HAWT. The results were summarized as $U_{\text{cut-in}} = 0.6$ m/s; $U_1 = 0.6$ m/s; $U_2 = 0.6$ m/s; and $U_{\text{rate}} = 5.0$ m/s. The lowest U is around 0.6 m/s which is possible to drive the turbine at β of 60° (low regions). The piezoelectric cantilever beam was used as the power generator to generate maximum energy around resonance frequency (single value). Therefore, to control the attacking angle corresponds to the variation of wind speed, the single value of rotational frequency (f_R) was focused.

The expectation value of f_R in this work is approximately around 3.0 Hz. This corresponded with 15 pieces of piezoelectric beams and 15 pieces of impact bars, which were induced to oscillate at about 15 pieces $\times$ 3.0 Hz = 45 Hz (1st mode of resonance frequency by the beam length of 52 mm). While the wind energy was increased until U reached to the interval of 0.6-1.6 m/s, attacking angle were set as 60°. That was because the highest torque was driven at this angle in low-regions; and the results of β at 60° for f_R, P_{mech}, and η_{mech} were 0.5-1.2 Hz, 0.5-1.6 mW, 2.0-6.2%, respectively. In case of the middle region of the U interval of 0.5-1.6 m/s, the MCU was assigned attacking angle of 45° degree. The obtained results of f_R, P_{mech}, and η_{mech} parameters for this condition were 2.0-3.5, 3.0-7.0 mW, and 3-8%.

High region is the widest range of wind speed of around 2.0-5.0 m/s for β of 40°. Due to an energy source of wind power for this experiment was limited at maximum speed of 3.24 m/s. The predicted turbine parameters, f_R, P_{mech}, and η_{mech} with variation of U were approximated by using polynomial trend for the parameter increment as well as the Betz limit's theory. The maximum constant of those results of f_R and P_{mech} parameters were occurred in this region. So a hybrid generator with dynamo is proposed as the best solution to get the maximum electrical energy because of its highest value of f_R. Parameter f_R, P_{mech}, and η_{mech} were respectively around 3.2-5.5 Hz, 5-45 mW, 8.5% - 48.5%.

In top region related to U over 5 m/s, the obtained constant of f_R and P_{mech} were at maximum values. The η_{mech} was evaluated in this U range following Betz's limit. At $U > 14$ m/s, the external driven part will be added as an option of rotational friction. The reduction of power was applied by slowing down the rotor speed to protect the damage

4.3.4) Efficiency

In this section, the efficiency can be estimated from mechanical (η_{mech}) and electrical conversion (η_{elec}). The rotational power output (P_{mech}) by SABSS-HAWT was divided by wind power input for η_{mech} and the η_{elec} was defined by electrical power output (P_{elec}) divided by mechanical power input (P_{mech}) as given by equation (3.7) and (4.7), respectively.

The piezoelectric cantilever acted like a generator with the dimensional of 45×7.5×0.25 mm attached on a steel of 59 mm length as described in section 4.2.2. The expectation value of resonance oscillation for this beam is 45 Hz, corresponding to the expectation value of rotor rotation frequency of 3 Hz. The rotation of 15 impact bars generated vibrational force acting on the cantilever beam as shown in figure 4.18. Rotational frequency of 15 bars (f_b) was related to resonance frequency of cantilever beams (f_N) as given by equation (4.9).

$$f_N \;=\; 15 \times 3\,(\text{Hz}) \;=45\;\;(\text{Hz}) \tag{4.9}$$
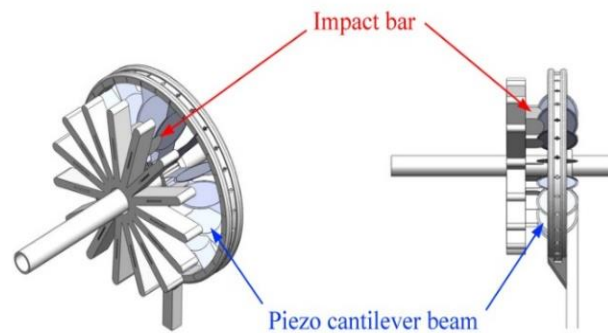
Figure 4.18 Schematic piezo-beam and impact bar configuration.

The wind speed variation responding to voltage output generated by piezoelectric cantilever beams under applied controllable β conditions in table 4.1 was as shown in figure 4.19 (a) β = 60°, (b) β = 45°, (c) β = 40°, β = 24°. In the low region in figure 4.13 (a), the minimum wind speed as "cut-in velocity: $U_{\text{cut-in}} \cong 0.6$ m/s" to 1.6 m/s, were related to generated torque with an output lower than a voltage. For the middle region, the resonance frequency of piezoelectric generator was occurred in this region and the obtained voltage output of about 4.3 volt. In the high region, the generated voltage was started at resonance frequency of the obtained voltage of 4.3 volt until 0.3 volt for the condition limit of $U = 5.0$ m/s in this region. Finally, the top region in figure 4.19 (d), the generated voltage output of 0.5 - 4.5 volt (4.5 volt is a resonance point) was appeared again before the $U_{\text{cut off}}$ was applied.
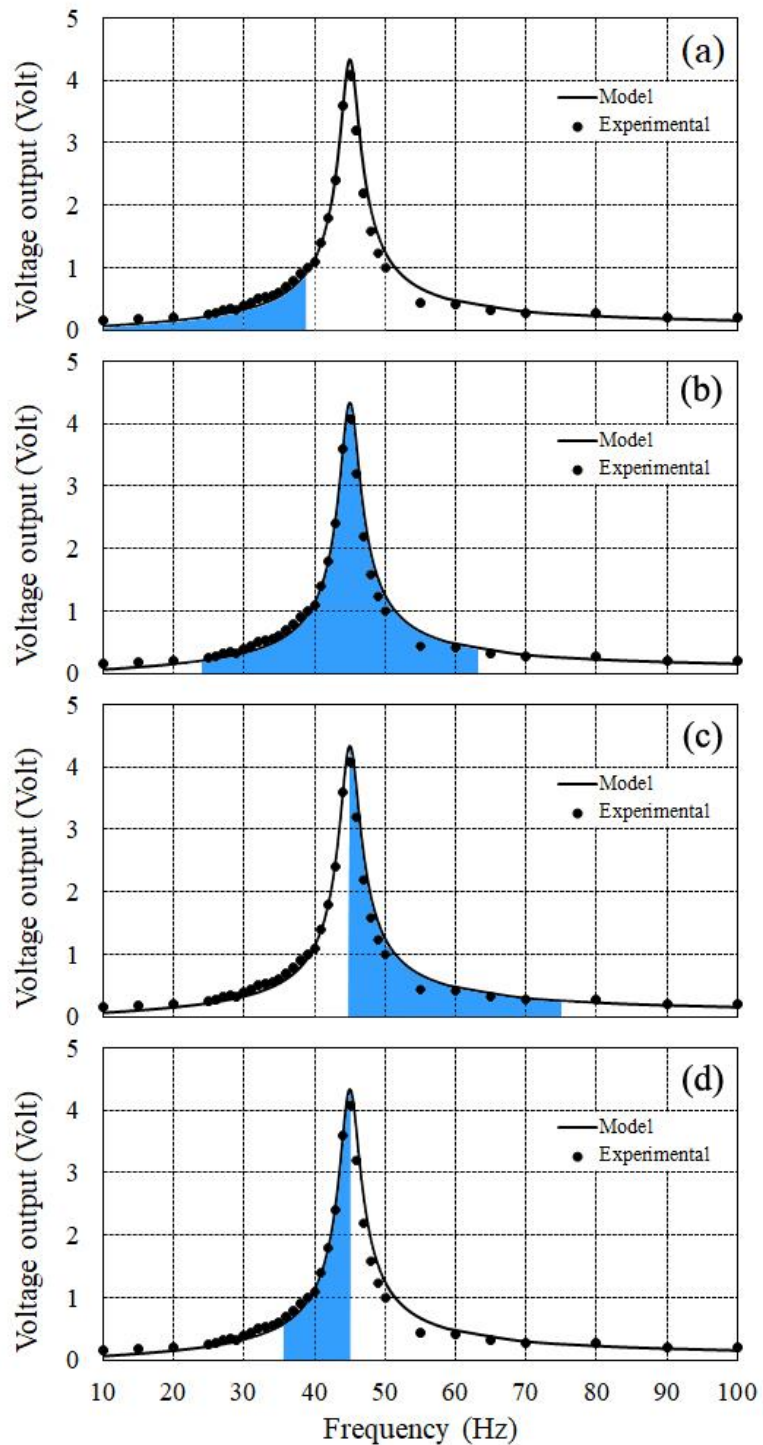
Figure 4.19 Voltage output by piezoelectric cantilever beams responding wind speed variations under applied controlling of β conditions (a) β=60°: (0.6 ≤ U ≤ 1.6), (b) β=45°: (1.2 ≤ U ≤ 2.0), (c) β=40°: (2.0 ≤ U ≤ 5.0), and β=24, (5.0 ≤ U), °.

To obtain the electrical efficiency conversion (η_{elec}), optimized resistances (R_{opt}) had been estimated by using equation (2.41). The maximum electrical power output with the variations of R shown that $R_{opt} \cong 100$ kΩ for 0.433 mW as presented in figure 4.20. The calculated the average value of U_{avg}, P_{mech}, δ_{elec}, η_{mech}, P_{elec}, η_{elec} and δ_{elec} were summarized in table 4.7.
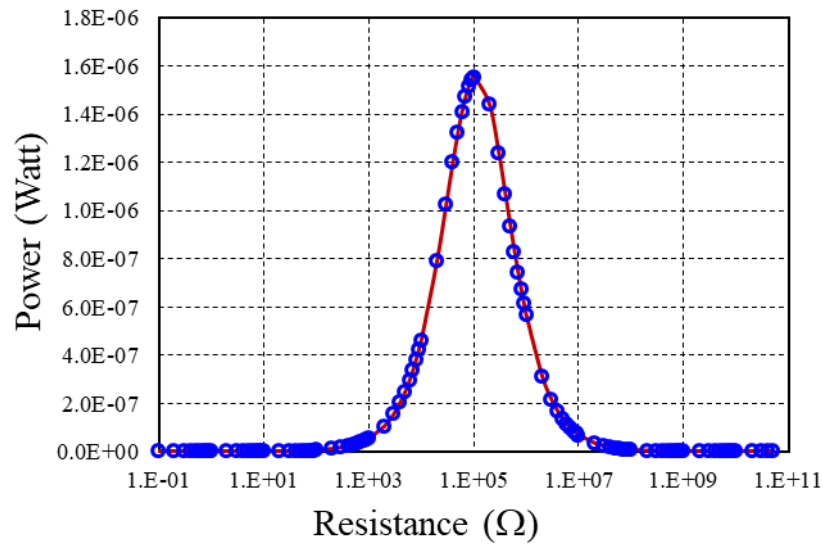
Figure 4.20 Modeling PZT-5A cantilever beam oscillation of generated powering output at R variation.

Table 4.7 Summarized average values of power, efficiency and loss in different regions.

Regions	$\overline{P}_w$ (W)	$\overline{P}_{mech}$ (mW)	$\overline{\delta}_{mech}$ (W)	$\overline{\eta}_{mech}$ (%)	$\overline{P}_{elec}$ (μW)	$\overline{\delta}_{elec}$ (mW)	$\overline{\eta}_{elec}$ (%)	C_p (%)
Region I	0.11	1.44	0.1086	2.5	3.41	1.4366	0.23	0.0250
Region II	0.48	4.02	0.4760	8.0	13.51	4.0065	0.34	0.1618
Region III	3.52	35.00	3.4850	10.0	12.14	34.9879	0.035	0.1220
Region IV	17.72	25.00	17.6950	1.4	13.72	24.9863	0.055	0.9732

4.4 Conclusions

The wind speed estimation for SABSS-HWTA was occupied by a work function of flow sensor YF-S201 based on Hall's effect principle. The standard calibration was approached by a digital anemometer TM-826, TECMAN. Four studied cases of wind speed power variation were performed. The detected signals by flows sensor YF-S201 and the measured of U data by TM-826 had been calibrated by a linear regression method.

Piezoelectric cantilever beam vibration acted like a generator unit for SABSS-HAWT energy harvester, four conditions of the beam length had been applied to the generated voltage output and the beam displacement. The results were strongly consistent with the resonance of LRC circuit model.

MCU was applied to SABSS-HAWT controlling system which separated four regions of wind speed conditions. High sensitivity (with the low speed of wind power); resonance behavior (which leading to maximum voltage power); high speed of the SABSS-HAWT rotation (which is the additional part by a dynamo available for future support), were the main reason to classify four conditions, corresponding to four regions of wind velocity.

The most advantage and a benefit of self-adjustable blades in this work is its capability to capture and convert the wind flow at a speed with U as low as 0.5 m/s.

CHAPTER 5

WIND ENERGY HEAVESTING IMPLIMENTATIONS

5.1 Literature of energy harvesting for wireless sensor network

Wind power energy harvesting by SABSS-HAWT was demonstrated as a monitoring system in a wireless sensor network described in the following sections. Webpage monitoring and mobile phone application monitoring were included.

5.1.1) Wireless sensor network

A wireless sensor network (WSN) is a network consisting of spatially distributed autonomous devices using sensors to monitor physical or environmental conditions. A WSN system incorporates a gateway that provides wireless connectivity as shown in figure 5.1. The selected wireless protocol depends on an application requirement. Some of available standards are 2.4 GHz radios based on IEEE 802.15.4, IEEE 802.11 (Wi-Fi) or individual radios which are usually 900 MHz.

Figure 5.1 WSN Components, gateway, and distributed nodes.

5.1.2) Low power WSN

A key to achieve longer lifetime for WSN is to design wireless sensor networks that minimize power consumption of wireless sensor devices, hence the name "low power". To cut down on overall power consumption, an active time or "awake time" of the devices (such as a radio or microcontroller) is controllable. This also limits the

current drawn when "sleeping". These can be accomplished by varying the power setting modes of the devices, such as "always on", "standby", or "hibernation" modes.

As an example, thinking about a basic remote temperature sensor collects data over a long period of time. In "active" mode, the device uses power to take temperature readings and to manipulate data using a sophisticated noise-filtering algorithm, but the device does not have to do this constantly. When not in active mode, the microcontroller can return to sleep mode until more sample measurements are taken. Then, at regular intervals, the Real-Time Clock and Calendar (RTCC) will wake up from sleep mode to see if there is another task to perform. If not, it will go back to sleep, conserving power usage. When the amount of time the microcontroller spends running is smartly managed and controlled, the overall amount of power consumption is drastically reduced.

A case of low power WSN in smart city is for monitoring the things such as parking, streetlights, traffic control, municipal transportation systems (buses), snow plowing, trash collection, and public safety. Data is collected from these devices, then interpreted into meaningful information to make informed decisions about allocating resources and delivering services.

5.1.3) Potential applications

WSN has been created applications for areas including health care, utilities, and remote monitoring. In health care, wireless devices make less invasive patient monitoring and health care possible. For utilities such as the electricity grid, streetlights, and water municipals, wireless sensors offer a lower-cost method for collecting system health data to reduce energy usage and better manage resources. Remote monitoring covers a wide range of applications where wireless systems can complement wired systems by reducing wiring costs and allowing new types of measurement applications. Remote monitoring applications include:

- Environmental monitoring of air, water, and soil
- Structural monitoring for buildings and bridges
- Industrial machine monitoring
- Process monitoring
- Asset tracking

5.1.4) WSN topologies

Since a WSN consists of several devices, network topologies have to be considered firstly the design topology. The most common network topologies are star, tree mesh or hybrid networks that combine the other ones. Each of these topologies presents its own set of challenges, advantages and disadvantages, as shown in table 5.1 and discussed below.

Table 5.1 Network topologies characteristics

Topology	Power usage	Communication range	Requires time synchronization
Star	Low	Short	No
Tree	Low	Long	Yes
Mesh	High	Long	No
Hybrid	Low (typically)	Long	Depends on configuration

(a)   (b)   (c)
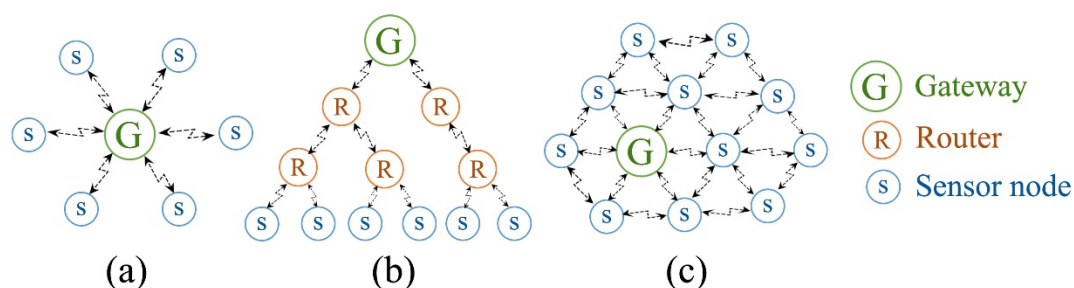
Figure 5.2 WSN of (a) star, (b) tree, and (c) mesh topologies

5.1.4.1) Star topology

A star topology, as shown in figure 5.2(a), is a single-hop system in which all nodes communicate bi-directionally with a gateway. This allows easy connection for small networks, but a hierarchical scheme with multiple subnet-works should be considered once a maximum number of nodes is reached. If a node fails in a star configuration, it does not affect other nodes, unless it is the central node that fails. The gateway can be a computer or a dedicated embedded device, and it acts both to communicate data and commands among nodes and to transfer data to an application or other network, such as the Internet. Nodes do not transmit data or commands to each other directly. They use the gateway as a coordination point where all data flow is concentrated. This topology is the lowest in overall power consumption but is limited by the transmission distance of 10 to 100 m.

5.1.4.2) Tree topology

In the tree topology, there are leaf nodes, relay nodes and parent nodes. This topology consists of a central node called the root node, and is the main communications router interfacing with other parts of a larger network. One level down from the root node in the hierarchy is a relay node that may have several children nodes connected to it and so on. An example of a tree network was shown in figure 5.2(b). This network configuration is designed to optimize power consumption and to extend the network communication range.

5.1.4.3) Mesh topology

This network topology connects each node to all the nodes within its radio range as shown in figure 5.3(c). It has the potential in reduction of power consumption for long distances. Each node can establish a radio link with the closest neighbors. However, the nodes are always waked up ready to be part of the path between any other node and the gateway.

5.1.4.4) Hybrid topology

A hybrid network consists of a combination of star and mesh topologies. This combination results on a star-mesh network that seeks to take advantage of the low power and simplicity of the star topology, as well as the extended range and self-healing nature of a mesh network topology. In this case, nodes serve to sense, extend the range of the network and provide fault tolerance.

5.1.5) Components of a WSN node

A WSN node contains several components, including the radio, battery, microcontroller, analog circuit, and sensor interface which need trade-offs. In battery-powered systems, higher radio data rates and more frequent radio consumes more power. Battery life time of three years is required, so many WSN systems today are based on Zig Bee due to its low-power consumption. The size and weight of batteries as well as shipping and availability are often concerned.

To extend battery life, a WSN node periodically wakes up and transmits data by powering on the radio and then powering it back off to conserve energy. WSN radio technology must efficiently transmit a signal and allow the system to go back to sleep with minimal power use. This means that the processor must also be able to wake, power up, and return to sleep mode efficiently. Microprocessor trends for WSNs include reducing power consumption while maintaining or increasing processor speed. Much like your radio choice, the power consumption and processing speed trade-off is a key concern when selecting a processor for WSNs. This makes the x86 architecture a difficult option for battery-powered devices.
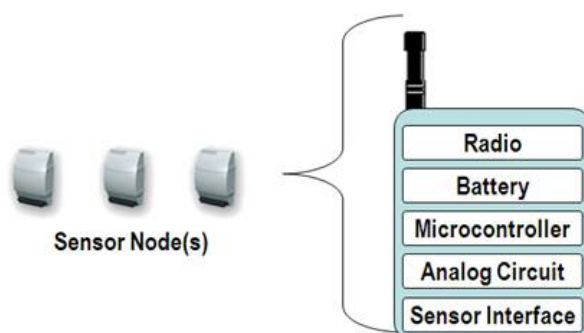

Figure 5.3 WSN sensor node components

5.2 Methodology

This section focuses on energy harvesting implementation for WSN. The designed energy harvesting for WSN monitoring application, which the components mentioned in section 5.1.4, were as shown in figure 5.3. For instead, the MCU had been under taken two roles communicated by sending the operating command and receiving the measured information data for transceiver, sensing, and harvester units. The MCU was received the measured wind speed data from wind speed estimator unit then sending pitch blades angles (β) provided position information corresponding to the previous investigated performance results in Chapter 4. Time delay of the measured data was defended in the controller unit by a user. The list of component devices for SABSS-HAWWT energy harvester of WSN implementation for the monitoring applications was in table 5.2.

Table 5.2 Components listed for SABSS-HAWWT implemented in WSN.

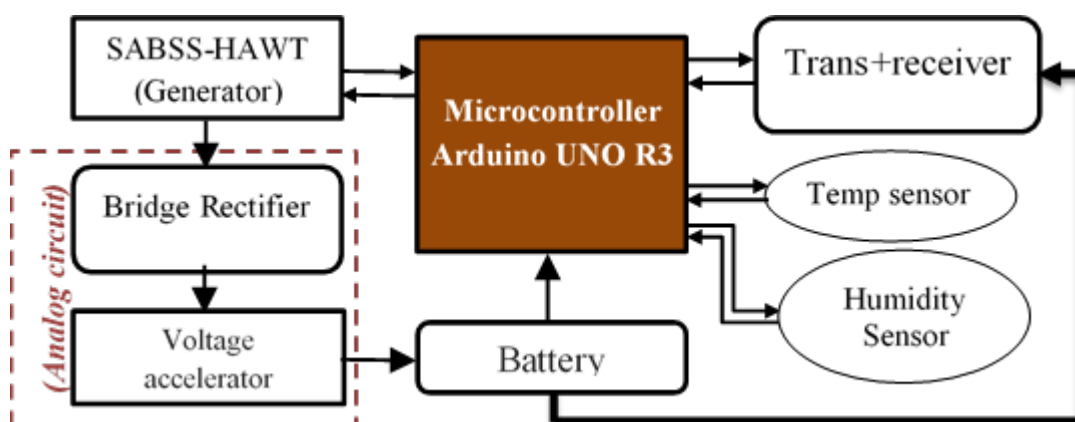| WSN component	Details
Power generator:	SABSS-HAWT
Analog circuit:	Regular bridge rectifier, electromagnetic coil with NPN-transistor: 2N-3904
Trans receiver (radio):	NodeMCU/ESP8266 version 2
Sensor:	DHT22; AM2302, temperature and humidity sensor module
Battery:	OKER model PB-569, 12000mAh, input: 5V/1A, output: 5V, 1A/2A
Microcontroller:	Arduino UNO R3

Figure 5.4 WSN node diagram for SABSS-HAWT energy harvesting implementation.

5.2.1) Analog circuit

The energy management using analog circuit is the combination of a regular bridge rectifier and an electromagnetic coil with NPN-transistor (2N-3904). To demonstrate the function of regular bridge rectifier and rectifier with magnetic coils of the circuitry for SABSS-HAWT energy harvester, NI-MultiSIM 14.0 was utilized as shown in figure 5.4(a) and 5.4(b), respectively. The SABSS-HAWT was exhibited as AC power generator, then AC voltage signal was converted to DC by the bridge rectifier circuit. Magnetic coil transformer with 1:10 turning ratio was combined with 2N-3904 NPN-transistor, series 1 kΩ resistor and parallel 50 µF capacitor.
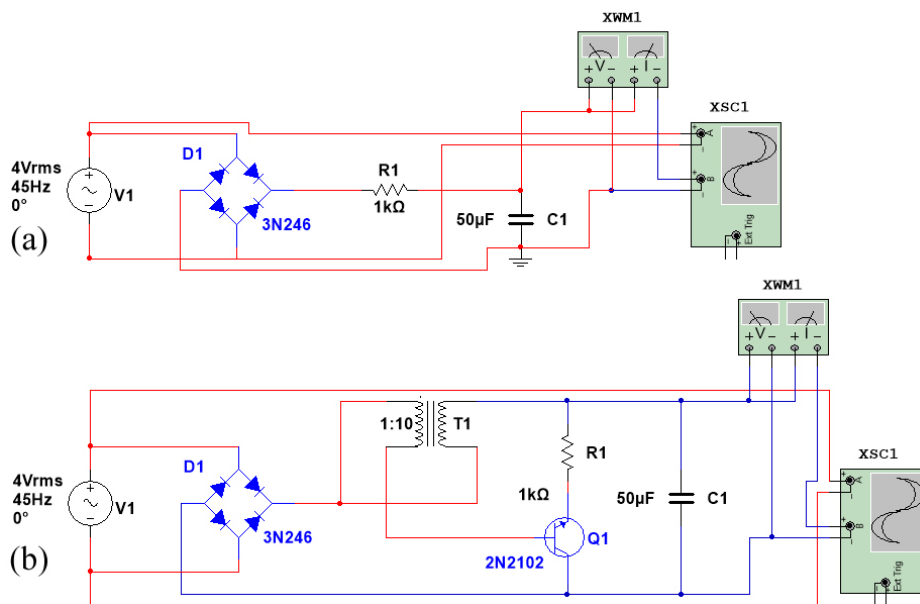
Figure 5.5 Energy management circuit for SABSS-HAWT energy harvester (a) rectifier, (b) rectifier added with magnetic coils and transistor.

5.2.2) Charging battery power

A voltage output generated by energy harvesting (*V*) must be higher than an input voltage of battery (V_b), Total charge and current (*I*) flow into the battery, the total charge and current flow into the battery are in accordance with equations (5.1), and (5.2), respectively; where *C* is the battery capacitance and *R* is the total resistance/impedance in the circuit. The voltage and current charging with time diagram were presented in figure 5.5.

$$Q = CV_b\left(1 - e^{-t/RC}\right) \qquad (5.1)$$

$$I = \frac{V_b}{R}\,e^{-t/RC} \qquad (5.2)$$
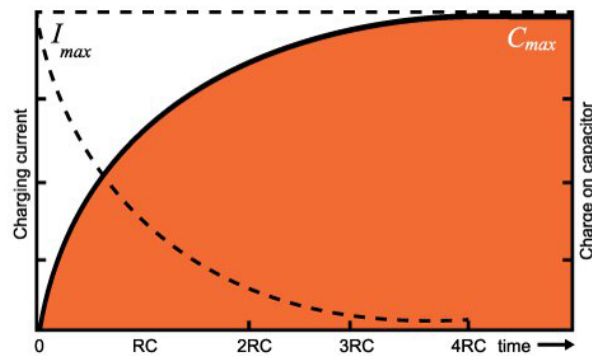
Figure 5.6 Battery charging with time diagram.

5.2.3) Wireless monitoring

To achieve the wireless monitoring data, DTH-22 and node MCU ESP8224 were together connected as shown in figure 5.6. The temperature and humidity sensor of DTH-22 were transmitted voltage signals varying to the detected of temperature and humidity level to node MCU. The ESP8224 contains a set of Transmission Control Protocol (TCP/IP) is used to communicate over the Internet: and including the processor (Microcontroller unit: MCU) for use in batch processing. To keep the device running follow to the proposal, it is necessary to generated commanding code. Then upload code that has the same structure a C++ to the memory of the MCU device. In this study were used Arduino IDE, V. 1.8.5 for the programming, and flows chart of the WSN monitoring is shown in figure 5.7.
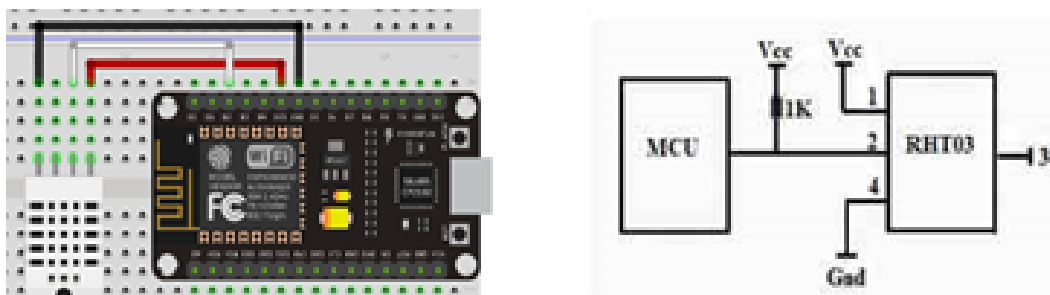
Figure 5.7 DTH-22 and MCU WiFi module ESP8224 configuration.
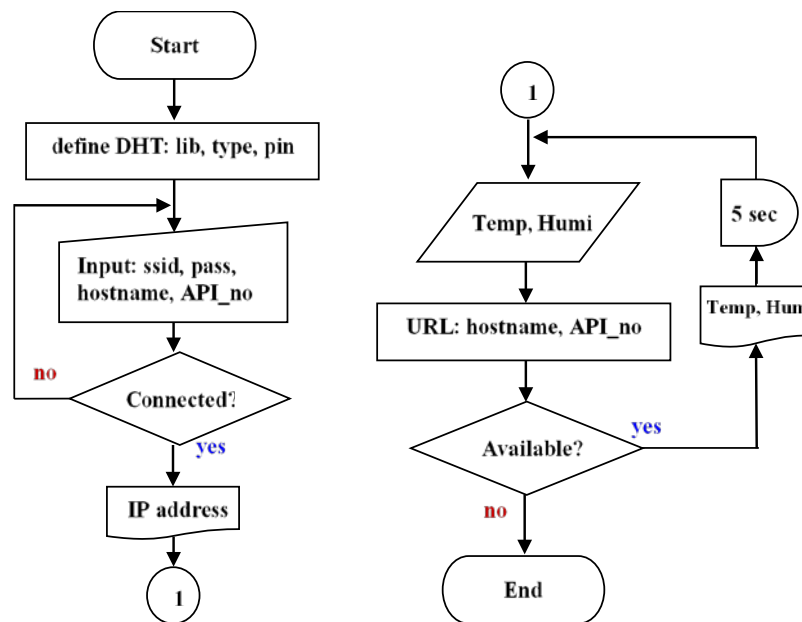
Figure 5.8 Flow chat of the programming for Trans/Receives monitoring data to WSN.

After the measured information data was transferred to a server, the sensing information was reported by two options, i.e. webpage or mobile application monitoring as described below.

5.2.3.1) Webpage monitoring: is related a one-way communication that only sending the real time of monitoring data to the network/server without any feedback interaction by user. There were backup collective database on clouds/network drive.

In this work the ThingSpeak was used as an Internet of Things (IoT) platform, allowing a collection and storage sensor data in the cloud and develop IoT applications. The ThingSpeak IoT platform provides applications for analyze and visualize the sensing data in MATLAB, and then act on the data. Sensor data can be sent to ThingSpeak from Arduino, Raspberry Pi, Beagle Bone Black, and other hardware. To handle this work function can be upload operating code to ESP8266 WiFi module, which it works independently from MCU. There capable MCU of web page monitoring code for ThingSpeak in this section were presented in Appendices B (II).

5.2.3.2) Mobile phone application monitoring: is related a two-way communication that sending the real time of monitoring of sensor data to the network/server. In the same time, this platform were support their real time commanding back to enable/disable functions for MCU by using the functional of mobile phone application. However, there were only real-time display the instant sensor data, it need to combined with another cloud platform for database management as cloud data storage.

In this work the Blynk was used as a Platform with I-OS and Android apps to control Arduino, Raspberry Pi and the likes over the Internet. It's a digital dashboard where the graphic interface on dashboard were generated by dragging and dropping widgets. Instead, it was supporting the variety of hardware such as Arduino or Raspberry Pi, there is linked to the Internet over Wi-Fi, Ethernet or new ESP8266 chip. Similarly to the webpage monitoring, there capable MCU of mobile monitoring code by Blynk application in this section were presented in Appendices B (II).

5.3 Results

5.3.1) Analog circuit

Assuming for 15 elements of piezoelectric cantilever beams were generated AC currents by voltage-peak of 4.4 volt which is comparison with the results in section 4.3.2 for each generator unit at resonance oscillation of 45 Hz. The results of NI-MultiSIM 14.0 circuit simulation of figure 5.4 were presented in figure 5.6. However, generated voltage by piezoelectric-generator had been achieved around 4 V (sinusoid; red line), the impedance loss by 4 diodes and resistor were decreased circuit' voltage that leading to the measured of $V = 675.7$ mV (blue line) and the observed currents related to 15.28 pW as shown in figure 5.8(a).

After magnetic coil transformer and 2N-3904 NPN transistor added into management circuit, there effort to increase the measured voltage to 22 volt, because of current (electrons) moving by helix motion in magnetic field. There were increased voltage transformer output corresponding to the turning ratio and magnetic flux density as described in Faraday's law of induction (Ulaby, 2007). The other reason of transformer is required, due to the voltage input of USB portable (battery) was higher than voltage of piezoelectric generator. The additional of 2N2102 transistor were occupied there increasing of current, which detected of powering of P about 447.0 nW by wattmeter as shown in figure 5.8(b).
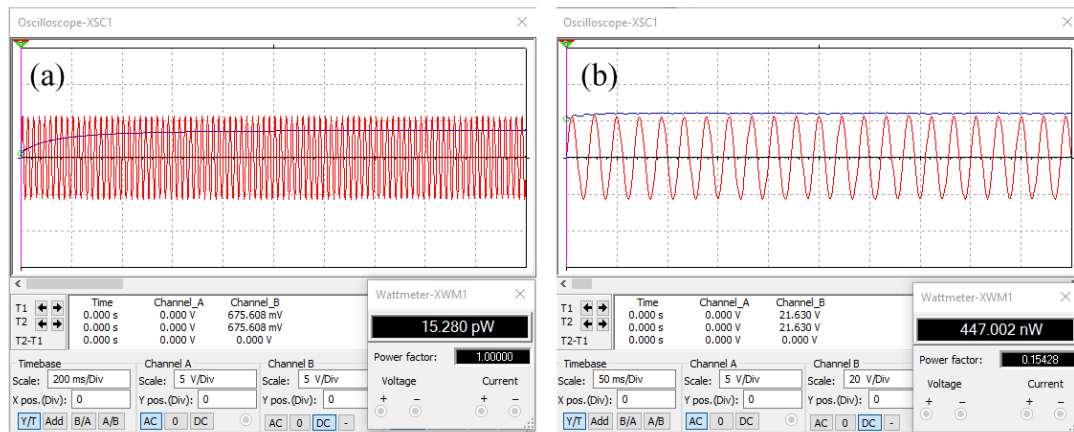
Figure 5.9 Measured (voltage and current) signals from analog circuit (a) regular bridge rectifier, (b) rectified by transformer with magnetic coil and transistor 2N2102.

5.3.2) Charging battery power

Referring to USB portable power bank of 5V with 12000 mAh specification indicated to power bank (battery) capacitance (*C*) of 8640 F, the generated powering by 15 pieces piezoelectric cantilever beams was 447×15 = 6.705 μW. So that substituted those related parameters into equation (5.1)-(5.2), were obtained voltage and currents charging to battery with time as presented in figure 5.7. Time (*t*) it take to charge this battery form 0 till its full is $18.242×10^6$ sec. or 211 days or 7 months.

However, fully changed state of battery before installation to WSN stations is the right choice, because we might setup the electrical consumption rate (by ESP8266) lower than the producing rate (by SABSS-HWTB). The electrical consumption of MCU ESP8266 WiFi module were presented in table 5.1.

Table 5.3 Electrical consumption of MCU ESP8266 WiFi module.

Mode	Energy consumption		Mode	Energy consumption
transmitting	135-215 mA		sleep	1 mA
receiving	60 mA		off	0.5 μA
Stand by	0.9 mA			

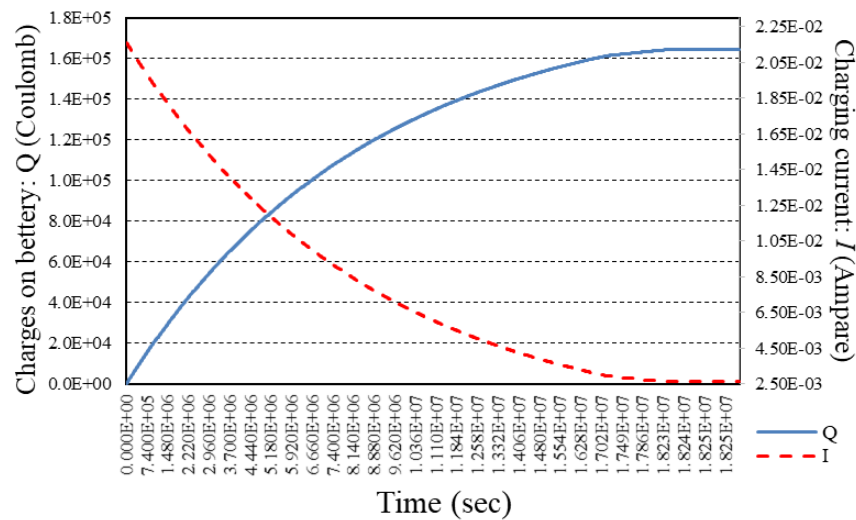**Figure 5.10** Charges on capacity and charging current with time for WSP of SABSS-HAWT energy harvesting.

5.3.3) Wireless monitoring

The harvested energy was accumulated into the battery and utilized as power supply for WSN node stations. Implementation of monitoring system by using wireless device as Node MCU ESP8224 and DTH‑22 sensor were utilized to Trans/receives sensing parameters as temperature and moisture. Trans/receives sensing informations testing results can be displayed via to the internet by the optional as describe bellows.

5.3.3.1) Web page monitoring

Measurable transmission testing results of temperature and humidity parameters vie internet and display on web page of ThingSpeak, the measured parameters was shown in figure 5.8(a). Moreover this platform supports mobile phone application of android and I-OS. Time delay of the transmitting data, which indicated to energy consumption rate, and it can defined by programing code corresponding to the energy production/consumption ratio.

5.3.3.2) Mobile phone applications monitoring

Measurable transmission testing results via internet to display on a mobile phone with Blynk's application had been established for real time monitoring. In addition, Blynk's application allowed the enable/disable transmission to node MCU for long-rang/global feedback controlling.

5.4 Conclusions

Although the generated electrical power (voltage and current) by piezoelectric cantilever beam vibrations are very low, transformer and amplifier were the optional to increase electrical power output. Magnetic coils act as voltage boosters to increases electrical potential by principle of current moving in magnetic field following to the Faraday's law. Increase in the voltage output depended on magnetic flux intensity and turning ratio. To amplify an electric current, a transistor configuration is applied in a circuit. Increase in a current depends on transistor types and multiplying number of transistor configurations.

On the other hand, there are ways to increases the electrical productivity such as:

- Addition of circular piezoelectric cantilever vibration beams parallelly in the rotor axis position.
- Combination the other type of the generator or technique which has higher efficiency, for example, high density dynamo, self-excitation generator, etc.

Environmental monitoring of air, water, and soil as well as in agriculture, farm industrial and other open air area are the main target for quality control. It can take place by SABSS-HAWT as a power supply for WSN node stations, because long distance wiring and costing for battery replacement were complicated. Another challenge for SABSS-HAWT implementation is energy consumption rate. In order to maintain work function of MCU the WiFi module is running continuously. This is achieved by controlling the energy consumption rate not to exceed the production rate by setting time delay for the sensing and transmission data. So the energy harvesting of SABSS-HAWT becomes a good candidate for WSN implementation of monitoring for quality control system.

CHAPTER 6

CONCLUSIONS

6.1) Summarization of the main conclusions

This thesis presents two types of materials which are PVDF polymer membrane and PZT-5A ceramics to act as a generator for fluid flows in piezoelectric energy harvesting implementation. Energy harvesting on fluid flow in this work was demonstrated experimentally and computationally. The developed systems are the "direct capture technique" where the polymer has been employed and the "captured device technique" based on the ceramics.

6.1.1) Using direct capture technique

The fluid flows energy harvesting experiment was conducted by flowing water in tube. The PVDF film works as a cantilever beam was attached on a rigid body along in the flow cannel. Mechanical beam oscillations had been generated by vortices induced vibration (VIV) effect of which the phenomena was describe by Re number. Oscillations of the vortices consist of lift force: F_L (vertical) and drag force: F_D (horizontal) was demonstrated by CFD simulation with COMSOL multi-physics. For the cases of "flow induced vibration" and "fluid structure interaction" studied by using Navier-Stokes and continuity equation. The results of the first case showed that FL increased with flow velocity (U) and increased diameter length (D). Frequencies of oscillating lift force (f_L) and drag force (f_D) were proportional to U, and inverse proportional with D. Similarly, the second case, F_D was proportional to U, and inverse proportional with U. The fluid structure interaction shows that the parameters indicated laminar, transition, and turbulence state following Re conditions which describe flow behavior. Not only a single frequency oscillation generated on the transition but also the turbulence state represented the vibrational mode of a given elastic beam. Moreover, the visual fluid velocity magnitude and the contour pressure equipotential line from CFD had been displayed for both F_L and F_D studied cases. Experimental results agreed well with the simulation of equivalent circuit model for PVDF oscillation by VIV effect at 0.6 Q/min, the voltage outputs were obtained for 1.3 mV, 0.23 Hz and 4.2 mV, 1.02 Hz.

6.1.2) Using captured device technique

Self-Adjustable Small Scale Horizontal Axis Wind Turbine (SABSS-HAWT) is a novel captured wind flow device of which the efficiency varied with wind power by adjustable attacking angle (β) of the blades related to changed wind speed. SABB-HAWT is consisted of three parts: estimator, capturing unit and controller which were designed by CAD and manufactured by a 3D printer. Turbulence state of the wind flow was estimated by Gaussian's distribution.

For the turbine performance parameters, the detected angular speed (ω) and acceleration (α) parameters were coincidentally agreed with CFA results which represented a net force direction acting on the blades. The turbine performance parameters are torque (Γ), power (P), and efficiency (η) which were at the maximum values when β was 45°.

For the controlling unit, the wind speed estimator was calibrated with a digital anemometer using a linear regression method. The vibrating PZT-5A system is working as an electric generator. The equivalent circuit model was strongly consistent with the experimental data of piezoelectric cantilever beam oscillation. The MCU received a wind speed signal from the estimator then processing them to define β potions varied in time driven by a servo. The program for operating of wind speed regions had been upload to MCU under conditions of cut-in velocity by 0.6<U<1.6 m/s and resonance frequency of cantilever oscillation by 1.6<U<2.0 m/s. Otherwise rating conditions were supported to the addition of dynamo generator at 2.0<U<7.0 m/s. The average harvested electrical power obtained from 15 pieces of piezo-oscillation in 'resonance' and 'rating' conditions were in the range of 3 mW. Finally, cut-off conditions for failure protection at U>7.0 m/s. The efficiency conversion (η) classified by mechanical (η_{mech}) and electrical conversion (η_{elec}) had been maximized at β of 45° for the given operating condition of the piezo-generator. The most advantage and a benefit of self-adjustable blades in this work is its capability to capture and convert the wind flow at a speed with *U* as low as 0.5 m/s.

6.1.3) Implementations

Implementations of fluid flow energy harvesting as the generator supplied to batteries for WSN application are possible although the harvested power was low due to the loss during the energy conversion processes. Webpage monitoring and mobile phone application monitoring were successfully demonstrated.

6.2 Future work

To improve SABSS-HAWT performance for the WSN application, future work may focus on the following issues:

6.2.1) The harvested efficiency

To increase the electrical power output, it can perform by multiplying the series of piezo-generator. The additional part would be replaced with dynamo generator which generated higher energy density than piezo-generator, it is a so-called "Hybrid generator".

To obtain the mechanical efficiency, it can be achieved by changing blade shape from thick to thin and long radius which expected to improve ω, and α parameters, leading to η_{mech} increased.

6.2.2) The management for WSN application

Increase in turning ration for magnetic coil and adding transistor configurations into management circuit is proposed here.

This research use the MCU WiFi-module for a Trans/receive unit. It is separated from the MCU for controlling unit which consumes more electrical consumption. Replacement by a Trans/receive module (without MCU) can reduce energy consumption for WSN application. On the other hand, increasing delay time for the data transition can also reduce energy consumption for WSN node. Furthermore, utilizing this technique in a large area should be investigated.

REFERENCES

Ahmad, M.A., Elshurafa, A.M., Salama, K.N. and Alshareef, H.N. (2012) Modeling of MEMS piezoelectric energy harvesters using electromagnetic and power system theories, Smart Materials and Structures, *20*(8): p. 12. DOI: https://doi.org/1 0.1088/0964-1726/20/ 8/085001.

Akaydin, H.D., Elvin, N., and Andreopoulos, Y. 2010. Energy harvesting from highly unsteady fluid flows using piezoelectric materials. Journal of Intelligent Material Systems and Structures. *21*(13): pp. 1263-1278. DOI: https://doi.org/ 10.1177/1045389X10366317

Allameh, S.M., Akogwu, O., Collinson, M., Thomas, J. and Soboyejo W.O., Piezoelectric generators for biomedical and dental applications: Effects of cyclic loading. Journal of Materials Science: Materials in Medicine. (2007), *18*(1): pp. 39–45. DOI: 10.1007/s108 56-006-0660-2.

Allen, J. J. and Smits, A.J. 2001. Energy harvesting eel, *Journal of Fluids and Structures* 15, pp. 629-640. doi:10.1006/j#s.2000.035

Amirtharajah, R., *Design of Low Power VLSI Systems Powered by Ambient Mechanical Vibration*, in *Department of Electrical Engineering*. 1999, Massachusetts Institute of Technology.

And`o, B., Baglio, S., Trigona, C., Dumas, N., Latorre, L. and Nouet, P. (2010) Nonlinear mechanism in MEMS devices for energy harvesting applications. Journal of Micromechanics and Microengineering, *20*(125020): p. 12. DOI: 10.10 88/0960-1317/20/ 12/125020

Baborowski, J. 2004. Microfabrication of piezoelectric MEMS. Journal of Electroceramics. *12*(1): pp. 33-51. DOI: 10.1007/0-387-23319-9_13

Batchelor, G.K. (1967). An Introduction to Fluid Dynamics. New York, NY: Cambridge University Press. ISBN 0-521-66396-2.

Bauer, S. and Bauer, F. (2008) Piezoelectric Polymers and Their Applications In Heywang, W., Lubitz, K. and Wersing, W. (Eds.), *Piezoelectricity*: *Evolution and Future of a Technology*. Series in Materials Science, *vol 144* (pp. 157-144). Springer International Publishing. DOI:10.1007/978-3-540-68683-5_6.

Beeby, S.P., Tudor M.J. and White, N.M. 2006. Energy harvesting vibration sources for microsystems applications. Measurement Science and Technology, *17*(12), pp. R175-R195.

Benaroya, R.D. and Gabbai, H. (2005) An overview of modeling and experiments of vortex-induces vibration of circular cylinders. Journal of sound and vibration. 282: pp.575-616. DOI: 10.1016/j.jsv. 2004.04.017.

Bernitsas, M.M., Raghavan, K., Ben-Simon, Y. and Garcia, E.M. (2008). VIVACE (Vortex Induced Vibration Aquatic Clean Energy): A New Concept in Generation of Clean and Renewable Energy from Fluid Flow. Journal of Offshore Mechanics and Arctic Engineering. *130*(4): p.15. DOI:10.1115/1.2 957913.

Betz, A., Das maximum der theoretisch möglichen ausnützung des windes durch windmotoren. Zeitschrift für das gesamte Turbinewesen, pp. 307–309, September 20, 1920.

Bhalla, S., Moharana, S., Kaur, N. and Talakokula, V. (2018) *Piezoelectric Materials: Aplication in SHM, Energy Harvesting and Biomechanics*. John Wiley & Sons. (pp. 352). ISBN: 1119265096, 9781119265092. Retrieved from http:// www.book.google.com/

Biadgo, A.M. and Aynekulu, G. (2017) Aerodynamic Design of Horizontal Axis Wind Turbine Blades. Faculty of Mechanical Engineering Transactions. *45*(4), pp.647-660. doi:10.5937/fmet1704647M

Bianchi. F.D., de Battista. H., Mantz, R.J. (2007) Wind Turbine Controlling Systems: Principle, Modeling and Gain Scheduling Desing, Springerpress, 208 p. ISBN: 978-1-84628-492-2, http://www.springer .com /978-1-84628-492-2.

Blevins, R.D. (1990) Flow-induced vibrations, New York: Van Nostrand Reinhold. ISBN 10:0442206518; 13:9780442206512.

Brown, D. 2008. Tracker, OSP Physics Style, June 2008, pp. 337-365.

Bulsara, A.R. and Gammaitoni, L. (1996) *Tuning in to noise*. *Physics Today*. *49*: pp. 39–45.

Carriveau, R. (2011) Fundamental and Advanced Topics in Wind Power, InTech, 422 p., ISBN 978-953-307-508-2.

Chiang, M.H., 2011. A novel pitch control system for a wind turbine driven by available-speed pump-controlled hydraulic servo system. Mechatronics 21, 753-761. https://doi.org/10.1016/j.mechatronics. 2011.01.003.

Cottone, F., Vocca. and Gammaitoni, L. (2009) Nonlinear Energy Harvesting, *Physical Review Letters.* 080601, p. 4. DOI: 10. 1103/ PhysRevLett. 102. 080601. Retrieved from https://pdfs.semantic scholar.org/1fd4/7133cd337fd9661865ff 8dc0a977baf 44492.pdf

Denmark: Gobal Wind Atlas. (November 27, 2017). Retrieved from https://global windatlas.info/

Digi-Key's European Editors. (2012, 28th March). Retrieved from http://www. digikey.com/en/articles/techzone/2012/mar/energy-harvesting-for-industrial-networking

Eiichi Fukada (2000) History and Recent Progress in Piezoelectric Polymers, IEEE transactions on ultrasonics, ferroelectrics, and frequency control; special issue, *47*(6); pp 1277- 1290.

Elfrink, R., Matova, S., De Nooijer, C., Jambunathan, M., Goedbloed, M., Van de Molengraft, J., Pop, V., Vullers, R.J.M., Renaud, M. and Van Schaijk, R., Shock induced energy harvesting with a MEMS harvester for automotive applications, 2011 International Electron Devices Meeting, (IEDM-2011), IEDM11: pp.677-680.

Erturk, A., Renno, J.M. and Inman, D.J., Modeling of Piezoelectric Energy Harvesting from an L-shaped Beam-mass Structure with an Application to UAVs. Journal of Intelligent Material Systems and Structures, 2008. *20*(5): p529-544. DOI: https://doi.org/10.1177/10 45389X0809809

Foster, F.S., Harasiewicz, K.A. and Sherar, M.D. (2000) A History of Medical and Biological Imaging with Polyvinylidene Fluoride (PVDF) Transducers, IEEE Transactions on ultrasonics, ferroelectrics, and frequency control, *47*(6); pp.1363-1371.

Gammaitoni, L. and Bulsara, A.R. (2002) Noise activated nonlinear dynamic sensors. *Physical Review Letters*. *88*: 230601.

Ghassoul, N. (2007) Multi-frequency piezoelectric power generator, Master Thesis, Universitete i Oslo. https://www.duo.uio.no/ bitstream/handle/10852/11250/ Ghassoul.pdf?sequence=1

Harrison, J.S. and Ounaies, Z. (2001) Piezoelectric Polymers (NASA/CR-2001-211422, ICASE Report No. 2001-43). Prepared for Langley Research Center under Contract NAS1-97046, ICASE NASA Langley Research Center Hampton, Virginia, USA.

142

Häsler, E., Stein, L. and Harbauer, G. (1984) Implantable physiological power supply with PVDF film. Ferroelectric, Section II: Applications to biomedical instrumentation. *60*(1): pp.277-282. DOI: https://doi.org/10.1080/0015019840 80 17528

Hau, E., and von Renouard, H., 2005. Wind Turbines: Fundamentals, Technologies, Application, Economics. Springer Berlin Heidelberg. ISBN 978-3-642-27151-9.

Hehn, T., Manoli, Y. (2015). Chapter 2: Piezoelectricity and Energy Harvester Modelling, *CMOS Circuit for Piezoelectric Energy Harvesters: Efficient Power Extraction, Interface Modeling and Loss Analysis.* (pp. 137). ISBN: 978-94-017-9287-5. Retrieved from http://www.springer.com/978-94-017-9287-5.

Heitzler, A.H. *An American National Standard: IEEE Standard on Piezoelectricity* (ANSI/IEEE STD 176-1987) New York, NY 10017, USA. Available online: http://ieeexplore.ieee.org/stamp /stamp.jsp? tp=&arnumber=26560

Hoang, D.C., Tan, Y.K., Chng, H.B. and Panda, S.K., Thermal energy harvesting from human warmth for wireless body area network in medical healthcare system, Power Electronics and Drive Systems, 2009. PEDS 2009: pp.1277-1282. DOI: 10.1109/PEDS.2009.5385 814

Hunt, J.F., Zhang, H., Guo, Z. and Fuc, F. (2013) Cantilever Beam Static and Dynamic Response Comparison with Mid-Point Bending for Thin MDF Composite Panels, BioResources, 8(1), pp. 115-129. https://www.fpl.fs.fed.us/documnts/p df2013/fpl_2013_hunt002.pdf

John D. Anderson, Jr., "Fundamentals of Aerodynamics", 3rd edition, McGrawHill, 2001.

Johnson, K., Wingerden, J.-W. Van, Balas, M.J., Molenaar, D.-P., 2011. Special issue on " Past, present and future modeling and control of wind turbines" . Mechatronics 21, 633. https://doi.org/10.1016/ j.mechatronics.2011.03.005.

Jordan, T.L. and Ounaies, Z. (2001). Piezoelectric Ceramics Characterization (NASA/CR-2001-211225, ICASE Report No. 2001-28). Prepared for Langley Research Center under Contract NAS1-97046, ICASE NASA Langley Research Center Hampton, Virginia, USA.

Kawai, H. (1969) The piezoelectricity of poly (vinylidene fluoride). Japanese Journal of Applied Physics, *8*(7):975. doi:10.1143/JJA P.8.975

Khameneifar, F., Arzanpour, S. and Moallem, M. (2013) A Piezoelectric Energy Harvester for Rotary Motion Applications: Design and Experiments. IEEE/ASME Transactions on Mechatronics, *18*(5): pp.1527-1534. DOI: 10.1109/TMECH.2012. 2205266

Kishorea, R. A. , Vučkovića, D. , Priya, S. , *Ultra- Low Wind Speed Piezoelectric Windmill*, Ferroelectrics, 2014. *460*(1), pp. 98-107. DOI: https://doi.org/10.10 80/ 00150193.2014.875315.

Kishore, R.A., Coudron, T., and Priya, S. (2014) Small-scale wind energy portable turbine (SWEPT). Journal of Wind Engineering and Industrial Aerodynamics, 116: pp. 21–31. http://dx.doi.org/10.1016 /j.jweia.2013.01.010.

Koyvanich, K., Smithmaitrie, P. and Muensit, N. (2015) Perspective microscale piezoelectric harvester for converting flow energy in water way, Advanced Materials Letters, *6*(6): pp. 538-543. DOI: 10.5185/amlett.2015.SMS4

Lallart, M., Garbuio, L., Petit, L., Richard, C. and Guyomar, D. 2008. Double synchronized switch harvesting (DSSH): a new energy harvesting scheme for efficient energy extraction. IEEE Transactions on Ultrasonics, Ferroelectrics, and Frequency Control. *55*(10): pp. 2119-2130. DOI: 10.1109/TUFFC.912.

Lanchester, F.W., A contribution to the theory of propulsion and the screw propeller. Trans. Institution of Naval Architects, Vol. XXX, p. 330, March 25, 1915.

Lefeuvre, E., Badel, A., Richard, C., Petit, L. and Guyomar, D. 2006. A comparison between several vibration-powered piezoelectric generators for standalone systems. Sensors and Actuators A. 126: pp. 405–416.

Lienhard, J.H. (1966) Synopsis of lift, drag, and vortex frequency data for rigid circular cylinders. [Bulletin] Washington: the Technical Extension Service, Washington state university.

Maheswari, R.U, and Tamilvendhan, J. 2012. Analysis of Modelling of Active Stall Controlled and Active Pitch controlled Variable Speed Wind Turbines, International Journal of Modern Engineering Research, *2*(4): pp. 2662- 2667. ISSN: 2249-6645

Martins, P., Lopes, A.C. and Lanceros-Mendez, S. (2014) Electroactive phases of poly (vinylidene fluoride): Determination, processing and applications, Progress in Polymer Science, *39*(4)" pp. 683–706. https://doi.org/10.1016/j.progpolymsci.2013.07.006.

Matiko, J.W., Grabham, N.J., Beeby S.P. and Tudor, M.J., Review of the application of energy harvesting in buildings. Measurement Science and Technology, 2013. *25*(1). DOI: https://doi.org/10.1088/0957-0233/25/1/012002.

Measurement Specialties, Piezo Film Sensors Technical Manual, Inc., P/N: 1005663-1, 1999. Web available URL: www.https:/www.spark fun.com/datasheets/Sensors/Flex/MSI-techman.pdf

Mineto, A.T. Braun, M.P.S., Navarro, H.A., and Varoto, P.S. (2010) Modeling of a cantilever beam for piezoelectric energy harvesting, 9th Brazilian Conference on Dynamic, Control and their Applications, DICON' 10: June 7-11, 2010, SP - ISSN 2178-3667.

Murayama, N., Nakamura, K., Obara, H. and Segawa, M. (1976) The strong piezoelectricity in polyvinylidene fluroide (PVDF), *14*(1): pp.15-24. DOI: https://doi.org/10.1016/0041-624X(76)90067-6.

Nechibvute, A.*, Akande, A.R. and Luhanga, P.V.C., (2011) Modelling of a PZT Beam for Voltage Generation, Journal of Adhesion Science and Technology, *19*(2): pp. 259-271, ISSN: 0128-7680, © Universiti Putra Malaysia Press. http://www.pertanika2.upm.edu.my/Pertanika%20PAPERS/JST%20Vol.%2019%20(2)%20Jul.%202011/6.pdf

Ottman, G.K., Hofmann, H.F., Bhatt, A.C. and Lesieutre, G.A. 2002. Adaptive piezoelectric energy harvesting circuit for wireless remote power supply. IEEE TRANSACTIONS ON POWER ELECTRONICS, *17*(5): pp. 669–676. DOI: 10.1109/ TPEL.20 02.802194.

Priya, S., *Advances in energy harvesting using low profile piezoelectric transducers.* Journal of Electroceramics, 2007. *19*(1): p. 165-182.

Priya, S., Chen, C.T., Fye, D., Zahnd, J., *Piezoelectric Windmill: A Novel Solution to Remote Sensing*, Japanese Journal of Applied Physics, 2004. *44*(2): pp. 1-7. DOI: https://doi.org/10.1143/JJAP.4 4.L104

Pobering, S. and Schwesinger, N. 2004. A novel hydropower harvesting device, Proceedings of the 2004 International Conference on MEMS, NANO and Smart Systems (ICMENS'04).

Power management – Linear Technology. Available online: http://www.linear.com/products/power_management (accessed on 2 March 2018).

Ragheb, M., (2013) Aerodynamic of rotor blades, Retrieved from https://pdfs.semanticscholar.org/cc14/9f9116ec01da06162a987b84ed93efba4cdf.pdf

Ragheb, M., (2014) Optimal rotor tip speed ratio, Retrieved from http://mragheb.com/NPRE%20475%20Wind%20Power%20Systems/Optimal%20Rotor%20Tip%20Speed%20Ratio.pdf

Renaud, M., Karakaya, K., Sterken, T., Fiorini, P., Van Hoof, C. and Puers., R. 2008. *Fabrication, modelling and characterization of MEMS piezoelectric vibration harvesters.* Sensors and Actuators A: Physical, 145-146: p. 380-386. DOI: https:// doi.org/10.1016/ j.sna.2007.11.005.

Roundy S (2003) Energy scavenging for wireless sensor nodes with a focus on vibration to electricity conversion. Dissertation, University of California at Berkeley. Available on https://pdfs.semanticscholar .org/5ce8/02253bb58dbff49de2d8bf6bbd76b4fde8b9.pdf

Roundy, S. and Wright, P.K. (2004) A piezoelectric vibration based generator for wireless electronics, Smart Materials and Structure, *2004*(13): pp. 1131-1142. http://iopscience.iop.org/0964-1726 /13/5/018

Ruan, L., Yao, X., Chang, Y., Zhou, L., Qin, G. and Zhang, X. (2018) Review: Properties and Applications of the Phase Poly(vinylidene fluoride) Polymers, 2018 (10): 228. doi:10.3390/polym10030228.

Sabah, N. (2008) Electric Circuits and Signals. New York, NY: Taylor and Francis. ISBN 9781420045895.

Sardini, E., Serpelloni, M., *Self-Powered Wireless Sensor for Air Temperature and Velocity Measurements with Energy Harvesting Capability*, IEEE Transactions on Instrumentation and Measurement, 2011. *6*(5): pp.1838-1844. DOI: 10.1109/TIM.2010.2 089090.

Servay R.A. and Jewett R.A. (2004) Physics for Scientists and Engineers, 6th edition. Retrieved from http://sciold.ui.ac.ir/~sjalali/book/ physics_serway.pdf

Shen, D., Park, J.H., Noh, J.H., Choe, S.Y., Kim, S.H., Wikle III, H.C. and Kim, D.J. 2009. *Micromachined PZT cantilever based on SOI structure for low frequency vibration energy harvesting.* Sensors and Actuators A: Physical, *154*(1): pp. 103-108. DOI: https://doi.org/ 10.1016/j.sna.2009.06.007.

Staworko, M. and Uhl, T. Modeling and Simulation of Piezoelectric Elements-Comparison of Available Methods and Tools. *Mechanics*, 2008, *27*(4), pp.161-171.

Swallow, L. M., Luo, J. K., Siores, E., Patel D. and Dodds, D., A piezoelectric fibre composite based energy harvesting device for potential wearable applications, Smart Materials and Structures, 2008, 17: 025017. DOI: https://doi.org/10.1088/0964-1726/17/2/02 5017.

Tan, Y.K. and Panda, S.K. (2010). Review of Energy Harvesting Technologies for Sustainable WSN, Sustainable Wireless Sensor Networks (pp.15-43). Yen Kheng Tan (Ed.), ISBN: 978-953-307-297-5, InTech, Available from: http://www.intechopen.com/books/ sustainable-wireless-sensor-networks/revie w-of-energy harvesting-technologies-for-sustainable-wsn.

Taylor, G.W., Burns, J.R., Kammann, S.M., Powers, W.B. and Welsh, T.R. 2001. The energy harvesting eel: a small subsurface ocean/river power generator. IEEE Journal of Oceanic Engineering, 26(**4**): pp. 539-547.

Telba, A. and Ali, W.G., Modeling and simulation of piezoelectric energy harvester, Proceeding of the World Congress on Engineering, London, U.K., Vol. II, 2012. (Conferences date: Tuesday, November 27, 2012). ISBN: 978-988-19252-1-3.

Tong, W. (2010) Chapter 1: Fundamental of wind energy; Wind Power Generation and Wind Turbine Design, WIT Transactions on State of the Art in Science and Engineering, WIT Press: vol. 44, pp. 3-48. ISSN: 1755-8336.

Ulaby, T.F. (2007). Fundamentals of applied electromagnetics (5th ed.). Pearson: Prentice Hall. p. 255. ISBN 0-13-241326-4.

Vinogradov, A and Holloway F. "Electro-Mechanical Properties of the Piezoelectric Polymer PVDF", Ferroelectrics, 226, pp. 169-181.

Wagner, J. (Photographer) (2014, October 21). *Visualisation of the Von Kármán vortex sheet behind a circular cylinder in air flow. The flow is made visible by means of the release of oil vapour near the cylinder* [digital image]. Retrieved from https://en.wikipedia.org/ wiki/Kármán_vortex_street.

Walters, T.S. (1967) The importance of diffusion along the mean wind direction for a ground-level crosswind line source, Atmospheric Environment, *3*(4): pp. 461-466. https://doi.org/10.1016/0004-6981 (69)90065-1

Wang, D. A. and Ko, H. H. 2010. Piezoelectric energy harvesting from flow-induced vibration, Journal of Micromechanics and Microengineering. *20*(2): 025019. DOI: https://doi.org/10.1088/09 60-1317/20/2/025019

Worthington, E. L. Techniques, Piezoelectric Energy Harvesting: Enhancing Power Output by Device Optimization and Circuit; Cranfield University: Bedford, UK, 2010. Available from: https://core.ac.uk/download/pdf/139679.pdf

Wolff, S., Jirasek, F., Beuermann, S. and Türk, M. (2015) Crystal phase transformation of α into β phase poly(vinylidene fluoride) via particle formation caused by rapid expansion of supercritical solutions, RSC Advances, 5; pp. 66644-66649. DOI: 10.1039/c5ra 12142f.

Xu, J., Dapino, M.J., Perez, D.G. and Hansford, D. (2009) "Microphone based on Polyvinylidene Fluoride (PVDF) micro-pillars and patterned electrodes", Sensors and Actuators A: Physical, *153*(1): pp. 24-32.

Yeatman, E. (2012.) Miniature Motion Energy Harvesters with Rotating Mechanisms [PowerPoint slides]. Available from http://www.nips lab.org/sites/nipslab.org / files/Yeatman% 20-% 20Miniature% 20Motion% 20EH.pdf (Accessed on Feb 20th, 2018)

Yi, J., Su, F., Lam, Y.H., Ki, W.H. and Tsui, C.Y. (2008) An Energy-Adaptive MPPT Power Management Unit for Micro- Power Vibration Energy Harvesting. *Proceeding on 2008 IEEE International Symposium on Circuits and Systems.* pp. 2570-2573. DOI: 10.1109/ISCAS.2008.4541981

APPENDICES

APPENDIX A

EXPERIMENTAL RESULTS

APPENDIX A (I)

WIND SPEED MEASUREMENT
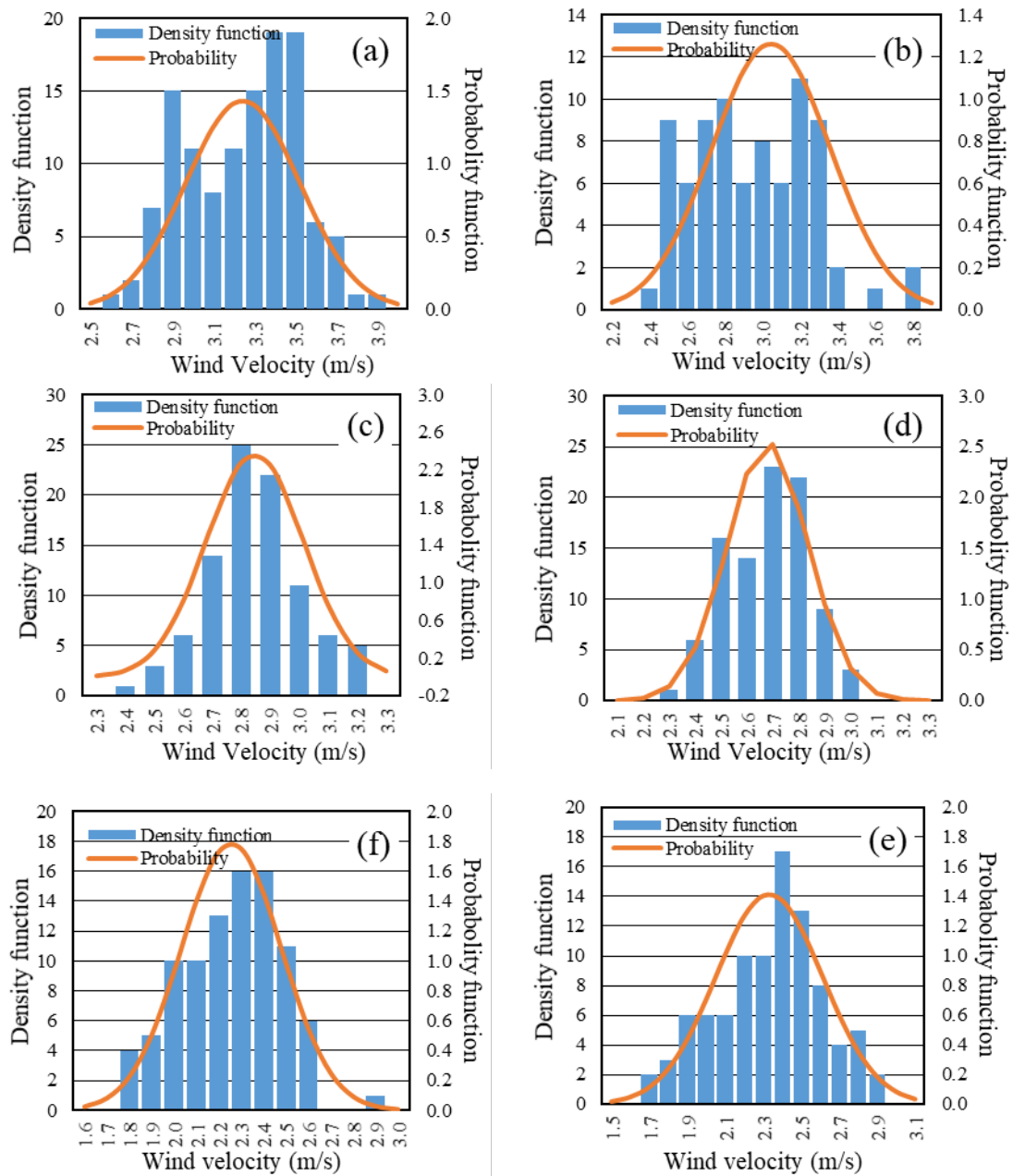
Figure A (I)-1 Density function and probability distribution of wind speed at the distance L of (a) 0.18 m, (b) 0.48 m, (c) , 0.78 m (d) 1.08 m, (e) 1.38 m, and (f) 1.68 m.
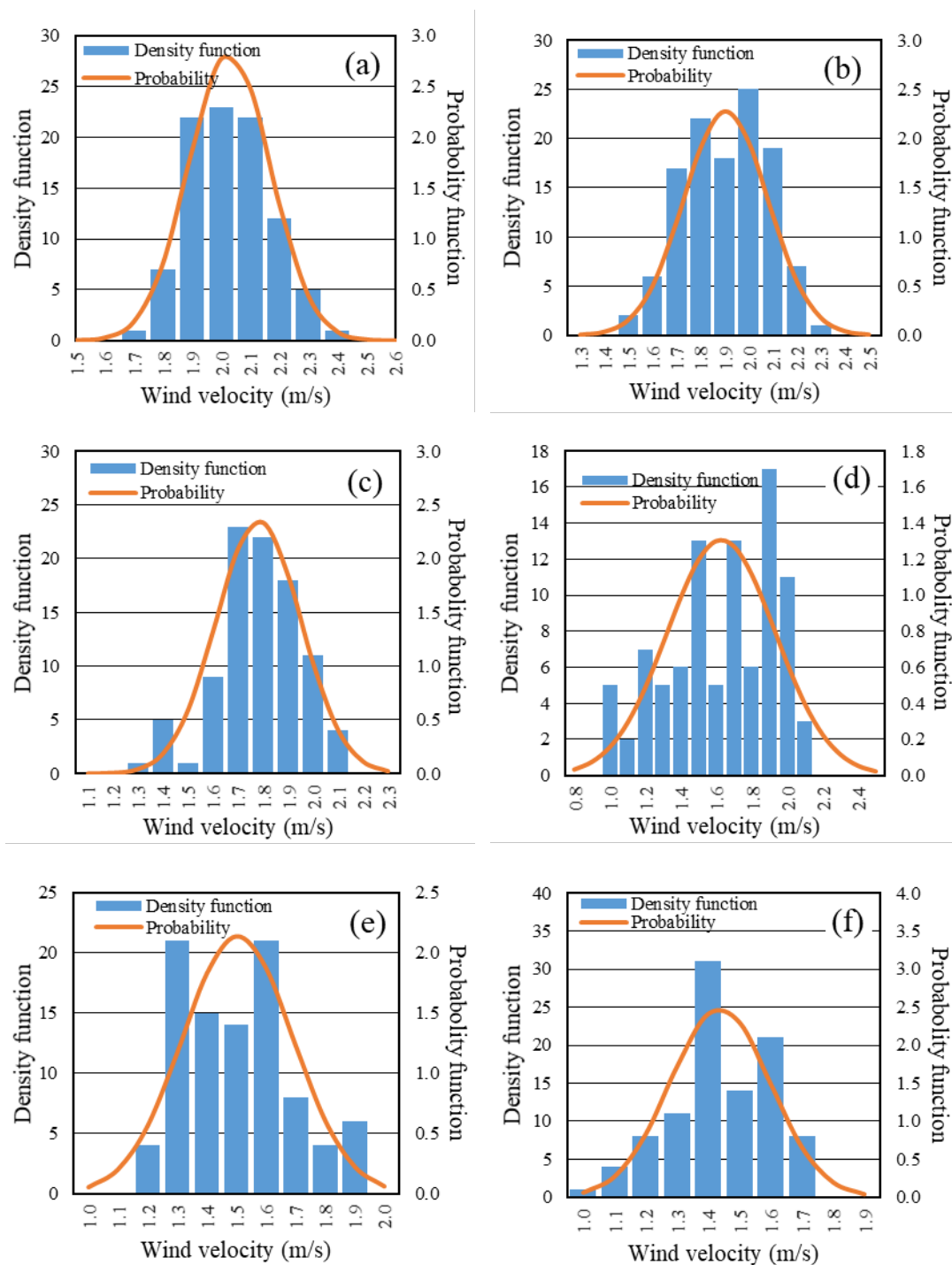
Figure A (I)-2 Density function and probability distribution of wind speed at the distance L of (a) 1.98 m, (b) 2.28 m, (c) 2.58 m, (d) 2.89 m, (e) 3.18 m, and (f) 3.48 m.
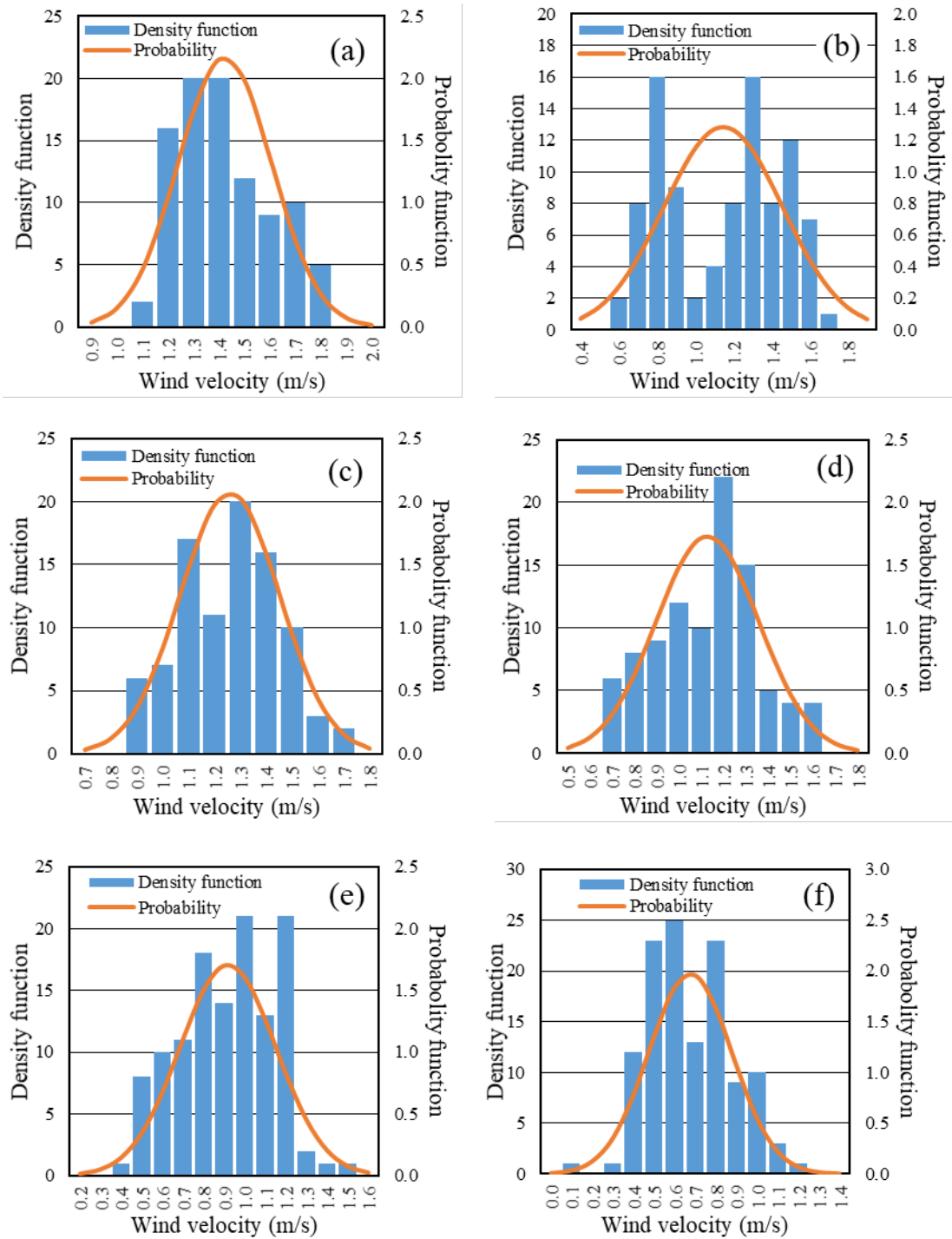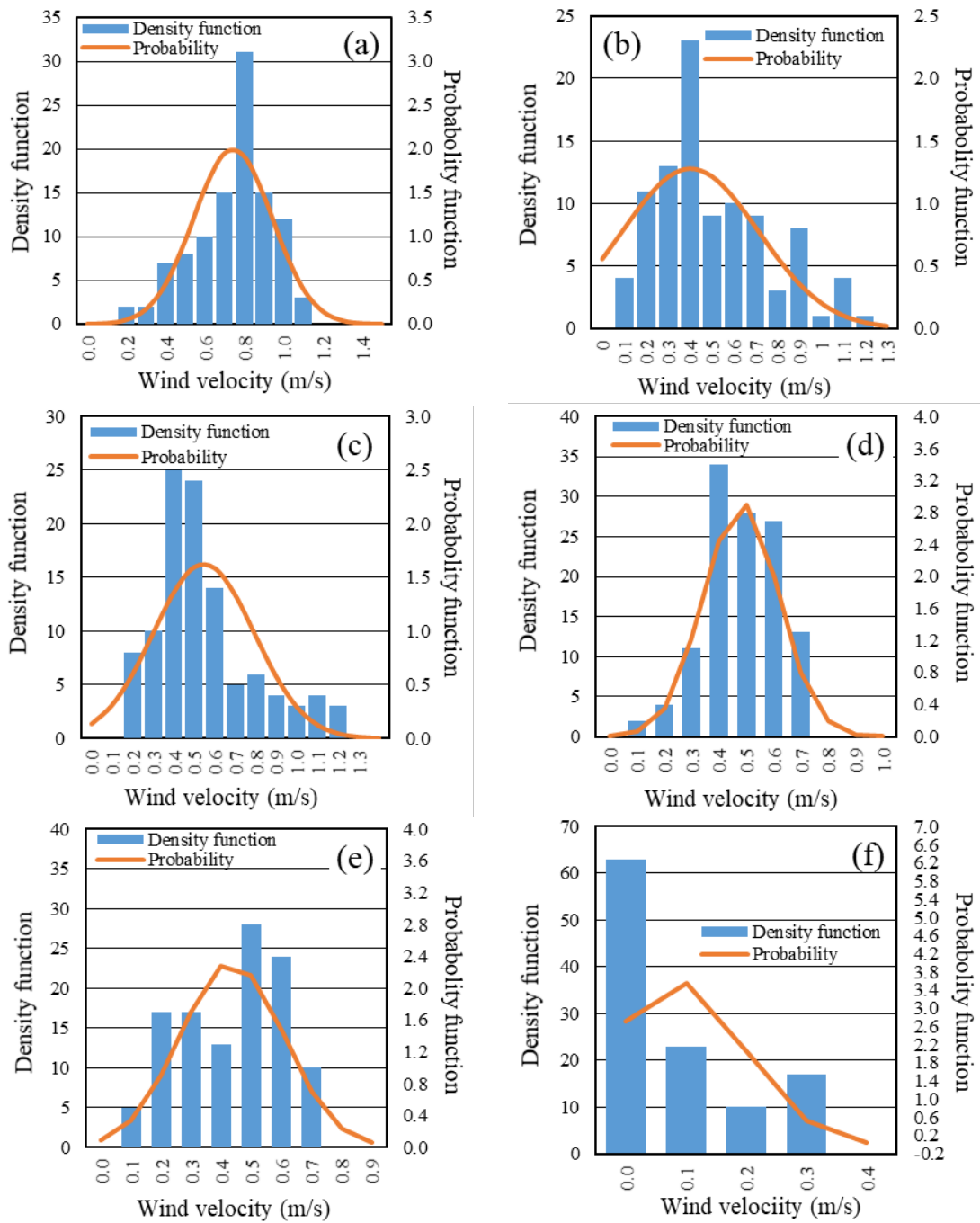
Figure A (I)-3 Density function and probability distribution of wind speed at the distance L of (a) 3.78 m, (b) 4.08 m, (c) 4.38 m, (d) 4.68 m, (e) 4.98 m, and (f) 5.28 m.

Figure A (I)-4 Density function and probability distribution of wind speed at the distance L of (a) 5.58 m, (b) 5.88 m, (c) 6.18 m, (d) 6.48 m, (e) 6.78 m, and (f) 7.08 m.

APPENDIX A (II)

ANGULAR SPEED ESTIMATION
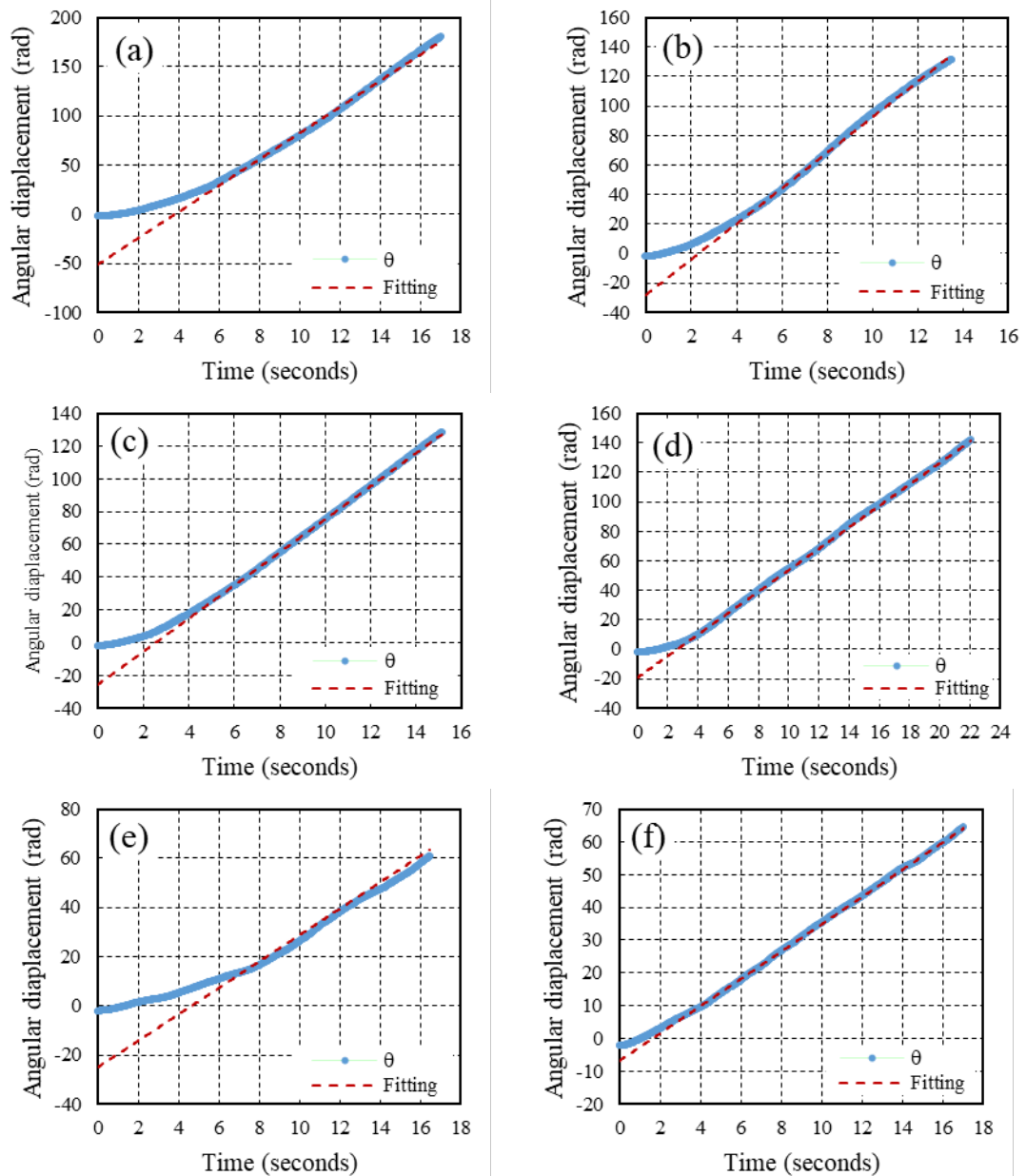
Figure A (II)-1 Linear plot by measurable data of angular displacement (θ) with time variation for angular speed estimation, β=24° at the distance L of (a) 0.18 m, (b) 0.48 m, (c) 0.78 m, (d) 1.08 m, (e) 1.38 m, and (f) 1.68 m.
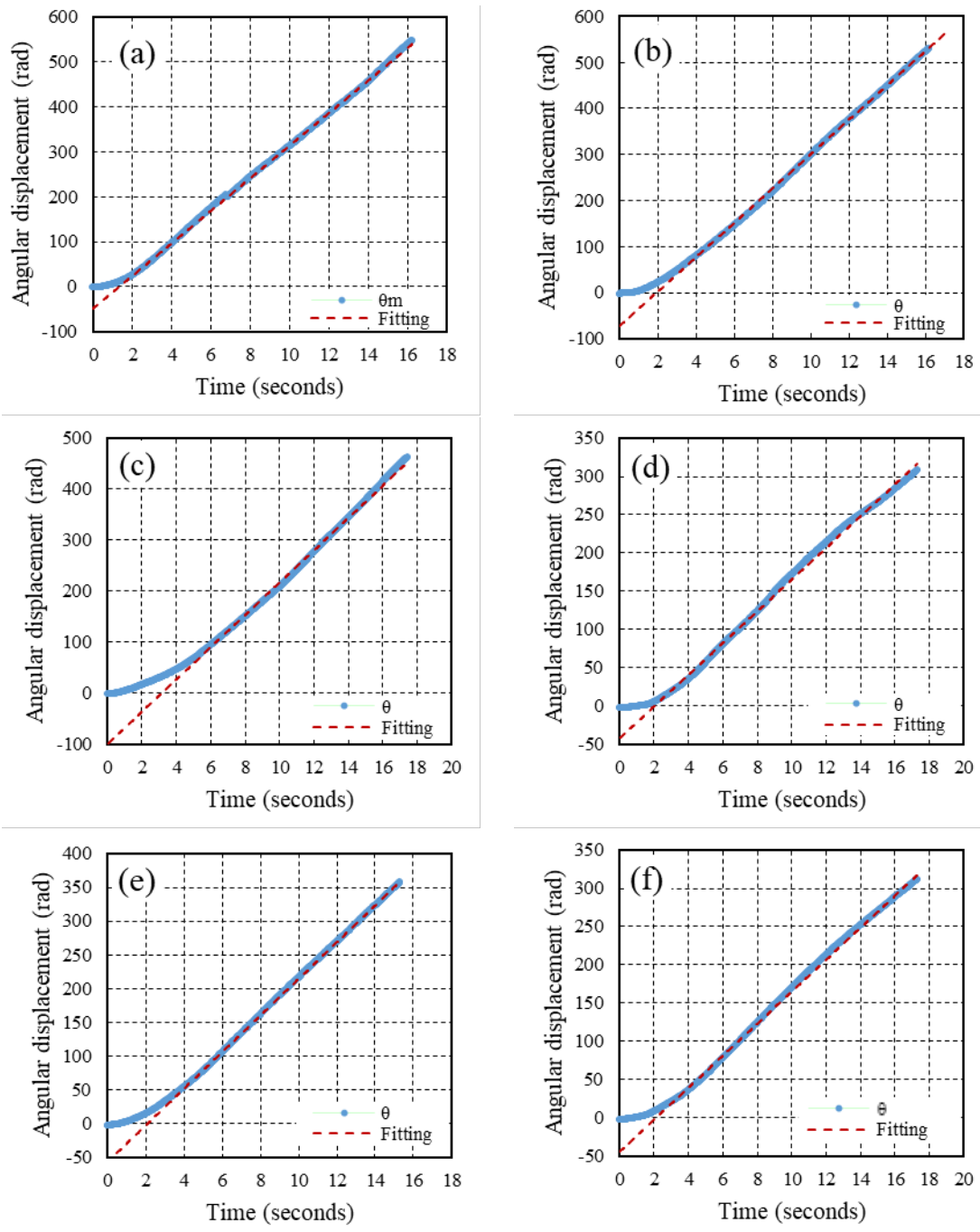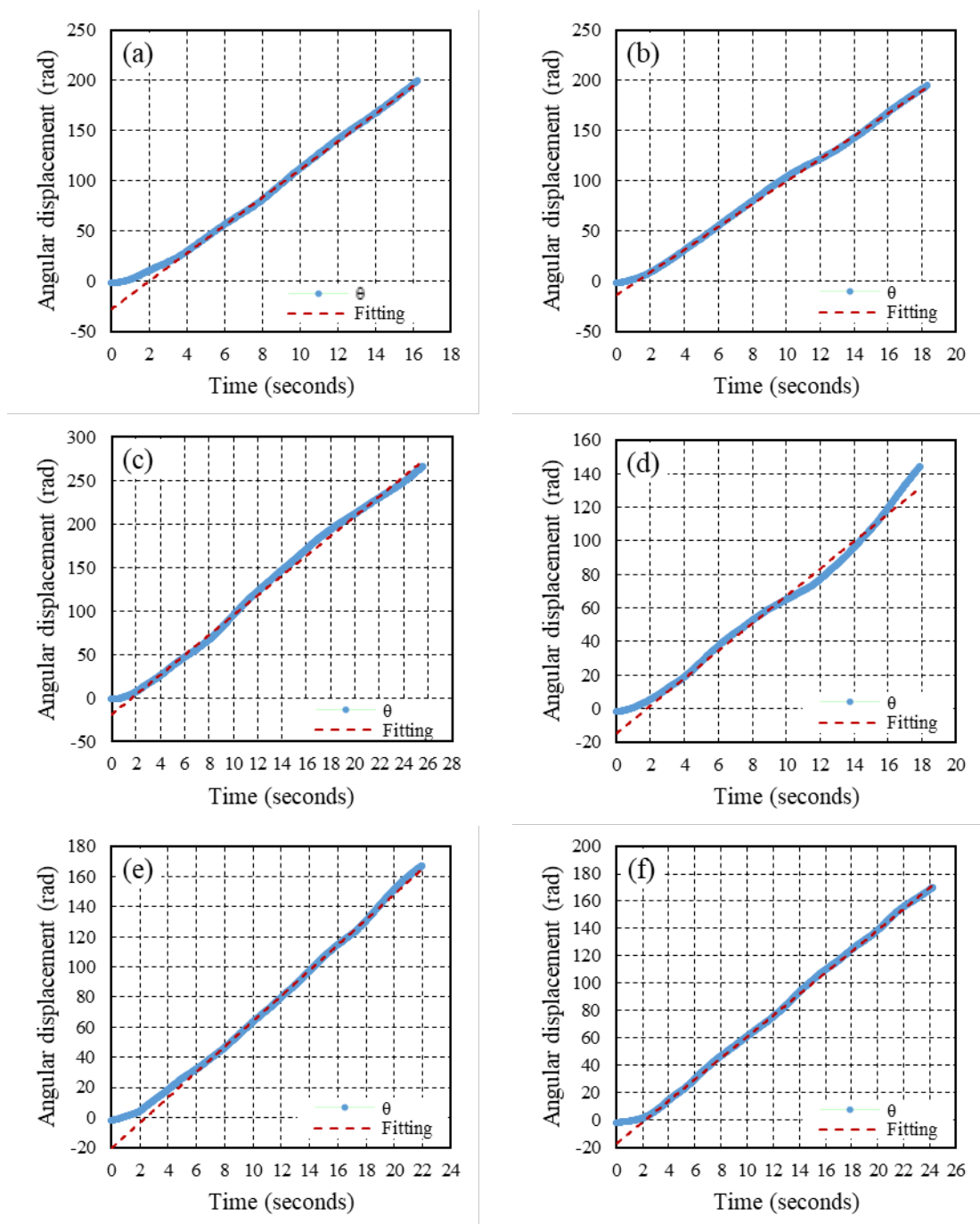
Figure A (II)-2 Linear plot by measurable data of angular displacement (θ) with time variation for angular speed estimation, β=40º at the distance L of (a) 0.18 m, (b) 0.48 m, (c) 0.78 m, (d) 1.08 m, (e) 1.38 m, and (f) 1.68 m.

Figure A (II)-3 Linear plot by measurable data of angular displacement (θ) with time variation for angular speed estimation, β=40° at the distance L of (a) 1.98 m, (b) 2.28 m, (c) 2.58 m, (d) 2.88 m, (e) 3.18 m, and (f) 3.48 m.
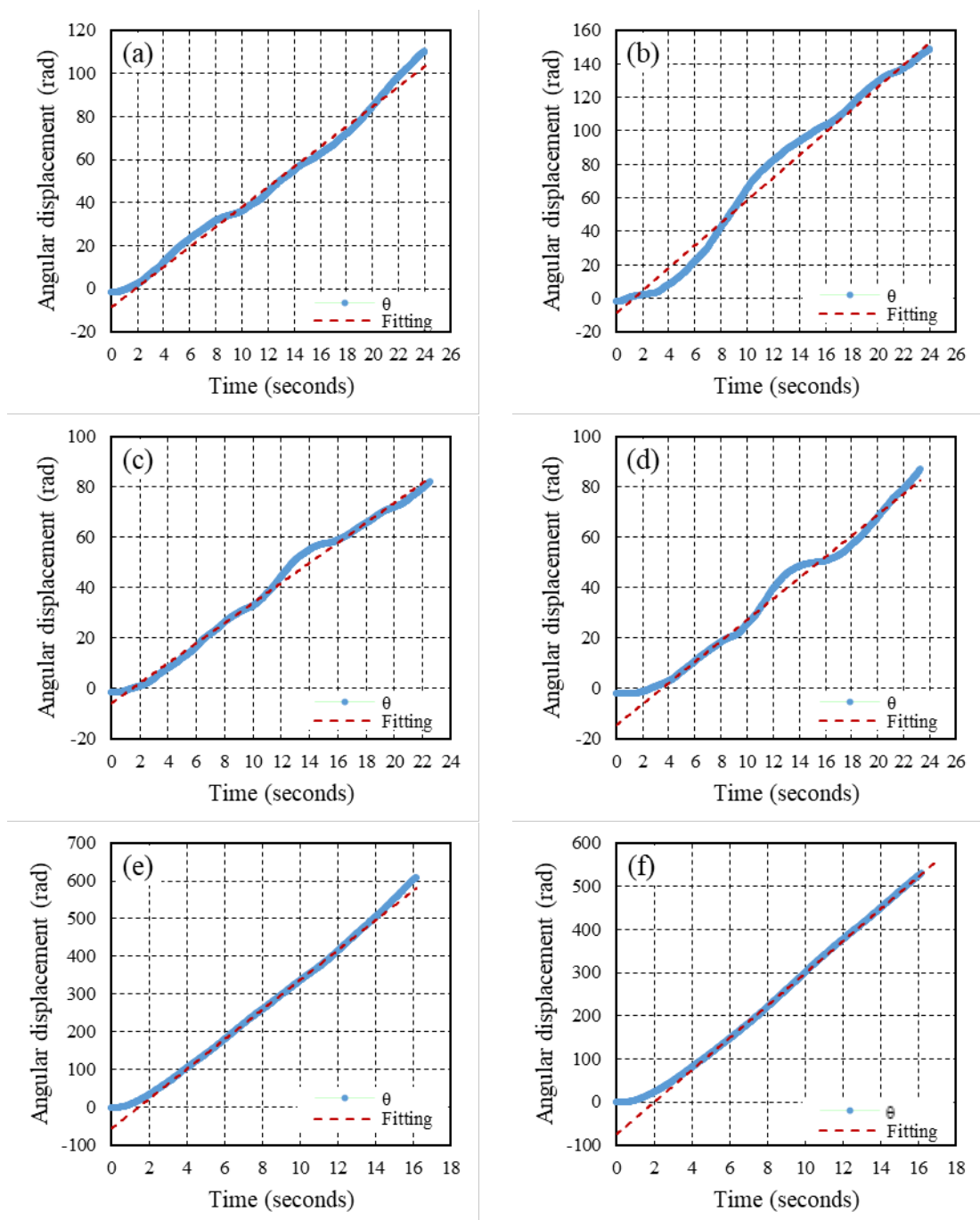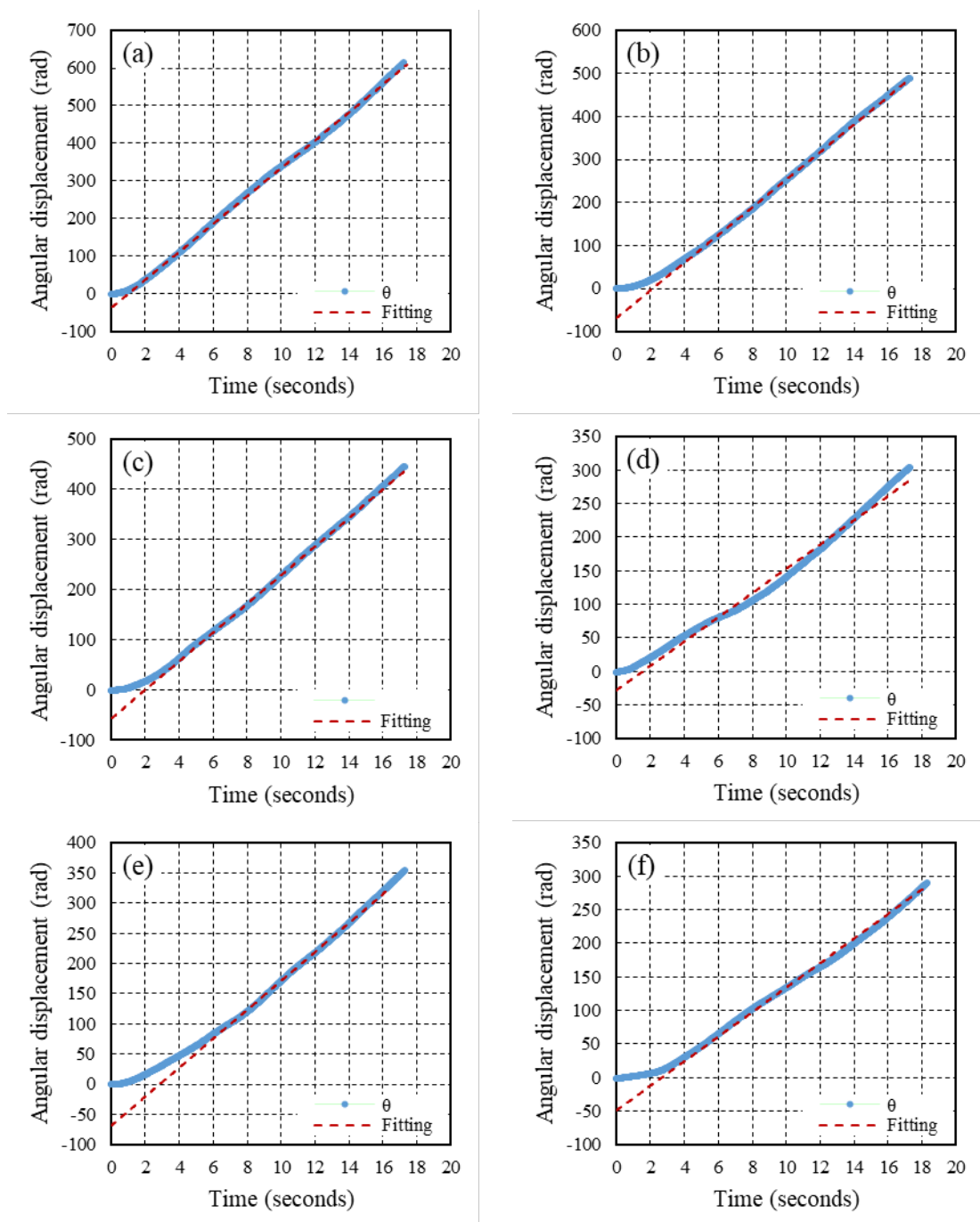
Figure A (II)-4 Linear plot by measurable data of angular displacement (θ) with time variation for angular speed estimation, β=40º at the distance L of (a) 3.88 m, (b) 4.08 m, (c) 4.38 m, and (d) 4.68 m; β=45º at the distance L of (e) 0.18 m, (f) 0.48 m.

Figure A (II)-5 Linear plot by measurable data of angular displacement (θ) with time variation for angular speed estimation, β=45° at the distance L of (a) 0.78 m, (b) 1.08 m, (c) 1.38 m, (d) 1.68 m, (e) 1.98 m, and (f) 2.28 m.

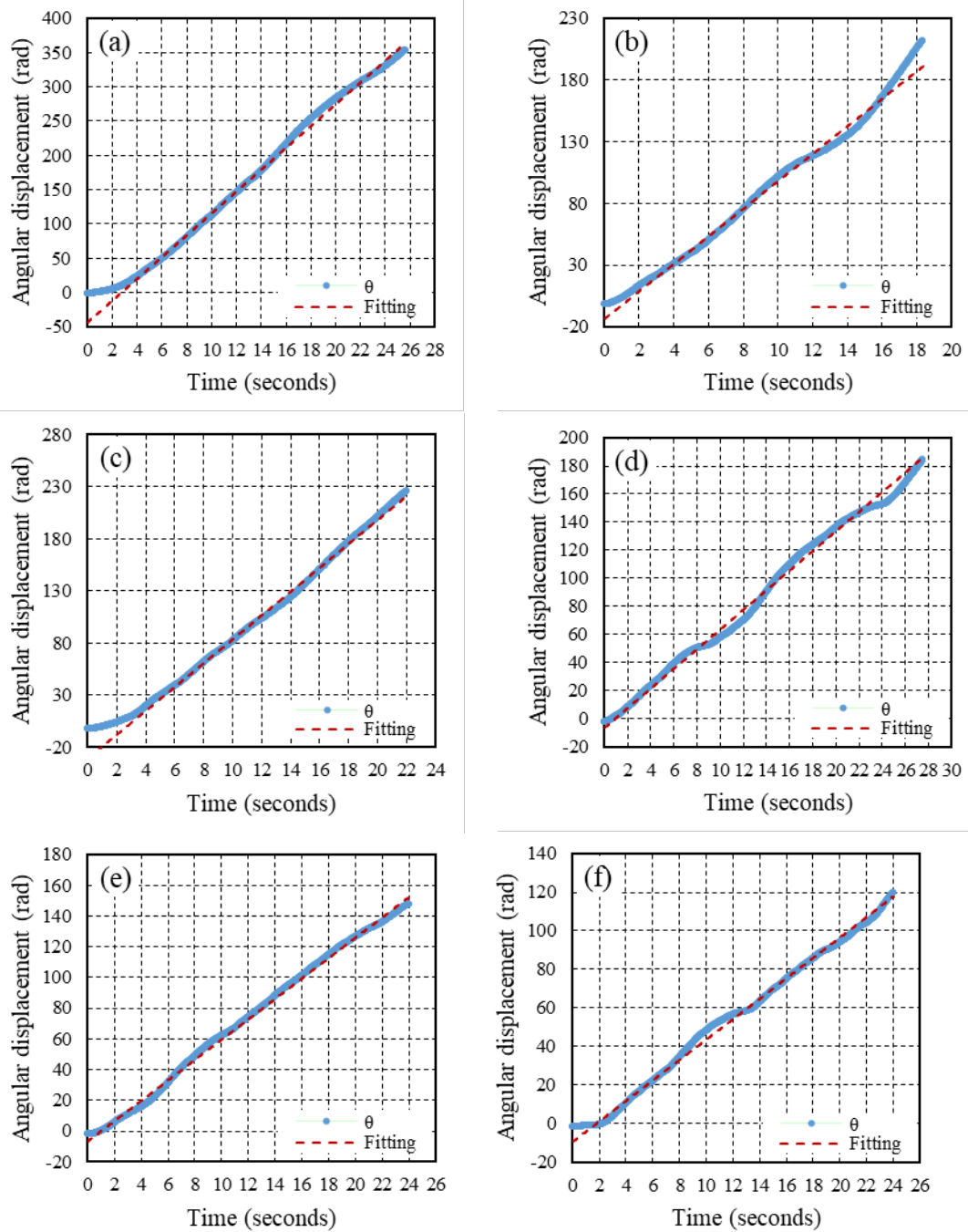**Figure A (II)-6** Linear plot by measurable data of angular displacement (θ) with time variation for angular speed estimation, β=45º at the distance L of (a) 2.58 m, (b) 2.88 m, (c) 3.18 m, (d) 3.48 m, (e) 3.78 m, (f) 4.08 m.

160

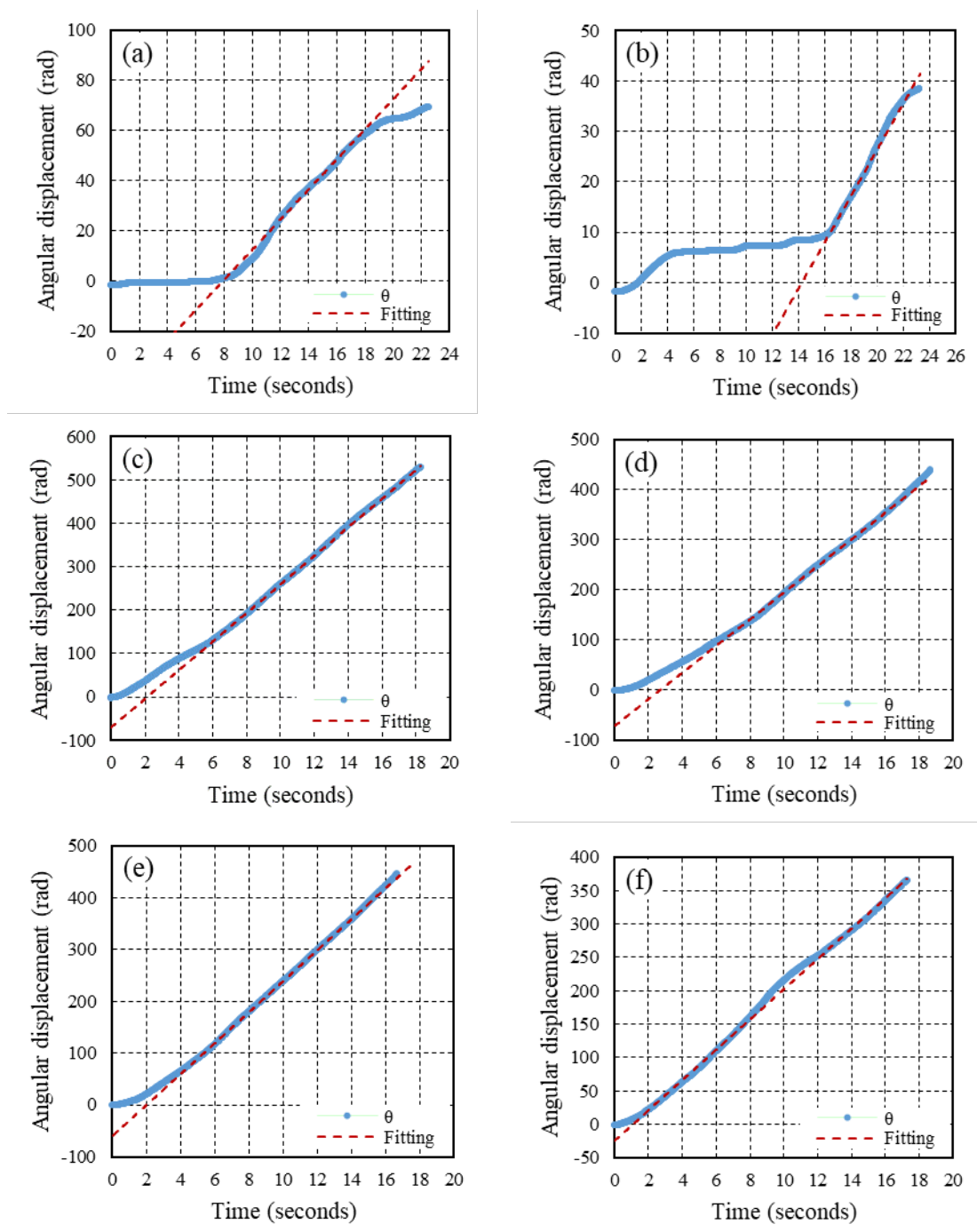**Figure A (II)-7** Linear plot by measurable data of angular displacement (θ) with time variation for angular speed estimation, β=45° at the distance L of (a) 4.38 m, (b) 4.68 m; β=60° at the distance L of (c) 0.18 m, (d) 0.48 m, (e) 0.78 m, and (f) 1.08 m.
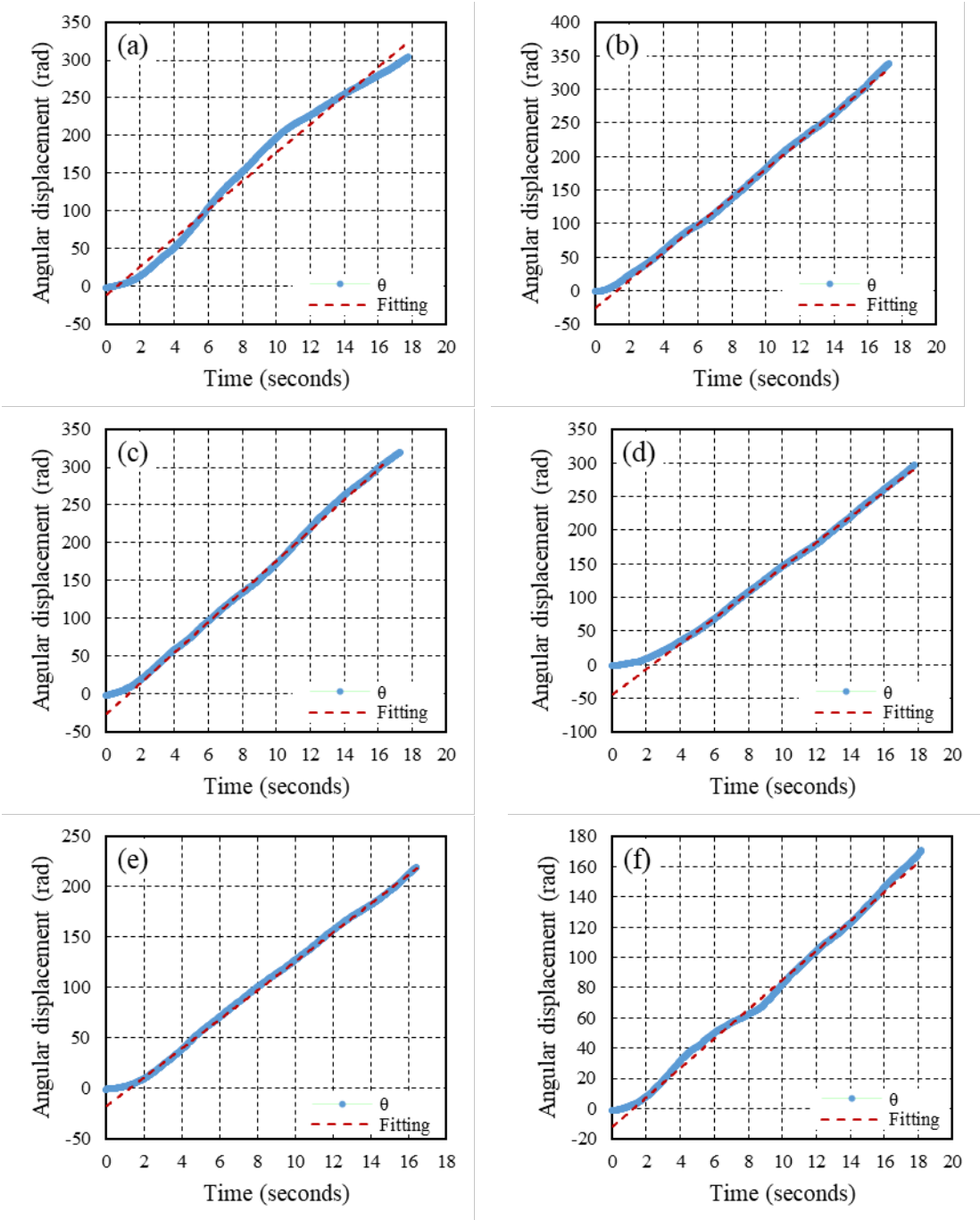
Figure A (II)-8 Linear plot by measurable data of angular displacement (θ) with time variation for angular speed estimation, β=60° at the distance L of (a) 1.38 m, (b) 1.68 m, (c) 1.98 m, (d) 2.28 m, (e) 2.58 m, (f) 2.88 m.
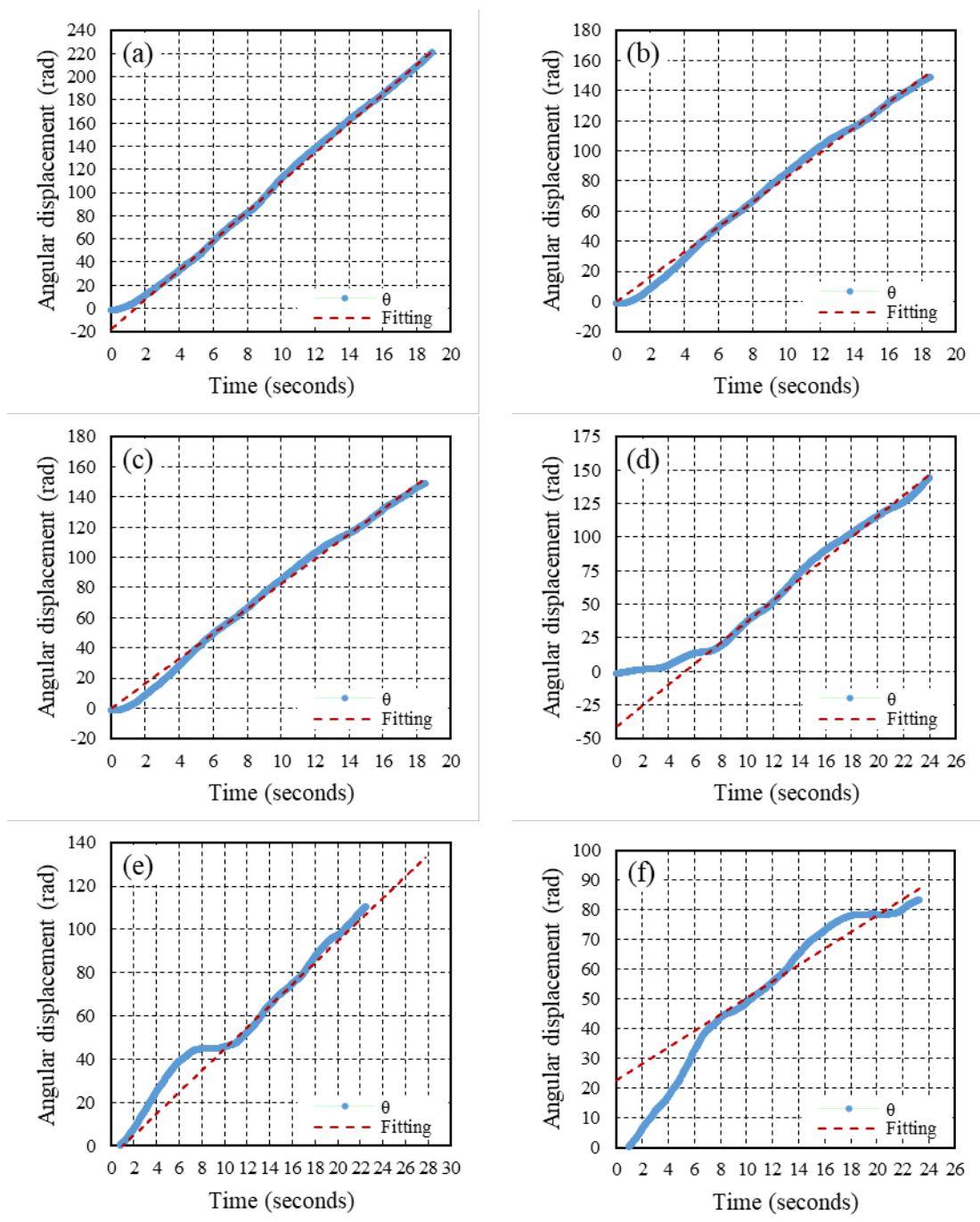
Figure A (II)-9 Linear plot by measurable data of angular displacement (θ) with time variation for angular speed estimation, β=60º at the distance L of (a) 3.18 m, (b) 3.48 m, (c) 3.78 m, (d) 4.08 m, (e) 4.38 m, (f) 4.68 m.
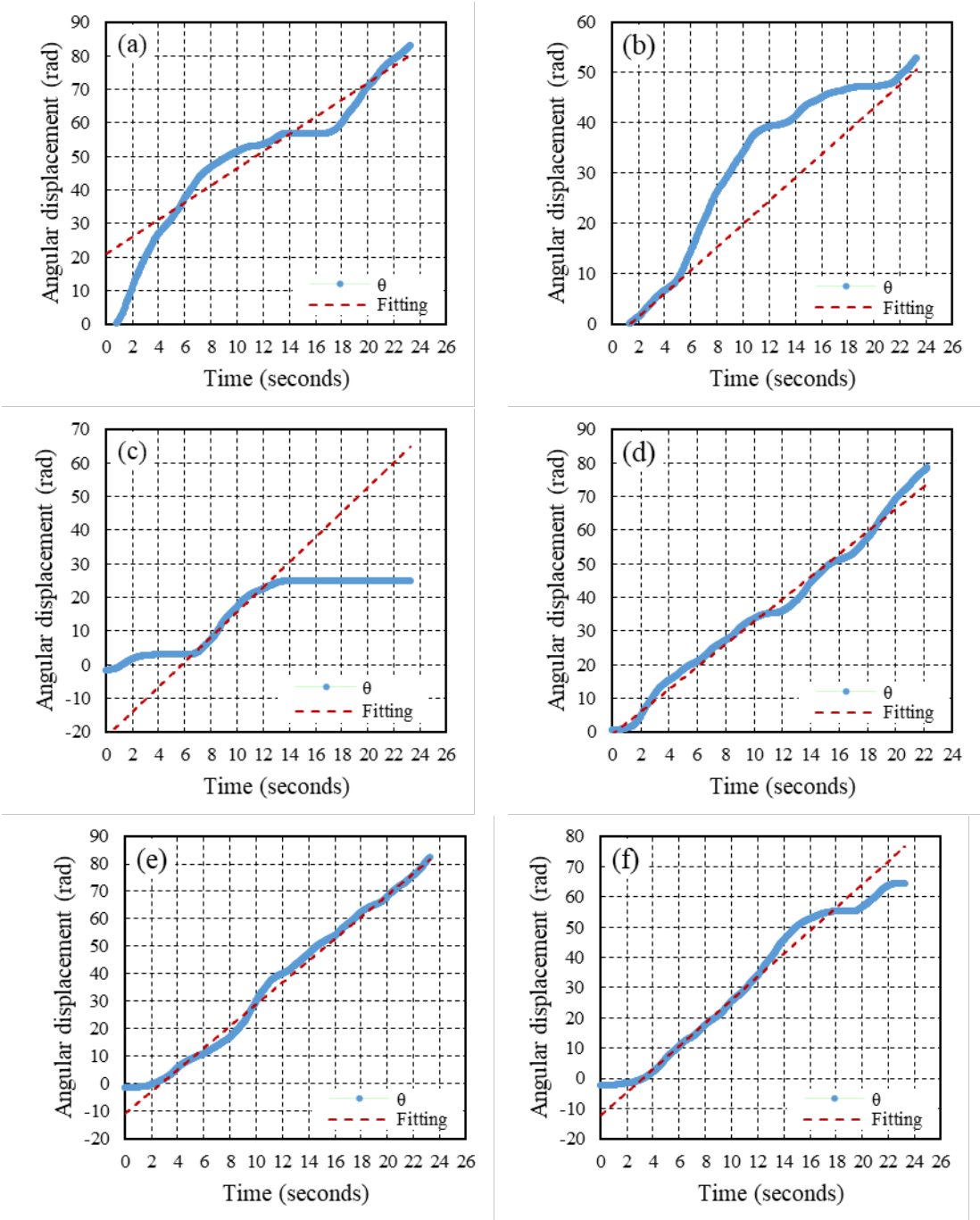
Figure A (II)-10 Linear plot by measurable data of angular displacement (θ) with time variation for angular speed estimation, β=60º at the distance L of (a) 4.98 m, (b) 5.28 m, (c) 5.58 m, (d) 5.88 m, (e) 6.18 m, (f) 6.48 m.

APPENDIX A (III)

ANGULAR ACCELERATION ESTIMATION
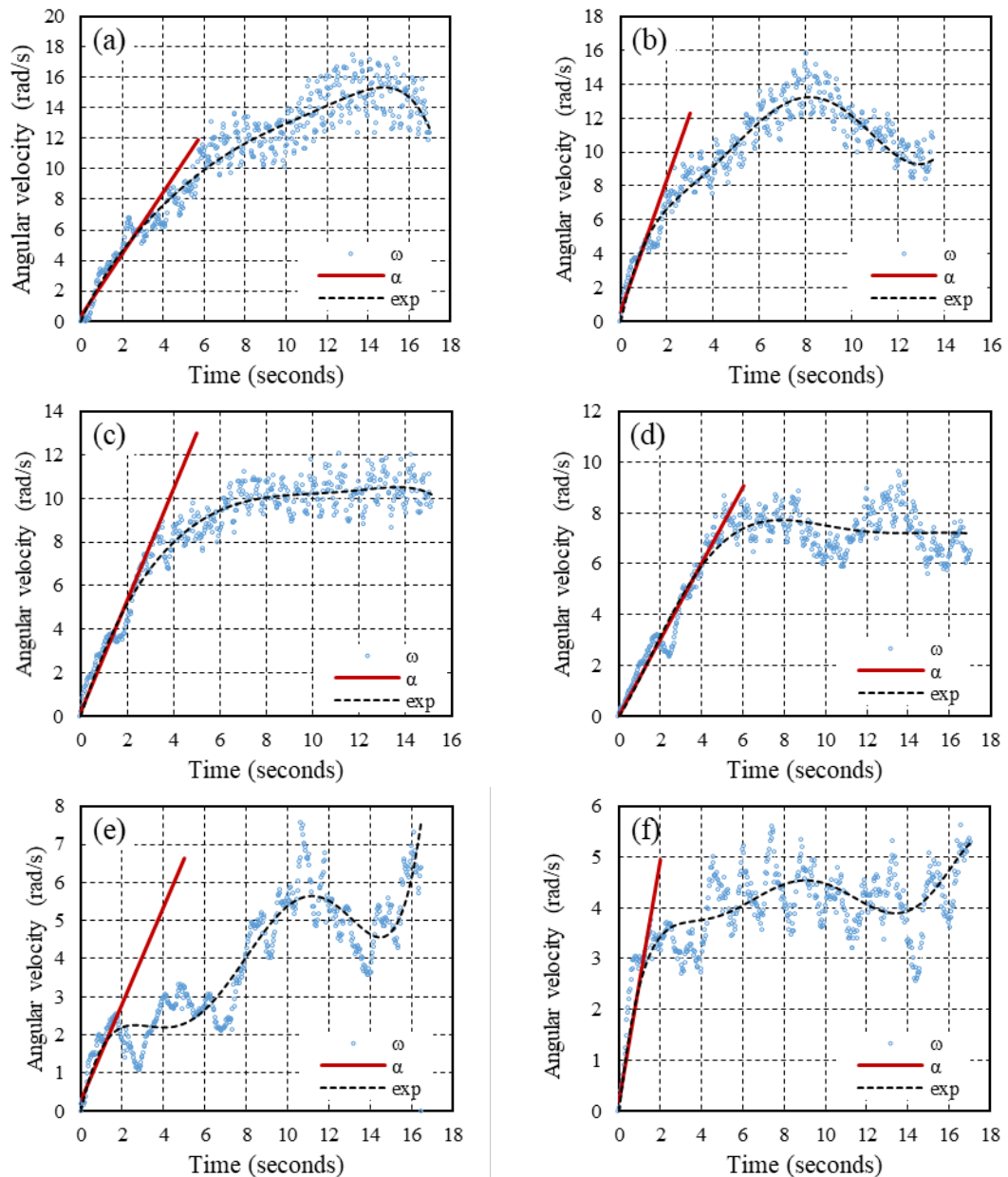

Figure A (III)-1 Linear plot by measurable data of angular speed (ω) with time variation for angular acceleration estimation, β=24° at the distance L of (a) 0.18 m, (b) 0.48 m, (c) 0.78 m, (d) 1.08 m, (e) 1.38 m, and (f) 1.68 m.

Figure A (III)-2 Linear plot by measurable data of angular speed (ω) with time variation for angular acceleration estimation, β=40° at the distance L of (a) 0.18 m, (b) 0.48 m, (c) 0.78 m, (d) 1.08 m, (e) 1.38 m, and (f) 1.68 m.

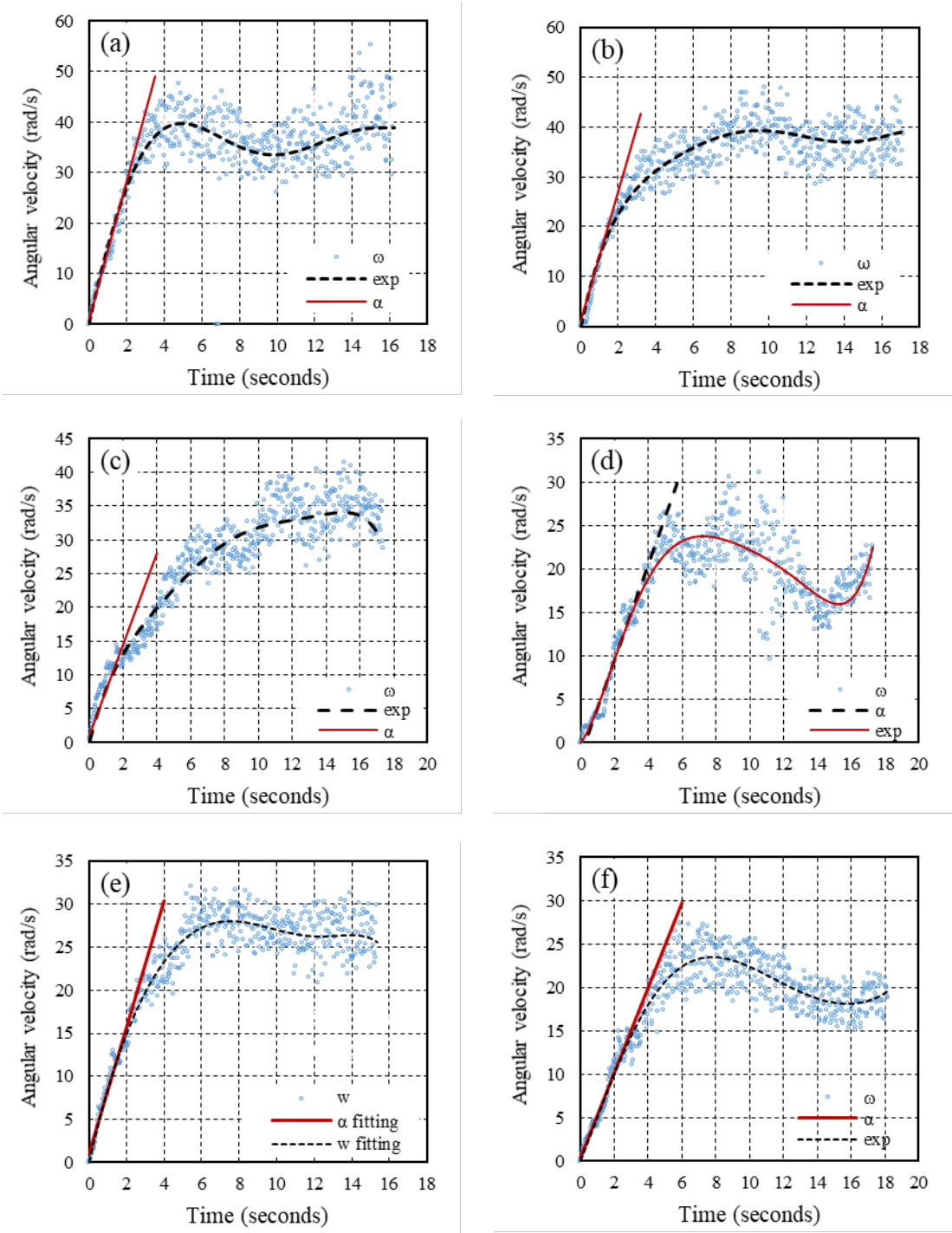**Figure A (III)-3** Linear plot by measurable data of angular speed (ω) with time variation for angular acceleration estimation, β=40º at the distance L of (a) 1.98 m, (b) 2.28 m, (c) 2.58 m, (d) 2.88 m, (e) 3.18 m, and (f) 3.48 m.

Figure A (III)-4 Linear plot by measurable data of angular speed (ω) with time variation for angular acceleration estimation, β=40° at the distance L of (a) 1.98 m, (b) 2.28 m, (c) 2.58 m, (d) 2.88 m; β=45° at the distance L of (e) 3.18 m, and (f) 3.48 m.
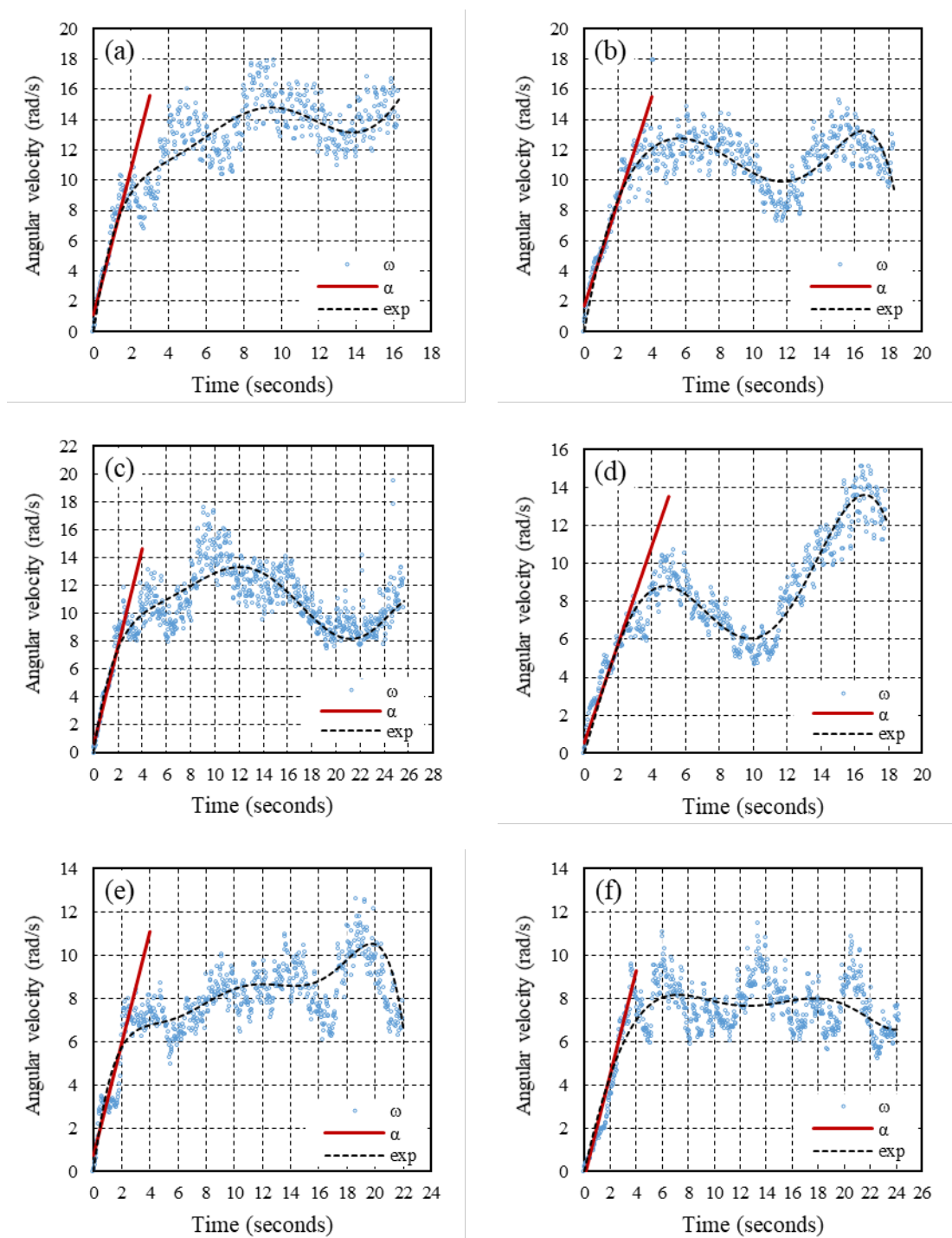
Figure A (III)-5 Linear plot by measurable data of angular speed (ω) with time variation for angular acceleration estimation, β=45° at the distance L of (a) 0.78 m, (b) 1.08 m, (c) 1.38 m, (d) 1.68 m, (e) 1.98 m, and (f) 2.28 m.

Figure A (III)-6 Linear plot by measurable data of angular speed (ω) with time variation for angular acceleration estimation, β=45º at the distance L of (a) 2.58 m, (b) 2.88 m, (c) 3.18 m, (d) 3.48 m, (e) 3.88 m, and (f) 4.08 m.
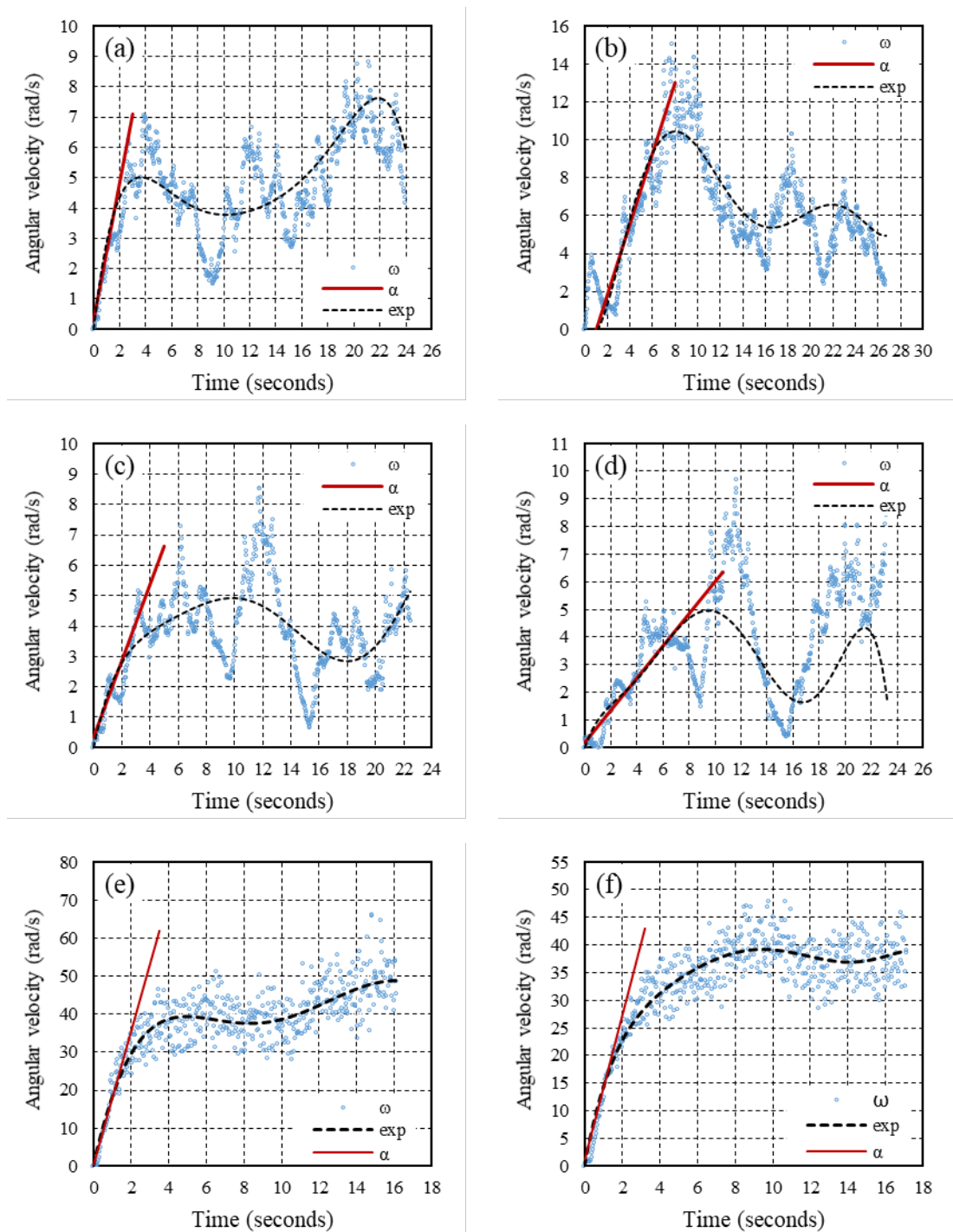
Figure A (III)-7 Linear plot by measurable data of angular speed (ω) with time variation for angular acceleration estimation, β=45º at the distance L of (a) 4.38 m, (b) 4.68 m, (c) 4.98 m, (d) 5.28 m; β=60º at the distance L of (e) 0.18 m, and (f) 0.48 m.
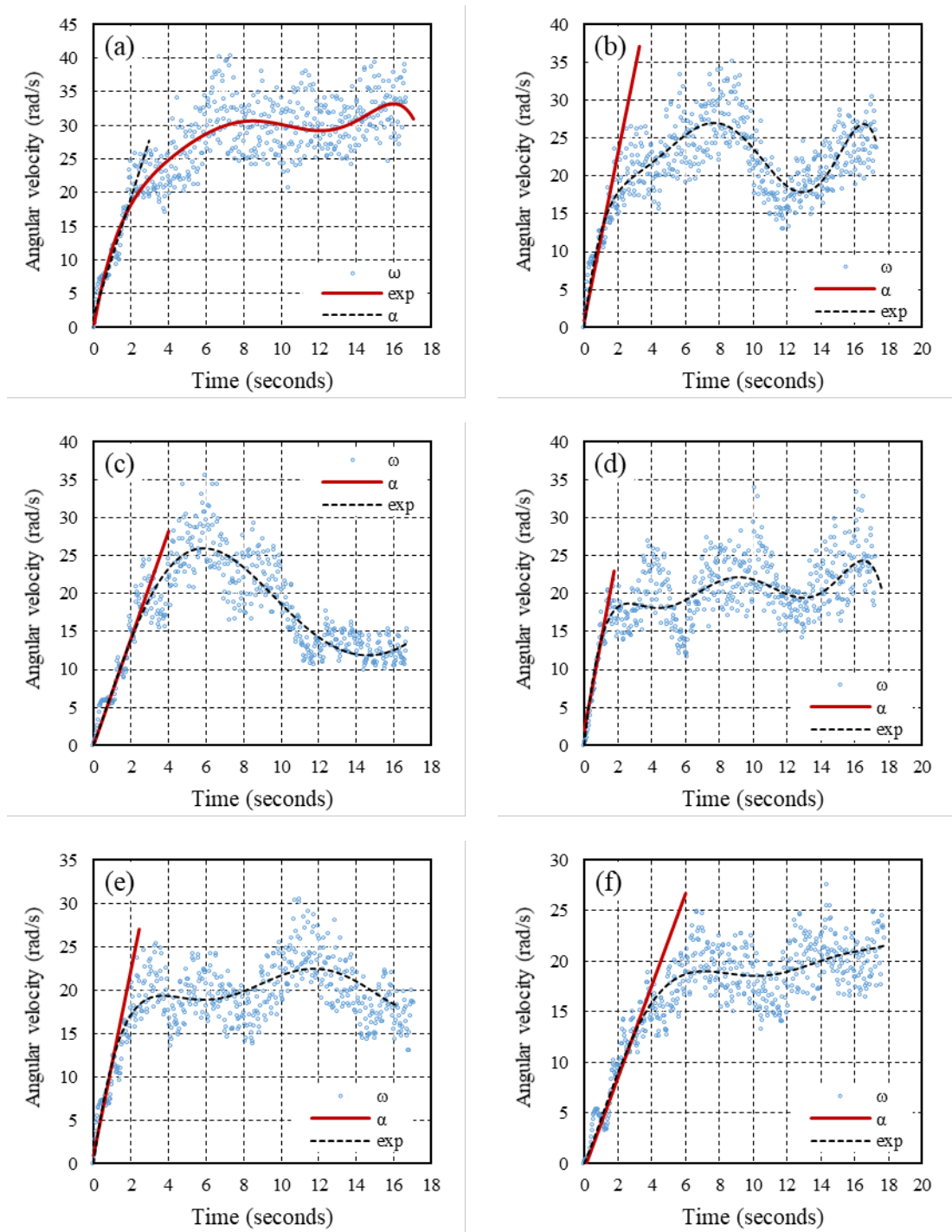
Figure A (III)-8 Linear plot by measurable data of angular speed (ω) with time variation for angular acceleration estimation, β=60º at the distance L of (a) 0.78 m, (b) 1.08 m, (c) 1.38 m, (d) 1.68 m, (e) 1.98 m, and (f) 2.28 m.
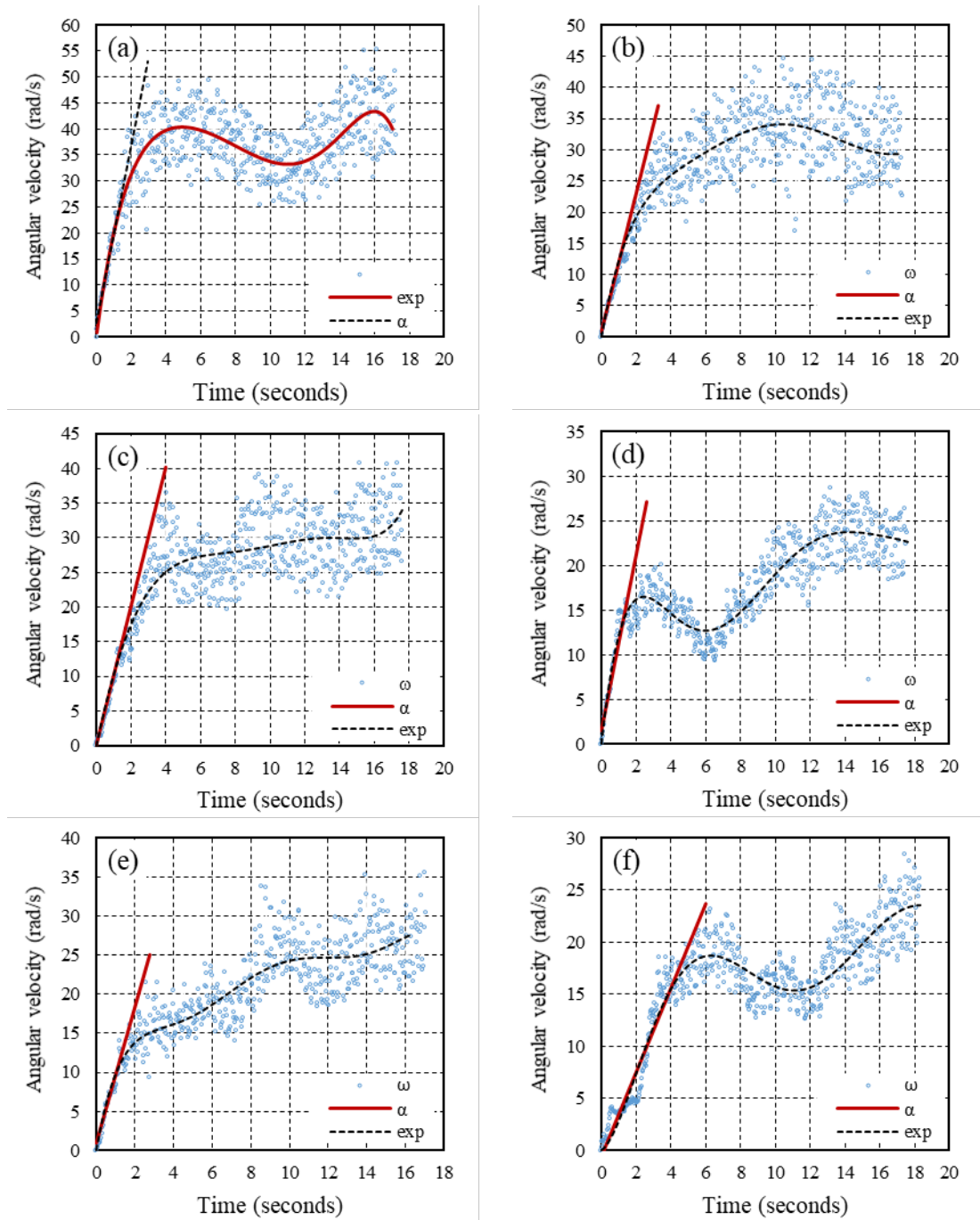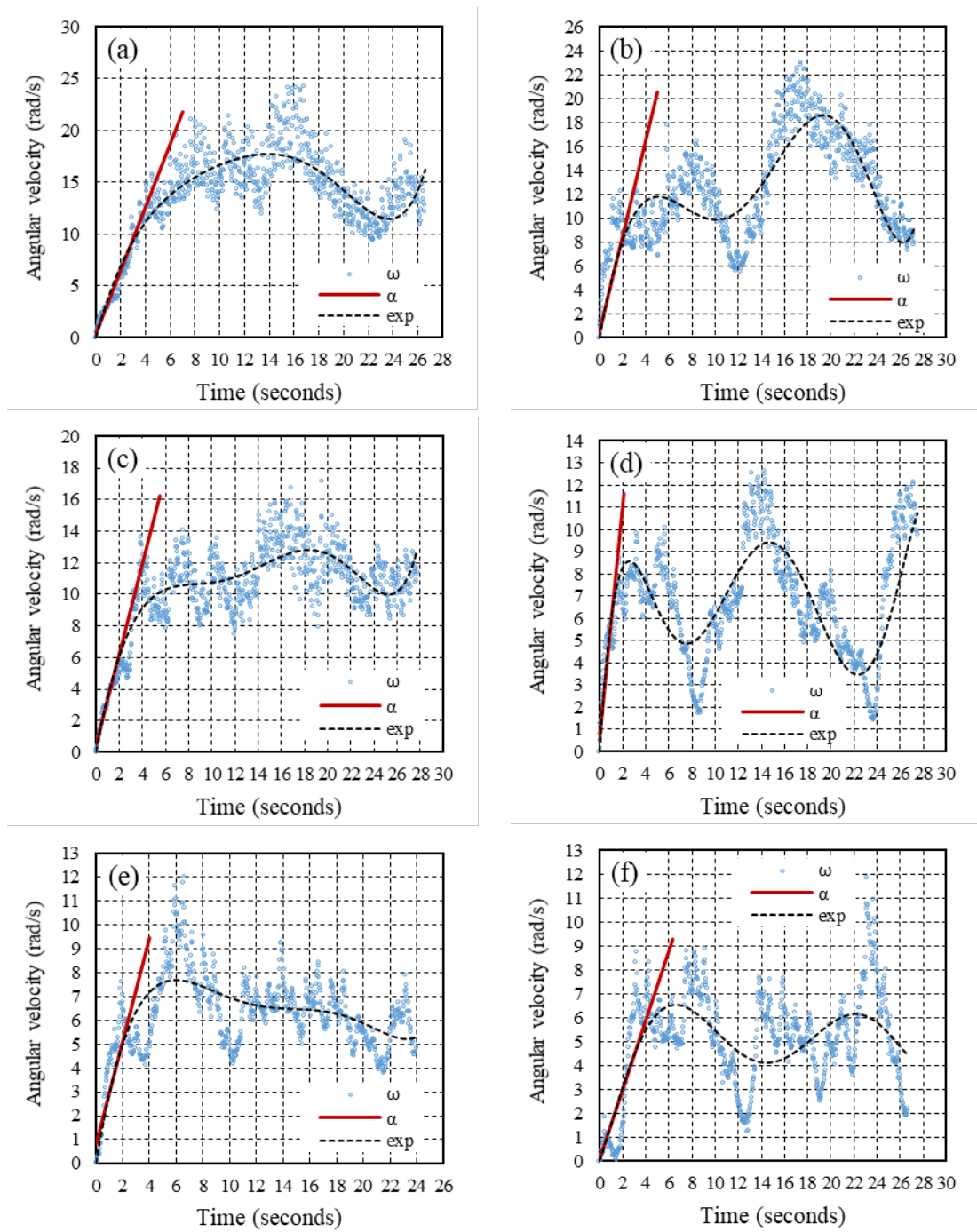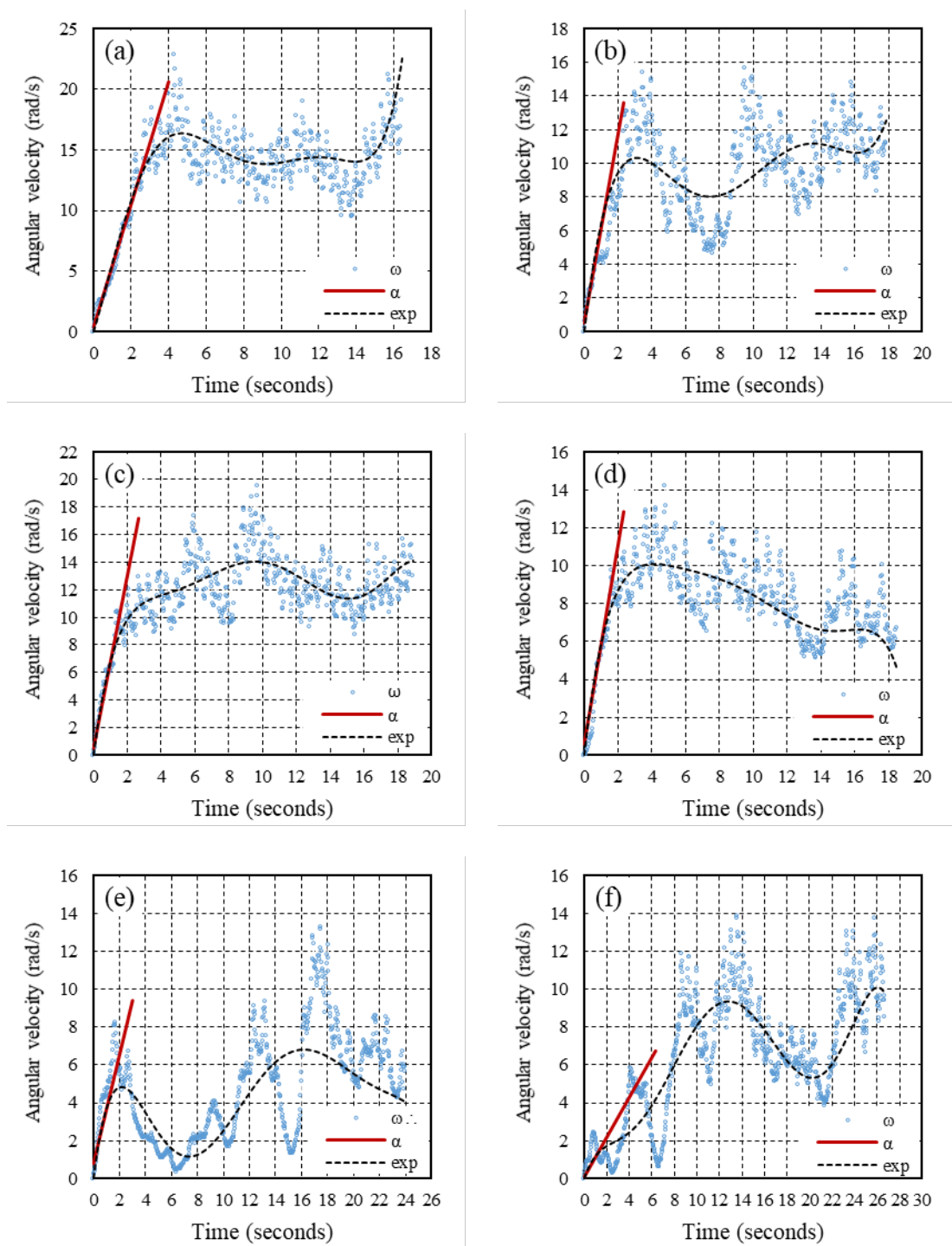
Figure A (III)-9 Linear plot by measurable data of angular speed (ω) with time variation for angular acceleration estimation, β=60° at the distance L of (a) 2.58 m, (b) 2.88 m, (c) 3.18 m, (d) 3.48 m, (e) 3.78 m, and (f) 4.08 m.

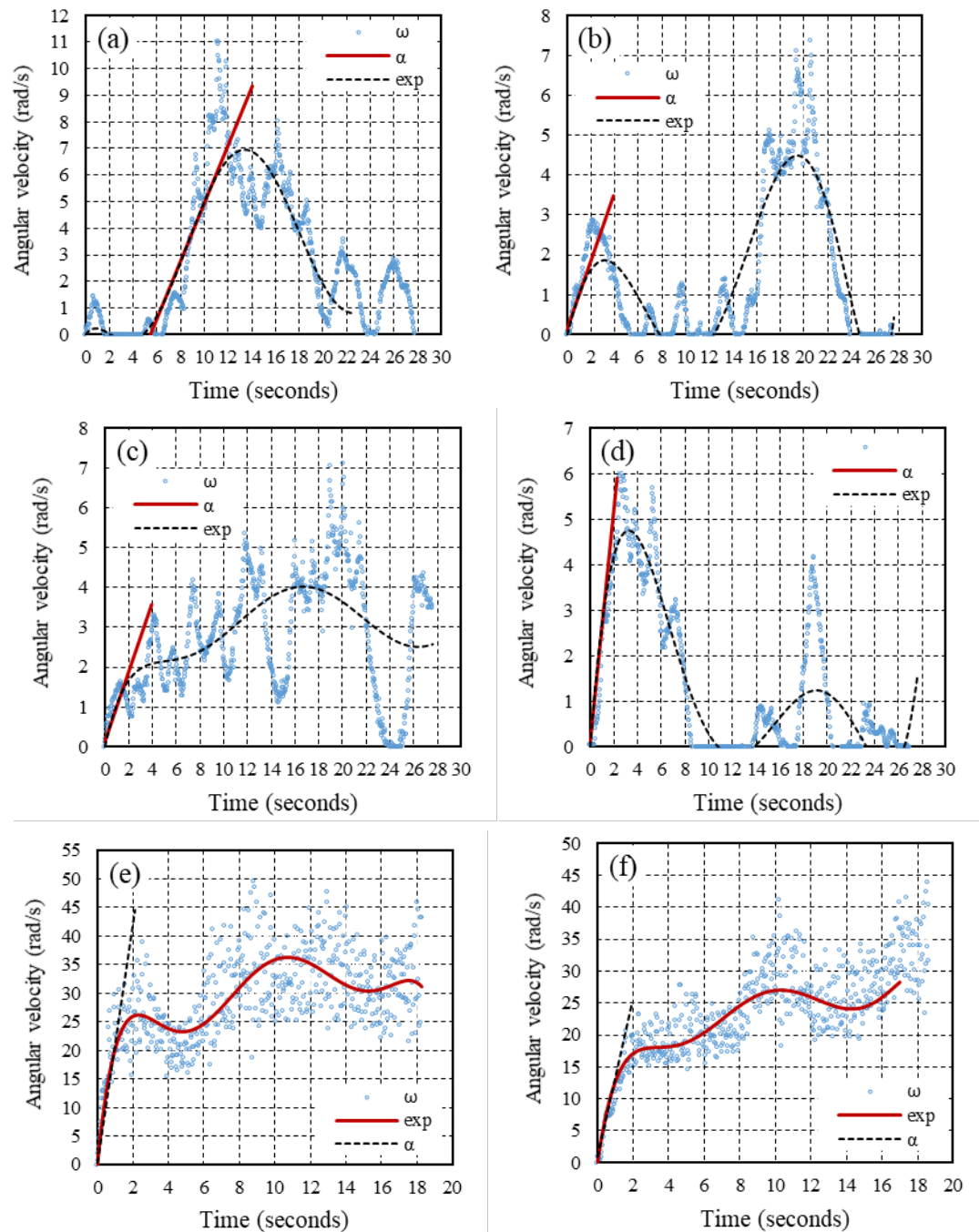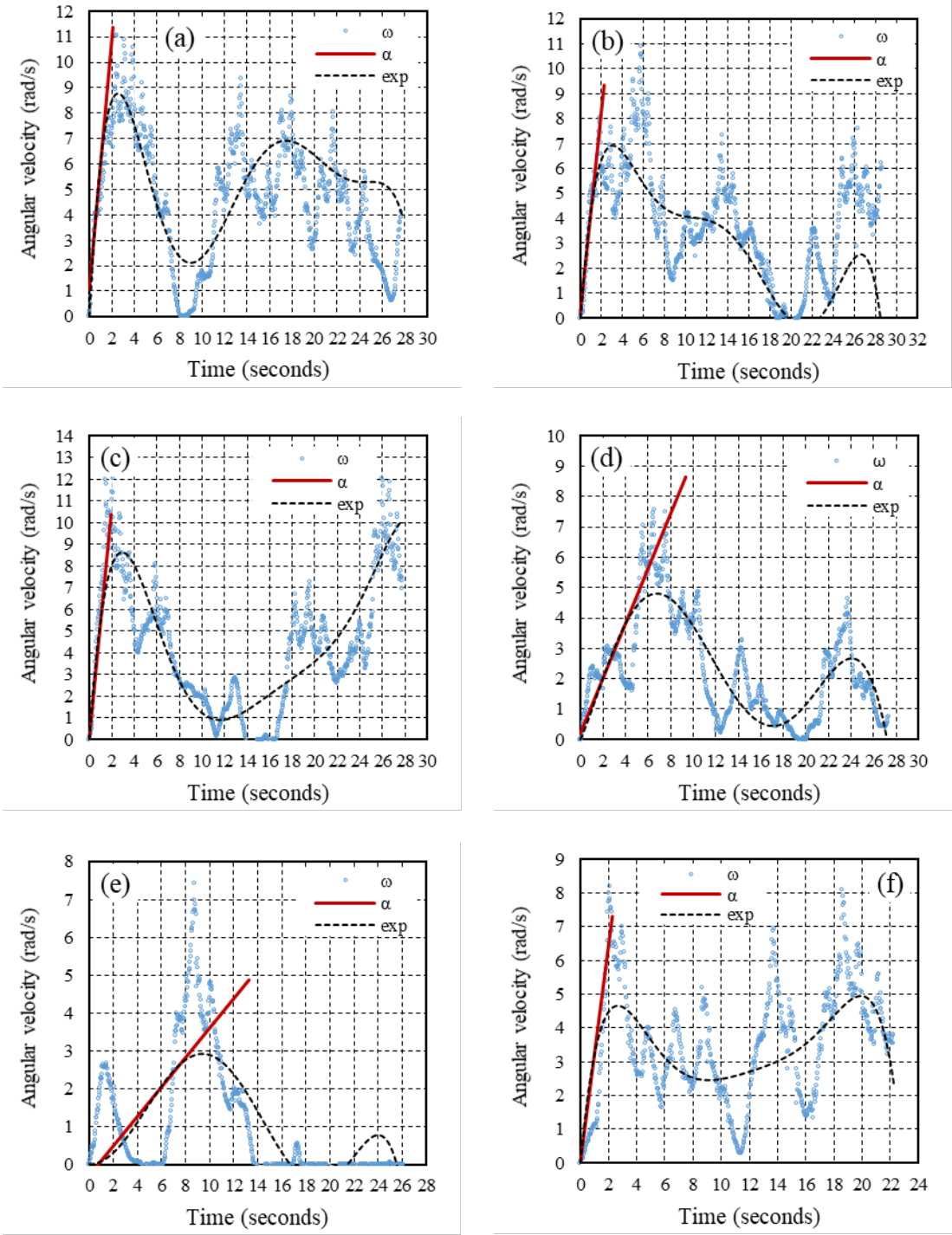**Figure A (III)-10** Linear plot by measurable data of angular speed (ω) with time variation for angular acceleration estimation, β=60° at the distance L of (a) 4.38 m, (b) 4.68 m, (c) 4.98 m, (d) 5.28 m, (e) 5.58 m, and (f) 5.88 m.
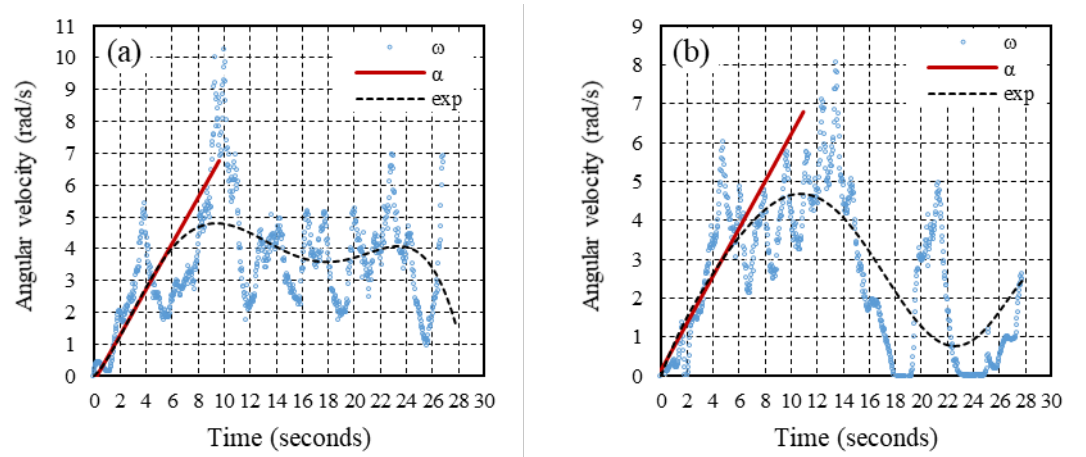
Figure A (III)-11 Linear plot by measurable data of angular speed (ω) with time variation for angular acceleration estimation, β=60° at the distance L of (a) 6.18 m, and (b) 6.48 m.

APPENDIX A (IV)

SPECTRUM PEAKS OF TURBINE ROTATION FREQUENCIES
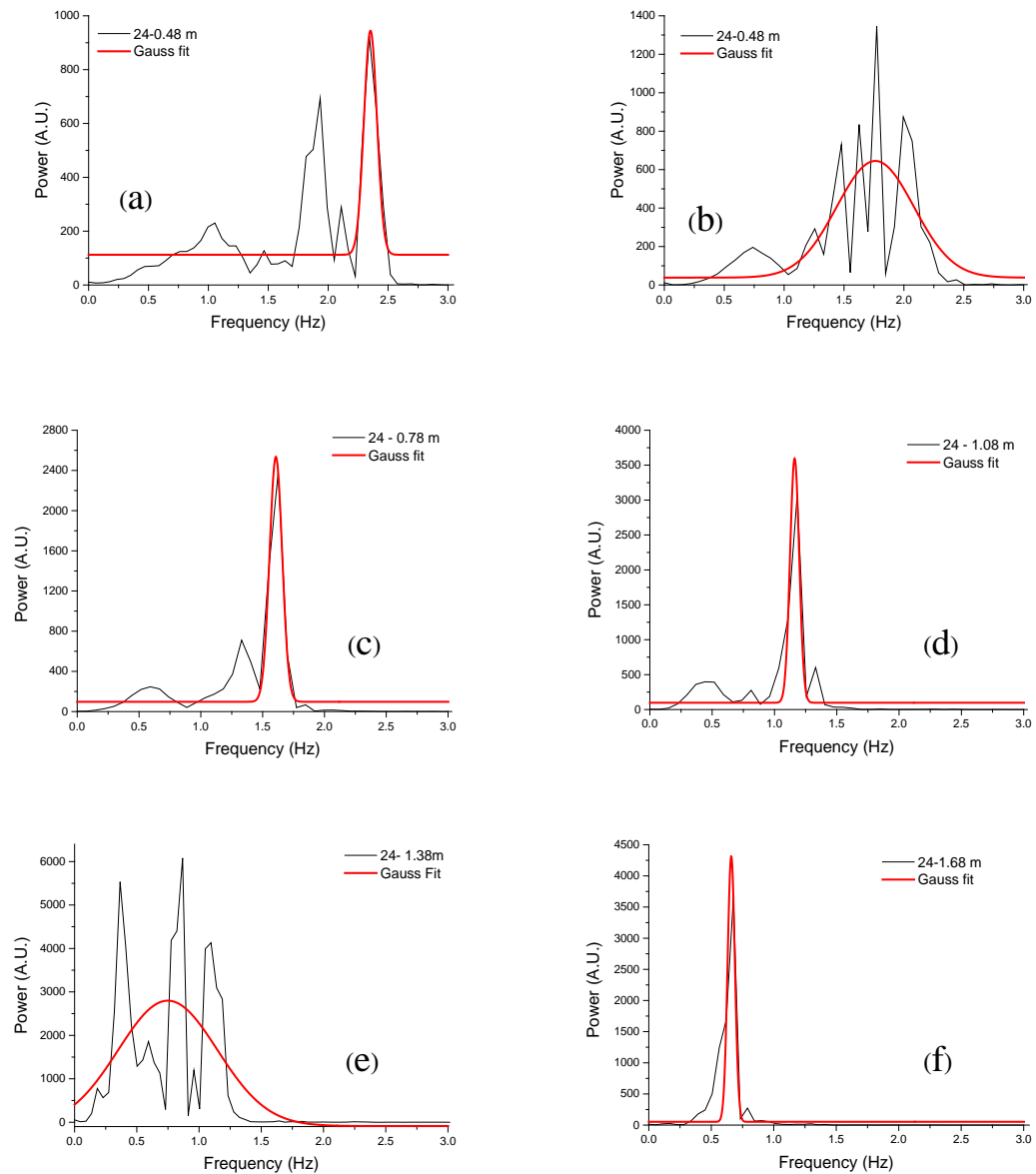
Figure A (IV)-1 The FFT spectrums and Gaussian fitting for turbine rotation frequencies; β=24° at the distance L of (a) 0.18 m, and (b) 0.48 m., (c) 0.78 m, (d) 1.08 m., (e) 1.38 m., and (f) 1.68 m.
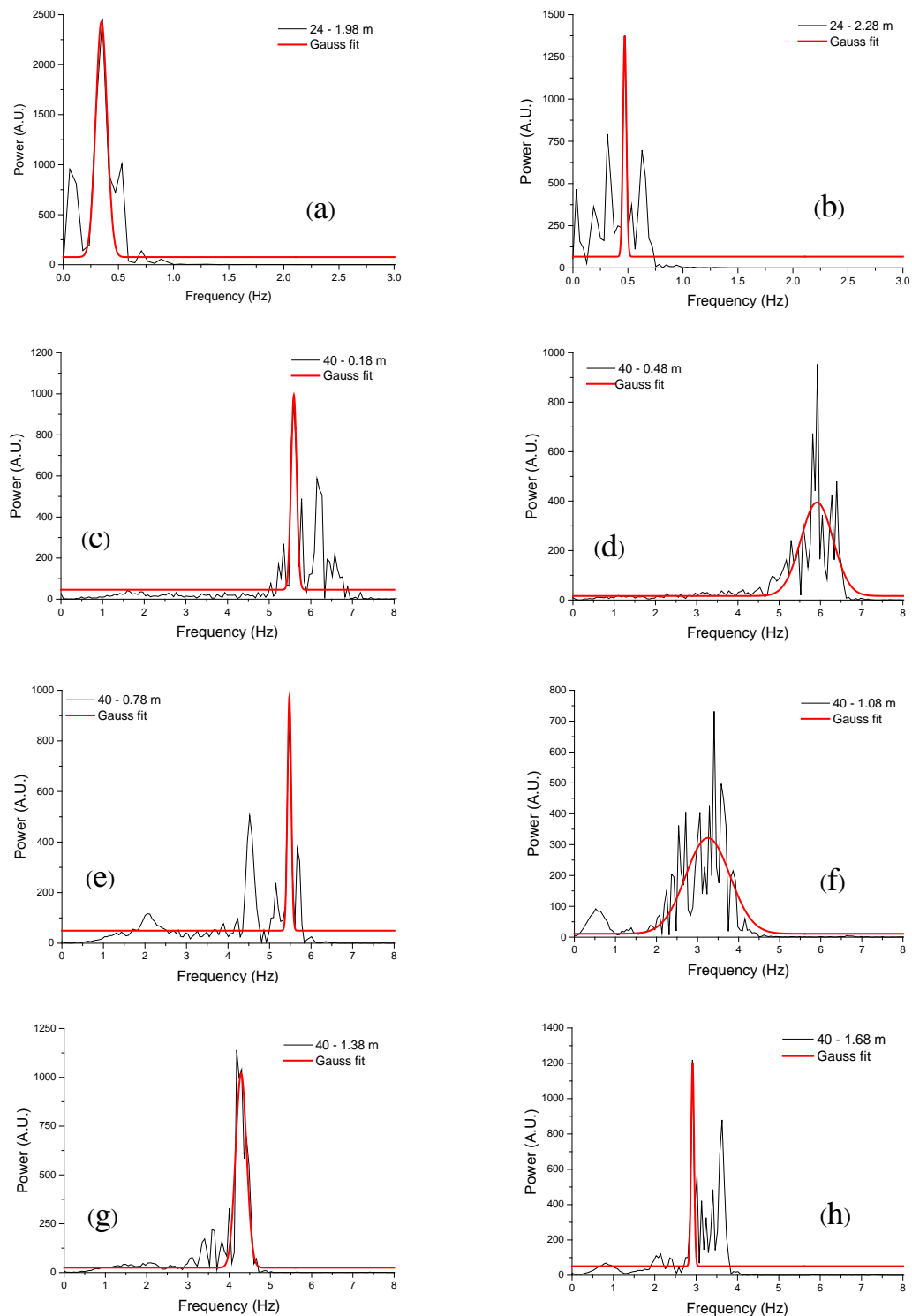
Figure A (IV)-2 The FFT spectrums and Gaussian fitting for turbine rotation frequencies; β=24° at the distance L of (a) 1.98 m, (b) 2.28 m.; β=40° at the distance L of (c) 0.18 m, (d) 0.48 m., (e) 0.78 m., (f) 1.08 m., (g) 1.38 m, and (h) 1.68 m.
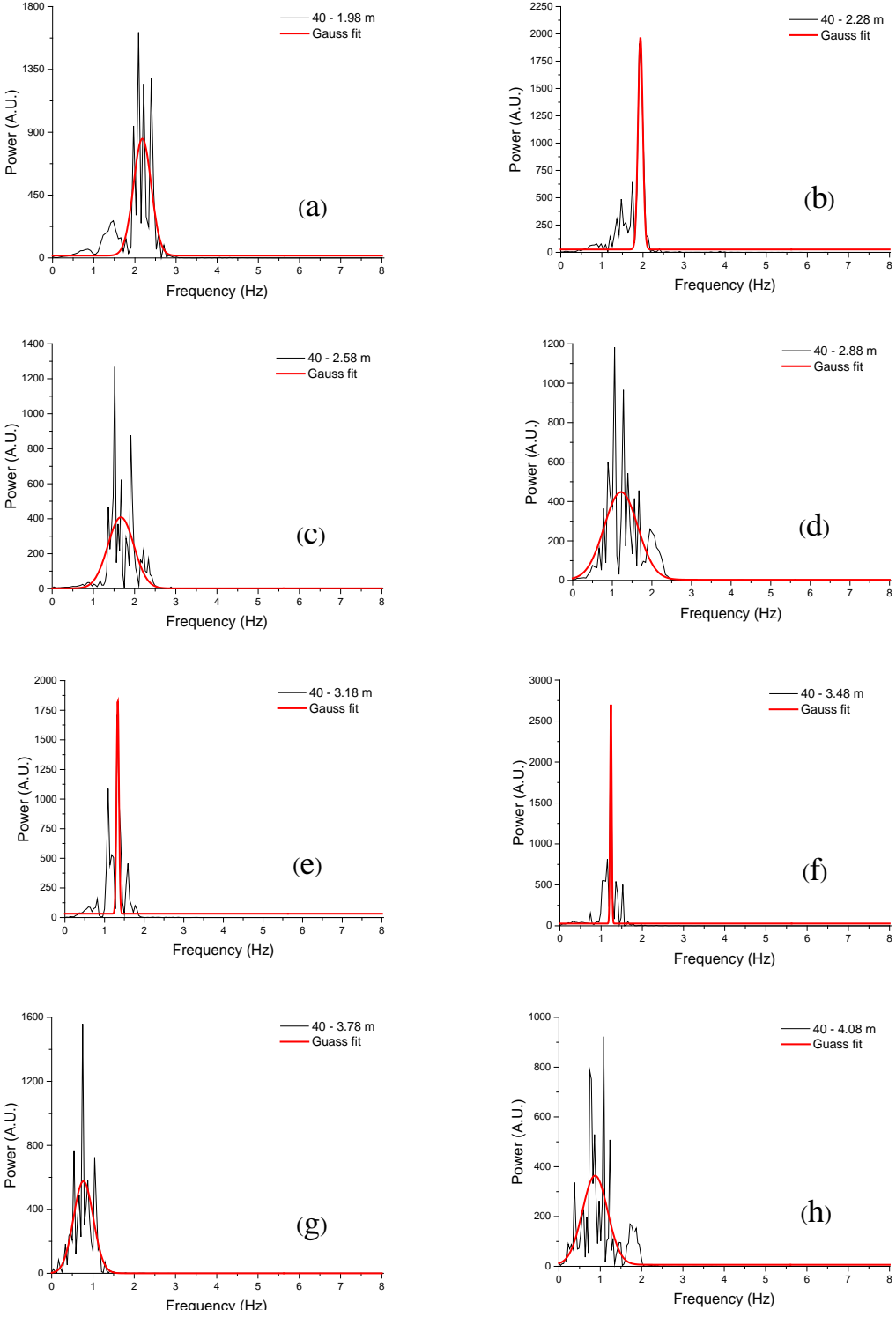
Figure A (IV)-3 The FFT spectrums and Gaussian fitting for turbine rotation frequencies; β=40° at the distance L of (a) 1.98 m, (b) 2.28 m, (c) 2.58 m, (d) 2.88 m, (e) 3.18 m, (f) 3.48 m, (g) 3.78 m, and (h) 4.08 m.
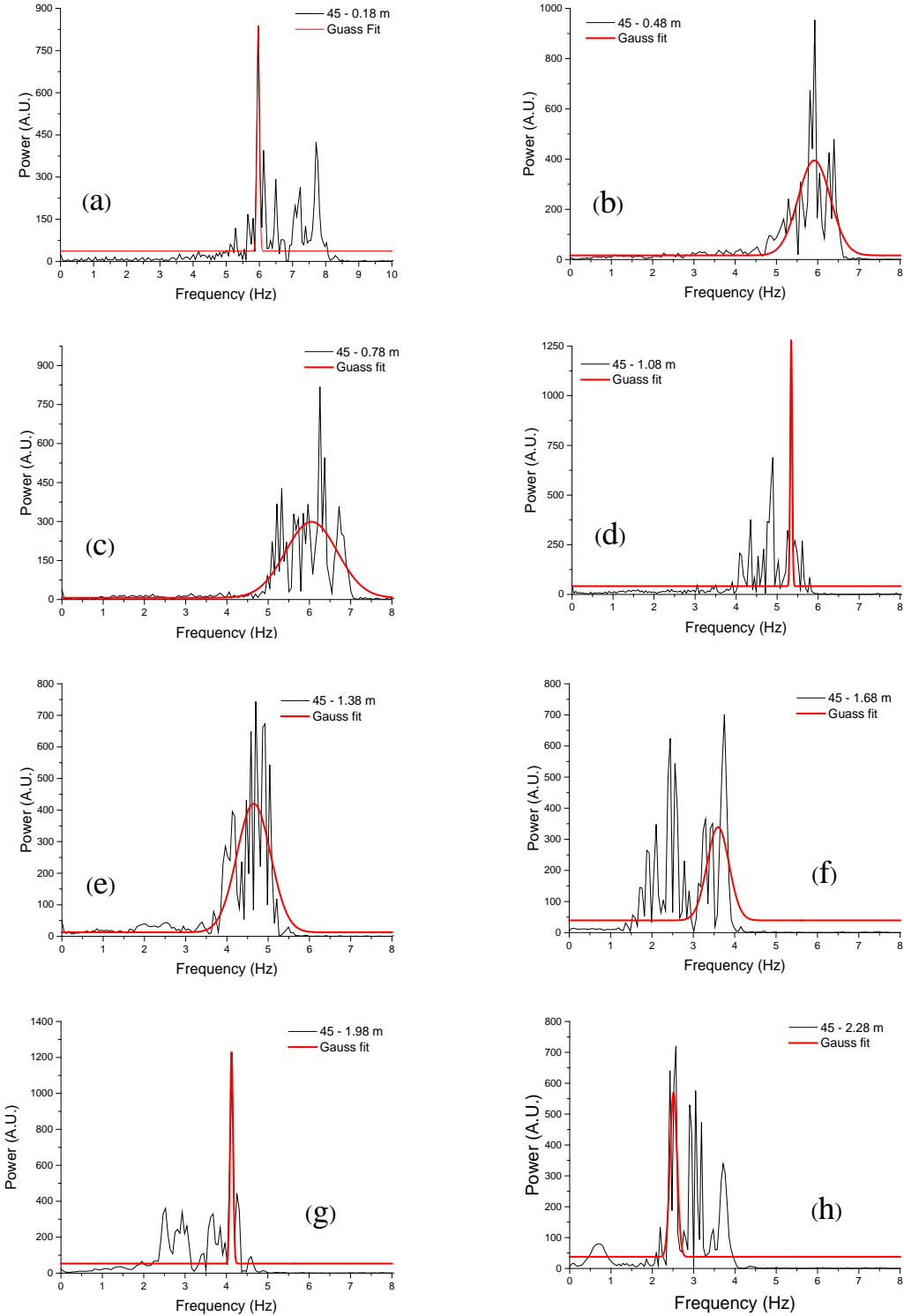
Figure A (IV)-4 The FFT spectrums and Gaussian fitting for turbine rotation frequencies; β=45° at the distance L of (a) 1.98 m, (b) 2.28 m, (c) 2.58 m, (d) 2.88 m, (e) 3.18 m, (f) 3.48 m, (g) 3.78 m, and (h) 4.08 m.
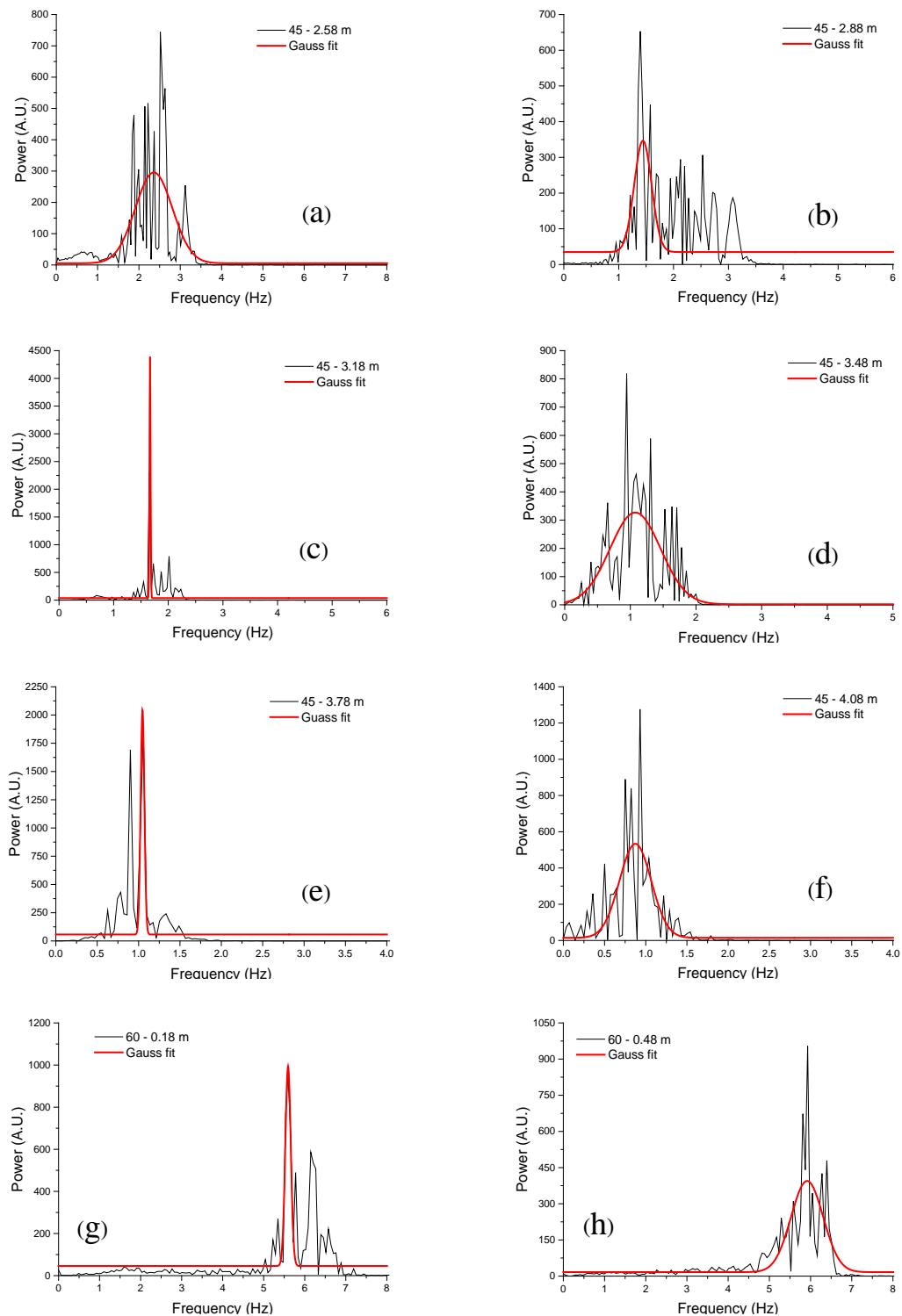
Figure A (IV)-5 The FFT spectrums and Gaussian fitting for turbine rotation frequencies; β=45° at the distance L of (a) 2.58 m, (b) 2.88 m, (c) 3.18 m, (d) 3.48 m, (e) 3.78 m, (f) 4.08 m; β=60° at the distance L of (a) 0.18 m, and (h) 0.48 m.
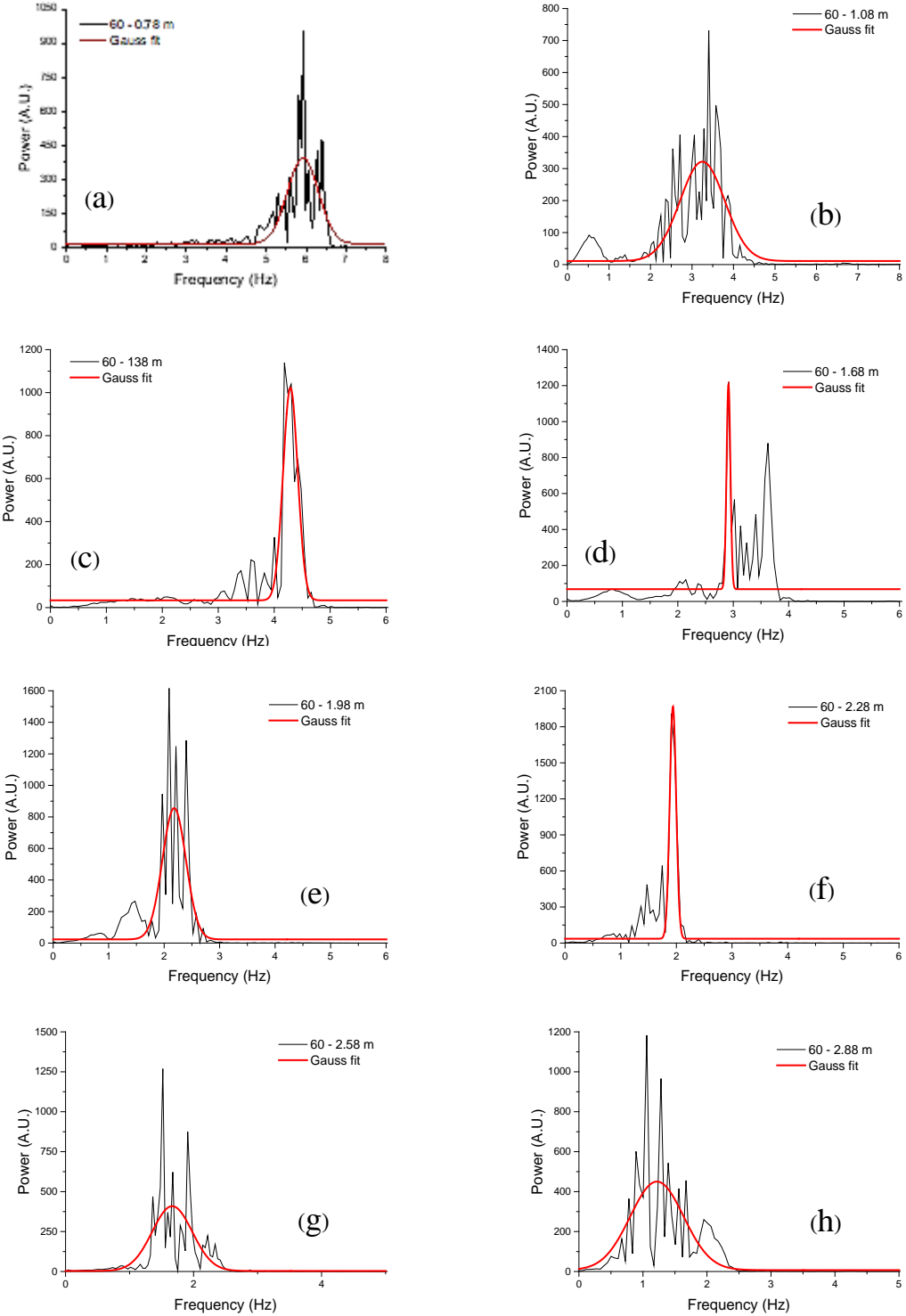
Figure A (IV)-6 The FFT spectrums and Gaussian fitting for turbine rotation frequencies; β=60° at the distance L of (a) 0.78 m, (b) 1.08 m, (c) 1.38 m, (d) 1.68 m, (e) 1.98 m, (f) 2.28 m, (g) 2.58 m, and (h) 2.88 m.
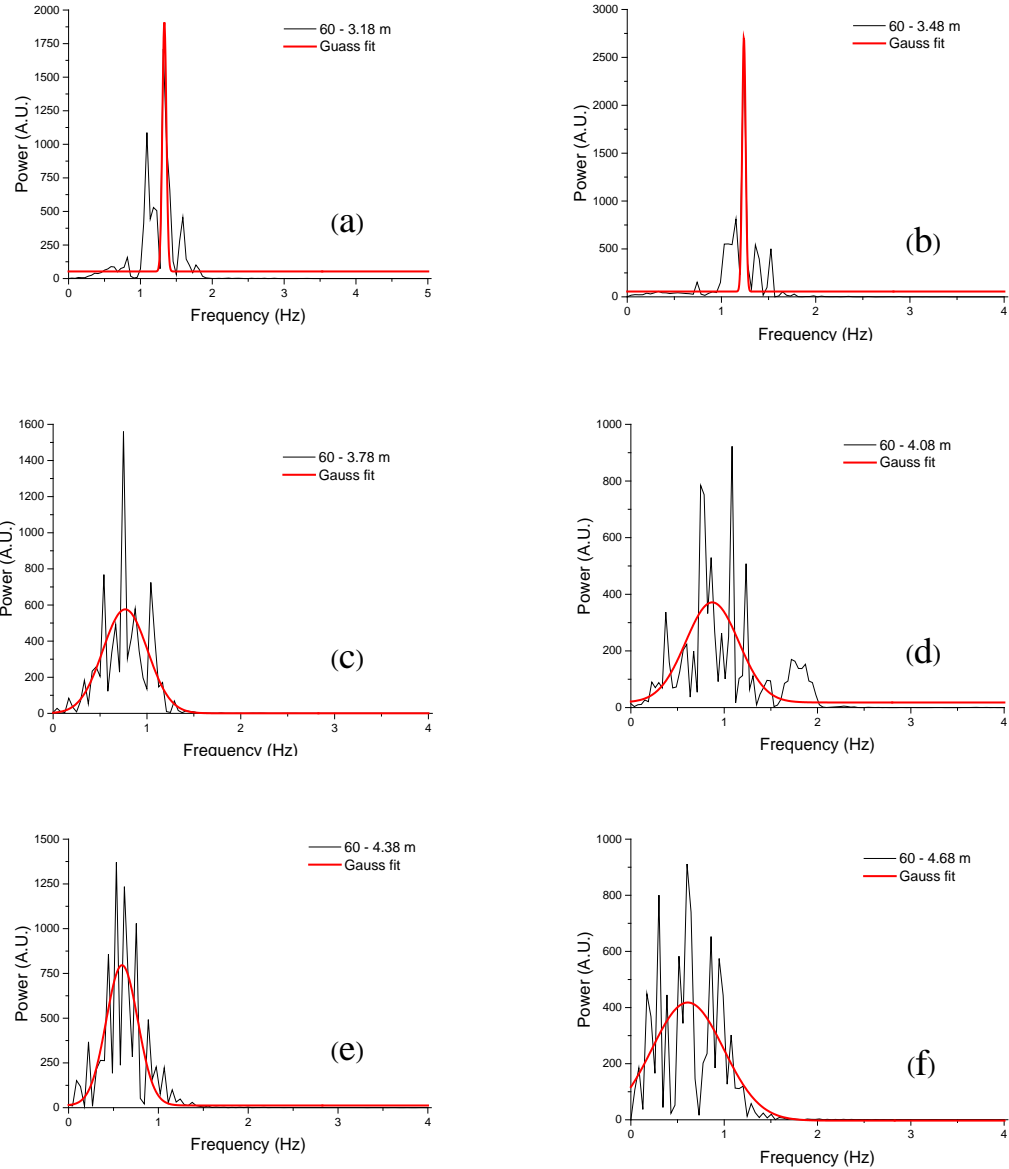
Figure A (IV)-7 The FFT spectrums and Gaussian fitting for turbine rotation frequencies; β=60° at the distance L of (a) 3.18 m, (b) 3.48 m, (c) 3.78 m, (d) 4.08 m, (e) 4.38 m, and (f) 4.68 m.

APPENDIX A (V)

**VOLTAGE OUTPUT FROM PIEZOELECTRIC VARIATION BY
VORTICES INDUCED VIBRATION GENERATED FROM
PVDF PIEZOELECTRIC OCILLATIONS**

(a) *Q = 0 G/min*   (b) *Q = 0.1 G/min*

(c) *Q = 0.2 G/min*   (d) *Q = 0.3 G/min*

(e) *Q = 0.4 G/min*   (f) *Q = 0.5 G/min*
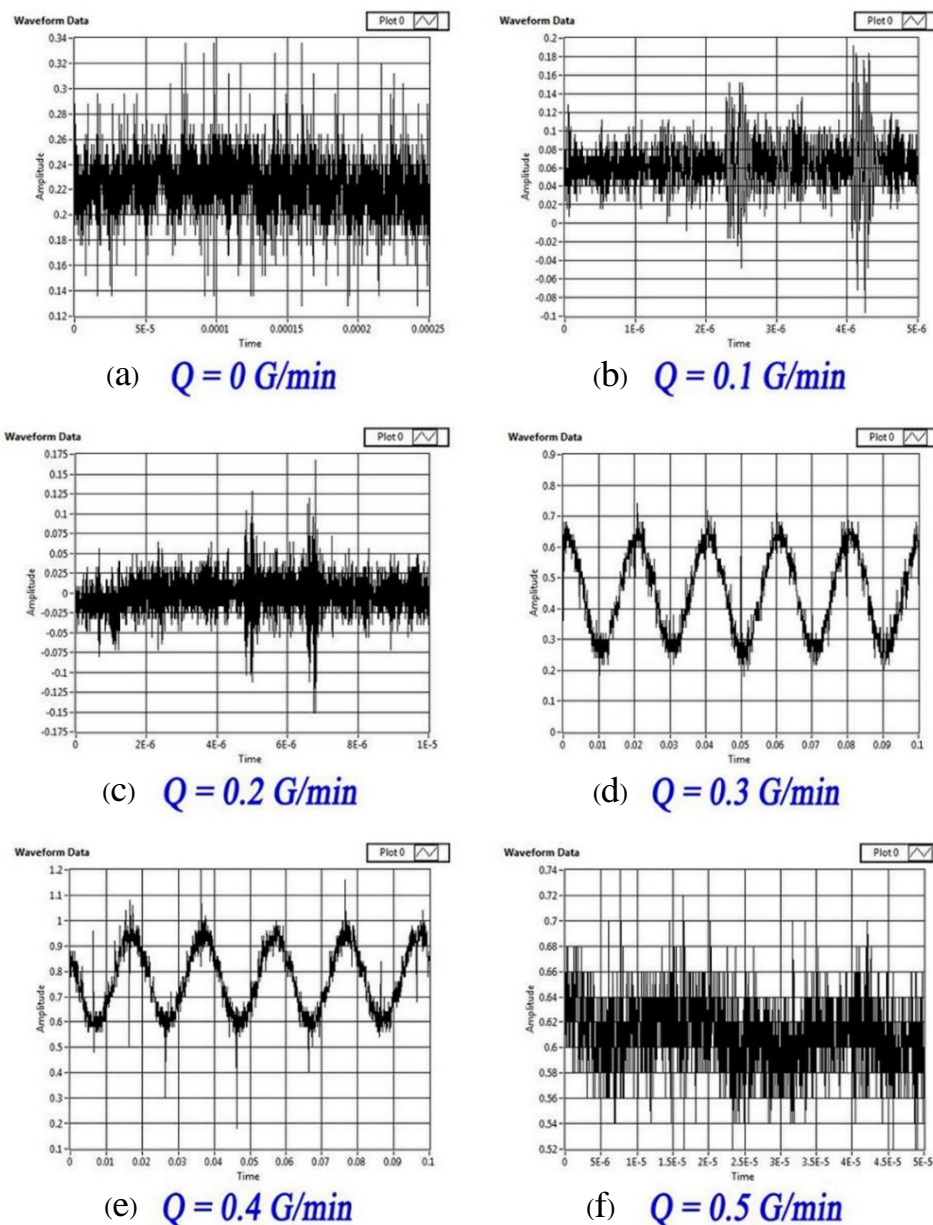
Figure A (V)-1 Signal output from piezoelectric variation by vortices induced vibration under the flow rate (Q) condition of (a) 0.0, (b) 0.1, (c) 0.2, (d) 0.3, (e) 0.4, and (e) 0.5 gallon/min.
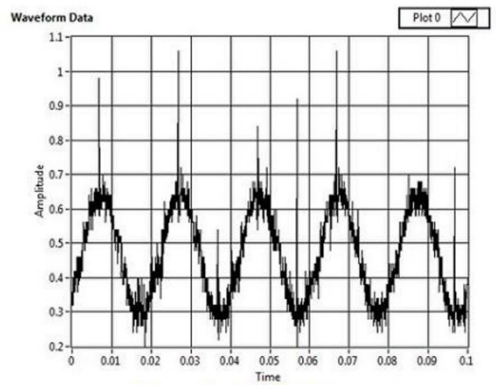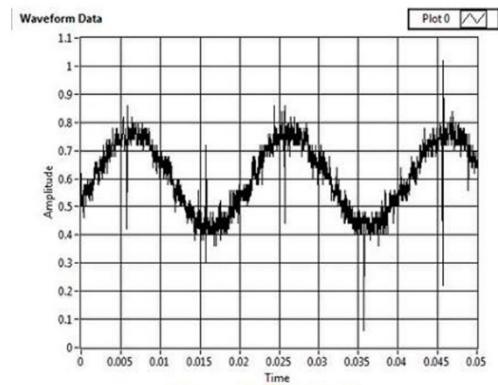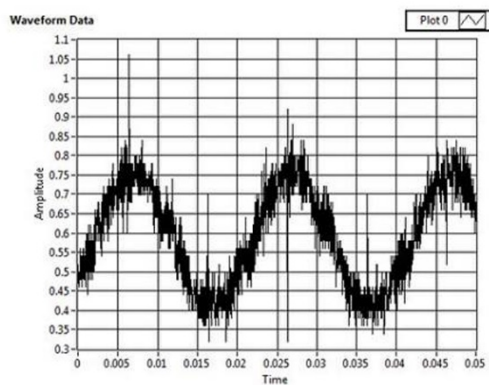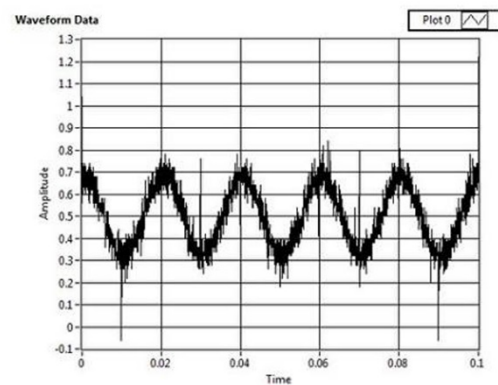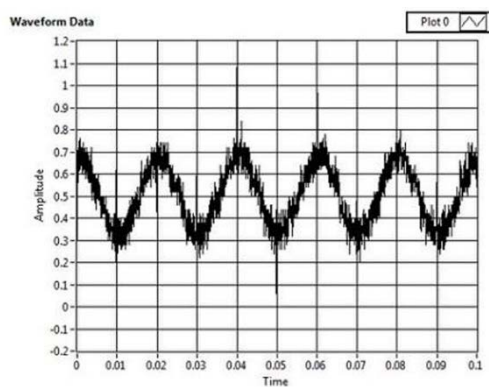
Figure A (V)-2 Signal output from piezoelectric variation by vortices induced vibration under the flow rate (Q) condition of (a) 0.6, (b) 0.7, (c) 0.8, (d) 0.9, and (e), 1.0 gallon/min.

APPENDIX A (VI)

MOMENT OF INERTIAL ESTIMATION

Table A (V)-1 Materials properties of SABSS-HAWT components.

Property (unit)	ABS Plastic (rotor and blades)	Stainless Steel: Ferritic (axis)
Elastic (N/mm^2)	2000	200000
Poisson's Ratio	0.394	0.28
Shear Modulus (N/mm^2)	318.9	77000
Mass Density (kg/m^3)	1020	7800
Tensile Strength (N/mm^2)	30	513.61
Compressive Strength (N/mm^2)	-	-
Yield Strength (N/mm^2)	-	172.34
Thermal Expansion Coefficient (/K)	-	1.1e-005
Thermal Conductivity (W/(m·K))	0.2256	18
Specific Heat (J/(kg·K))	1386	460
Material Damping Ratio	N/A	N/A

Table A (V)-2 Angular momentum and inertial characteristics of SABSS-HAWT assembly for β of 24º.

24 degree		
Mass properties of moment		
Configuration	: Default	
Coordinate system:	-- default --	
Mass	= 390.81 grams	
Total weld mass	= 0.00 grams	
Volume	= 226.09 cubic centimeters	
Surface area	= 167005.84 mm^2	
Center of mass: (mm)		
X = -0.00	Y = -0.00	Z = -157.98
Principal axes of inertia and principal moments of inertia: (g*mm^2) Taken at the center of mass.		
Ix = (-0.00, 0.00, 1.00) Iy = (0.71, -0.71, 0.00) Iz = (0.71, 0.71, 0.00)		Px = 659777.97 Py = 13877417.96 Pz = 13877417.96
Moments of inertia: (g*mm^2) Taken at the center of mass and aligned with the output coordinate system.		
Lxx = 13877415.76 Lyx = 0.11 Lzx = -68.77	Lxy = 0.11 Lyy = 13877420.17 Lzy = -1.43	Lxz = -68.77 Lyz = -1.43 Lzz = 659777.97
Moments of inertia: (g*mm^2), Taken at the output coordinate system.		
Ixx = 23630992.45 Iyx = 0.11 Izx = -1.11	Ixy = 0.11 Iyy = 23630996.86 Izy = -0.24	Ixz = -1.11 Iyz = -0.24 Izz = 659777.97
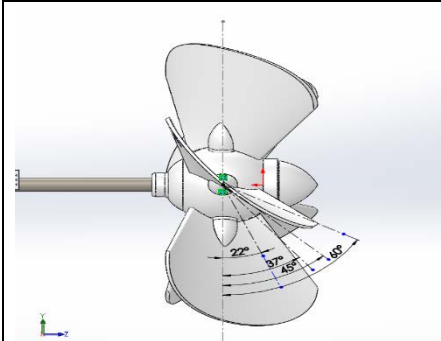
Table A (V)-3 Angular momentum and inertial characteristics of SABSS-HAWT assembly for β of 40º.

	40 degree		
	Mass properties of moment		
	Configuration	: Default	
	Coordinate system:	-- default --	
	Mass	= 390.81 grams	
	Total weld mass	= 0.00 grams	
	Volume	= 226.09 cm³	
	Surface area	= 167005.84 mm²	
	Center of mass: (mm)		
	X = -0.00	Y = -0.00	Z = -157.72
Principal axes of inertia and principal moments of inertia: (g*mm²) Taken at the center of mass.			
Ix = (-0.00, 0.00, 1.00) Iy = (0.71, -0.71, 0.00) Iz = (0.71, 0.71, 0.00)		Px = 649806.17 Py = 13853339.04 Pz = 13853339.04	
Moments of inertia: (g*mm²) Taken at the center of mass and aligned with the output coordinate system.			
Lxx = 13853336.83 Lyx = 0.11 Lzx = -69.17	Lxy = 0.11 Lyy = 13853341.24 Lzy = -1.42	Lxz = -69.17 Lyz = -1.42 Lzz = 649806.18	
Moments of inertia: (g*mm²) Taken at the output coordinate system.			
Ixx = 23575010.61 Iyx = 0.11 Izx = -1.63	Ixy = 0.11 Iyy = 23575015.02 Izy = -0.23	Ixz = -1.63 Iyz = -0.23 Izz = 649806.18	

Table A (V)-4 Angular momentums and inertial characteristics of SABSS-HAWT assembly for β of 45º.

	45 degree		
	Mass properties of moment		
	Configuration	: Default	
	Coordinate system:	-- default --	
	Mass	= 390.81 grams	
	Total weld mass	= 0.00 grams	
	Volume	= 226.09 cm³	
	Surface area	= 167005.84 mm²	
	Center of mass: (millimeters)		
	X = -0.00	Y = -0.00	Z = -157.60
Principal axes of inertia and principal moments of inertia: (g*mm²) Taken at the center of mass.			
Ix = (-0.00, 0.00, 1.00) Iy = (0.71, -0.71, 0.00) Iz = (0.71, 0.71, 0.00)		Px = 639705.05 Py = 13839041.80 Pz = 13839041.80	
Moments of inertia: (g*mm²) Taken at the center of mass and aligned with the output coordinate system.			
Lxx = 13839039.59 Lyx = 0.11 Lzx = -69.41	Lxy = 0.11 Lyy = 13839044.00 Lzy = -1.41	Lxz = -69.41 Lyz = -1.41 Lzz = 639705.05	
Moments of inertia: (g*mm²) Taken at the output coordinate system.			
Ixx = 23545901.08 Iyx = 0.11 Izx = -1.92	Ixy = 0.11 Iyy = 23545905.49 Izy = -0.22	Ixz = -1.92 Iyz = -0.22 Izz = 639705.05	

Table A (V)-4 Angular momentum and inertial characteristics of SABSS-HAWT assembly for β of 45°.

	60 degree		
	Mass properties of moment		
	Configuration	: Default	
	Coordinate system:	-- default --	
	Mass	= 390.81 grams	
	Total weld mass	= 0.00 grams	
	Volume	= 226.09 cubic centimeters	
	Surface area	= 167005.84 mm^2	
	Center of mass: (mm)		
	X = -0.00	Y = -0.00	Z = -157.51
Principal axes of inertia and principal moments of inertia: (g*mm^2) Taken at the center of mass.			
Ix = (-0.00, 0.00, 1.00) Iy = (0.71, -0.71, 0.00) Iz = (0.71, 0.71, 0.00)		Px = 620640.15 Py = 13820182.88 Pz = 13820182.88	
Moments of inertia: (g*mm^2) Taken at the center of mass and aligned with the output coordinate system.			
Lxx = 13820180.67 Lyx = 0.11 Lzx = -69.72	Lxy = 0.11 Lyy = 13820185.08 Lzy = -1.40	Lxz = -69.72 Lyz = -1.40 Lzz = 620640.15	
Moments of inertia: (g*mm^2) Taken at the output coordinate system.			
Ixx = 23515706.15 Iyx = 0.11 Izx = -2.27	Ixy = 0.11 Iyy = 23515710.56 Izy = -0.22	Ixz = -2.27 Iyz = -0.22 Izz = 620640.15	

APPENDIX B
CONTROLLING SYSTEM

APPENDIX B (I)

Coding for controlling pitch blades position

```
#include <Servo.h>                    //add servo libraly
Servo myservo;                        //create servo object to control a servo
volatile int flow_frequency;          // Measures flow sensor pulses
int flowPin = 2;                      //This is the input pin on the Arduino
double flowRate;                      //This is the value we intend to calculate.
volatile int count;                   //This integer needs to be set as volatile to ensure it
                                        updates correctly during the interrupt process.

void Flow() // Interrupt function
{   flow_frequency++;    }

void setup()
{
// put your setup code here, to run once:
  myservo.attach(9);                  //attachs the servo on pin 9 to servo object
  pinMode(flowPin, INPUT);            //Sets the pin as an input
  attachInterrupt(0, Flow, RISING);   //Configures interrupt 0 (pin 2 on the Arduino Uno) to
                                        run the function "Flow"
  Serial.begin(9600);                 //Start Serial
}

void loop()
{
                                      // put your main code here, to run repeatedly:
  count = 0;                          // Reset the counter so we start counting from 0 again
  interrupts();                       //Enables interrupts on the Arduino
  delay (1000);                       //Wait 1 second
  noInterrupts();                     //Disable the interrupts on the Arduino

  if(count >20) {myservo.write(24);}
  if(count >5) {myservo.write(40);}
  if(count >2) {myservo.write(45);}
  else {myservo.write(60);}

}
```

APPENDIX B (II)

Web page monitoring code for Thingspeak

```
#include <ESP8266WiFi.h>
#include "DHT.h"

#define DHTPIN D2                    // define  Sensor Out connected to D4 for Esp8266
//define sensortype
//#define DHTTYPE DHT11       //DHT 11 //#define DHTTYPE DHT21
// DHT 21 (AM2301)         // DHT 22  (AM2302), AM2321

#define DHTTYPE DHT22
DHT dht(DHTPIN, DHTTYPE);

const char* ssid = "vivo 1606";
const char* password = "1a418915953a";

const char* host = "api.thingspeak.com";            // Host thingspeak
const char* api   = "IP29C2GZ83CCWRFQ";            //API Key

void setup() {
  Serial.begin(9600);
  delay(10);
                                 // We start by connecting to a WiFi network
  Serial.println();
  Serial.println();
  Serial.print("Connecting to ");
  Serial.println(ssid);
  WiFi.begin(ssid, password);
  while (WiFi.status() != WL_CONNECTED) {
    delay(500);
    Serial.print(".");
  }
  Serial.println("");
  Serial.println("WiFi connected");
  Serial.println("IP address: ");
  Serial.println(WiFi.localIP());
  Serial.println("DHTxx test!");
  dht.begin();
}
int value = 0;

void loop() {
  delay(5000);
  ++value;
  float h = dht.readHumidity();
  float t = dht.readTemperature();
  float f = dht.readTemperature(true);
```

```cpp
  if (isnan(h) || isnan(t) || isnan(f)) {
    Serial.println("Failed to read from DHT sensor!");
    return;
  }
  float hif = dht.computeHeatIndex(f, h);
  float hic = dht.computeHeatIndex(t, h, false);
  Serial.print("Humidity: ");
  Serial.print(h);
  Serial.print(" %\t");
  Serial.print("Temperature: ");
  Serial.print(t);
  Serial.print(" *C ");
  Serial.print(f);
  Serial.print(" *F\t");
  Serial.print("Heat index: ");
  Serial.print(hic);
  Serial.print(" *C ");
  Serial.print(hif);
  Serial.println(" *F");
  Serial.print("connecting to ");
  Serial.println(host);
  // Use WiFiClient class to create TCP connections
  WiFiClient client;
  const int httpPort = 80;
  if (!client.connect(host, httpPort)) {
    Serial.println("connection failed");
    return;
  }
  // We now create a URI for the request
  String url = "/update?api_key=";
  url += api;
  url += "&field1=";
  url += t;
  url += "&field2=";
  url += h;

// We will sent https://api.thingspeak.com/update?api_key=IP29C2GZ83CCWRFQ&field1=
(อุณหภูมิ)&field2=(ความชื้น)
  Serial.print("Requesting URL: ");
  Serial.println(url);
  // This will send the request to the server
  client.print(String("GET ") + url + " HTTP/1.1\r\n" +
            "Host: " + host + "\r\n" + "Connection: close\r\n\r\n");
  delay(10);
  // Read all the lines of the reply from server and print them to Serial
  while(client.available()){
    String line = client.readStringUntil('\r');
    Serial.print(line);   }
  Serial.println();
  Serial.println("closing connection"); }
```

APPENDIX B (III)

Mobile App monitoring code by Blynk

```
#define BLYNK_PRINT Serial  // Hardware: NodeMCU Blynk Board
#include <ESP8266WiFi.h>
#include <BlynkSimpleEsp8266.h>
#include "DHT.h"            // including the library of DHT11 temperature and humidity sensor
#include <SimpleTimer.h>    //including the library of SimpleTimer
#define DHTTYPE DHT22       // DHT 22  (AM2302), AM2321

#define dht_dpin D2
DHT dht(dht_dpin, DHTTYPE);
SimpleTimer timer;
char auth[] = "f243ac1c782c41bcb1217ad83643a7ca"; // Auth Token by the Blynk App.
                                                   // Go to the Project Settings (nut icon).

char ssid[] = "vivo 1606";
char pass[] = "1a418915953a";
float t;                         // Declare the variables
float h;

void setup()
{
   Serial.begin(9600);// Debug console
   Blynk.begin(auth, ssid, pass);
   dht.begin();
   timer.setInterval(2000, sendUptime);
}

void sendUptime()
{
 float h = dht.readHumidity();
 float t = dht.readTemperature();
 Serial.println("Humidity and temperature\n\n");
 Serial.print("Current humidity = ");
 Serial.print(h);
 Serial.print("%  ");
 Serial.print("temperature = ");
 Serial.print(t);
 Blynk.virtualWrite(V0, t);
 Blynk.virtualWrite(V1, h);
 }

void loop()
{       Blynk.run();
        timer.run();        }
```

APPENDIX C

**LIST OF ABSTRACT FOR PAPER
AND PROCEEDING PUBLICATIONS**

APPENDIX C (I)

ABSTRACT OF PARER

Abstract of paper 1 (Published)

Perspective microscale piezoelectric harvester for converting flow energy in water way

Krit Koyvanich[1], Pruittikorn Smithmaitrie[2], Nantankan Muensit[1,3*]

[1]Department of Physics, Faculty of Science, Prince of Songkla University (PSU), Songkhla, Thailand
[2]Department of Mechanical Engineering, Faculty of Engineering, Prince of Songkla University (PSU), Songkhla, Thailand
[3]Center of Excellence in Nanotechnology for Energy (CENE), Prince of Songkla University (PSU), Songkhla, Thailand

*Corresponding author. Tel: (+66) 74288766; Fax: (+66) 74554489; E-mail: nantakan.m@psu.ac.th

ABSTRACT

This work proposes an energy harvester that captures the mechanical energy caused by water flow and converts into an electrical energy through the piezoelectric effect. A flexible piezo-film has been used as a transducer in the energy harvesting system and the kinetic energy of the water flow is produced by using the vortex induced vibration technique. When placing in water way the transducer is fluctuating in the vortex of the fluid flow, producing the kinetic energy of 44 µW at a low fluid velocity of 6.8 m/s and low frequency of 0.4 Hz. This configuration generates a corresponding open-circuit voltage of 6.6 mV at a matching load of 1 MΩ, leading to the maximum output power of 0.18 µW. An efficiency power conversion of the harvesting system was evaluated to be about 4.4 %. It is possible to use the proposed unit under gravitational force where there is a difference in the levels of the fluid no matter in water way or transporting parts such as petroleum pipes. However, rectifying the output voltage generated by the present micro generator is compulsory in order to feed small scale electronics and communication, for instance, wireless sensor networks. Furthermore, multiple arrays of the piezoelectric unit are also promising for delivering higher output power. Copyright © 2015 VBRI Press.

Keywords: Piezoelectric; PVDF; energy harvesting; hydropower.

Krit Koyvanich is a research scholar in the Department of Physics of Prince of Songkla University, Songkhla, Thailand. He received B.Sc. from Thaksin University in 1998 and M.Sc. in Physics from Kasetsart University in 2004. His research interest is in design and implementation of micro-scale power generator including energy harvesting systems.

Pruittikorn Smithmaitrie received his B.Eng. degree in mechanical engineering from Prince of Songkla University, Thailand, in 1996. After his graduation, he received a Royal Thai Government Scholarship to pursue his M.S. and Ph.D. degrees in the United States. In 2000, he obtained the M.S. degree in mechanical engineering from Vanderbilt University, Nashville, TN. In 2004, he received the Ph.D. degree in mechanical engineering from University of Kentucky, Lexington, KY. He has been a faculty member of the Mechanical Engineering Department, Prince of Songkla University, since 1996 and became an Associate Professor in 2008. His research interests are the analysis and design of mechatronic systems and piezoelectric applications.

Nantankan Muensit received her B.Sc. degree from Prince of Songkla University in 1983 and M.Sc. degree from Chulalongkorn University in 1986. In 1999, she obtained a Ph.D. degree in Material Physics from Macquarie University, Sydney, Australia. She has been a faculty member at Prince of Songkla University since 1987 and became an Associate Professor in 2004. Her research interest is mainly the preparation and applications of energy harvesting materials. Her publications including books and patents comprise more than 100 papers in various refereed journals and conference proceedings.

Introduction

For many years there have been remarkable evolutions of self-powered devices such as airborne and stationary surveillance cameras, medical sensors, and wearable personal electronics [1-3]. These devices are conceived to work in a standalone manner, in particular, in rural places or in unmanned vehicles. While there is a decrease in powering various electronic components, there is an increase in developing microgenerators to provide sufficient electrical energy for those low power consumption devices. One of the most recent technologies is the piezoelectric power generator where a mechanical

Abstract of paper 2 (Published)

Research Article

Electrostrictive Energy Conversion of Polyurethane with Different Hard Segment Aggregations

Pisan Sukwisute,[1,2] Krit Koyvanitch,[1,2] Chatchai Putson,[1,2] and Nantakan Muensit[1,2]

[1] *Department of Physics, Faculty of Science, Prince of Songkla University (PSU), Hat Yai 90112, Thailand*
[2] *Center of Excellence in Nanotechnology for Energy (CENE), PSU, Hat Yai 90112, Thailand*

Correspondence should be addressed to Nantakan Muensit; nantakan.m@psu.ac.th

This work reported the electrostriction of polyurethane (PU) with different aggregations of hard segments (HS) controlled by dissimilar solvents: N,N-dimethylformamide (DMF) and a mixture of dimethyl sulfoxide and acetone denoted as DMSOA. By using atomic force microscopy and differential scanning calorimetry, the PU/DMSOA was observed to have larger HS domains and smoother surface when compared to those of the PU/DMF. The increase of HS domain formation led to the increase of transition temperature, enthalpy of transition, and dielectric constant (0.1 Hz). For the applied electric field below 4 MV/m, the PU/DMSOA had higher electric-field-induced strain and it was opposite otherwise. Dielectric constant and Young's modulus for all the samples were measured. It was found that PU/DMF had less dielectric constant, leading to its lower electrostrictive coefficient at low frequency. At higher frequencies the electrostrictive coefficient was independent of the solvent type. Consequently, their figure of merit and power harvesting density were similar. However, the energy conversion was well exhibited for low frequency range and low electric field. The PU/DMSOA should, therefore, be promoted because of high vaporizing temperature of the DMSOA, good electrostriction for low frequency, and high induced strain for low applied electric field.

1. Introduction

Polyurethane (PU) is a versatile thermoplastic polymer, with a variety of physical and chemical electroactive properties. These properties allow PU to be used in numerous applications such as medical materials, sport goods, and coatings [1–3]. In the field of electroactive polymers, PUs are of great interest for actuation and energy conversion since they are capable of generating an electric-field-induced strain above 10% under an electric field 20 MV/m [4] and have an effective piezoelectric strain coefficient of 184 pC/N under a bias electric field of 25 MV/m comparable to that of a commercial piezoelectric PZT ceramic [5]. In addition, Guyomar and coworkers [6–9] proposed an analytical modeling based on the electrostrictive equations in order to explain the energy harvesting of PU elastomers, PU composites, and an electrostrictive poly(vinylidene fluoride-trifluoroethylene-chlorofluoroethylene) terpolymer. It was found that the energy harvesting ability of these polymers increases with increasing figure of merit (FoM) which is related to the dielectric constant and Young's modulus. Therefore, several

authors [3, 10–12] have studied and have modified structures of PU in order to control the dielectric constant and Young's modulus. Guillot and Balizer [11] reported that the electrostrictive coefficient decreases as the phase separation of HS and soft segments (SS) increase. Furthermore, the HS/SS ratio affected the electrostrictive response because the high HS contents (high polarized groups) led to the high dielectric constant, and Young's modulus [3]. Petrović et al. [10] found that PU with 50% SS concentration, the dielectric constant, and Young's modulus depend on the degree of chemical cross-link of HS. In fact, as the HS in PU tends to form strong intermolecular hydrogen bonds, the HS will aggregate and perform as the physical cross-link in nature [13, 14]. Hence, the properties of PU can also be improved by controlling the HS aggregations through the physical cross-link.

In the present study, PU thick films with different HS aggregations controlled by different solvents were prepared. The energy conversion ability and electrostriction effect, including the dielectric constant, Young's modulus, and the electric-field-induced strain of the PUs, were comparatively

APPENDIX C (II)

ABSTRACT OF PROCEEDING

Micro-scale Piezoelectric Harvester from Fluid Flow at Low Velocity

Krit Koyvanich [1], Pruittikorn Smithmaitrie [2], Nantankan Muensit [1,*]

ABSTRACT

We have developed a newly designed energy harvester for the utilization of energy from water flow with vortices based on cantilever beam energy conversion. It converts fluid flow energy into electrical energy through the vibration of a piezoelectric film. The full wave oscillation of the piezoelectric film was induced by vortex induced vibration phenomena to the piezoelectric film sheet (polyvinylidene fluoride, PVDF). Variations in the vibration frequencies have been created by pressure fluctuations in vortices of the fluid flow from the bluff body. The PVDF attachment obtained the oscillation from flow kinetic energy. The coupling mathematical model of energy harvesting technique and experimental data were established. Experiments were carried out to verify the validity of the numerical simulation results. It shows that the power output and the peak frequency obtained from the numerical analysis were in good agreement with the experimental results. This approach leads to the potential of hydropower harvesting and converting it into electrical energy for powering wireless devices. The micro-scale of the output power from this harvesting can be improved by increasing the piezoelectric constant of piezoelectric materials or by an optimization of the design harvesting process. Multiply arrays of this harvester together with a rectifier can be made available to be part of a hydropower harvesting devise placed into a flowing river.

Keywords: piezoelectric, fluid flow, PVDF, energy harvesting.

1. INTRODUCTION

Flow energy is readily available in the form of air and water streams for in and/or outside the building base. Energy conversion of ambient wind energy into electricity for wireless sensor networks (WSNs) have been explored by using small scale turbine systems [1]-[4]. However, complexity, a complicated fabrication, and high maintenance costs due to unfavorable viscous drag and baring loss are disadvantages. Moreover, piezoelectric materials propose the potential as a flow energy harvester by convert flow induced vibrations (FIV) or vortex induced vibrations (VIV) into electrical energy [5]. The designed harvester device in this work is proposed to show "eel/flag" motion based on an ultralow range of fluid velocity (<0.2 m/s). Generated powers of this device were estimated on possible harvesters' dimensions and experiments of flow harvesting setup, as well the computational simulation are calculated and the results discussed.

2. FLUID FLOW HARVESTING

The piezoelectric flag energy harvester consists of piezoelectric polymers attached behind a vortex generator (bluff body) in in small channel (pipe line) structure. Fluid-solid interaction induces AC voltage generation in the converter. An analytical VIV interacted to laminate film has been proposed by finite element methods (FEM), and the results are shown in Figure 1. Film's amplitude and frequency oscillation data have been obtained in various flow velocities by COMSOL multiphysics software. The combination of mechanical and piezoelectric equivalent circuits of the converter for electrical energy output is achieved by MATLAB Simulink. Physical and piezoelectric properties of film are presented in Table 1. Different flow velocities (U) and other properties of the elastic film, e.g. density, Poisson's ratio, Lame coefficient, have been used for FEM analysis.
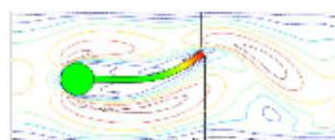

Figure 1: Contour diagram of the total displacement of film and velocity magnitude in the fluid [6].

The fluid flow energy harvesting setup is consisting with power flow supply, converter, and measurement units. Water flow velocity has been controlled by a vale. Open voltage output (V_{oc}) signals of the piezo film were detected by an oscilloscope. To calculate the electrical power generated (P) and the energy conversion coefficient of the device, principles to fluid flow and electrical AC power based calculations can be employed [7]-[8].

Table 1: Piezoelectric, mechanical properties [9], and the estimated power generated by PVDF.

The piezoelectric harvester generates random voltage amplitudes. On the other hand, the DC voltage amplitude depends on the fluid flow velocity generated. The maximum Voc. signal at low rang velocity that can be observed is about a micro watt. High frequency voltages of the harvested signal were from electromagnetic radiation of the measurement device. A low passed filter circuit is applied to the harvester unit to cut the not related frequencies off, which were over 30 Hz. A rectifier by a full wave bridge was added as well as a capacitor for energy storage. Energy management electronics must be matched to the sleep/measure/wake/transmit cycles to achieve maximum efficiency of the whole measurement system.

VITAE

Name   Mr. Krit Koyvanich
Student ID   5610230001
Educational Attainment

Degree	Name of Institution	Year of Graduation
Master of Science (Physics)	Kasetsart University	2005
Bachelor of Science (Physics)	Thaksin University	1998

Scholarship Awards during Enrolment

- Prince of Songkla University-Ph.D. Scholarship, Graduated school, 2013.
- Graduate School Dissertation Funding for Thesis, Graduated school.
- Research Innovation Funding, Research and Development Office (RDO), PSU

List of Publication and Proceeding

- Koyvanich, K., Smithmaitrie, P., Muensit, N. (2015). Perspective microscale piezoelectric harvester for converting flow energy in water way. Advanced Materials Letters, (6)6: 538-543. DOI: 10.5185/amlett.2015.SMS4.

- Koyvanich, K., Smithmaitrie, P., and Muensit, N. (2014. August 26-18). Micro-scale Piezoelectric Harvester from Fluid Flow at Low Velocity. Proceeding presented at International Conference on Smart Materials and Surfaces International Conference Proceeding: SMS 2014, Bangkok, Thailand, (Article 13), p.20. http://www.setcor.org/conferences/SMS-Bangkok-2014

- Sukwisute, P., Koyvanitch, K., Putson, C., and Muensit, N. (2013). Electrostrictive Energy Conversion of Polyurethane with Different Hard Segment Aggregations. Advances in Materials Science and Engineering, 2013: 318185. http://dx.doi.org/10.1155/2013/318185.